Functional Triazine-Based Porous Organic Networks

DISSERTATION

zur Erlangung des akademischen Grades eines

Doktors der Naturwissenschaften (Dr. rer. nat.)

an der Fakultät für Biologie, Chemie und Geowissenschaften

der Universität Bayreuth

vorgelegt von

Mario R. Liebl

aus Deggendorf

Bayreuth, 2018

Die vorliegende Arbeit wurde in der Zeit von September 2008 bis September 2018 in Bayreuth am Lehrstuhl für Anorganische Chemie III unter Betreuung von Herrn Prof. Dr. Jürgen Senker angefertigt. Die Laborarbeiten zu dieser Dissertation wurden im Zeitraum von September 2008 bis Januar 2013 durchgeführt.

Vollständiger Abdruck der von der Fakultät für Biologie, Chemie und Geowissenschaften der Universität Bayreuth genehmigten Dissertation zur Erlangung des akademischen Grades eines Doktors der Naturwissenschaften (Dr. rer. nat.).

Dissertation eingereicht am: 13.12.2018

Zulassung durch die Promotionskommission: 09.01.2019

Wissenschaftliches Kolloquium: 11.07.2019

Amtierender Dekan: Prof. Dr. Stefan Peiffer

Prüfungsausschuss:

Prof. Dr. Jürgen Senker (Gutachter)

Prof. Dr. Birgit Weber (Gutachterin)

JProf. Dr. Anna Schenk (Vorsitz)

Prof. Dr. Andreas Greiner

Für meine Familie

“Here are the most important pieces of advice that I´ve passed on to my children.
One, remember to look up at the stars and not down at your feet.
Two, never give up work. Work gives you meaning and purpose and life is empty without it.
Three, if you are lucky enough to find love, remember it is rare and don´t throw it away.”

- Stephen W. Hawking (1942-2018) -

Table of Contents

1 Summary

The aim of the present thesis was the synthesis and characterization of triazine-based porous organic networks. The pore structure of the networks and their gas sorption properties were investigated.
The overall synthesis strategy is based on two key concepts. First, the synthesis of porous permanently stable network structures with high specific surface areas and high gas sorption capacities. Therefore, the choice of suitable monomer connector and linker molecules was essential.
The second concept focuses on the introduction of functional groups into the porous network structures to influence the interaction between adsorbed gas molecules and sorbent surface. The synthesized porous networks aim at a high affinity and sorption selectivity towards gaseous CO_2, which was achieved by implementation of polar functionalities, e.g. triazine, imide, carbonyl or sulfonyl moieties, into the network structure. The energetically beneficial interaction with CO_2 results from strong dipole-quadrupole and quadrupole-quadrupole interactions between sorptive and sorbent.
The synthesized porous imide-based network materials were investigated for their potential as gas storage and gas separation materials for simulated CO_2/N_2 gas mixtures.

The triazine nodes which are characteristic for the organic polymer networks in this thesis were synthesized by cyclotrimerization of aromatic nitrile building blocks under different reaction conditions.
In a straightforward approach, the introduction of methyl groups in a structure similar to CTF-1 by cyclotrimerization of 2-methylterephthalonitrile in molten zinc(II) chloride was investigated. Infrared and ^{13}C MAS NMR spectroscopy of the resulting non-porous polymer confirmed successful triazine formation. The presence of considerable amounts of unreacted nitrile groups was ascribed to incomplete cyclotrimerization due to sterical hindrance effects caused by methyl groups in *ortho*-position to the nitrile groups. An increase of reaction temperature and time decreased the amount of methyl groups and overall nitrogen content.
To avoid an undesired sterical hindrance effect of *ortho*-methyl groups on nitrile cyclotrimerization, a similar reaction of 2,2'-dimethyl-4,4'-dicyanobiphenyl in molten zinc(II) chloride was conducted. The obtained porous material showed a high specific surface area of almost 1600 $m^2 g^{-1}$, however, only minor amounts of methyl and triazine groups were found in the synthesized material most likely due to thermal decomposition. A network material synthesized by cyclotrimerization of 4,4'-dicyanobiphenyl in molten zinc(II) chloride yielded corresponding results.

To avoid two different routes to synthesize porous triazine networks were performed by cyclotrimerization of 1,4-dicyanobenzene under autoclave conditions using $Y(OTf)_3$, $La(OTf)_3$ and $Zn(OTf)_2$ in combination with either piperidine or ammonium chloride, respectively, as catalyst systems. Infrared and ^{13}C MAS NMR spectroscopy confirmed successful triazine formation in all synthesized materials. For both catalyst systems the obtained materials did not show any considerable gas uptakes, however, contrary to the amorphous ATP-P polymers, powder XRD measurements detected long-range order in the three ATP-A materials.
The materials SMP-1 and SMP-2 were synthesized by nitrile cyclotrimerization of 1,4-dicyanobenzene in two different eutectic salt mixtures, SM-1 and SM-2. The lower melting points of the eutectic salt mixtures compared to neat zinc(II) chloride enabled nitrile cyclotrimerization at lower reaction temperatures. Again, ^{13}C MAS NMR and infrared spectroscopy confirmed successful triazine formation in SMP-1 and SMP-2. Both materials were found to be non-porous and powder XRD measurements revealed long-range order within both structures.

The syntheses of porous triazine-based polyimides (TPIs) were conducted in a facile one-pot polycondensation reaction of 2,4,6-tris(*p*-aminophenyl)-1,3,5-triazine (TAPT) with various aromatic tetracarboxylic acid dianhydride monomers. Solid state NMR and infrared spectroscopy measurements confirmed the formation of cross-linked polyimide networks and the successful introduction of functional groups for all TPI polymers. All investigated TPIs were insoluble in common organic solvents and exhibited high thermal stability up to 450 °C under air. Argon sorption measurements showed specific BET equivalent surface areas up to 809 $m^2\ g^{-1}$. The pore structure of TPIs was characterized as mainly microporous with pore diameters dominating in the range between 0.4 and 3 nm.
The highest CO_2 uptakes at 273 K and 1 bar were reported at 2.45 mmol g^{-1}. The isosteric enthalpies of adsorption ranged from 29 kJ mol^{-1} to 34 kJ mol^{-1}. The highest gas sorption selectivity for CO_2 over N_2 at 298 K and 1 bar yielded a value of 56 calculated from initial slope calculations. It was shown that the nature of the applied functionalities have a considerable influence on the gas sorption selectivities of the respective polymer networks.

The crystal structures of 2,4,6-tris(*p*-bromophenyl)-1,3,5-triazine (TBPT) and TAPT were solved from powder X-ray diffraction data. The synthesis of TBPT yielded a white, microcrystalline material. The crystal structure of TBPT was determined by X-ray diffraction analysis (orthorhombic, $P2_12_12_1$, a = 4.5359(4) Å, b = 19.7809(11) Å, c = 21.6744(11) Å, V = 1944.70(24) $Å^3$). The material 2,4,6-tris(*p*-aminophenyl)-1,3,5-triazine was obtained as a yellow, microcrystalline material. The crystal structure of TAPT was determined by X-ray diffraction analysis (orthorhombic, *Pbcn*, a = 17.7386(6) Å, b = 12.6142(4) Å, c = 7.7503(2) Å, V = 1734.18(9) $Å^3$).

2 Zusammenfassung

Das Ziel der vorgelegten Arbeit war die Synthese und Charakterisierung Triazin-basierter, poröser organischer Netzwerke. Weiterhin wurden die Porenstruktur und die Gassorptionseigenschaften der einzelnen Netzwerke untersucht.
Die angewandte Synthesestrategie basiert im Wesentlichen auf zwei Schlüsselkonzepten. Zum einen steht der Aufbau poröser und dauerhaft stabiler Netzwerkstrukturen mit großen spezifischen Oberflächen und hoher Aufnahmekapazität für Gase im Mittelpunkt. Hierbei erweist sich die Wahl geeigneter Konnektor- und Linkermoleküle als Ausgangsmonomere als essentiell wichtig. Zum anderen richtet sich der Fokus der Strategie auf der konsequenten Implementierung funktioneller Gruppen in die Netzwerkstruktur, um so die Wechselwirkung zwischen adsorbierten Gasmolekülen mit der Oberfläche des Sorbens in gewünschter Weise zu beeinflussen. Im Besonderen wurde bei der Synthese eine spätere hohe Affinität der Netzwerke zu CO_2, einhergehend mit einer hohen Selektivität gegenüber CO_2 im Vergleich zu anderen Gasen, berücksichtigt. Dieses wurde durch den gezielten Einbau polarer Funktionalitäten, wie beispielsweise Triazin-, Imid-, Carbonyl- oder Sulfonylgruppen, in die Netzwerkstruktur bewerkstelligt. Aufgrund starker Quadrupol-Dipol und Quadrupol-Quadrupol-Wechselwirkungen entsteht eine energetisch günstige Wechselwirkung zwischen Sorbat und Sorbens.

Die für die porösen organischen Netzwerke in dieser Arbeit charakteristischen Triazin-verknüpfungen wurden durch Cyclotrimerisierung aromatischer Nitrile unter verschiedenen Reaktionsbedingungen synthetisiert.
Zunächst wurde die Einführung von Methylgruppen in eine Struktur analog zu CTF-1 durch Cyclotrimerisierung von 2-Methylterephthalonitril in geschmolzenem Zink(II)-chlorid untersucht. Durch Infrarotspektroskopie und ^{13}C MAS NMR-Messungen konnten Triazin-Einheiten in dem erhaltenen unporösen Material nachgewiesen werden. Eine beträchtliche Anzahl an unreagierten Nitrilgruppen im Material kann mit einer sterischen Hinderung der Triazinbildung durch benachbarte Methylgruppen erklärt werden. Eine Erhöhung der Reaktionstemperatur bzw. eine Verlängerung der Reaktionszeit führten beide zu einer Verringerung der Anzahl der Methylgruppen sowie einem niedrigeren Stickstoffanteil im Material.
Um diesen negativen Effekt der sterischen Hinderung auf die Cyclotrimerisierung durch der Anwesenheit einer Methylgruppe in *ortho*-Position zu unterbinden, wurde die Synthese mit 2,2'-Dimethyl-4,4'-dicyanobiphenyl unter vergleichbaren Bedingungen in geschmolzenem Zink(II)-chlorid durchgeführt. Das entstandene poröse Material zeigte eine hohe spezifische BET Oberfläche von knapp 1600 $m^2\ g^{-1}$.

Aufgrund thermischer Zersetzung des Materials konnten jedoch nur geringe Mengen an Triazin- und Methyleinheiten nachgewiesen werden. Die Verwendung von 4,4‘-Dicyanobiphenyl als Ausgangsmaterial lieferte unter vergleichbaren Reaktionsbedingungen entsprechende Ergebnisse.

Um eine thermische Zersetzung der organischen Polymere zu verhindern, wurde die Cyclotrimerisierung von Terephthalonitril unter milderen Bedingungen in einem Autoklaven, unter Anwendung eines Katalysesystems aus $Y(OTf)_3$, $La(OTf)_3$ und $Zn(OTf)_2$ in Kombination mit Piperidin bzw. Ammoniumchlorid, durchgeführt. Infrarotspektroskopie und ^{13}C MAS NMR-Messungen konnten eine erfolgreiche Bildung von Triazineinheiten in allen Fällen bestätigen, wobei Gasadsorptionsmessungen in keinem Fall nennenswerte Porosität feststellen konnten. Im Gegensatz zu den amorphen Piperidin-katalysierten Materialien, konnte im Falle einer Katalyse mit Ammoniumchlorid mittels Röntgenpulverdiffraktometrie eine Fernordnung in den entsprechenden Materialien festgestellt werden.
Alternativ wurde eine Cyclotrimerisierung von Terephthalonitril in zwei verschiedenen eutektischen Salzschmelzen, SM-1 und SM-2, durchgeführt. Die, im Vergleich zu reinem Zink(II)-chlorid, niedrigeren Schmelzpunkte der beiden eutektischen Mischungen ermöglichten die Bildung von Triazin-Einheiten bei niedrigeren Reaktionstemperaturen. Auch in diesen beiden Fällen, konnten durch Infrarotspektroskopie und ^{13}C MAS NMR-Messungen die Bildung von Triazingruppen bestätigt werden. Sorptionsmessungen konnten bei beiden Materialien keine nennenswerte Porosität im relevanten Porenbereich feststellen, jedoch wurde in beiden Fällen mittels Röntgenpulverdiffraktometrie eine Fernordnung nachgewiesen.

Die Synthesen poröser Triazin-verknüpfter Polyimidnetzwerke (TPIs) wurden im Rahmen dieser Arbeit in einer Eintopfreaktion durch Polykondensation von 2,4,6-Tris(*p*-aminophenyl)-1,3,5-triazin (TAPT) mit verschiedenen aromatischen Carbonsäure-dianhydriden durchgeführt. Die Aufbau einer quervernetzten Polyimidstruktur und der erfolgreiche Einbau von funktionellen Gruppen konnte durch Festkörper-NMR- und infrarotspektroskopische Messungen bei allen TPI-Materialien nachgewiesen werden. Die untersuchten TPI-Polymere waren nicht löslich in organischen Lösungsmitteln und zeigten hohe thermische Stabilität bei Temperaturen von bis zu 450 °C unter Luft. Die spezifischen Oberflächen aus Argonsorptionsmessungen erreichten Werte von bis zu 809 $m^2\ g^{-1}$. Die Porenstruktur der TPIs war überwiegend mikroporös, wobei die gefundenen Porendurchmesser sich hauptsächlich im Bereich zwischen 0.4 und 3 nm bewegten.
Bei der Aufnahmekapazität für CO_2 bei 298 K und 1 bar wurden Werte von bis zu 2.45 mmol g^{-1} erreicht. Die isosterischen Adsorptionsenthalpien wurden in einem Bereich von 29 bis 34 kJ mol^{-1} bestimmt. Die höchste Adsorptionsselektivität für CO_2 über N_2

erreichte einen Wert von 56 bei 298 K und 1 bar. Die erzielten Ergebnisse zeigen, dass die Art der in die Netzwerkstruktur eingebauten funktionellen Gruppen in essentieller Weise auf die Adsorptionsselektivitäten der entsprechenden organischen Polymernetzwerke beeinflussen.

Im letzten Teil dieser Arbeit wurden die Kristallstrukturen von 2,4,6-Tris(*p*-bromophenyl)-1,3,5-triazin (TBPT) und TAPT mittels Röntgenpulverdiffraktometrie gelöst. Die Synthese von TBPT lieferte ein weißes, mikrokristallines Material. Die Kristallstruktur von TBPT wurde aus den Daten der Röntgenpulverdiffraktometrie bestimmt (orthorhombisch, $P2_12_12_1$, a = 4.5359(4) Å, b = 19.7809(11) Å, c = 21.6744(11) Å, V = 1944.70(24) Å^3). Die Synthese von TAPT lieferte ein gelbliches, mikrokristallines Material. Die Kristallstruktur von TAPT wurde ebenfalls aus den Daten der Röntgenpulverdiffraktometrie bestimmt (orthorhombisch, *Pbcn*, a = 17.7386(6) Å, b = 12.6142(4) Å, c = 7.7503(2) Å, V = 1734.18(9) Å^3).

3 Introduction

The constant growth of the global population and the increasing industrialization are accompanied with a substantial demand for resources and energy. Nowadays, fossil fuels like petroleum, natural gas and coal are still regarded as the world´s most important energy sources, due to their worldwide availability, their abundance and the inherent energy density.[1] The combustion of fossil energy sources produces CO_2, a greenhouse gas which is considered to be one of the major causes of global warming.

From 1960 to 2010, the global CO_2 level in the atmosphere has increased from 310 ppm to 390 ppm.[1] A correlation of the ability of CO_2 gas to store heat in the atmosphere and an increase of the average temperature on the planet´s air and surface is regarded to be very likely.[2,3] Further consequences expected to be directly related to higher CO_2 concentrations in the atmosphere are the occurrence of natural disasters such as droughts, floods and hurricanes as well as rising sea levels and the melting of glaciers and polar ice caps.[2] An impact of the increased surface temperature on the aquatic fauna caused by ocean acidification from elevated levels of CO_2 dissolved in the global oceans is still under discussion.[4-7] Due to the already visible effects of the rising global surface temperature the scientific community and policymakers especially in highly developed industrialized countries have agreed to start efforts to reduce greenhouse gas emissions significantly in the near future.[3]

In Germany, more than 90% of the greenhouse gas emissions in 2011 originated from industrial and energy production (Figure 3-1a).[8]

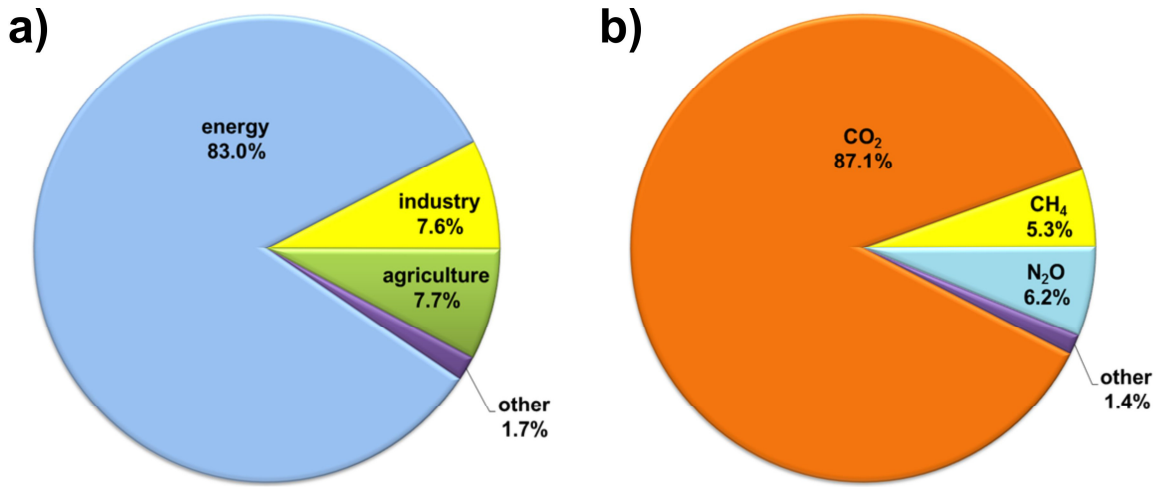

Figure 3-1: *Contributions to greenhouse gas emissions in Germany in 2011 by a) emission sources and by b) greenhouse gas types.*[8]

The majority of the total emissions are covered by CO_2 generated by fossil fuel combustion (Figure 3-1b).[8] The share of emissions contributed to road traffic (excluding agricultural and military sector) in 2011 has been estimated at roughly 16 % with reference to total CO_2 emissions.[8]
Generally, the most effective way to reduce greenhouse gas emissions from these sources might of course be the development of sustainable energy solutions and production cycles. However, such sustainable technologies, that are on the one hand able to cover the present energy demand and on the other hand compete with conventional power plants are currently not available and will presumably not be in the near future.

A promising short-term solution to reduce emissions is to capture CO_2 before it is released into the atmosphere. Therefore, several different approaches under the concept of CO_2 capture and sequestration (CCS) are currently discussed.[9,10] The fundamental concept behind CCS is to remove large quantities of CO_2 from the atmosphere, convert it into a disposable form which can be stored in subterranean deposits, e.g. porous rock formations or depleted oil and gas fields.[11] A more detailed overview on this topic can be obtained from a number of review articles published recently.[1,2,12-14]
The most straightforward approach by simply trapping gaseous CO_2 on the planet´s surface, however, is considered to be inefficient due to its high degree of dilution in air. Therefore, it is more reasonable to capture CO_2 directly from the various emitting sources like industrial production sites, refineries, oil and gas production sites or power plants. In a recent report, CO_2 has been applied to produce hydrocarbon fuels *via* Fischer-Tropsch synthesis after conversion to CO.[15]

The separation of CO_2 from gas mixtures before (pre-combustion) or after (post-combustion) the combustion process turned out to be one of the most promising approaches. Among several different concepts for CO_2 capture and separation, there are three key fields of application regarded to be very promising for an efficient reduction of CO_2 emissions:[13] 1) CO_2/H_2 separation from fuel gas (e.g. syngas), 2) CH_4/CO_2 separation from natural ("natural gas sweetening") or landfill gas and 3) CO_2/N_2 separation from flue gases.
The two applied processes performing pre-combustion gas separations are characterized by separating CO_2 from either CH_4 or H_2 at high pressures. The high amount of CO_2 and N_2 (over 40%) in typical natural gas mixtures has a negative effect of the utilization of the gas production sites.[13] Therefore, the separation of CO_2 from the original gas stream right at the source of production increases the efficiency of the gas field significantly. When regarding landfill gas sources the amount of CO_2 between 40 and 60% in the emitted gas streams is even higher compared to natural gas.[14] The improvement of the gas purity of landfill or natural gas on the one hand and the reduction of pipeline corrosion on the other hand might be the most striking arguments for efficient CH_4/CO_2 separation techniques.[14]

The separation of CO_2 from H_2 is an essential step in hydrogen fueled gas power plants to produce hydrogen from methane rich fuel gas.[13] In a two-step process, natural methane-containing fuel gas is converted into syngas (gasification), followed by a water-gas shift reaction to eliminate CO from the gas mixture.[13] After these two steps, the remaining gas mixture mainly consists of CO_2 and H_2, which have to be separated prior to the combustion process.[13]
The established oxy-fuel combustion might be one of the best known applications for post-combustion CO_2 separation and has been investigated thoroughly in the past.[16,17] The basic concept behind this process is to burn fossil fuels with pure oxygen under elevated pressure in order to yield water and CO_2 in higher concentrations compared to conventional combustion in air. The main fraction of the high CO_2 content in the flue gas stream (typically between 65 and 85%) could be captured and sequestrated, while minor amounts of flue gas CO_2 are recycled into the fuel gas stream.[17] Due to the exclusion of nitrogen throughout the whole combustion process, the emitted gas volume is significantly lower compared to conventional air combustion while the energy output efficiency is increased.[13] However, a considerable drawback of the oxy-fuel technique is the energy intensive, and thus cost intensive production of sufficient amounts of pure oxygen by cryogenic separation.[2] Furthermore, an efficient separation of CO_2 and H_2O requires further resources.

As another example for post-combustion CO_2 capture, the solvent scrubbing approach has been well established and commercially available in the oil and gas industry for more than 60 years.[14] During a typical solvent scrubbing process at atmospheric pressure and temperatures below 100 °C a mixed flue gas stream is passed through an aqueous adsorbent solution a where the weakly acidic CO_2 gas is selectively bound and thus removed from the flue gas stream.
Basically, the concept of removing CO_2 by solvent absorption can be distinguished in physical and chemical absorption. In physical solvent scrubbing processes, CO_2 is bound by weak non-covalent bonding in the respective medium. Thereby, the actual CO_2 uptake is proportional to the applied CO_2 partial pressure at constant temperature. The physical adsorption of CO_2 on solid surfaces exhibits a good trade-off between comparatively low gas/surface interaction energies, important for an energy efficient regeneration, and sufficient CO_2 adsorption capacities.[18] The determination of the enthalpy of adsorption could serve as benchmark for the adsorption energy between CO_2 and the sorbent surface. In this context adsorption enthalpies between 25 and 50 kJ mol^{-1} are accepted to be a good balance between selectivity and reversibility.[19] Thus, the applicability of the process for CO_2 capture from flue gas is rather limited at atmospheric pressure. Typical examples for physical CO_2 solvent scrubbing are the Selexol process, Rectisol process, Purisol process and fluorinated solvent processes.[2]

Different to physical solvent scrubbing, the processes of chemical solvent scrubbing are based on strong covalent bonding between acidic CO_2 molecules and basic solvents, e.g. aquaeous amine solutions. The process is described schematically in Figure 3-2.

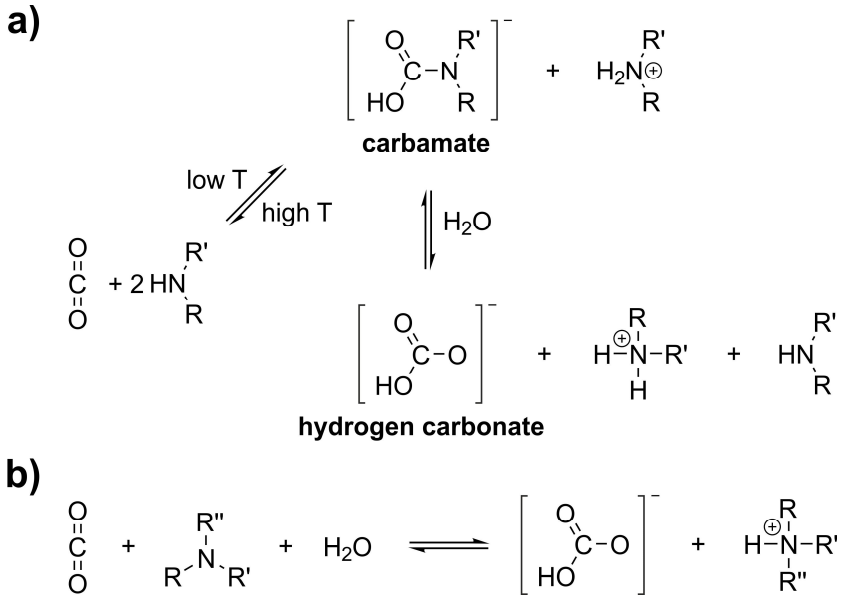

Figure 3-2: *Reaction scheme of chemical absorption of CO_2 in a) primary or secondary and b) tertiary amine solvents.*[13]

While being selectively and covalently bound in the solvent, CO_2 can be removed efficiently from flue gas streams even at low partial pressures. The solvent can be regenerated at elevated temperatures by removing gaseous CO_2. However, it is generally accepted that different factors like the degradation of amine solvents caused by reactive impurities in flue gas streams and an energy-intensive solvent regeneration step have a considerable effect on the process operating costs.[11,13,14] For instance, the presence of oxygen, even in low amounts of 3-4% e.g. in flue gas streams, could lead to serious degradation of amine solvents and lower the efficiency of CO_2 absorption significantly.[20]

For the concepts based on physical and chemical absorption, it is a major challenge to deal with the trade-off between efficient gas absorption and energy efficient sorbent regeneration. Both will have a considerable impact on feasibility and profitabilty of potential solutions when regarding large-scale applications.

Beside solvent scrubbing methods a number of alternative concepts for CO_2 capture and separation at low pressures from gas streams have been investigated in the past. Considerable efforts on efficient CO_2 capture and separation have been put into research on several different approaches like membrane gas separation,[1,21,22] chemical looping,[23] clathrate trapping[24] or absorption in ionic liquids.[25]

One of the most promising approaches in low pressure CO_2 capture and separation is the adsorption of CO_2 on porous solid sorbents. Several different solid adsorbent materials like zeolites, activated carbons, amine grafted silica or MOFs are investigated for their potential towards post-combustion CO_2 capture and separation applications. Recently, The National Energy Technology Laboratory (NETL) of the United States Department of Energy (DOE) defined a general framework for the performance of adsorbent materials for post-combustion CO_2 capture applications.[20]

In order to perform an efficient separation of CO_2 from gas streams, a number of specific challenges have to be overcome by potential sorbent materials. Beside the well known zeolites and activated carbon materials, tremendous efforts have been taken to develop and investigate different types of solid sorbents like metal-organic frameworks (MOFs), amine-functionalized mesoporous silicas and porous organic polymers (POPs).[2,26-30]
Zeolites, for instance, exhibit high specific surface areas and good adsorption performance for CO_2.[30,31] The high affinity of zeolites to water, however, might lower the CO_2 adsorption capacity significantly and increase the efforts for regeneration when moisture is present in the gas stream at low temperatures.[2,13,32] Activated carbons are cost-effective sorbent materials but show poor selectivity for CO_2 in the presence of other gases.[13,14,32] Amine-grafted mesoporous silica, e.g. derived from MCM-41,[33] are able to adsorb high amounts of CO_2 and show good selectivity for CO_2 over N_2.[12,34-37] The two major drawbacks for these materials for low pressure gas storage applications, however, are the moderate stability in the presence of moisture in the gas stream and the energy intensive regeneration of the adsorbent due to carbamate formation between CO_2 and amine groups on the sorbent surface.[13,20,35]

Beside the mainly inorganic sorbent materials there is a number of porous organic/inorganic hybrid and organic materials that have drawn remarkable attention in the past few years.
The class of porous metal-organic framework (MOF) materials is without doubt one of the most promising for CO_2 capture and separation applications at low temperature and atmospheric pressure.[29,38] Three-dimensional porous organic polymer networks (POPs) developed shortly after MOFs show comparable properties.[18,39,40] Similar to MOFs, the three-dimensional POP networks can be built up from a large pool of suitable organic building blocks. Generally, the applied monomers and the chosen reaction conditions mainly define the properties of the final network material.
Many of the published POP structures combine desirable features like high thermal and chemical stability, high specific surface areas and micropore volumes with cost-effective and modular synthesis procedures.

The modular system enables a tailored design of porous organic network structures for certain fields of application like heterogeneous catalysis, drug delivery systems, optoelectronics, sensor materials, membranes or gas storage and separation devices.[28,40-44]

The following paragraph will give a short outline on the present thesis. Chapter five is dedicated to give an overview on the theoretical background of porous materials as well as on the concept of porosity itself. Starting with a discussion on the current literature on porous organic materials, with a distinct emphasis on purely organic networks. The theoretical concepts of adsorption on solid surfaces and porosity according IUPAC classification will also be highlighted.

The results of the experimental work on triazine networks synthesized by cyclotrimerization are presented in chapter six. The first part presents the results of the works on functionalization of covalent triazine frameworks. The synthetic potential of the synthesis method by Kuhn *et al.* to introduce functional groups in covalent triazine frameworks are discussed profoundly.[45] Furthermore, the catalyzed cyclotrimerization of nitriles at lower temperatures under solvothermal conditions and its applicability for network formation and functionalization have been evaluated. The main subject of the last section of this chapter discusses the cyclotrimerization of dicyanobenzene (DCB) in zinc(II) chloride containing salt melts.

In the second part of chapter six the experimental results on synthesis and characterization of porous triazine-based polyimide materials (TPIs) are presented and discussed. The results in this chapter have already been published.[46] The porous networks have been synthesized by a condensation reaction of 2,4,6-tris(*p*-aminophenyl)-1,3,5-triazine (TAPT) with various commercially available dianhydrides. The influence of the rigidity of the dianhydride linkers on the porosity of the respective polyimide network is dicussed. The synthesized polyimide networks have been thoroughly investigated and characterized by infrared and CP MAS NMR spectroscopy, elemental analysis and thermogravimetric analysis.

Furthermore, porosity and gas sorption properties of the synthesized polyimide networks have been investigated. The porous structure has been characterized by argon and carbon dioxide sorption measurements. From the resulting isotherms different characteristic properties of porous materials like specific BET surface area, pore volume and pore size distribution have been determined by applying non-local density functional theory (NLDFT) and quenched solid density functional theory (QSDFT) methods. Additionally, the gas sorption uptakes and gas sorption selectivities of the polyimide networks for CO_2 over N_2 have been evaluated. The gas sorption selectivity is determined by applying the Henry method and the IAST method on the adsorption isotherms of the synthesized TPI networks.

The CO_2 uptake capacity and CO_2 sorption selectivity of a given material are regarded as two important indicators for a potential application of a sorbent in low-pressure CO_2 separation.

The last part of chapter six presents the crystal structures of the microcrystalline solids 2,4,6-tris(*p*-bromophenyl)-1,3,5-triazine (TBPT) and TAPT solved from powder XRD data. These two new crystal structures will be discussed in detail and compared to the already known crystal structure of 2,4,6-triphenyltriazine (TPT).

The experimental details concerning the work for this thesis are presented in chapter seven.

4 Aim and Motivation

The scope of this thesis is to synthesize and characterize functionalized thermally and chemically stable porous organic polymers by applying different synthesis strategies. In the following, the CO_2 sorption properties of the synthesized polymer networks at low pressures shall be analyzed.

The efficiency of a potential CO_2 sorbent material based on physisorptive interactions mainly depends on two key features, high gas uptake capacities and high sorption selectivity towards the desired adsorptive. High CO_2 gas uptakes and a good CO_2 selectivity at ambient conditions in a reversible adsorption process are characteristic features for several POP networks.[47]

First, the sorbent must be able to adsorb a sufficiently high amount of the desired type of gas, e.g. CO_2, by providing the required amount of adsorption sites. For porous organic polymers (POPs) the amount of available adsorption sites is closely related to the apparent pore volumes and surface area of the sorbent. Consequently, the synthesized porous frameworks should possess high surface areas and pore volumes on the one hand, and a stable and permanent framework structure to withstand a collapse of the pore system at given operation conditions on the other hand. For the latter, the structure of the sorbent requires a certain degree of rigidity, e.g. by introducing rigid monomer units or by enabling a high degree of cross-linking within the network. In most cases, the final structure of the porous network material strongly depends on the applied synthesis conditions and is difficult to predict, especially for amorphous pore systems. For example, porous materials with tunable pore sizes might be very useful for gas capture and separation applications. The concept has been demonstrated successfully by Tilford *et al.* by adjusting the pore sizes of highly ordered boronate-based covalent organic framewoks (COFs).[48]

The second feature can be described as the ability of a given sorbent material to "distinguish" between different gas adsorptives to be adsorbed on its surface. Therefore, the sorbent material should provide a high selectivity towards a desired adsorptive to be adsorbed preferably on the available adsorption sites. In this thesis, the main focus lies on the gas sorption selectivity for CO_2 over N_2 at low pressures up to 1 bar. The chemical composition of the sorbent surface could influence the interaction with a given adsorptive significantly, e.g. dipole-dipole or dipole-quadrupole interactions.

An ambitious challenge in the synthesis of porous organic polymers is the functionalization of the inner pore walls, while at the same time maintaining the porous properties of the organic network structure. By incorporating various functional groups into the pore structure, the tunable structural and chemical properties of the synthesized porous materials

could be useful for a broad spectrum of different applications. In a recent review D'Alessandro *et al.* reported that polar surfaces seem to have a positive effect on the CO_2 storage capacity of a material.[13] In a recent study, Klumpen *et al.* have shown that the presence of ultramicropores and polar groups within the framework have a beneficial effect on CO_2 uptake and CO_2 sorption selectivity towards other gases like CH_4 and N_2.[49] The CO_2 uptake of a porous network material can also be increased when substituting phenyl units against triazine rings.[50] The increased uptake might be ascribed to the increased dipole-quadrupole interaction between the nitrogen atoms and the CO_2 molecules.

The syntheses of the porous networks within this thesis follow the basic concepts towards an effective interaction between the sorbent surface with CO_2 gas as adsorptive, namely the introduction of polar functionalities in a mainly microporous or even ultramicroporous pore system.
In the first part of the thesis the synthesis of triazine-based porous polymeric network materials is performed by pursuing two different pathways. One synthesis approach concentrates on the build-up of porous triazine-based networks *via* cyclotrimerization of different organic building blocks carrying nitrile groups under reversible conditions at high temperatures. The influence of the applied building blocks and salt melts on the composition and properties of the resulting networks will be investigated. Furthermore, the possibility to introduce functional groups into triazine networks under comparatively harsh ionothermal conditions will be evaluated.
In an alternative approach, triazine-based networks should be synthesized by a low-temperature synthesis route under solvothermal reaction conditions. Therein, the cyclotrimerization of nitrile building blocks are catalyzed by pyridine or ammonium chloride and selected trifluoromethanesulfonate salts under comparatively mild reaction conditions. The access to a synthesis method at milder reaction conditions theoretically offers the possibility to introduce a larger number of different functional groups into triazine networks. The influence of the reaction conditions and the catalyst on the network formation and network composition will be discussed. Additionally, cyclotrimerization of DCB in $ZnCl_2$-containing salt melts will be investigated. The two investigated eutectic mixtures - one consisting of NaCl, KCl and $ZnCl_2$, the other of KCl and $ZnCl_2$ – show lower melting points compared to neat zinc(II) chloride. The lower melting point of the eutectic salt melts might enable triazine cyclotrimerization at lower temperatures compared to the synthesis route described by Kuhn *et al.* for CTF-1.[45] Again, the lower synthesis temperatures for the triazine network might be beneficial for the introduction of a broader variety of functional groups by avoiding thermal decomposition and possible side reactions.

In the second part of this thesis, the synthesis of porous polyimide network materials shall be performed by a kinetically controlled polycondensation reaction. The synthesis concept

for the polyimide networks described in this thesis is based on a condensation reaction of the trigonal triamine TAPT with various commercially available aromatic dicarboxylic acid dianhydrides. Regarding the potential for gas separation applications a polar polyimide connection itself will be probed on their potential to physisorb polar gases like CO_2. Additionally, the triazine ring in TAPT should be beneficial for CO_2 adsorption on the network surface compared to common aryl rings. The rigidity of the triamine is supposed to withstand a collapse of the pores in the network system and be able to maintain permanent porosity. The structure and composition of the resulting polymer networks will be determined and evaluated comprehensively.

Additionally, the correlation of gas sorption properties and the respective structural properties of the synthesized polyimide networks will be discussed on the basis of gas sorption experiments with different adsorptive gases at different temperatures. The gas sorption selectivity of porous polyimide networks towards CO_2 will also be investigated. Although, these materials should be applicable for several different CO_2-containing gas mixtures reported in the literature, e.g. CO_2/N_2, CO_2/H_2 or CO_2/CH_2, the main focus of the sorption selectivity experiments within this thesis aims on the sorption selectivity for CO_2 over N_2.

5 State of the Art

5.1 Porous Materials

In everyday life, materials containing internal voids are generally labeled as porous.[51] However, for a more differentiated discussion, it is very useful to establish a consistent terminology for the characterization of porous materials. A generally accepted collection of recommendations on this issue has been published by the IUPAC a few years ago.[52] Therein, porosity is generally described as the ratio of the volume of void space to the total volume occupied by the solid.[52] As a convention these void spaces or surface cavities are called pores, if they are deeper than wide.[52,53] This definition separates pores from conventional roughness of the material surface.

A fundamental aspect in the characterization of porous materials is the distinction between structural and textural porosity.[54] The term structural porosity is applied, if pores are generated directly from the structural setup of a material. For ordered materials, e.g. zeolites, MOFs or certain COFs, the pore dimensions could be directly derived from the respective crystal structures.[54,55] It should be noted that the applied terminology for MOF and zeolite materials is similar.[56-58] Textural porosity, however, is generated by interparticular voids arising from a statistical packing of particles.[54] The nature and dimension of the voids is closely related to the size and shape of the packing particles. For some materials it is possible to convert textural porosity into structural porosity by sintering.[54]

An alternative method in the characterization of porous solids is to distinguish between open and closed pores.[52] Closed pores are defined as isolated hollows within the structure of porous materials.[52] As an exchange of matter is not possible, these pores could not be detected by gas sorption methods.[52] A high amount of closed pores, especially when implemented in a polymer matrix, are able to reduce the polymer´s heat transfer rate significantly compared to the respective non-porous material.[54] Spray foams, as an example, containing a high amount of closed pores (closed-cell foams) are used as thermal insulators in the construction industry. In an open pore system the different pore types are connected and able to communicate with each other. These open pores allow an exchange of matter with the outer environment making them accessible to an external gas or fluid.[52] Hence, the internal pore volume and surface area of open pores can be determined by applying gas sorption techniques.

Probably the most versatile and popular characterization of porous materials has been presented by the IUPAC in 1985.[59] Herein, the classification of the pores depends on the internal pore width within the respective porous material. The internal pore width is defined as the pore diameter in cylindrical and spherical shaped pores and as the wall-to-wall distance for slit-like pores.[59] According to the IUPAC, pores which are characterized by gas sorption analysis can be divided in three fractions of size:[59,60] (i) Micropores with a maximum pore width of 2 nm, (ii) mesopores exhibiting internal widths between 2 and 50 nm and (iii) macropores with internal pores larger than 50 nm in diameter.[59] In some reports in the literature the micropore fraction has been further divided into supermicropores (> 0.7 nm) and ultramicropores (< 0.7 nm).[54] Well known examples for microporous materials are activated carbons and zeolites, while porous silica materials, like MCM-41 and SBA-15, are typically mesoporous systems.[31,54] The classification fits to both, ordered and disordered materials. Especially highly disordered materials might contain pores of all three size ranges, which are then described as hierarchical pore systems.[54] The hierarchical structure combines the high specific surface areas of microporous materials and the decreased transport and diffusion restrictions of meso- and macroporous materials.[61]

To date, a broad variety of porous polymeric materials derived from different synthetic approaches has been developed.[62] Zeolites and active carbons have been known for a long time as sorbent materials for gas and liquid adsorption purposes. In the late 90s the development of zeolite-analogous coordination polymers started a new era in the field of porous materials.[63-66] These materials, today widely known as metal-organic frameworks (MOFs), consist of metal atoms or metal oxide clusters (“nodes” or “joints”) connected by coordinating organic molecules (“connectors” or “linkers”) to form two- or three-dimensional networks. By varying different types of linkers and nodes a large number of metal-organic frame works could theoretically be synthesized.[67] The self-assembly of the networks built up from a reversible coordination of the organic linkers and metal centers provides crystalline structures with a high degree of regularity.

By selecting linkers of sufficient rigidity, e.g. aromatic carboxylates or amines, three-dimensional MOF structures with defined internal voids and pores on nanometer scale could be synthesized. These pores do not collapse even after removal of the solvent. The size of the generated pores is directly related to the applied linker molecules and some of the synthesized MOFs exhibit ultrahigh specific BET surface areas over 6000 $m^2\ g^{-1}$.[68-74] The regular nano-sized pores are capable of confining guest molecules comparable to zeolitic molecular sieves. The combination of a high degree of pore regularity, tunable pore sizes and shapes as well as the possibility to functionalize the inner pore surfaces are considerable and advantageous features of MOFs compared to common activated carbons and zeolites.

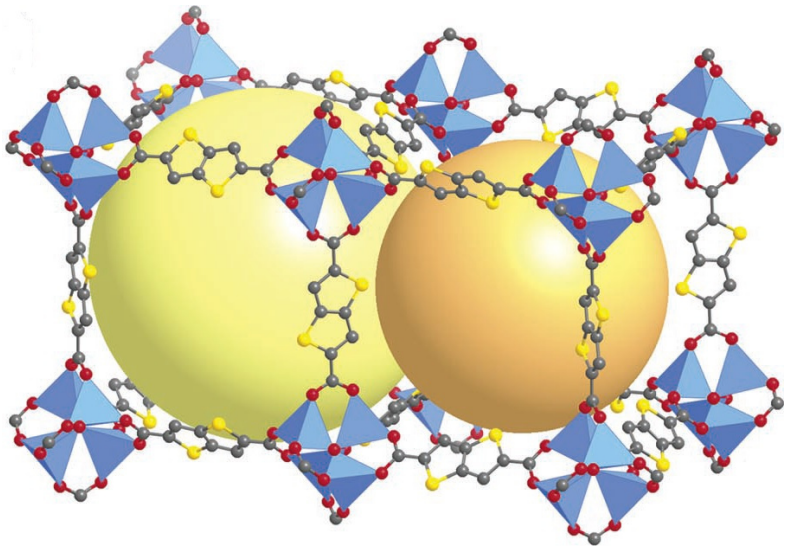

Figure 5-1: *Structural display of the framework connectivity of IRMOF-20. Tetrahedral zinc coordination spheres are marked blue. Large orange and yellow spheres mark the present voids in the framework. Atom colors: dark gray (C), red (O), orange (S). Adapted with permission from* [75]. *Copyright 2018 American Chemical Society.*

In the past ten years tremendous efforts have been made to investigate the features of MOFs thoroughly. Thus, MOFs have been considered for applications like e.g. chemical separation,[76-78] gas storage,[79-84] heterogeneous catalysis,[85-87] sensing,[88] membanes,[89,90] drug delivery[91,92] and ion conduction.[93,94] Due to high specific surface areas and large pore volumes MOFs have also been investigated for their potential as adsorbent materials in carbon dioxide and hydrogen sorption,[13,95-99] nitric oxide capture,[100] water and amine sorption.[101,102] Especially for possible applications in CO_2 capture and separation a remarkable number of studies could be found in the literature.[1,2,13,14,29,103,104] Some examples like Mg-MOF-74 (Mg_2(dobdc)), Mg_2(dobpdc) or mmen-CuBTTri exhibit extraordinary high CO_2 uptakes up to 6.42 mmol g^{-1} and IAST sorption selectivity ratios of CO_2 over N_2 up to 327, which are among the highest values reported to date.[29,105,106] It is suggested that the CO_2 uptake and adsorption selectivities are not only influenced by inner surface area and total pore volume but also from the nature of the metal ions, functionalization of the networks, pore sizes and adsorption enthalpies.[26]

In a recent report, Lyndon *et al.* developed a photo-sensitive MOF showing structural changes induced by dynamic light with direct influence on the materials CO_2 sorption properties.[107] Even though the development is in an early stage, the material serves as an example for energy-efficient sorbent regeneration.

Nonetheless, there are some drawbacks that might limit the application of MOFs in certain areas. Surely one of them is the usually limited hydrolytic stability of MOFs where even normal humidity could lead to a decomposition of the framework.[108] However, recently published ZIF-[109,110] and MIL-[111-113] materials as well as Bio-MOF-14[114] and $Ni_3(BTP)_2$[115] show a remarkable stability even in boiling water and under steam conditions.

Porous organic polymers (POP) are a new class of materials characterized by covalently linked organic polymers showing permanent porosity.[116] The choice of suitable organic monomers with a sufficient degree of rigidity to withstand the collapse of the pores in the porous system is essential in POP synthesis.[117] Characteristic properties like thermal and chemical stability, low density, high specific surface areas and pore volumes make POPs interesting candidates for applications such as e.g. adsorbents, catalysts or sensoring materials.[28,116,118] The modular synthesis concept provides numerous different network structures by connecting suitable monomers using methods known from organic chemistry.

The field of POPs could be further divided into porous polymer networks and polymers of intrinsic microporosity (PIMs).[119] The difference between the two sub-classes is related to their structural properties. While POPs generate porosity by rigid building blocks and sufficient cross-linking within the polymer structure to form a stable framework, PIMs obtain porosity by usage of rigid and non-linear building blocks preventing a space-efficient packing of the formally one-dimensional polymer chains.[119-123] The packing pattern of the stiff polymer chains creates internal voids in the PIM structure which are accessible for guest molecules.[124-139] Exemplarily, the synthesis of PIM-1 from tetrafluoroterephthalonitrile (*ortho*-dihalide monomer) and the sterically constrained 5,5',6,6'-tetrahydroxy-3,3,3',3'-tetramethyl-1,1'-spirobisindane (catechol monomer) is illustrated in Figure 5-2.[137] Some PIMs show good solubility and processability making them suitable for producing porous membranes.[140,141]

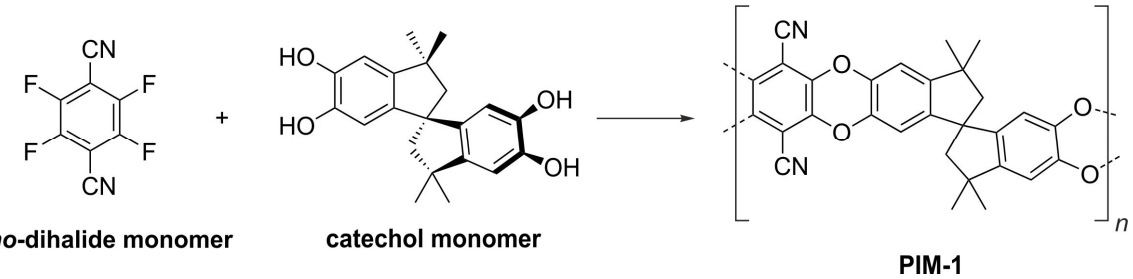

Figure 5-2: *Synthesis scheme of PIM-1.*[137]

The sub-class of three-dimensionally linked POP networks represents the larger fraction in the field of POPs and will be regarded in more detail within this thesis. Due to the wide range of possible synthesis methods, a remarkable number of different highly cross-linked and porous organic polymer network materials have been reported to date.[18,116,117] Although there are several synthesis concepts that have been proven to be suitable to produce POP networks,[142-151] the materials known as COFs, CTFs, CMPs, and PAFs are probably the most popular and promising examples.[116,152-154] The structural aspects of the latter materials will be discussed in the following paragraphs.

The presence of permanent porosity including high specific surface areas and pore volumes is a characteristic feature of POPs. Typically, the pore diameters found in POP networks range from micropores to small mesopores. The structure of the materials requires a certain degree of rigidity in order to withstand capillary pressures and prevent the pores from collapsing in the dry state.[155,156] Therefore, the use of sufficiently rigid monomer units is recommended.[117]

The numerous existing POPs can be divided in two classes, namely ordered and disordered network structures. The chemical composition and morphology of POP networks significantly depend on the applied reaction conditions. The synthesis of crystalline ordered network structures generally requires reversible reaction conditions. The reversibility of the reaction eliminates defects in the networks and enables the generation of thermodynamically stable structures showing uniform pore sizes. Kinetically controlled reaction mechanisms, in contrast, provide disordered materials with predominantly amorphous morphology. The presence of permanent porosity in both types of materials depends on the rigidity of the polymer network.[156] The absence of reversibility in the synthesis reactions yields non-uniform pore size distributions which are characteristic for amorphous POP networks.

5.2 Ordered Porous Organic Polymer Networks

5.2.1 Covalent Organic Frameworks from Boroxine and Boronate Linkages

After the reports of the first metal-organic frameworks a new class of porous networks named covalent organic frameworks (COFs) has been introduced by Yaghi *et al.* in 2005.[157] Contrary to MOFs these new framework materials consist of light non-metal elements linked by strong covalent bonding. The COFs networks are typically synthesized either by condensing rigid organic monomers containing at least two boronic acid groups to form boroxine rings (B_3O_3) or, alternatively, by condensation of boronic acid with aromatic 1,2-diols, e.g. HHTP, to form boronate ester linkages (Figure 5-3).[158,159]

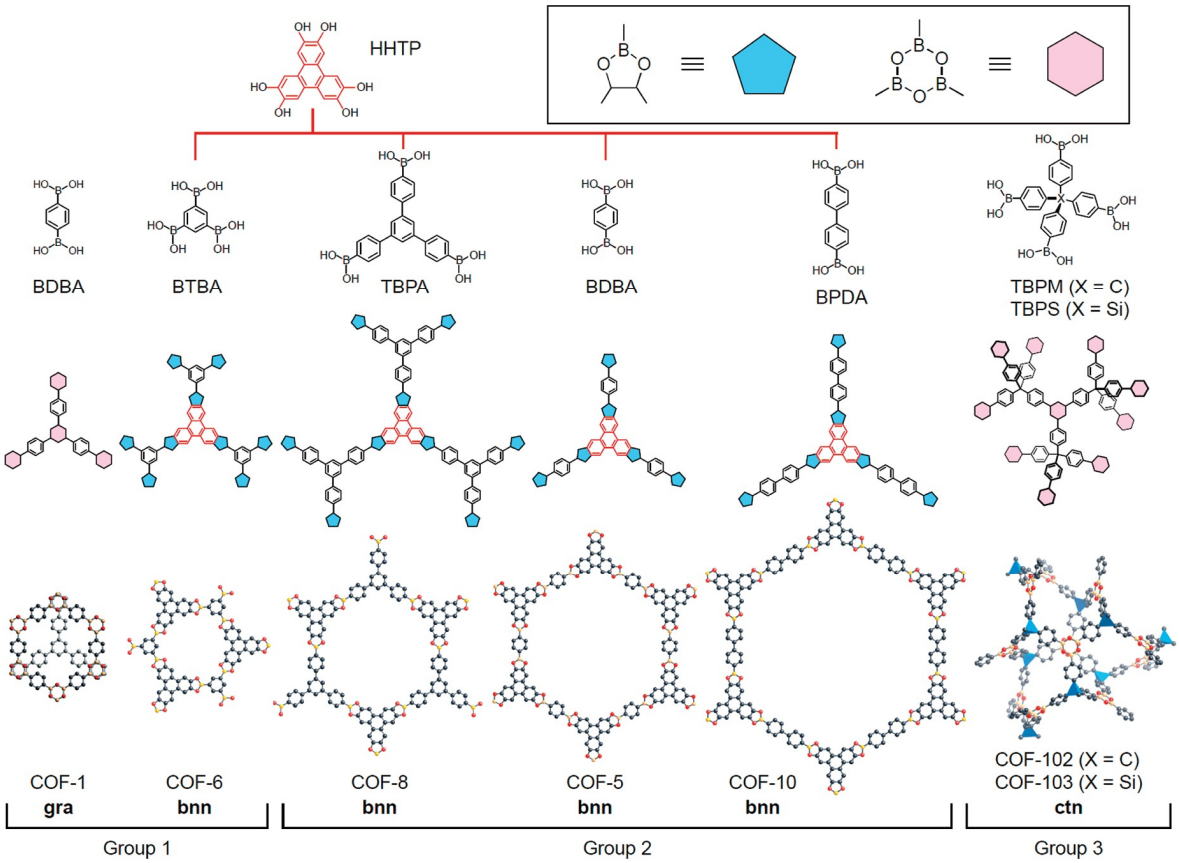

Figure 5-3: *Classification of COFs according to Furukawa* et al. *showing monomers (top) and network structures (bottom) of crystalline 2D and 3D COFs.[160] Structures are grouped in 2D structures with small 1D pores (group 1), 2D structures with large 1D pores (group 2) and 3D structures with medium 3D pores (group 3). Atoms: B (orange), O (red), C (black). Inset window: C_2O_2B (blue) and B_3O_3 (pink) rings. Blue tetrahedrons for group 3 COFs mark tetrahedral arrangements at C (TBPM) and Si (TBPS) central atoms. Hydrogen atoms are omitted for clarity. Adapted with permission from* [160]. *Copyright 2018 American Chemical Society.*

The appearance of a highly ordered network structure is characteristic for COFs. The crystallinity of the networks can be ascribed to the reversible thermodynamically controlled reaction mechanism. Under solvothermal conditions the COF framework is able to eliminate defects by recrystallization leading to a reduction of the internal energy of the structure. This energetic benefit can be regarded as the driving force of the network formation. Therefore, the control of reversible reaction conditions, e.g. by using sealed reaction vessels, is essential to overcome the so-called “crystallization problem” described in the literature.[118]

A number of alternative COF synthesis pathways can be found in the literature. In a report by Kalidindi *et al.* the network COF-1 has been synthesized at room temperature in presence of ammonium hydroxide.[161] A time-efficient synthesis of COF-5 under microwave irradiation reducing the reaction time from 72 h to 20 min has been reported.[162] Another method of COF synthesis has been reported by Hunt *et al.* where COF-202 has been synthesized by condensation of *tert*-butylsilane triol and tetrakis(4-dihydroxyboryl-phenyl)methane.[163]

Generally, two dimensional frameworks appear in defined layers exhibiting eclipsed AB or staggered AB stacking patterns (e.g. COF-1 (staggered) and COF-5 (eclipsed) in Figure 5-3). The determination of the present stacking pattern could be performed by comparing the experimental XRD pattern with the respective calculated patterns.[45,157,159] However, MD and DFT simulations suggest a slight offset between the 2D sheets in the structure of some COFs compared to a perfect AA stacking.[164,165] Du *et al.* have demonstrated in a recent report that the AB stacking of COF-1 after synthesis changes to AA stacking after thermal treatment.[166] This structural transformation has not been found to be reversible when again lowering the temperature.

Synthesized from sufficiently rigid building blocks to avoid a collapse of potential voids, COFs exhibit porosity in the region of micropores and small mesopores with defined pore sizes up to 5 nm, e.g. Star-COF-3 or HHTP-DPB COF.[164,167] Recently, Jin *et al.* synthesized two mesoporous and crystalline COF structures containing diimide linkers with extraordinary large pores at a pore width of 5.3 nm.[168] Some COF materials show extremely low crystal densities down to 0.17 g cm^{-3} (COF-108) and specific BET surface areas up to more than 4000 m^2 g^{-1} (COF-103, S_A = 4210 m^2 g^{-1}).[117,157,159] The combination of these features makes COFs promising materials for several gas storage applications. In fact, the potential of COFs as solid adsorbents for different gases like hydrogen, carbon dioxide, methane and also ammonia have been investigated recently.[160,169-172] According to these reports, COF-102 and COF-103 are able to adsorb about 1200 mg g^{-1} or 27 mmol g^{-1} of CO_2 at 298 K and a pressure of 55 bar. Regarding low pressure adsorption a remarkable CO_2 amount of 85 cm^3 g^{-1} or 3.79 mmol g^{-1} at 1 bar and 273 K has been reported for COF-6.[160] However, the applicability of COFs as sorbents in the presence of considerable amounts of water, e.g. flue gases, might be limited due to the poor stability of the boronate or boroxine linkages against hydrolysis.[173] Recently, Kahveci *et al.* synthesized the crystalline TDCOF-5 network exhibiting a specific BET surface area of 2497 m^2 g^{-1} and a CO_2 uptake of 2.09 mmol g^{-1} and 273 K and 1 bar.[174]

The possibility to introduce functionalities in the framework structure further increases the broad variety of COF properties. Therefore, functionalized COFs have been synthesized either by using functionalized building blocks or by post-synthetic modification.[160,175] Tilford *et al.* investigated the influence of different pore sizes on the hydrogen sorption properties four different networks based on a similar structure motif.[48,176] The networks have been built up by applying 2,6-dialkyl-1,2,4,5-tetrahydroxybenzene building blocks carrying alkyl chains of different lengths. It has been shown that an increase of the alkyl chain length also increases the molar amount of adsorbed hydrogen.[48] The introduction of functional groups on the inner pore walls of COF networks could also have a considerable influence on the hydrolytic stability. In a recent study of Lanni *et al.* the hydrolytic decay of the networks COF-5 and COF-18Å in aqueous environments has been reduced by

functionalizing the inner pore surfaces with hydrophobic alkyl chains.[173] The boronate ester linkages of COF-10 have been widely prevented from hydrolyzation in humid air by post-synthetic modification with pyridine.[177] A similar effect has been reported by functionalizing boroxine-linked COF-1 with APTES.[178]

A very interesting approach to synthesize functionalized COF-102 structures has been developed by partly replacing one of the four phenylboronic acid moieties of the tetragonal tetra(boronic acid) building blocks with the desired functional group, e.g. alkyl or allyl chains.[179] Further functionalization of allyl-containing COF-102 by post-synthetic modification with e.g. propanethiol yields COF-102-SPr. It should be noted that crystallinity and porosity of the original material could almost be fully retained after the post-synthetic modification step.[180]
A very effective strategy of COF pore surface engineering has been introduced by Nagai *et al.*, recently.[181] Starting from a common COF-5 structure, variable amounts of BDBA between 5% and 100% have been exchanged by azide-carrying BDBA units. Once the azide-modified network structures have been formed the pore walls can be further functionalized post-synthetically by quantitative click reaction with alkynes.[181] The click chemistry approach combined with a considerable number of available and suitable alkyne reagents demonstrates a high potential for pore surface engineering in porous networks in general and is, in theory, not limited to boronate or boroxine-based COFs.

A few years ago, conductive and semi-conductive COFs structures have been synthesized from electroactive monomers. A series of COFs containing thiophene units have been reported by Bertrand *et al.* recently.[182] Therein, the network T-COF 4, synthesized from H_4TTDB and HHTP, has been reported to form a charge-transfer complex with tetracyanoquinodimethane. Wan *et al.* synthesized two networks from pyrene-based PDBA building blocks by self-condensation of PDBA yielding a photoconductive COF with a specific BET surface area of 923 m^2 g^{-1} and a pore width of 1.88 nm.[183] The pyrene-based semi-conductive crystalline network TP-COF has been synthesized by condensation of PDBA and HHTP in a 1,4-dioxane/mesitylene mixture.[184] In both cases the eclipsed arrangement of 2D layers is assumed to be beneficial for effective charge carrier transport throughout the entire framework.[183,184]
Insertion of macrocyclic porphyrin[185-188] or phthalocyanine[189-192] moieties in COF structures yields electrically conducting networks. Recently, Feng *et al.* have demonstrated that the nature of the atom coordinated in the center of the porphyrin ring could have a significant influence on the conducting properties of the material.[185] The electronic properties of porphyrin and phthalocyanine-based COFs make them interesting for photovoltaic and optoelectronic applications. Furthermore, due to the porous structure and availability of metals coordinated in the incorporated macrocycle centers, a potential application in catalysis, similar to related PIM structures, is also conceivable.[139]

Porous borazine-linked COFs are structurally related to boroxine-linked COFs to a certain extent. These materials have been synthesized in the group of El-Kaderi by thermolysis of arylamine-borane or arylamine-boron trihalide adducts.[193-196] The networks synthesized from boron trihalide are amorphous with specific BET surface areas up to 1364 $m^2 g^{-1}$.[193] The polymers synthesized from arylamino-borane addicts exhibit higher specific BET surface areas with values up to even 2244 $m^2 g^{-1}$ for BLP-12(H).[195] While the materials BLP-1(H) and BLP-12(H) possess amorphous morphology, Jackson *et al.* reported a crystalline BLP network showing an AA stacking motif (Figure 5-4).[196]

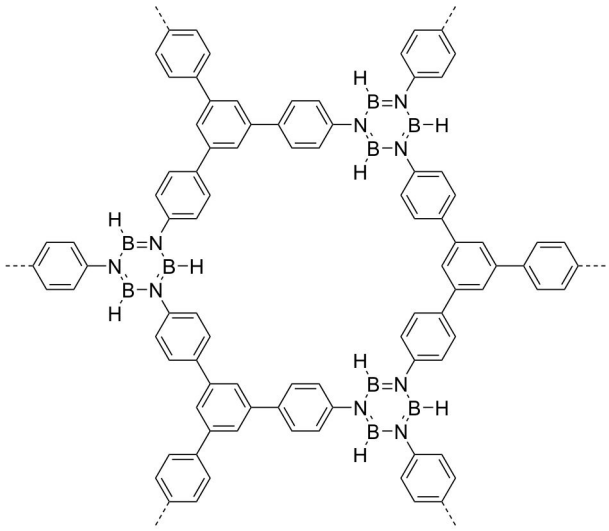

Figure 5-4: *Structure motif of crystalline borazine-linked COF BLP-2 according Jackson et al.*[196]

The CO_2 uptake capacities of BLPs are 0.93 mmol g^{-1} (BLP-1(H)), 1.41 mmol g^{-1} (BLP-10(Cl)) and 1.68 mmol g^{-1} (BLP-12(H)) at 298 K and 1 bar.[194,195] The CO_2/N_2 selectivity of BLP-10(Cl) is 16 according to initial slope calculations.[194] The respective IAST selectivities at a pressure of 1 bar range between 10 and 12 depending on the applied CO_2/N_2 molar ratio.[194]

5.2.2 Covalent Triazine-Based Frameworks

Similar to COFs, covalently linked framework materials can be synthesized by cyclotrimerization of nitrile functionalities to form triazine connectors. The first synthesis of covalent triazine-based frameworks has been reported by Kuhn *et al.* in 2008.[45] The networks have been synthesized by Zn-catalyzed cyclotrimerization of aromatic di- and trinitriles in molten zinc chloride at 400 °C. Under the given reaction conditions the network CTF-1 exhibits remarkable crystallinity due to a reversible reaction mechanism

comparable to COF synthesis. The mechanism of triazine formation will be discussed in detail in chapter 6. It has been shown that the applied monomer/$ZnCl_2$ ratio could not only influence the morphology of the networks, but also their porosity. For instance, the specific BET surface area of CTF-1 has been increased by more than 40% by changing the ratio of 1,4-DCB and $ZnCl_2$ in the reaction vessel from 1:1 to 1:10.[45] However, the increase of the specific surface area is accompanied by a loss of long range order in the CTF-1 structure.

Crystallinity and porosity in CTF networks, however, do not solely depend on the chosen reaction conditions but also on the applied monomers. The cyclotrimerization of 4,4'-dicyanobiphenyl (DCBP) at 400 °C in two equivalents of $ZnCl_2$ yields a highly porous (S_{BET} = 1150 m^2 g^{-1}) but amorphous material.[197] The specific BET surface area and total pore volume of the polymeric network can be further increased either by varying the $ZnCl_2$ amount in the reaction or by increasing the applied reaction temperature.[197] By raising the $ZnCl_2$/monomer ratio to 10, the CTF network synthesized from DCBP at 400 °C exhibits a specific surface area of 2475 m^2 g^{-1} and a total pore volume of 2.44 cm^3 g^{-1}.
In most cases, an increase of the reaction temperature significantly above 400 °C leads to higher surface areas and pore volumes in CTF materials. Some materials reached specific surface areas up to 3270 m^2 g^{-1}.[61] At the same time a significant increase of the C/N ratio in the respective materials has been observed in several reports.[61,197-199] The reduced nitrogen content at elevated reaction temperatures could be attributed to a partial decay of triazine nodes and C-C bond formation in the networks creating additional voids in the network structure.[45,197,200,201] The temperature-induced generation of larger micropores or mesopores creates hierarchical pore systems which facilitate the penetration of the pore structure and increase the pore volume accessible to guest molecules, e.g. Ar and N_2.[61,201] This behavior could explain the significantly higher specific surface areas and pore volumes compared to low temperature analogues.

Most of the CTF structures reported in the literature show amorphous morphology with a mixture of different pore sizes and more or less broad pore size distributions. Some of the structures, however, show a distinct long range order and can be described as rather crystalline. Up to now three ordered CTF polymer networks have been reported synthesized from 1,3,5-tricyanobenzene (CTF-0), 1,4-DCB (CTF-1), and 2,6-dicyanonaphthalene (CTF-2).[45,199,201] The molecular structures of the respective building blocks are displayed in Figure 5-5.

All three networks can be described by an eclipsed or AAA stacking pattern of two-dimensional sheets forming a hexagonal array of large slit pores with distinct pore diameters. The pore diameters of 7.3 Å for CTF-0, 1.4 Å for CTF-1 and 2.0 Å for CTF-2 derived from the respective XRD patterns coincide with theoretical models in the literature.[45,199,201]

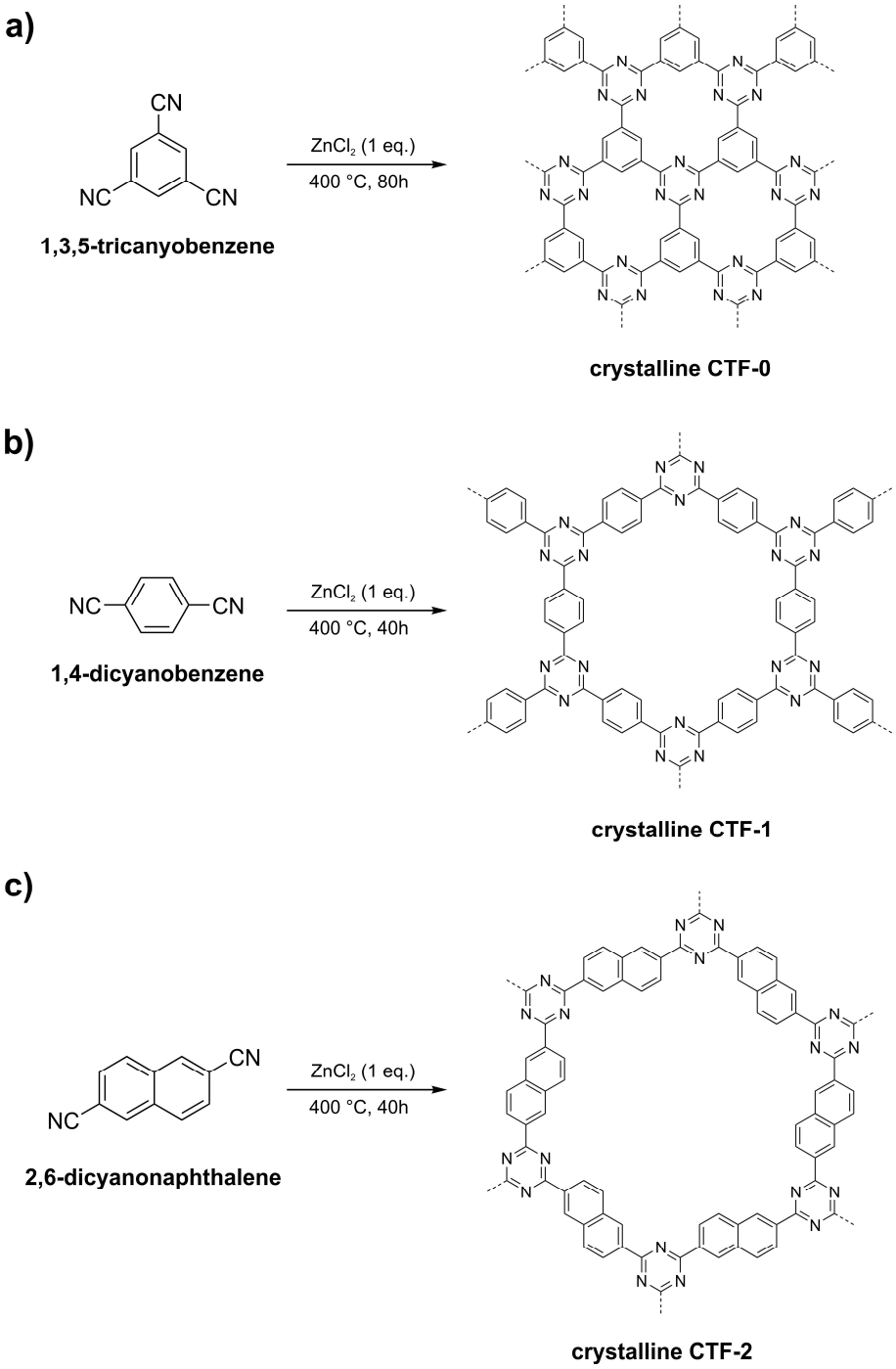

Figure 5-5: *Synthesis schemes for the three known crystalline CTF structures CTF-0 (a), CTF-1 (b) and CTF-2 (c).*[45,199,201]

It is worth mentioning that the long range order of all three networks is closely related to the respective reaction conditions illustrated in Figure 5-5. Variation of the reaction temperature or the monomer to $ZnCl_2$ ratio results in a decay of structural order yielding amorphous materials.[201] Interestingly, only CTF-1 shows considerable porosity in its crystalline form. For crystalline CTF-0 and CTF-2 no considerable porosity has been detected.[199,201] For both of the latter network structures pores could be generated by increasing the reaction temperature and adjusting the monomer to salt ratio, but only at the expense of crystalline order.[199,201]

A series of structurally related networks HBF-1, HBF-2 and HBF-3 linked by heptazine instead of triazine units have been synthesized by Bojdys *et al.* recently.[202] The synthesis of the networks is based on a self-condensation of aromatic building blocks bifunctionalized with dicarbonitrile and diaminotriazine moieties. The proposed mechanism is similar to the formation of melem from dicyanamide and melamine.[203] The three networks show a certain degree of long range order with theoretical pore sizes in the micro- and mesopore region. However, none of the structures exhibited remarkable porosity in gas sorption experiments.[202]

An alternative microwave-assisted synthesis method for CTF-1 has been reported by Zhang *et al.* in 2010.[204] Therein, the reaction time has been reduced to 60 min yielding an amorphous network with a specific BET surface area of 2390 $m^2\ g^{-1}$.

The trimerization of nitrile groups can also be induced by strong Brønsted acids like trifluoromethanesulfonic acid. In a report by Ren *et al.* a set of amorphous triazine networks has been synthesized by acid catalyzed nitrile cyclotrimerization at room temperature and under microwave irradiation.[205] The synthesized products exhibited specific BET surface areas up to 1152 $m^2\ g^{-1}$ and total pore volumes up to 0.58 $cm^3\ g^{-1}$.[205] Interestingly, gas sorption measurements of the two CTF-1 analogous networks, P1 and P1M, synthesized from 1,4-DCB did not detect any considerable porosity. With exception of the non-porous structures P1 and P1M, the reported CO_2 uptakes for the networks at 273 K and 1 bar varied in a range between 1.85 mmol g^{-1} (P4M) and remarkable 4.17 mmol g^{-1} (P6M).[205] The IAST selectivities for CO_2 over N_2 at varied between 14.2 (P6M) and 24.1 (P5). Noteworthy, the networks synthesized from 4,4',4'',4'''-methanetetrayl-tetrabenzonitrile, P6 and P6M, showed the highest CO_2 uptakes together with the lowest CO_2/N_2 selectivities.[205]

In a later report, Bhunia *et al.* also prepared a series of triazine-based networks (PCTFs) *via* the ionothermal and the strong acid route with remarkable CO_2 uptakes up to 3.23 mmol g^{-1} at 273 K and 1 bar.[206] The synthesis of a cost-effective network by coupling cyanuric chloride with piperazine linkers has also been reported.[207] The resulting network performed a CO_2 uptake of 1.36 mmol g^{-1} at 273 K.[207] In another study, a network synthesized from tetragonal Si-centered building block tetrakis(*p*-cyanophenyl)silica has been able to adsorb 1.88 mmol g^{-1} CO_2 at STP.[208]

The chemical and thermal stability in combination with the porous properties of covalent triazine frameworks make these materials interesting for applications in several different fields like catalysis,[198,209-211] drug delivery,[212] liquid phase sorption[213-215] and gas sorption.[205] Especially the potential usage of CTFs as sorbent material in CO_2 capture and separation application is currently investigated. The comparably high nitrogen content of CTFs in contrast to other organic sorbents might be regarded as advantageous, because of potential acid-base interactions between the Lewis-basic nitrogen atoms and the slightly acidic CO_2 molecules.[104,216]

Two amorphous networks synthesized in molten $ZnCl_2$ from 1,4-DCB, analogously to CTF-1, and tetrafluoroterephthalonitrile, respectively, at 400 °C and 600 °C and a salt/monomer ratio of 1:1 exhibited specific BET surface areas between 662 and 1535 $m^2\ g^{-1}$.[217] The networks FCTF-1 and FCTF-1-600, built from fluorinated monomers at 400 °C and 600 °C, were able to adsorb considerable amounts of 4.67 mmol g^{-1} and respectively 5.53 mmol g^{-1} of CO_2 at 273 K and 1 bar while showing moderate CO_2/N_2 selectivities.[217] It is worth mentioning that no more fluorine has been detected in the best performing material FCTF-1-600 after synthesis.[217]

Recently, Hug *et al.* described a series of porous networks synthesized from ionothermal cyclotrimerization of 9*H*-fluorene-2,7-dicarbonitrile at different temperatures.[218] The material *fl*-CTF350 with a specific BET surface area of 1350 $m^2\ g^{-1}$ adsorbed the highest amount of 4.28 mmol g^{-1} CO_2 at 273 K and 1 bar.[218] Although, the network *fl*-CTF400 exhibited a higher specific BET surface area and pore volume the CO_2 uptake decreased compared to *fl*-CTF350.[218] A possible explanation for this phenomenon might be the influence of the residual unreacted nitrile moieties still present in the network of the latter.

A similar synthesis concept has been applied by Hug *et al.* on cyclotrimerization of the nitrogen rich building blocks pyrimidine-2,5-dicarbonitrile (*pym*-CTF), 2,6-dimethyl-pyridine-3,5-dicarbonitrile (*lut*-CTF) and 5,5'-dicyano-2,2'-bipyridine (*bipy*-CTF) to obtain the respective porous network materials (Figure 5-6).[216] In all three cases, the specific BET surface area and the CO_2 uptake increased significantly with the reaction temperature. The networks *lut*-CTF500, *bipy*-CTF500 and *bipy*-CTF600 show the highest CO_2 uptakes of 5.04 mmol g^{-1}, 5.34 mmol g^{-1} and 5.58 mmol g^{-1} at 273 K and 1 bar.[216] The value for bipy-CTF600 is the highest CO_2 uptake of a CTF network to date.

The selectivities for CO_2 over N_2 decrease with increasing reaction temperatures, which might be related to the lower nitrogen contents of CTFs formed at higher reaction temperatures. Noteworthy, *pym*-CTF500 outperformed the other materials in the report with an exceptionally high CO_2/N_2 selectivity of 189 evaluated *via* Henry´s law method and 502 *via* IAST method (CO_2/N_2 ratio 15:85) at 298 K, respectively.[216]

In a recent report, Tao *et al.* varied the reaction conditions of the cyclotrimerization reaction of the uncommon dinitrile building block 2-(*p*-cyanophenyl)-1*H*-benzo[*d*]imidazole-5-carbonitrile (DCBI) in molten $ZnCl_2$.[219]

Interestingly, the material yielded from a DCBI/$ZnCl_2$ ratio of 1:1 did not exhibit any considerable porosity. At higher $ZnCl_2$ contents and temperatures of at least 400 °C CTF networks with high specific BET surface areas up to 1549 $m^2\ g^{-1}$ and pore volumes up to 0.88 $cm^3\ g^{-1}$ for CTF-BI-11. The highest CO_2 uptakes at 273 K and 1 bar have been reported for CTF-BI-11 (4.93 mmol g^{-1}), CTF-BI-4 (4.85 mmol g^{-1}) and CTF-BI-5 (4.49 mmol g^{-1}). At a temperature of 303 K CTF-BI-4 still adsorbs up to 2.46 mmol g^{-1} CO_2 and shows a remarkable selectivity for CO_2 over N_2 of 102 according to initial slope calculations.[219]

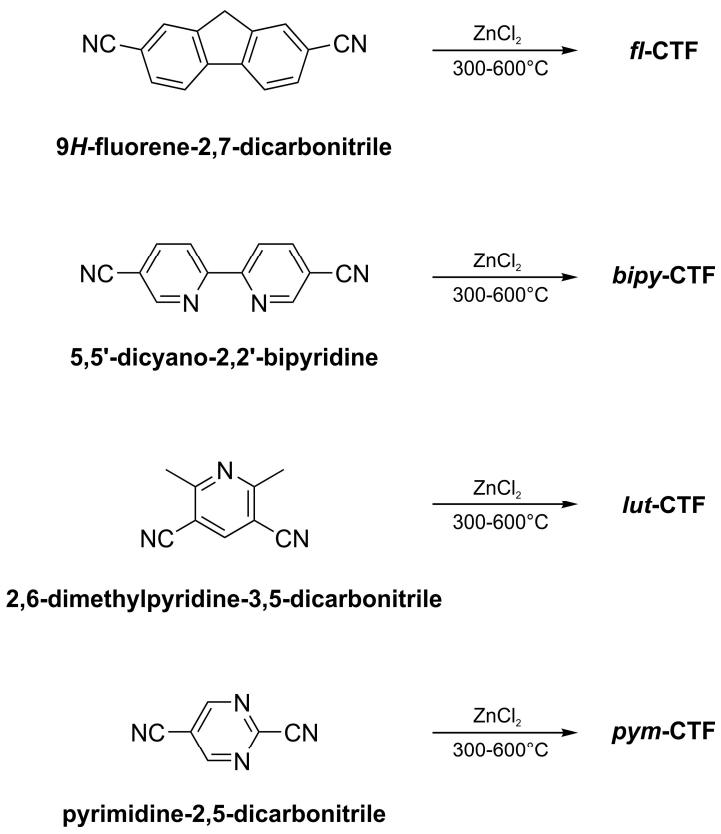

Figure 5-6: *Molecular structures of the precursor molecules and schematic synthesis for network materials* fl-*CTF,* bipy-*CTF,* lut-*CTF and* pym-*CTF synthesized by Hug* et al.[216,218]

Liu *et al.* introduced porphyrin moieties in a CTF network synthesized by the ionothermal route showing CO_2 uptakes up to 3.16 mmol g^{-1} at 273 K and 1 bar.[220]

5.2.3 Covalent Organic Frameworks from Imine and Hydrazone Linkages

The formation of extended ordered network structures can also be achieved by imine linkages formed in a reversible condensation of aldehydes or ketones and amines. The imine structures derived from aldehydes are called aldimines, while imines derived from ketones are described as ketimides. In both reactions the carbonyl oxygen atom is formally exchanged by nitrogen in a condensation reaction with one water molecule as leaving group.

An interesting feature of the imine bond is the concept of 'proof-reading' and 'error-checking' known from reversible reactions under the term dynamic covalent chemistry (DCC).[221-223] According to the DCC concept, the reaction mechanism ensures the formation of the most thermodynamically stable product in a given sufficient time frame.[221]

A structurally similar alternative to imine bonds, a so-called hydrazone linkage, can be synthesized by substituting the amine carrying reactant with an *N*-substituted hydrazine precursor. The general structures of imine and hydrazone compounds are displayed in Figure 5-7. Imine compounds carrying an aryl or alkyl group at position R'' are also known as azomethines or Schiff bases.[222,224]

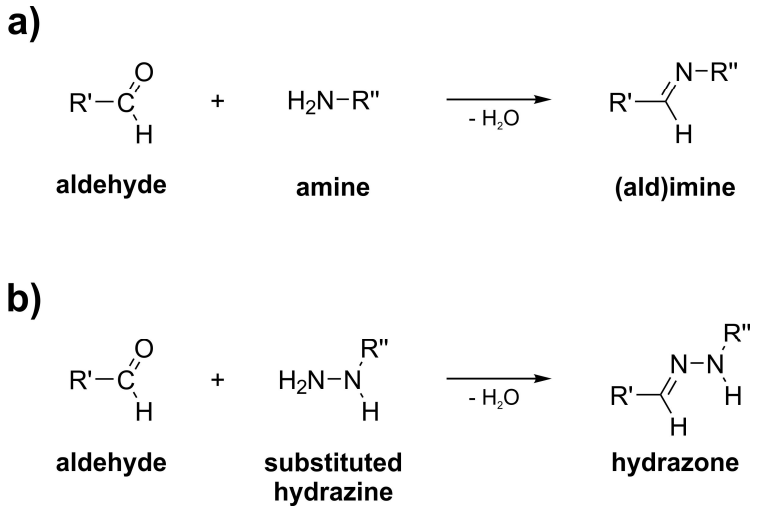

Figure 5-7: *a) Formal formation of an (ald)imine bond by a condensation reaction between aldehyde and amine precursors; b) Formal formation of a hydrazone bond by a condensation reaction between aldehyde and substituted hydrazine precursors; R', R'' = aryl and/or alkyl group.*

The first imine-linked framework, COF-300, has been reported by Uribe-Romo *et al.* in 2009.[225] The crystalline network has been synthesized by condensation of the tetrahedral precursor molecule tetrakis(*p*-aminophenyl)methane (TAPM) and 1,4-DCM. The structure model of the resulting 3D-framework possesses an interpenetrated diamond topology forming dimensional channels with a diameter of approximately 7.8 Å.

Argon adsorption measurements of COF-300 detected permanent porosity with a specific BET surface area of 1360 $m^2\ g^{-1}$ and a total pore volume of 0.72 $cm^3\ g^{-1}$.[225]
In a report by Pandey *et al.* an imine-based network synthesized from 1,3,5-tri-formylbenzene and *p*-phenylenediamine in DMSO yielded a remarkable specific BET surface area of 1063 $m^2\ g^{-1}$.[226] The accessible surface area could be increased up to 1521 $m^2\ g^{-1}$ by changing the diamine precursor to *m*-phenylenediamine. However, according to powder XRD measurements both networks did not show any long-range order under the given reaction conditions.
The choice of the reaction conditions, e.g. solvent, monomer concentration, monomer ratio and catalyst selection, is regarded to be critical for the crystallinity of the resulting network products.[223,225] A recent study by Duncan *et al.* revealed a significant influence of the applied solvents and catalysts on reaction kinetics and reaction equilibrium of imine bond

formation.[227] When applying amine precursors like melamine or 2,6-diaminopyridine, some of the amine groups perform a nucleophilic attack on the imine linkages forming aminal moieties. Such networks are characterized by high nitrogen contents and specific BET surface areas up to 1377 m^2 g^{-1} which might both be desirable features for potential gas sorbent materials, e.g. for CO_2 sorption.[228,229]
The first single crystal structure of an imine-linked covalent organic framework COF-320 has been reported recently.[230] The synthesis of COF-320 has been conducted from TAPM and 4,4'-biphenyldialdehyde in dioxane/acetic acid at 120 °C.[230] The structure model, based on electron diffraction data, suggests a 9-fold interpenetrated diamond net containing 1D channels along the *c*-axis.[230] However, the two applied temperature settings during measurement, 89 K and 298 K, lead to slightly different data sets and, in consequence, to different crystal structures.

A growing number of reports on possible applications for crystalline and non-crystalline porous imine linked networks as catalysts,[231-233] catalyst supports,[234-236] gas sorbents.[237-243] Through the well-known and versatile reaction mechanism in combination with the accessibility of a large variety of precursor molecules it is possible to introduce a number of different functional groups in the network structures. For instance, acyl functionalities have been successfully implemented into the structure of COF-300 by post-synthetic modification.[244] Unfortunately, the originally high specific surface area of COF-300 decreased significantly after functionalization under the given reaction conditions.
Similar to boronate-linked COF, porphyrin rings have been successfully incorporated into an ordered imine-linked network named COF-366 which shows high charge carrier mobility and might be interesting for potential applications in electronic systems.[186] A study based on porphyrin-based imine networks described a relationship of the network crystallinity and occurring π-stacking interactions between the ecliptically arranged layers.[245] Obviously, an increased crystallinity of the materials leads to increased specific BET surface areas.
Recently, Lin *et al.* synthesized two crystalline imine networks containing functional cobalt porphyrin sites linked by 1,4-benzenedicarboxaldehyde (COF-366-Co) and biphenyl-4,4'-dicarboxaldehyde (COF-367-Co), respectively.[233] Both structures exhibit considerably high activity and selectivity in the electrocatalytic reduction of CO_2 to CO in water.
In two different approaches reported by Kandambeth *et al*. chemical stability of functionalized imine-based networks has been improved significantly by intramolecular hydrogen bonds.[242,246] In one method, linear diamines react in a first step with 1,3,5-triformylphloroglucinol to form imine-linked structures following common Schiff-base chemisty.[246] Through the structural properties of the phloroglucinol node, the present enol moieties rapidly change to the more stable keto form (Figure 5-8). This irreversible tautomerization is driven by the basicity of three imine nitrogen atoms dominating the

energy gain of the aromatic system by forming three hydrogen-bonded six-membered rings.[246] The resulting networks are stable in acidic, basic and aqueous medium, but their crystallinity seems quite low most likely due to the irreversibility of the tautomerization.

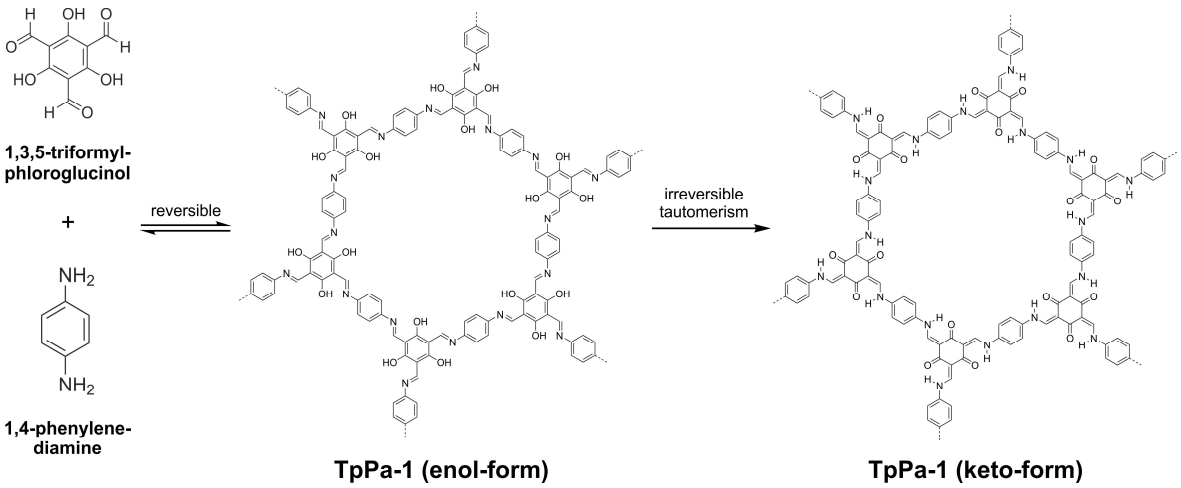

Figure 5-8: *Schematic synthesis scheme of network TpPa-1 showing the structure of the reversible enol form followed by an irreversible tautomerization step to the stable keto form.*[246]

Recently, Kandambeth *et al.* presented network DhaTab-COF synthesized from 1,3,5-tris(*p*-aminophenyl)benzene (TAPB) and 2,5-dihydroxyterephthalaldehyde with very high degree of crystallinity and a specific BET surface area of 1480 $m^2 g^{-1}$ (Figure 5-9).[242] Again, the hydroxyl groups and the imine bonds form planer six-membered rings by strong intramolecular hydrogen bonding keeping the phenyl rings in plane. The high planarity is beneficial for the stacking interaction between the AA stacked layers and thus increases the crystallinity of the material.[242] Additionally, the presence of intramolecular hydrogen bonding impedes nucleophilic attacks on the imine bond resulting in an increased hydrolytic stability.[242] The weak basic imine groups in combination with high specific surface area, inherent micro- or mesoporosity and high chemical and thermal stability render imine-based networks potential candidates for CO_2 capture applications.

In one of the first reports on post-combustion CO_2 separation from flue gas Xu and Hedin prepared imine networks TAPB and three dialdehyde linkers.[241] Although the moderate specific BET surface areas, the CO_2 uptakes of the materials ranged from 1.34 to 2.71 mmol g^{-1} at 273 K and 1 bar together with IAST selectivities of CO_2 over N_2 between 56 and 77. The network DhaTab-COF described above is able to adsorb a CO_2 amount of 3.48 mmol g^{-1} at 273 K and 1 bar.[242] The crystalline network ILCOF-1 possesses a specific BET surface area of 2723 $m^2 g^{-1}$, which is currently the highest reported value for imine based networks.[247] The CO_2 uptake of ILCOF-1 at 273 K and 1 bar yields a moderate value of 1.36 mmol g^{-1} or 6.0 wt.%. According to the authors the relatively low CO_2 uptake might be related to the high amount of mesopores in the structure.[247]

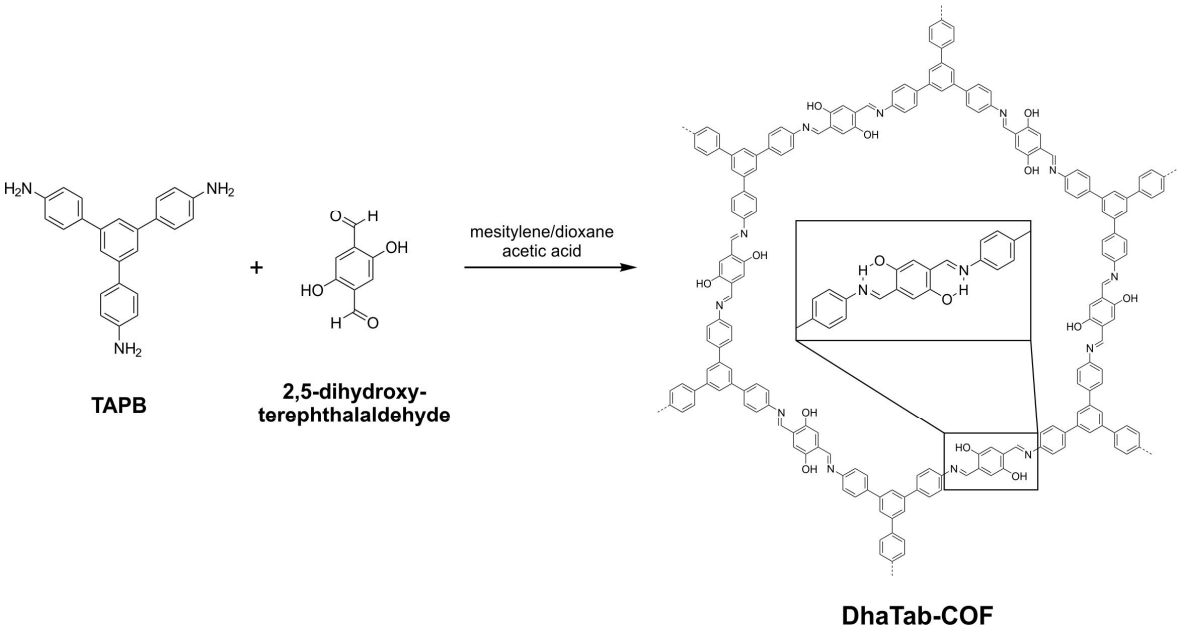

Figure 5-9: *Schematic synthesis of DhaTab-COF by Schiff base reaction. The insert displays the structure stabilizing hydrogen bonding between hydroxyl and imine groups.*[242]

In 2015, Gomes *et al.* synthesized a porous network from TAPT and terephthalaldehyde with a certain long-range order within the postulated layer structure.[248] The material TRITER-1 has a CO_2 uptake of 13.38 mmol g^{-1} at 273 K and 3.11 mmol g^{-1} at 298 K at a pressure of 5 bar. At a pressure of 1 bar the CO_2 uptakes are at approximately 2.5 mmol g^{-1} at 273 K and 1 mmol g^{-1} at 298 K.[248]

Another series of amorphous imine networks synthesized and tested for CO_2 sorption application has been reported by Zhu *et al.* recently.[243] The networks in the report follow a [3+4] structure motif, based on tetrahedral TAPM and various trigonal trialdehydes, yielding three dimensional imine linked materials. The four synthesized networks PPF-1 to PPF-4 exhibit specific BET surface areas between 419 m^2 g^1 (PPF-3) and 1740 m^2 g^{-1} (PPF-1). The CO_2 uptakes at 273 K and 1 bar range from 2.09 mmol g^{-1} (PPF-3) and 5.54 mmol g^{-1} (PPF-2) up to 6.07 mmol g^{-1} (PPF-1) at IAST selectivities of CO_2 over N_2 between 14.5 (PPF-1) and 20.4 (PPF-3).[243] The CO_2 uptakes of PPF-1 and PPF-2 are currently the highest reported values for imine-based networks and among the highest CO_2 uptakes for organic porous materials.

A very interesting imine-based network possessing ionic adsorption sites within its structure has been reported by Popp *et al.* recently.[240] The incorporated protonated imine units stabilized by sulfonic counterions provide good CO_2/N_2 selectivity ratios at moderate CO_2 uptakes.[240] However, in case of application in real flue gas streams the presence of considerable amounts of moisture might severely lower the CO_2 sorption capacity of the networks.

Beside imine-based porous organic frameworks, some examples of porous hydrazone linked networks could be found in the literature.[249,250] The hydrazone bond, formed in a condensation reaction from hydrazides and aldehydes, is more stable against hydrolysis compared to imines due to extended electron delocalization in the hydrazone moiety causing a decreased electrophilicity of the C-N bond.[251]

The first hydrazone linked crystalline and porous frameworks have been reported by Yaghi and coworkers in 2011.[249] The networks COF-42 and COF-43 have been synthesized by condensation of 2,5-diethoxyterephthalohydrazide (DETH) and 1,3,5-triformylbenzene or 1,3,5-tris(*p*-formylphenyl)benzene, respectively (Figure 5-10).[249]

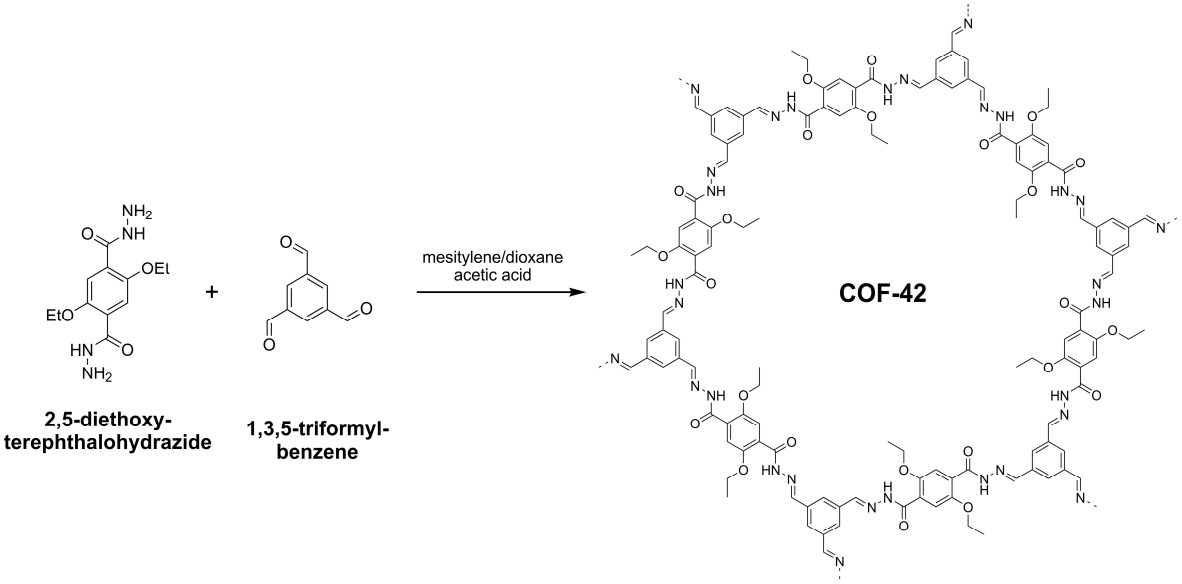

Figure 5-10: *Schematic synthesis of COF-42 by condensation reaction from 2,5-diethoxy-terephthalo-hydrazide and 1,3,5-triformylbenzene.*[249]

Both networks crystallize in layers showing an eclipsed stacking mode. As reported for other COF structures, the crystallinity of the materials is closely related to the applied reaction conditions. The two ethoxy groups improve the solubility of the hydrazide precursor molecule and are essential for the development of porosity in the network structure.[249] Argon adsorption measurements yielded specific BET surface areas of 710 $m^2 g^{-1}$ (COF-42) and 620 $m^2 g^{-1}$ (COF-43) with dominating pore sizes in the lower mesopore region. Recently, the successful exfoliation of COF-43 in common solvents like dioxane, water and DMF has been demonstrated.[252]

Recently, Stegbauer *et al.* evaluated the photocatalytic properties of the hydrazone based network TFPT-COF synthesized from DETH and 1,3,5-tris(4-formylphenyl)triazine. The determined pore widths of the crystalline network are comparable to those of COF-42. The network has been proven to be a potent non-metal photocatalyst for hydrogen production. Interestingly, after exfoliation in aqueous solution, long-range order and porosity of TFPT-COF can be restored to a certain extent when applying the initial synthesis conditions.[250]

The enhanced hydrolytic stability compared to imine bonds might render hydrazone linked network materials interesting as potential gas sorbents in humid environments, e.g. CO_2 sorption from flue gases.

5.2.4 Covalent Organic Frameworks from Azine Linkages

In a recent study, Dalapati *et al.* described a new class of crystalline COFs linked by azine bonds.[253] The network Py-Azine COF has been synthesized by a thermodynamically controlled condensation of tetraaldehyde 1,3,6,8-tetrakis(*p*-formylphenyl)pyrene and hydrazine in presence of 6M acetic acid under solvothermal conditions at 120 °C (Figure 5-11).[253] As already reported for other COF structures, Py-Azine COF is characterized by a 2D layer structure arranged in an eclipsed AA stacking pattern (Figure 5-11).[253]
Similar to other COFs, the applied reaction conditions have a direct influence on the structural properties of the material. For instance, synthesis of Py-Azine in *o*-dichlorobenzene yielded a highly crystalline material with a specific BET surface area of 599 m^2 g^{-1}.[253] The surface area of Py-Azine COF has been increased to 1210 m^2 g^{-1} by changing the solvent to *o*-dichlorobenzene/*n*-BuOH (19:1), while the crystallinity of the material decreased slightly. Interestingly, the network maintained its long-range order

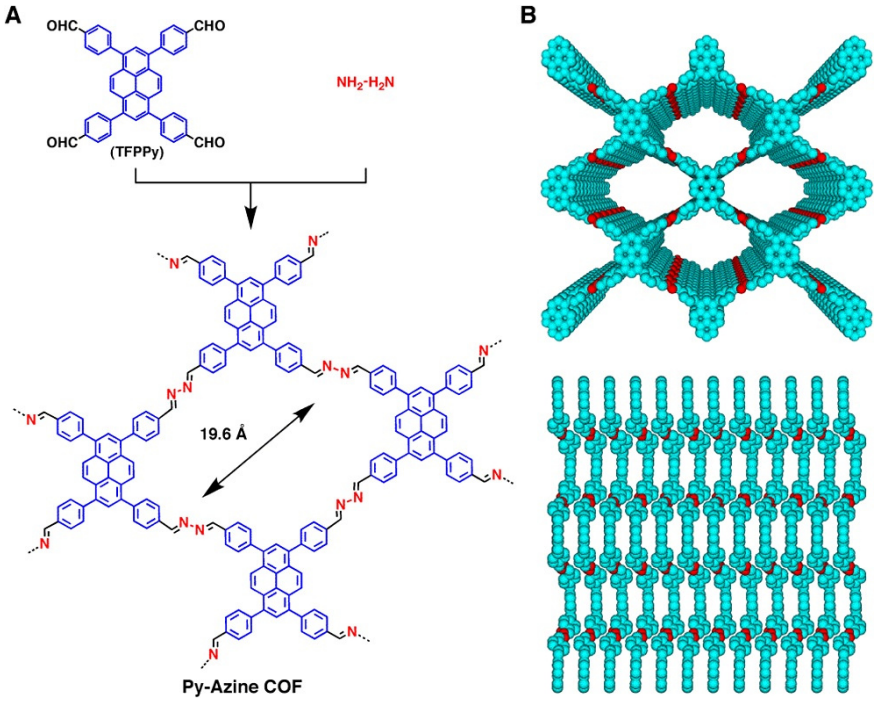

Figure 5-11: *Synthesis of Py-Azine COF (A) and illustration of the eclipsed 2D stacking structure of Py-Azine COF (B). Adapted with permission from* [253]. *Copyright 2018 American Chemical Society.*

almost completely when treated with different polar and non-polar solvents such as hexane, THF or aqueous HCl and NaOH.[253] A series of porous azine-linked COFs based on 1,3,5-triphenylarene nodes with varying nitrogen content in the central aryl ring and remarkable performance as polymeric photocatalysts in hydrogen production has been reported recently (Figure 5-12).[254] Although, the four synthesized networks within the study exhibited certain long-range order with an eclipsed layer stacking pattern, an increased nitrogen content in the central aryl node has been regarded to be beneficial for the overall crystallinity of the respective material. An explanation for this phenomenon might be found in the higher planarity of the triphenylarene nodes at higher nitrogen contents due to the reduced sterical hindrance between the central and the peripheral aryl rings.[254] Following the argument, XRD measurements confirm the highest crystallinity for network N_3-COF. The specific BET surface areas of N_x-COF range from 326 (N_1-COF) to 1537 $m^2\ g^{-1}$ (N_3-COF).

The increased chemical stability and Lewis-basic nitrogen sites in the pore walls make azine-linked COFs interesting as potential sorbents for CO_2 capture and separation from flue gas streams.

Li *et al.* investigated the gas sorption properties for CO_2, CH_4 and N_2 of a porous and crystalline azine network.[255] The material ACOF-1 has been synthesized from 1,3,5-triformylbenzene and hydrazine hydrate under solvothermal conditions in a sealed reaction vessel. Nitrogen sorption measurements of ACOF-1 yielded a high specific BET surface area of 1176 $m^2\ g^{-1}$ with a total pore volume of 0.91 $cm^3\ g^{-1}$.[255]

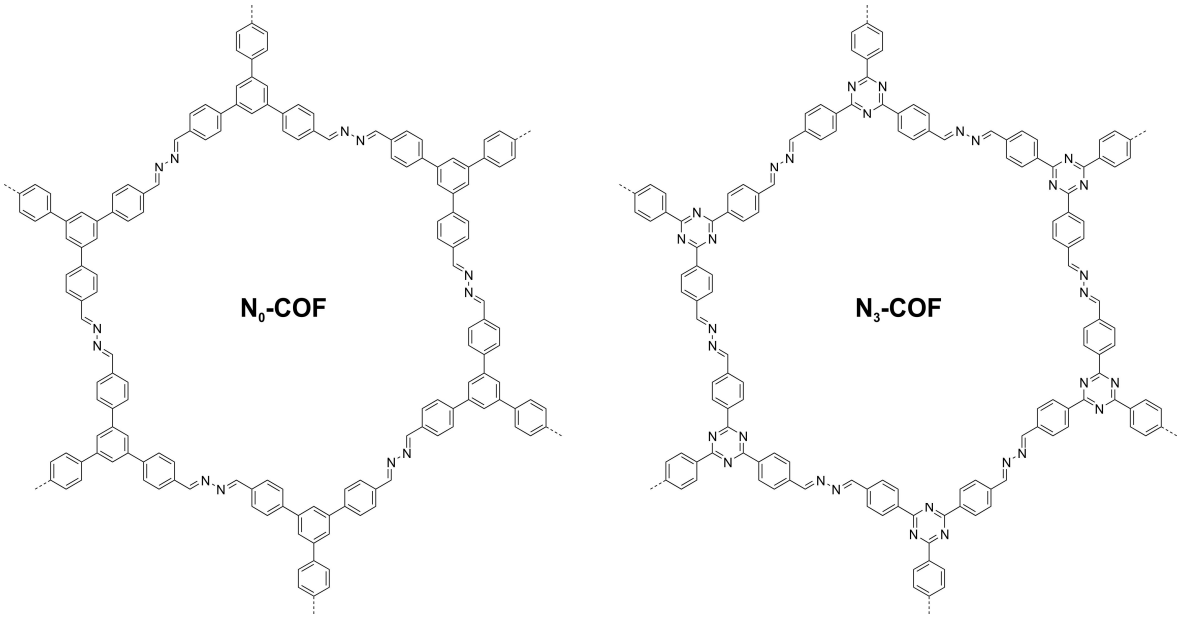

Figure 5-12: *Network structures of N_0-COF and N_3-COF exemplarily for N_x-COFs by Vyas et al.[254] Structures of N_1-COF and N_2-COF are not displayed. Subscripted numbers refer to the number of nitrogen atoms in the aromatic nodes.*

The CO_2 sorption capacity of 4.02 mmol g^{-1} at 273 K and 1 bar is among the highest values for COF structures. Furthermore, the CO_2/N_2 and CO_2/CH_4 adsorption selectivities at 273 K determined from initial slope calculations show remarkable values of 40 and 37, respectively.[255]

5.3 Disordered Porous Organic Polymer Networks

5.3.1 Conjugated Microporous Polymers and Hypercrosslinked Polymers

One of the most popular classes of porous polymers is known as hypercrosslinked polymers (HCPs) for several decades. HCPs generate porosity by introducing cross-linking agents to conventionally linear polymers synthesized from benzene,[256,257] biphenyl,[258] styrene,[257,259-263] phenol,[256,264] xylene,[258,265] aniline,[266-268] carbazole,[269] thiophene,[270] or pyrrole[55,270] monomers.
Following the established *Davankov* synthesis approach, precursor polymers are initially swollen in an appropriate solvent in order to separate the polymer chains and generate extended internal volumes.[271,272] In a second step, the solvated polymer chains are cross-linked by suitable reactions, e.g. *Friedel-Crafts* alkylation, to conserve the present structural arrangement. At certain degrees of cross-linking, the porous structure of the polymeric materials can be maintained even after solvent removal.[268,271] HCPs show specific BET surface areas of almost 2000 m^2 g^{-1}, CO_2 uptakes up to 3.92 mmol g^{-1} at 273 K and CO_2/N_2 adsorption selectivities up to 117.[265,270,273,274]

Conjugated microporous polymers (CMPs) can be regarded as a subclass of HCPs. Similar to COFs, these permanently porous polymeric materials were synthesized from modular building blocks and form a characteristic extended conjugated network. Even if the conjugation of the π-electron system is limited to the linker units and could not be extended throughout the whole network structure, e.g. when tetrahedral nodes are implemented, the networks are still labeled as CMPs.
CMP materials usually lack of long range order due to kinetically controlled non-reversible synthesis reaction mechanisms like Friedel-Crafts,[275-277] Sonogashira-Hagihara,[50,278-285] Suzuki-Miyaura,[285-290] Yamamoto[283,291-296] or Eglinton[297] coupling. Contrary to thermodynamically controlled ordered network structures, CMPs often form hierarchical pore systems with broad pore size distributions and extraordinary high specific surface areas. These pore systems might be advantageous for gas sorption applications as they are able to overcome the diffusion and transport limits that could occur in materials with

micropores of uniform size. As a consequence, the higher diffusion and transport rates might be beneficial as they could have a significant influence on adsorption rates in e.g. dynamic systems, where contact times are preferentially short. Nonetheless, contrary to common hypercrosslinked polymers, a certain control over the pore system can be obtained by selecting suitable monomer units and careful adjustment of reaction conditions.[298,299] Alternatively, CMP structures exhibiting specific surface areas of more than 1000 m^2 g^{-1} have been synthesized by other synthesis routes like cobalt-catalyzed trimerization of ethynyl groups or by "click" chemistry.[283,300-303]

The first CMPs have been synthesized by palladium-catalyzed Songashira-Hagihara coupling of different aryl halides and aromatic alkynes by Jiang *et al.* in 2007 (Figure 5-13).[298] The resulting porous poly(aryleneethynylene) (PAE) networks exhibit specific BET surface areas between 522 and 834 m^2 g^{-1} and pore volumes up to 0.53 cm^3 g^{-1}. The networks show a direct relation between with the length of the linkers between the nodes on one side and the specific surface area and micropore volume on the other. The network with the largest distance between the nodes (CMP-3) exhibits the lowest BET surface area and micropore volume, whereas the network with the shortest linker (CMP-1) possesses the highest surface area and micropore volume. This correlation has been confirmed in a subsequent paper by Jiang *et al.* wherein the length of the linker molecules between the network nodes has been further increased (CMP-5) and decreased (CMP-0), respectively (Figure 5-13).[299]
A close relation in the different networks where increasing length of the linker molecules results in decreased surface areas and total pore volumes has been observed.[299] This could be explained with an increasing node to node distance in CMP networks leading to a denser structural packing through the higher structural flexibility and the possibility of chain interpenetration.[299]

Networks synthesized from monomers containing tetrahedral carbon, silicon or adamantane central nodes can reach very high specific BET surface areas up to 3180 m^2 g^{-1}.[283,297,304] The extraordinary high surface areas might be ascribed to the rigidity of the applied monomers and the high degree of cross-linking within these CMP structures. Similar to ordered porous organic polymers, the applied synthesis reaction conditions play a crucial role for the properties of CMP networks. For instance, it has been demonstrated that the applied reaction solvent influences the morphology of the resulting CMP network significantly.[305] Accordingly, the choice of the reaction solvent can also influence the specific surface area and the total pore volume.
In a report by Dawson *et al.* a CMP network synthesized from 1,3,5-triethynylbenzene and 1,4-dibromobenzene by palladium-catalyzed Sonogashira-Hagihara cross-coupling in toluene exhibited a specific surface area of 867 m^2 g^{-1} and a total pore volume of 0.99 cm^3 g^{-1}.[281] When changing the reaction solvent to dioxane while leaving the

remaining parameters unchanged, the specific surface area and total pore volume of the network decrease to 609 $m^2 g^{-1}$ and 0.36 $cm^3 g^{-1}$, respectively.

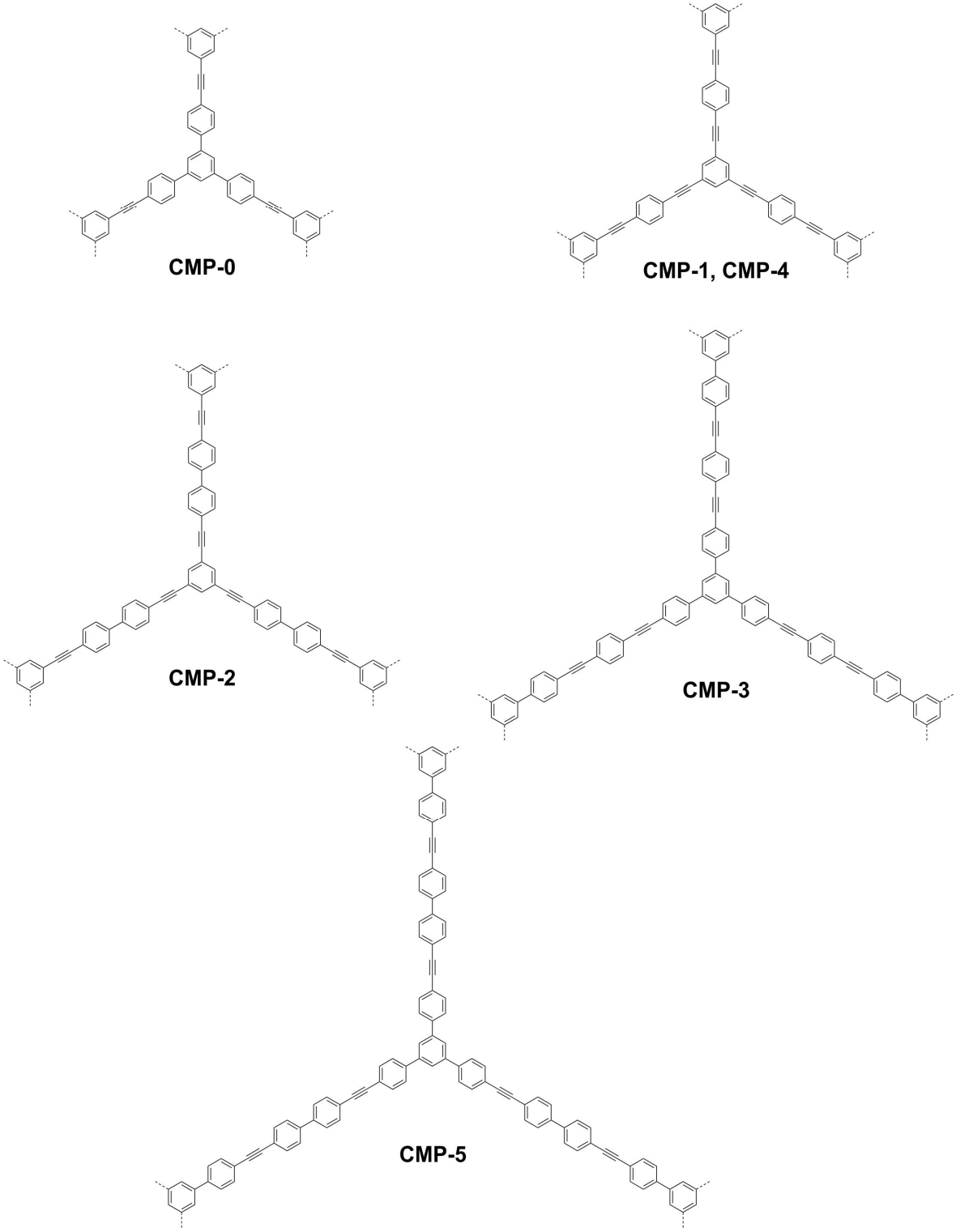

Figure 5-13: *Molecular structures representing porous networks CMP-1 to CMP-5 according to Jiang* et al.[298,299]

Interestingly, for a network synthesized at similar conditions from 1,3,5-triethynylbenzene and 4,4'-dibromobiphenyl the specific surface area increases from 204 m^2 g^{-1} (toluene) to 744 m^2 g^{-1} (dioxane) while the total pore volume also increases from 0.43 cm^3 g^{-1} (toluene) to 0.55 cm^3 g^{-1} (dioxane).[281]

Porous aromatic frameworks (PAFs) are a subclass of CMPs with trigonal or tetrahedral nodes connected by aromatic linkers, e.g. phenyl or triazine units. The first PAF, PAF-1, has been synthesized by Ben *et al.* in 2009 via nickel(0)-catalyzed Yamamoto-type Ullmann cross-coupling of tetrakis(*p*-bromophenyl)methane (Figure 5-14).[306] The material PAF-1 shows extraordinary chemical and thermal stability together with an extremely high specific BET surface area of 5600 m^2 g^{-1} and a total pore volume of 2.43 cm^3 g^{-1}.[306,307] Additionally, a very high CO_2 uptake of 29.5 mmol g^{-1} at a pressure of 40 bar and 298 K make PAF-1 an interesting candidate of CO_2 sorption applications. The gas sorption selectivity of PAF-1 for CO_2 over N_2 could be further increased by carbonization.[307]

The hydrophobicity of PAF-1, PAF-2 and PAF-5 mainly caused by extended aromatic systems within the network structures render these materials interesting candidates for selective benzene or toluene sorption.[215,306,308]

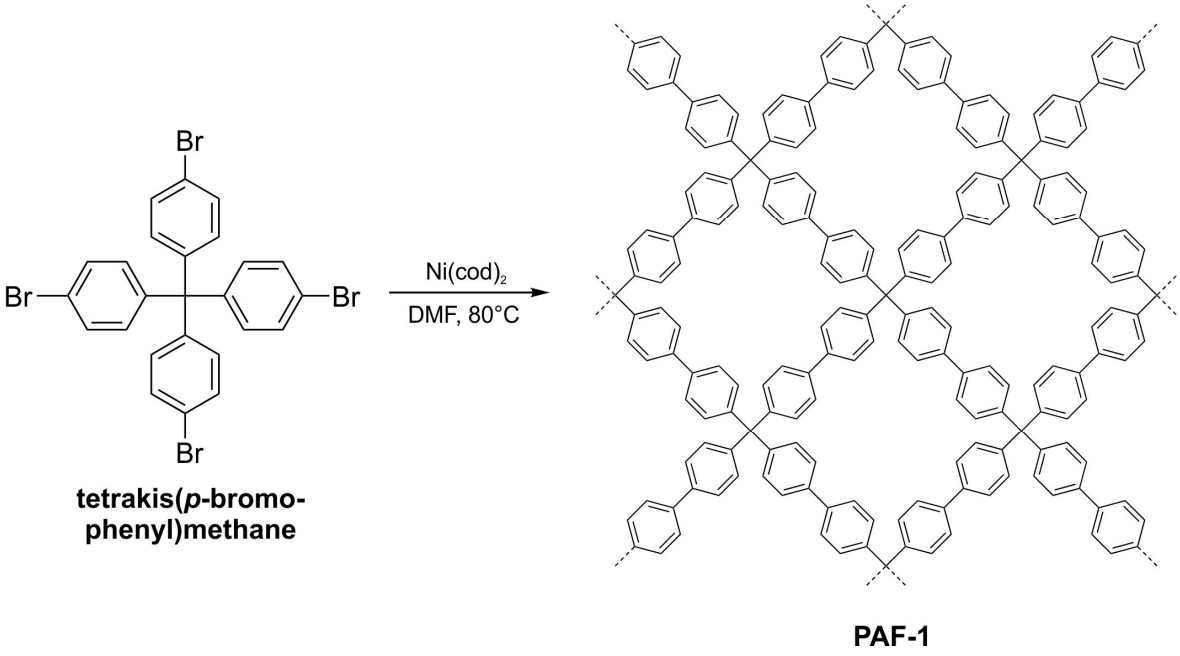

Figure 5-14: *Synthesis scheme for network PAF-1 via nickel(0)-catalyzed Yamamoto-type Ullmann cross-coupling reaction according Ben et al.*[306]

It is worth noting that the synthesis of triazine-containing PAF-2 has been conducted according to the synthesis protocol of Kuhn *et al.*, however, the resulting network structures did not exhibit any long-range order.[45,215] The incorporation of Si and Ge centers in the tetrahedral nodes of PAF networks turned out to have a significant influence on the gas sorption properties.

PAF-3 (Si-centered) and PAF-4 (Ge-centered) synthesized by Yamamoto-type Ullmann-coupling even slightly outperform the CO_2 sorption capacities of PAF-1 at low pressures. At 273 K and 1 bar, PAF-3 and PAF-4 are able to adsorb 3.48 mmol g^{-1} and 2.43 mmol g^{-1} CO_2 compared to 2.07 mmol g^{-1} for PAF-1.[47] At 298 K and 1 bar the networks PAF-1, PAF-3 and PAF-4 could store 1.09 mmol g^{-1}, 1.82 mmol g^{-1} and 1.16 mmol g^{-1} of CO_2.[47] Recently, Ben *et al.* increased the CO_2 uptake of PAF-1 by post-synthetic carbonization of the network at 450 °C to 4.50 mmol g^{-1} at 273 K and 1 bar.[307] The IAST CO_2/N_2 (15:85) selectivity of PAF-1-450 at 273 K and 1 bar exhibits a quite high value of 209.[307]

Recently, three different porous polymer networks, PPNs, have been reported by Zhou and coworkers.[297,309] The networks PPN-4, PPN-5 and PPN-6 are structurally similar to PAF-3, PAF-4 and PAF-1 synthesized at slightly different reaction conditions (Figure 5-15).[47,306,309] Interestingly, all three PPNs show higher specific BET surface areas compared to the respective PAF analogues, which might be a result of slight deviations in the synthesis conditions. With a value of 6461 m^2 g^{-1} the material PPN-4 holds the current record for the highest specific BET surface area of all POP materials to date, surpasses even the surface area of MOF-210 (6240 m^2 g^{-1}) and almost reaches the specific BET surface area of NU-1103 (6550 m^2 g^{-1}), NU-109E and NU-110E.[68-70,309]
Until today, a large number of different CMP structures for potential applications as catalysts,[290,310-316] molecular sensors,[282,293,295,306,317,318] electronic devices[279,319-323] or gas and liquid sorbents[273,277,279,283,285,288,297,307,308,324-330] have been reported. Due to the broad variety of different synthesis pathways of CMPs combined with comparatively mild reaction conditions, the potential for functionalization of the porous networks is obvious.

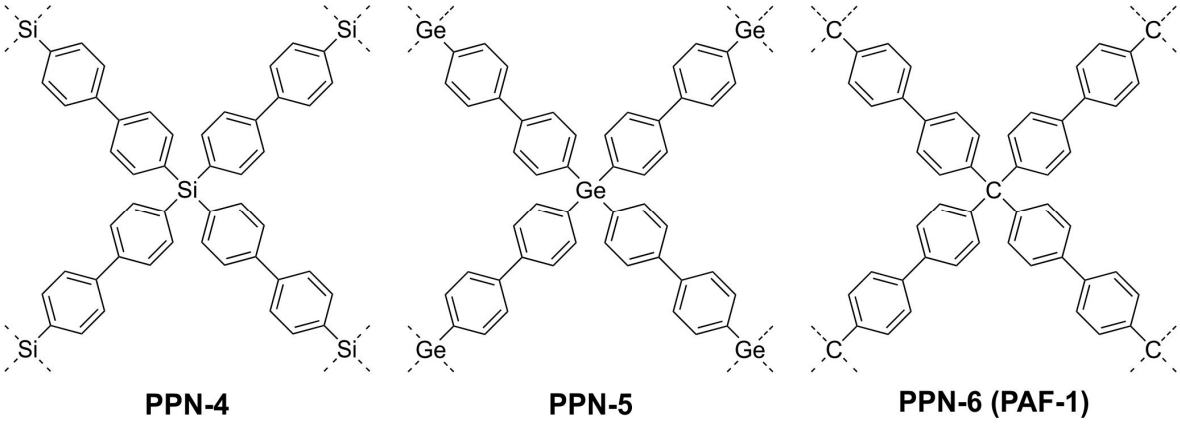

Figure 5-15: *Molecular structures PPN-4, PPN-5 and PPN-6 networks.*

In 2009, Dawson *et al.* synthesized a number of functionalized CMP networks *via* palladium-catalyzed Sonogashira-Hagihara cross-coupling including hydroxyl, amino, nitro, methoxy, fluoro and methyl functionalizations.[284] Although, not all of the networks are porous some candidates exhibit remarkable specific surface areas over 800 m^2 g^{-1}.

Recently, Xiang *et al.* presented a series of functionalized CMPs, assigned as COPs in the study, based on tetrakis(*p*-bromophenyl)methane synthesized *via* Yamamoto-type Ullmann cross-coupling.[331] It is worth noting that the hydroxy-functionalized material COP-20 possesses the highest total pore volume (3.5 cm^3 g^{-1}) in the field of covalent organic framework materials to date.[331] In a report by Jiang *et al.* quaternary nitrogen sites have been implemented successfully by applying triphenylamine-based nodes.[332] Recently, Wang *et al.* synthesized nitrogen rich CMPs carrying amino and azo functionalizations with CO_2 uptakes up to 3.72 mmol g^{-1} at 273 K and 1.13 bar combined with remarkable IAST selectivities for CO_2 over N_2 (15:85) ranging from 60 to 80.[333] The amine functionalized CMP NPOF-1-NH_2 shows high CO_2 uptake capacities at 298 K of 3.77 mmol g^{-1} at 1 bar and still 1.07 mmol g^{-1} at 0.15 bar.[334]
Dawson *et al.* successfully introduced amino, carboxyl, hydroxyl and methyl functionalities in a CMP-1 network structure.[281,324] Lim *et al.* performed post-synthetic modification of adamantane-based CMPs by Friedel-Crafts reaction where functionalization with nitro groups significantly increase the CO_2 sorption capacity of the respective porous polymer networks.[275]
Modak *et al.* synthesized a set of porous networks containing Fe-porphyrin rings showing a remarkable CO_2 uptake of 4.30 mmol g^{-1} at 273 K and 1 bar.[325]
Alkordi *et al.* reported a series of nine CMPs with different functionalization and demonstrated a significant effect on the CO_2 adsorption enthalpies depending on the respective functional group.[326]

Porous polymer network PPN-6, which is structurally similar to PAF-1, has been modified by treatment with chlorosulfonic acid (PPN-6-SO_3H) and a subsequent neutralization with lithium hydroxide (PPN-6-SO_3Li) .[335] The functionalized PPN-6-SO_3Li network showed an increased CO_2 uptake of 3.7 mmol g^{-1} and an also increased IAST selectivity for CO_2 over N_2 of 414 at 295 K and 1 bar compared to the non-functionalized PPN-6 with an uptake of 2.24 mmol g^{-1} and a IAST selectivity of approximately 7.[335]
Accordingly, the network PPN-6-SO_3NH_4 has been synthesized by treating PPN-6-SO_3H with ammonium hydroxide.[336] With a value of 796 for a CO_2/N_2 (15:85) gas mixture the material exhibits the highest IAST selectivity for CO_2 over N_2 to date and a remarkable CO_2 uptake of approximately 2.8 mmol g^{-1} at 313 K and 1 bar.[336] The functionalization of PPN-6 with diethylenetriamine (DETA) yielded material PPN-6-CH_2DETA with a high CO_2 uptake of 4.3 mmol g^{-1} and a IAST selectivity of CO_2 over N_2 (15:85) of 442 at 295 K and 1 bar.[337]
Regarding the number of reports on this topic in the current literature, the number of CMP structures and CMP applications will surely grow in the next years. The relatively mild synthesis conditions of several CMPs enable the incorporation of functional groups in the network structures and will even expand the field of possible applications for porous CMP materials.

5.3.2 Porous Benzimidazole- and Azo-linked Networks

Porous networks built from benzimidazole and azo linkages have come up only recently in the field of disordered organic polymer networks. Both network types are potentially interesting for CO_2 capture and separation due to the nitrogen atoms in the polymer structure which might interact with the polarizable and slightly acidic CO_2 molecules.

The benzimidazole linkage is potentially interesting for the construction of porous sorbent materials due to its rigidity and the remarkable chemical and thermal stability. In early reports on these materials, porous benzimidazole-linked polymer (BILP) networks with moderate surface areas and pore volumes have been obtained by using templating agents as porogens.[135,338,339] The first synthesis of a porous benzimidazole-linked network, BILP-1, by condensation of tetrakis(*p*-formylphenyl)methane (TFPM) and 2,3,6,7,10,11-hexaaminotriphenylene (HATP) with high specific BET surface area and a potential application as gas sorbent materials has been reported by Rabbani *et al.* in 2011.[340]

The template-free synthesis concept of porous polybenzimidazole networks is based on a condensation of aromatic *ortho*-diamines and aryl-aldehydes in a two-step reaction (Figure 5-16). In the first step, a poly(benzimidazole) precursor is formed at low temperatures. The oxygen-assisted formation of imidazole ring at high temperatures is performed in a second step.[341] A slow addition of the aldehyde source has been found to be crucial for the porous properties of the respective material.[342] Due to the non-reversible nature of the ring formation mechanism all porous benzimidazole network structures presented to date did not exhibit considerable long-range order.

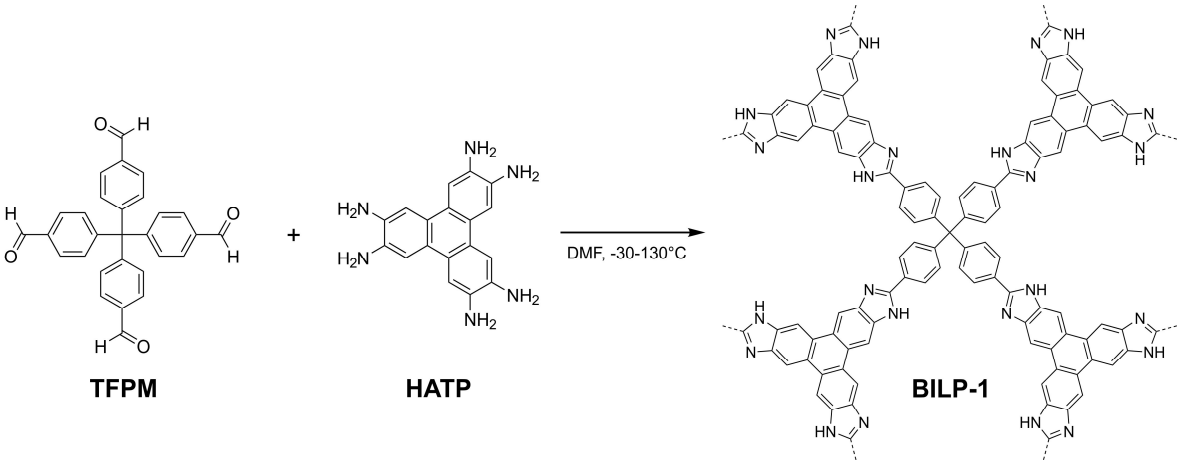

Figure 5-16: *Schematic synthesis of BILP-1 from TFPM and HATP.*[340]

In the past few years, the gas sorption properties of benzimidazole-linked networks including pyrene,[341,343] triptycene,[342-345] 2,4,6-triphenyltriazine,[344] porphyrin,[346] tetraphenylmethane,[342] triphenylene[340,342] and tetraphenylsilane[347] moieties have been investigated. It is obvious that the nitrogen-containing imidazole moieties in the polymer backbone might be advantageous for gas storage and separation applications. In more detail, the protonated and non-protonated nitrogen sites of imidazole are capable of

performing hydrogen bonding and dipole/quadrupole interactions with acidic gases, e.g. CO_2.[342,345] Additionally, the benzimidazole linkage has been proven to be stable under acidic conditions which prevail in, for instance, flue gas streams. In contrast to imine groups, an established benzimidazole network has been found to remain unaffected by 2M HCl or 2M NaOH.[340]

The group of El-Kaderi and coworkers thoroughly investigated the CO_2 sorption properties of several BILP network structures in the past.[340-345,348] The BILP networks in general possess rather high specific BET surface areas between 599 m^2 g^{-1} (BILP-5) and 1497 m^2 g^{-1} (BILP-12).[342,343] The networks BILP-3 and BILP-4 exhibit the highest CO_2 uptakes of all reported BILP structures with 5.11 mmol g^{-1} and 5.34 mmol g^{-1} at 273 K and 1 bar.[342,345] At 278 K and 1 bar the CO_2 uptakes still reach 3.30 mmol g^{-1} for BILP-3 and 3.59 mmol g^{-1} for BILP-4.[342,345]
The triazine-containing benzimidazole network TBILP-2 presented recently by Sekizkardes *et al.* could adsorb up to 5.18 mmol g^{-1} at 273 K and 3.32 mmol g^{-1} at 298 K and a pressure of 1 bar.[344]
The adsorption selectivity of several BILPs for CO_2 over N_2 has been determined by initial slope method or IAST method.[343,344,348] The CO_2/N_2 selectivity of BILP-2 with a value of 113 is the highest to date of all BILP networks based on initial slope calculations at 273 K followed by BILP-10 with a value of 111.[342,343] At 298 K the respective selectivities of BILP-2 (71) and BILP-10 (59) have been surpassed quite recently by network BILP-101 with a CO_2/N_2 initial slope selectivity of 80.[342,343,348] The highest IAST selectivities at 298 K for a gas mixture of CO_2/N_2 (10:90) have been determined for BILP-10, TBILP-1 and BILP-101 with values of 57, 62 and 80, respectively.[343,344,348]
Recently, Zhang *et al.* synthesized a porous benzimidazole network PN-101 with a CO_2 uptake of 5.14 mmol g^{-1} almost reaching the top performing network BILP-4.[347] The evaluation of the IAST sorption selectivity of PN-101 for CO_2 over N_2 in a gas mixture of 15:85 at 273 K yielded a very high value of 199.[347]
Porous network structures for gas capture and separation connected by azo-linkages have been introduced by Patel *et al.* in 2013.[349] Three azo-linked network materials have been synthesized by direct coupling of tetrakis(*p*-nitrophenyl)methane (TNPM) with TAPM (azo-COP-1), *p*-phenylenediamine (azo-COP-2) and benzidine (azo-COP-3) under basic conditions (Figure 5-17).[349]
To date quite a number of different networks connected by azo-linkages have been synthesized by different synthesis protocols such as azo coupling,[350] direct coupling of nitro aromatic compounds with arylamines in the presence of KOH,[349] copper(I)-catalyzed homocoupling,[351,352] oxidative polymerization by using t-BuOCl/NaI[353] or Zn-induced reductive homocoupling.[354,355] Typically, azo-linked polymer networks are amorphous and stable against hydrolysis and elevated temperatures which make them potentially interesting for application as gas sorbents in industrial plants.[349,351,352]

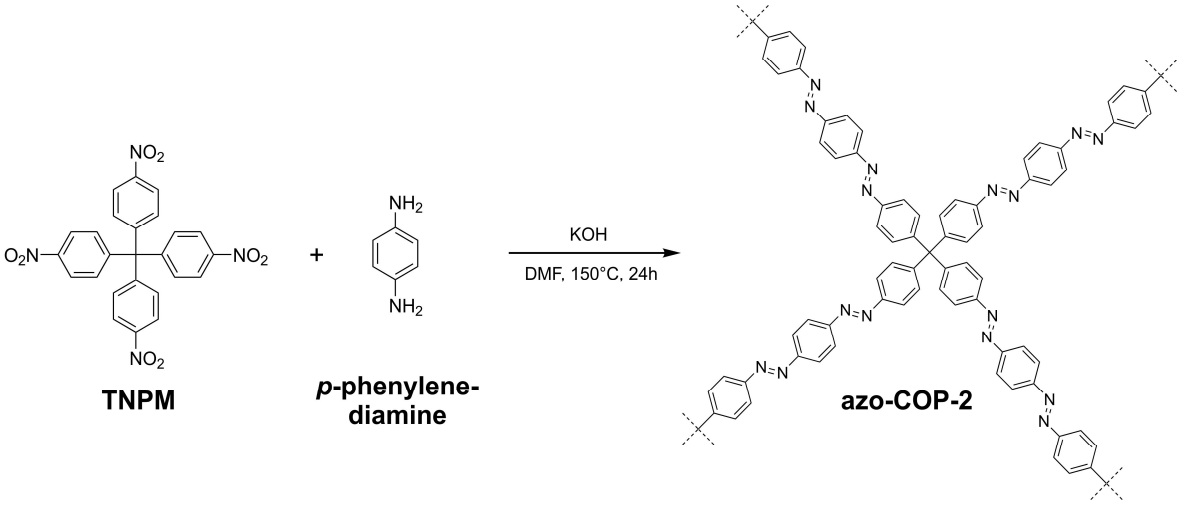

Figure 5-17: *Exemplaric synthesis scheme for azo-COP-2 from TNPM and* p-*phenylenediamine under basic conditions.*[349]

Despite of moderate specific BET surface areas azo-COPs exhibit good CO_2 uptake capacities and exceptionally high gas sorption selectivities for CO_2 over N_2.[349] In contrast to other porous organic network materials, the gas sorption selectivity of azo-COPs for CO_2 over N_2 at low pressures increases with temperature.[349] Azo-COP-2 reaches a remarkably high IAST selectivity of 288 for a CO_2/N_2 gas mixture (15:85) at 323 K and 1 bar.[349] The network azo-COP-2 is able to adsorb 0.71 mmol g^{-1} of CO_2 at this temperature and pressure.[349]

In the past few years, the group of El-Kaderi and coworkers synthesized a number of azo-linked networks which might have potential for application in CO_2 capture and separation applicatins.[351,352]

The polymer network ALP-1 synthesized by Arab *et al.* could adsorb 5.36 mmol g^{-1} of CO_2 at 273 K and 1 bar being one of the highest CO_2 uptake capacities to date.[351] At 273 K, ALP-5 could adsorb 4.46 mmol g^{-1} of CO_2 at a quite high IAST selectivity of 60 for a CO_2/N_2 (10:90) gas mixture.[352] Interestingly, similar to the results of Patel *et al.*, the gas sorption selectivity of the networks ALP-5, ALP-6 and ALP-7 also increases with temperature.[349,352]

In a report by Lu et al. Azo-POF networks have been synthesized in a facile approach by Zn-induced reductive coupling of building blocks carrying four nitro groups.[354] Therein, the network Azo-POF-2 exhibits very good sorption selectivity for CO_2 over N_2 of 76 at 273 K and 54 at 298 K according to the Henry´s law or initial slope method.[354] The IAST selectivities of Azo-POF-2 for a gas mixture CO_2/N_2 (15:85) are 55 at 273 K and still 42 at 298 K.[354]

Beside the potential application as gas sorbents azo-linked networks have also been investigated as catalysts for methylation of *N*-methylaniline by applying CO_2 as C1 source and as potential adsorbent material for radioactive iodine.[353,355]

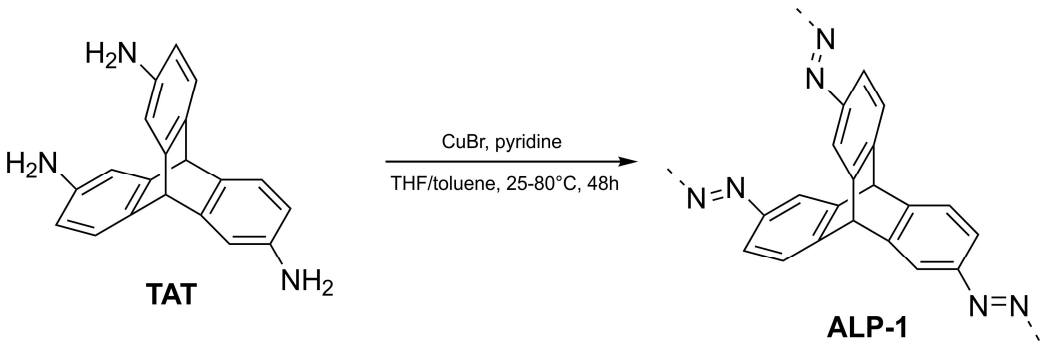

Figure 5-18: *Exemplary synthesis scheme of the porous azo-linked network ALP-1 from 2,6,12-triamino-triptycene (TAT).*[351]

5.3.3 Porous Polyimide Networks

Polyimide materials are widely known for decades as high temperature plastics, adhesives, dielectrics, photoresists or membrane materials due to a number of characteristic and desirable properties such as thermo-oxidative stability, enhanced chemical stability, radiation resistance and high mechanical strength.[356-358] Porosity in polyimide materials without the usage of templating agents can be generated by effective cross-linking of rigid anhydride and amine building blocks, where at least one of the monomer units carries more than two of the respective functionalities. Due to its Lewis-acidic character and its quadrupolar momentum CO_2 is expected to interact strongly with the highly polar imide functionalities on the polymer surface, rendering porous polyimides interesting as potential sorbents for CO_2 capture and separation applications.

Although the presence of cavities or pores in rigid polymer structures such as branched aromatic polyimides has at least been expected since the early 1990s,[359-361] two of the first porous polyimides consisting of a highly cross-linked network and pore structure characterized by gas sorption measurements have been reported by Weber *et al.* in 2008.[362] In this study, the porous polyimide PI1 has been synthesized from 2,2',7,7'-tetra-aminospirobifluorene (TABF) and pyromellitic dianhydride by applying a *m*-cresol/isoquinoline solvent system in almost quantitative yield (Figure 5-19a). The resulting networks exhibit specific BET surface areas of nearly 1000 $m^2\ g^{-1}$.[362] Obviously, the contorted structural motif of the spirobifluorene moiety and the rigidity of both monomer units prevent an effective dense packing of the polymer network and promote the formation of large inner surfaces.[362]

Wang *et al.* synthesized two different porous polyimide networks by linking pyromellitic dianhydride (PI-1) and 1,4,5,8-naphthalenetetracarboxylic dianhydride (PI-2) with tetrahedral-shaped TAPM nodes (Figure 5-19b).[363] Again, the condensation has been

performed as an isoquinoline-catalyzed one-step polymerization reaction in *m*-cresol.[363] Both polyimide networks were obtained in quantitative yields showing very high specific BET surface areas of 1407 m^2 g^{-1} for PI-1 and 732 m^2 g^{-1} for PI-2, respectively. The authors attribute the significant differences in the surface areas to the larger volume of the naphthalene unit compared to the benzene unit and the larger dihedral angle between the imide and the benzene ring in PI-2.[363]

Recently, Shen *et al.* applied an almost similar reaction concept to obtain the first porous polyimide network PI-ADPM linked by 1,3,5,7-tetrakis(*p*-aminophenyl)adamantane (TAPAD) nodes (Figure 5-19c).[364] Again, by using *m*-cresol as solvent and isoquinoline as catalyst combined with a slow and stepwise increase of the temperature the desired porous polyimide networks have been synthesized with specific BET surface areas of 868 m^2 g^{-1} and a CO_2 uptake of 3.32 mmol g^{-1} at 273 K and 1 bar.[364]

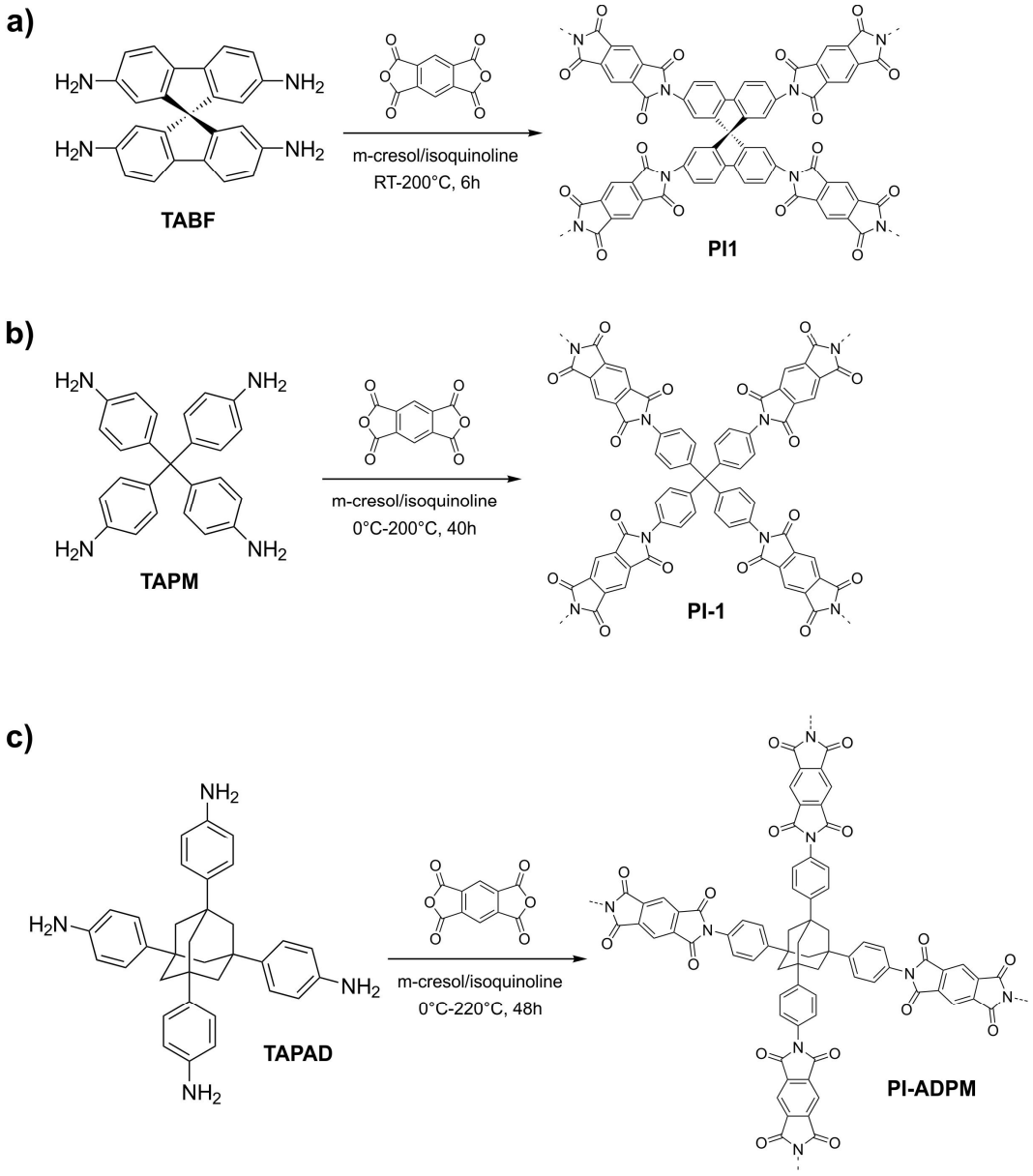

Figure 5-19: *Schematic syntheses of porous polyimide networks (a) PI1 by Weber* et al.*, (b) PI-1 by Wang* et al. *and (c) PI-ADPM by Shen* et al.[362-364]

Some examples of porous three-dimensional polyimide materials have been set up by linking tetrahedral amines and tetracarboxylic acid dianhydrides, but also trigonal amine building blocks are capable of generating extended porous network structures. Recently, Wang *et al.* reported four porous polyimide structures based on trigonal linking nodes (Figure 5-20).[365] The networks have been formed in a condensation reaction of the amine monomers TAPB and tris(*p*-aminophenyl)amine (TAPA) with pyromellitic dianhydride (PMDA) and naphthalene tetracarboxylic acid dianhydride (NTDA) in *m*-cresol catalyzed with isoquinoline.

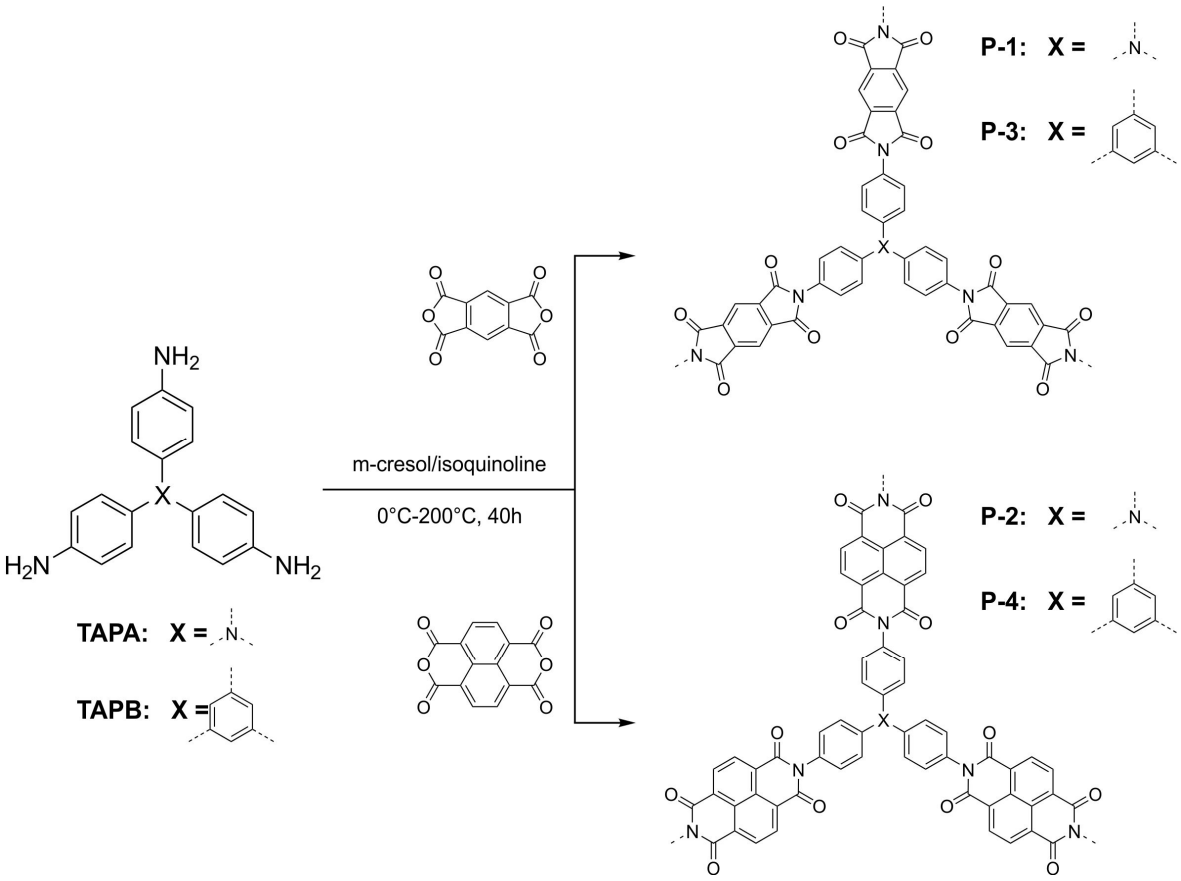

Figure 5-20: *Synthesis of polyimide networks P-1 to P-4 according to Wang et al. from trigonal triamine monomers TAPA and TAPB.*[365]

Although, the amorphous polyimide networks were obtained in quantitative yields, the specific BET surface areas between 232 m^2 g^{-1} and 818 m^2 g^{-1} do not reach the values reported for comparable materials containing tetrahedral nodes.[363] The lower surface area could be explained by a more efficient packing of the polymer structure when considering almost planar triangular linking nodes instead of bulky tetrahedral nodes. Wang *el al.* suggest a significant influence of electronic interactions like donor-acceptor interactions and π-π-stacking between the aromatic and imide moieties on the packing motives of the respective networks.[365] Additionally, the higher flexibility in the structure of TAPA might favor a collapse of the pores and thus decrease the accessible surface area.

Another interesting synthesis concept has been reported by Farha *et al.* in 2009.[366] The porous polyimide network introduced in this study was synthesized from the same starting materials, namely TAPM and NTDA, as the network polymer by Wang *et al*. named PI-2.[363] Farha *et al.* used a mixture of DMF and propionic acid in a one-pot reaction to obtain a porous polyimide network. The reaction temperature has been kept constantly at 170 °C throughout the entire reaction process (Figure 5-21).

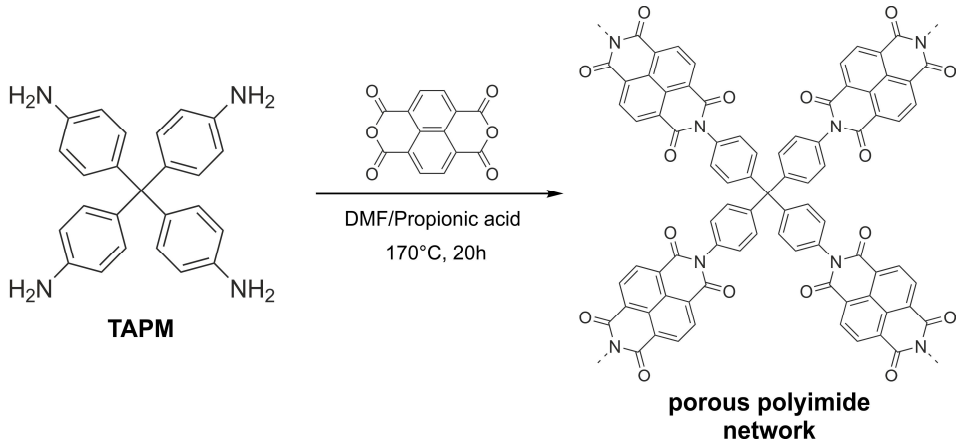

Figure 5-21: *Synthesis of a porous polyimide material according to Farha et al.*[366]

Although the absolute yields have not been stated, the authors suggest a complete conversion due to the absence of amine bands in the respective infrared spectra.[366] It is worth mentioning that the condensed water has obviously not been removed from the reaction vessel, as the reaction has been carried out under reflux conditions. However, the obtained specific BET surface area of the final polyimide (750 m^2 g^{-1}) calculated from the nitrogen adsorption isotherm is by far lower than the specific BET surface area of PI-1 (1407 m^2 g^{-1}).[363,366] Post-synthetic reduction of the porous polyimide network enabled a significant improvement of the CH_4 over CO_2 selectivity especially at elevated pressures.[367]

Recently, Rao *et al.* presented two porous polyimide networks containing the uncommon 3,4,9,10-perylene diimide linker (Figure 5-22).[368] The difference between the two described polyimide networks lies in the applied amine building blocks. The network material Tr-PPI has been synthesized by a condensation reaction from 3,4,9,10-perylenetetracarboxylic acid dianhydride (PTDA) and the trigonal TAPA, while the tetragonal TAPM has been applied in the synthesis of the network Td-PPI. Both materials were synthesized in a solvent mixture of dimethylacetamide and imidazole in quantitative yields. Due to the high melting point of imidazole, the amine compounds were added at temperatures above 150 °C. According to the data obtained from nitrogen sorption measurements, Tr-PPI and Td-PPI exhibit specific BET surfaces of 400 m^2 g^{-1} and 2213 m^2 g^{-1}, respectively. The latter shows one of the highest specific BET surface areas of all porous polyimide materials reported to date.

In a successive paper Rao *et al.* investigated the CO_2 and H_2 sorption properties of the PPI networks and synthesized a new set of polyimide networks containing trigonal and tetragonal nodes connected by bulky coronene linkers (Figure 5-23).[369] At lower pressures of about 1 bar and 195 K Tr-NPI exhibited the highest CO_2 uptake of approximately 11 mmol g^{-1} (approximately 50 wt%) followed by Tr-PPI (10.2 mmol g^{-1}) and Td-PPI (7.0 mmol g^{-1}).[369]

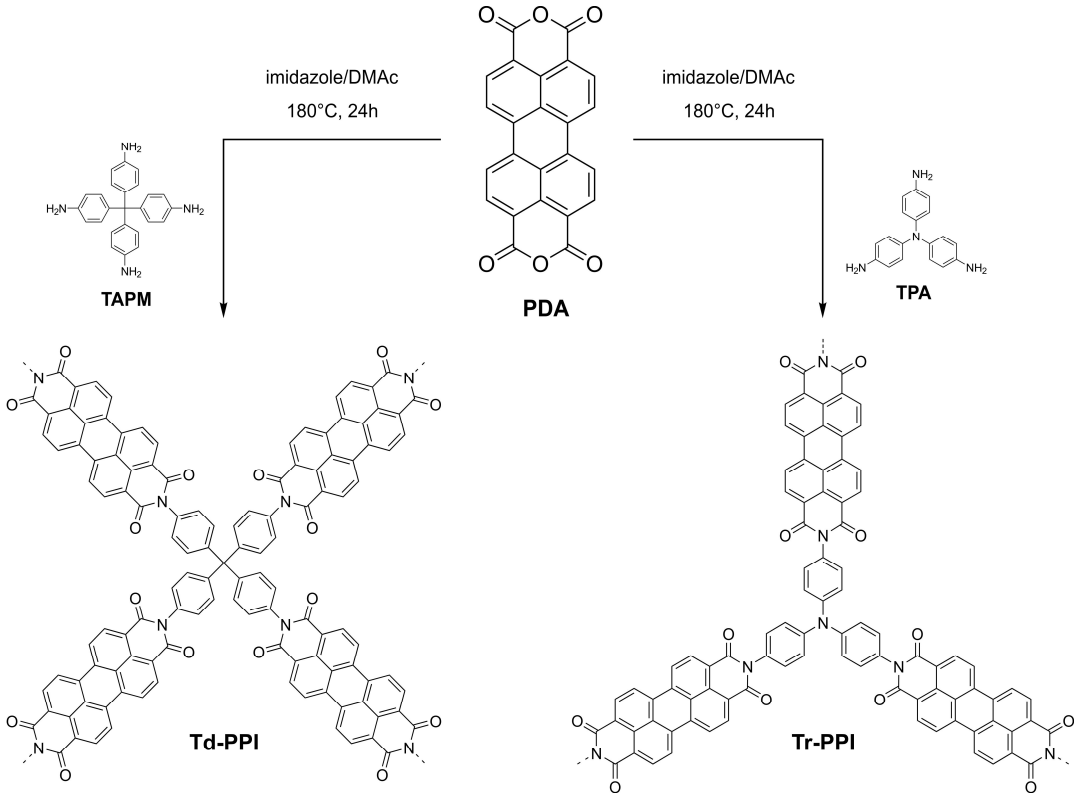

Figure 5-22: *Schematic synthesis of porous polyimide networks Td-PPI and Tr-PPI from perylene tetracarboxylic acid dianhydride (PDA) according to Rao* et al.[368]

The adsorption selectivities of CO_2 over N_2 at 298 K have been determined by the initial slope method for Tr-PPI (12), Tr-NPI (22) and Td-PPI (25).[369]

Luo *et al.* presented an alternative synthesis of triazine-containing porous polyimide materials in DMSO.[370] Three porous networks have been synthesized by imidization of melamine and the respective dianhydride building blocks PMDA (PI1), 3,3',4,4'-biphenyltetracarboxylic dianhydride (PI2) and NTDA (PI3). The respective reaction scheme is illustrated in Figure 5-24.

It should be noticed that the moisture resulting from the condensation reaction is removed from the reaction vessel by azeotropic distillation with toluene. However, the obtained yields have been significantly lower (37-65%) compared to other polyimide synthesis methods discussed in this chapter. The obtained specific BET surface areas calculated from the respective nitrogen sorption isotherms range from 265 $m^2 g^{-1}$ to 660 $m^2 g^{-1}$.[370]

It is worth mentioning that the results from elemental analysis presented in the study reveal an unexpectedly high nitrogen content in all three polymers.[370] Furthermore, the low signal intensity of the aromatic units at about 130 ppm seems to be quite uncommon, especially for PI2 and PI3. The ^{13}C MAS NMR spectra also contain a series of signals in the region between 40 and 70 ppm, which is not discussed in the publication.

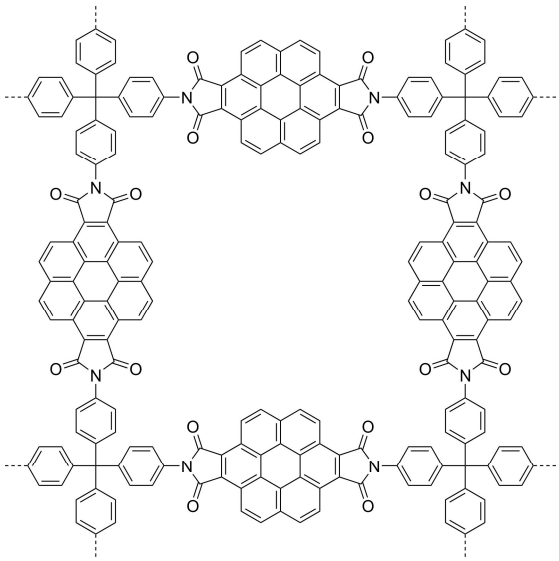

Td-CPI

Figure 5-23: *Molecular structure of coronene-linked porous polyimide Td-CPI.*[369]

The unknown signals might result from the presence of immobilized DMSO molecules on the surface of the porous materials. The observations made above indicate that condensation reaction for all three polyimide networks might not be complete under the given reaction conditions.

Yang *et al.* reported a series of sulfonated polyimide networks with different degrees of functionalization and investigated their gas and liquid sorption properties.[371] The synthesis of the networks has been carried out in *m*-cresol in presence of trimethylamine and benzoic acid as catalyst.[371] While the specific BET surface areas of the networks decrease from 574 $m^2\ g^{-1}$ to 23 $m^2\ g^{-1}$ with increasing sulfonate content, the adsorption selectivity for CO_2 over N_2 at 1 bar and 273 K significantly increases from 29.5 (SMPI-0) to 57.6 (SMPI-100).[371]

In another recent study, Li and Wang demonstrated the potential of porous polyimide networks as efficient CO_2 and organic vapor sorbent materials.[372] Therein, three polymer networks have been synthesized by condensation of TAPM (MPI-1), TAPA (MPI-2) and TAPB (MPI-3) with pyromellitic dianhydride in *m*-cresol/isoquinoline in quantitative yield.[372] All three networks are microporous with predominant pore sizes between 0.5 and 0.6 nm. The specific BET surface areas range from 586 $m^2\ g^{-1}$ (MPI-3) to 1454 $m^2\ g^{-1}$

(MPI-1). Regarding the CO_2 sorption properties, MPI-1 and MPI-2 show remarkable CO_2 uptakes of 3.82 mmol g^{-1} and, respectively, 3.14 mmol g^{-1}at 273 K and 1 bar.[372] Furthermore, the gas adsorption selectivity of MPI-1 for CO_2 over N_2 has been determined to 102 from initial slope calculations.

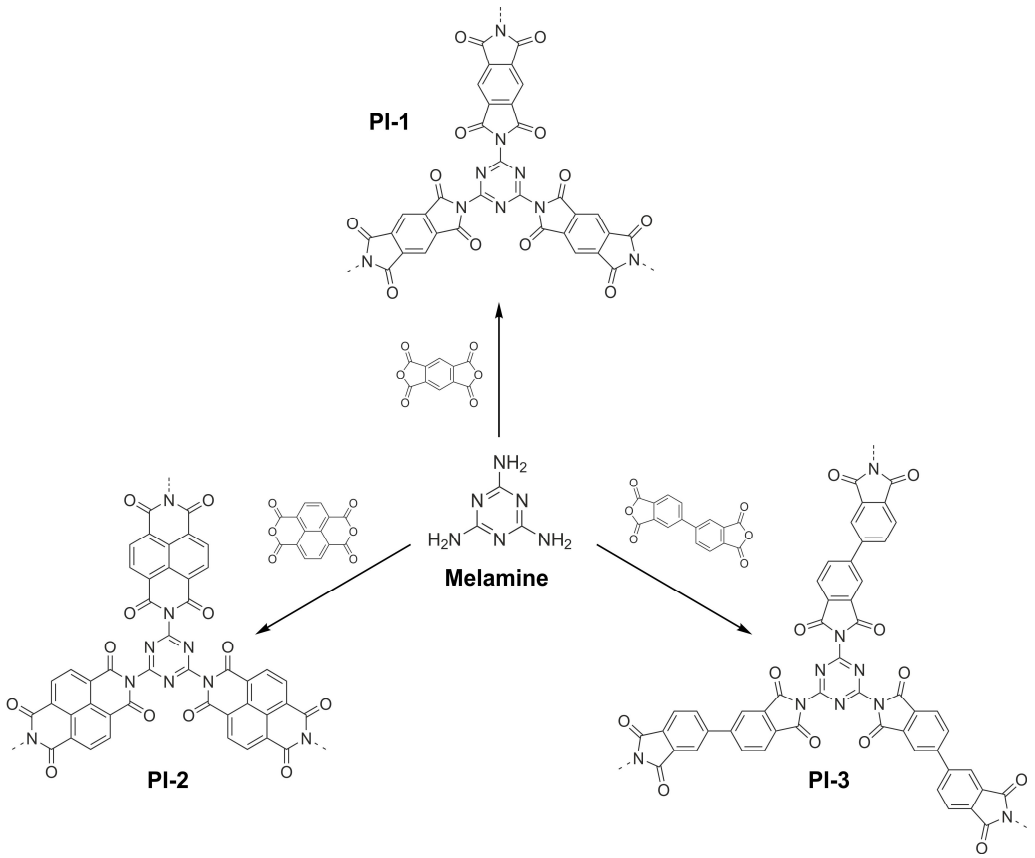

Figure 5-24: *Schematic syntheses of melamine-based porous PI networks according to Luo.*et al.[370]

The authors attribute the high affinity towards CO_2 to the uniform network pore size of about 5 Å, which might favor the smaller CO_2 (kinetic diameter 3.3 Å) molecules over the larger N_2 (3.64 Å) molecules.

Shen and Wang functionalized a porous polyimide network synthesized from TAPAD and NTDA by treatment with fuming nitric acid.[373] The nitro-functionalized network PI-NO_2-1 shows a CO_2 uptake of 4.03 mmol g^{-1} at 273 K and 1 bar which is the highest value for porous polyimides to date.[373]

In a very recent study, Klumpen *et al.* synthesized various functionalized polyimides from TAPM and the respective functionalized dianhydride building blocks and investigated the CO_2, CH_4 and H_2O sorption properties of the resulting networks.[49] Interestingly, the specific surface areas calculated by BET and QSDFT methods from Ar sorption isotherms do not correlate with the respective CO_2 uptakes of the polymer networks. The network MOPI-V, for instance, exhibits the highest specific BET surface area of all polymers (921 m^2 g^{-1}) in the report and, at the same time, the lowest CO_2 uptakes at a given temperature (Figure 5-25). The difference in the specific surface areas might be explained

by the presence of micropores in the networks structures which are not accessible to Ar molecules. The reported functionalized MOPI networks show high CO_2 uptakes at 1 bar and temperatures of 273 K (2.9 – 3.8 mmol g^{-1}), 298 K (1.6 - 2.3 mmol g^{-1}) and 313 K (1.3 - 1.7 mmol g^{-1}).[49] The CO_2 uptake of 3.8 mmol g^{-1} of MOPI-IV at 273 K is one of the highest reported for porous polyimide networks to date. MOPI-I possesses a good sorption selectivity for CO_2 over N_2 of 65 (IAST, CO_2/N_2 = 15:85) and 78 (initial slope method) at 298 K and 1 bar, however, a relatively high water affinity might be a drawback for a potential application in moist flue gas streams.

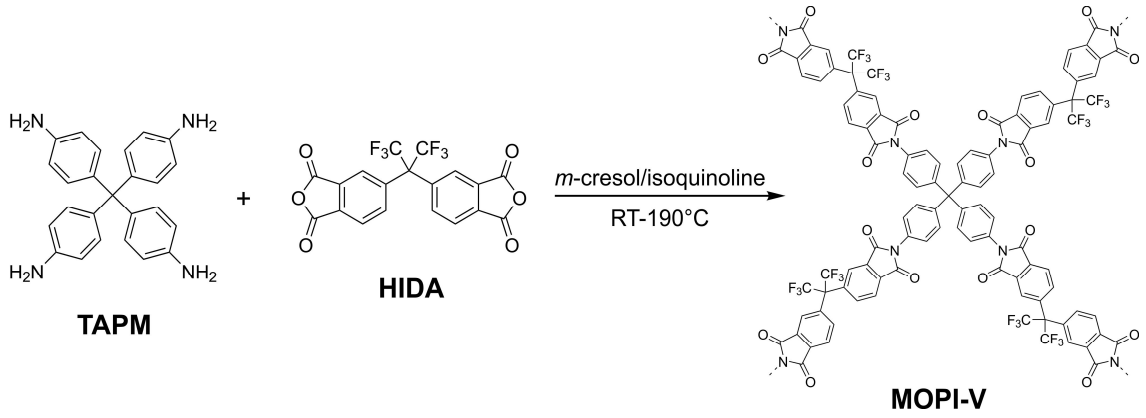

Figure 5-25: *Schematic synthesis of functionalized polyimide network MOPI-V.*[49]

Li *et al.* synthesized porous polyimide networks structurally similar to MOPI-III and MOPI-V by Klumpen *et al.* at slightly modified reaction conditions.[374] It is worth noting that the properties of the respective polymer networks coincide to a large extent pointing to a good reproducibility of polyimide synthesis *via* the m-cresol/isoquinoline route.

For a successful synthesis development of porous organic polymer networks suitable for CO_2 capture and separation applications, a number of certain key aspects can be drawn from the literature review within the present chapter.

The sorption capacity of a sorbent material is generally closely related to its accessible surface area. A high surface area can be achieved by carefully adjusting the synthesis conditions towards the targeted type of application. For CO_2 sorbent materials a high amount of micropores turned out to be beneficial for high CO_2 uptakes and, in some cases, also for the sorption selectivity towards CO_2.

The actual reaction type, regarding kinetic or thermodynamic control, might as well have an influence on the sorption properties of the given sorbent. Reversible reaction mechanisms under thermodynamic control usually provide materials with fairly uniform pore sizes and good tunability. However, these materials are often prone to pore blocking and require comparatively harsh synthesis conditions.

Porous sorbent synthesized under kinetic control usually show pore sizes over a broad size range. Due to the irreversibility of the reaction mechanism the control over pore sizes and

uniformity of the pores is rather difficult. However, a combination of pores of different sizes might reduce the effects of pore blocking in some cases. Generally, the surface areas of porous materials synthesized from kinetically controlled reaction mechanisms are hard to predict.

The introduction of functional groups on the inner pore walls of porous organic networks could have a major influence on the sorption selectivity of the sorbent. Of course, the sorption selectivity also depends on the nature of the adsorbed materials and on the strength of the interaction between a given sorptive and sorbent pair. The latter could be critical when regarding the applicability of a porous organic sorbent material. A strong interaction between sorbent and sorptive could be beneficial for the sorption selectivity but, at the same time, energetically disadvantageous if a reversible sorption process is required. Therefore, a good trade-off between selectivity and reversibility can be regarded as essential.

A table showing selected examples of porous organic polymers including data for CO_2 uptakes, CO_2/N_2 sorption selectivity, enthalpies of adsorption and other could be found in the appendix section.

5.4 Characterization of Porous Materials by Gas Adsorption Methods

During the past few decades, numerous methods for the characterization of porous materials have been developed.[52] Among these, gas sorption is the predominant method of choice for materials with pore sizes in the nanometer scale. Gas sorption techniques show a number of advantages compared to other methods, like cost-effective and non-hazardous experimental setup. Furthermore, gas sorption analysis is a non-destructive technique and allows a simultaneous investigation over the whole range of macro-, meso- and micropores. The following chapter gives an overview on the characterization of porous materials by gas sorption methods starting with basic sorption theory and applied terminology.

5.4.1 Adsorption of Gases on Surfaces

The detailed evaluation of the sorption process of gaseous matter on solid surfaces is essential for a substantial characterization of porous materials. Adsorption in general describes the enrichment of particles or molecules from a liquid or gaseous phase in the

vicinity of an interface, e.g. a solid surface.[60] In gas/solid systems the gas particles enrich at the surface of the solid material, named adsorbent or sorbent. The non-adsorbed particles in the gaseous phase are called adsorptive, while the term adsorbate is used for particles already attached to the sorbent surface. Desorption describes the inversion of the adsorption process. The basic principle of the sorption of gas molecules on a solid surface is displayed in Figure 5-26. As the focus in the scope if this thesis is put on gas sorption analysis, mainly interactions concerning the gas/solid interface will be discussed in the following.

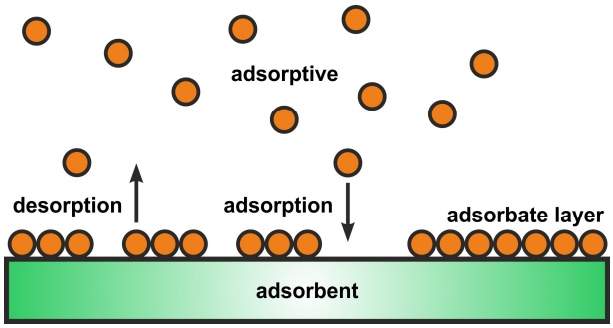

Figure 5-26: *Sorption processes at gas/solid interfaces.*

As the adsorption phenomenon itself is a spontaneous process, thus the Gibbs free energy

$$\Delta G = \Delta H - T\Delta S \tag{5.1}$$

is necessarily negative. The entropy of the adsorptive molecules decreases when adsorbed on a sorbent surface, resulting in a negative term ΔS. The decreasing entropy can be explained by fewer degrees of freedom for a particle in the adsorbate layer compared to a particle in the gaseous phase. Consequently, the adsorption enthalpy ΔH has to be negative, rendering all adsorption processes as exothermic. At sufficiently low temperatures T, the term ΔH overcompensates the energetically disadvantageous loss of entropy caused by the adsorption process and provides negative values for ΔG.

The adsorption mechanism itself can be classified as physisorption or chemisorption, depending on the type of interaction between the adsorbate and the sorbent. When regarding the literature it has been practical to distinguish between the two adsorption phenomena by labeling sorption processes involving binding energies below 40 kJ mol^{-1} as physisorption and above 40 kJ mol^{-1} as chemisorption.
However, it might be more reasonable to differentiate by the nature of interaction, where the term physisorption is restricted to physical and chemisorption to chemical interactions, respectively. In fact, there might be examples of surface adsorption processes resulting from ionic or strong dipolar interactions and despite of adsorption energies clearly above

40 kJ mol^{-1} such processes should still be denoted as physisorption. Due to the low energy barrier, physisorption occurs whenever an adsorptive gas is brought in contact with a solid or liquid surface. The attraction between adsorptive/adsorbate and sorbent is mainly caused by Van-der-Waals forces, including London dispersion forces, dipole/dipole and quadrupolar interactions. As an already formed adsorbate layer can also act as adsorption site itself, the formation of multiple adsorbate layers on a sorbent surface is possible. The formal consecutive formation of several stacked adsorbate layers is described by the term multilayer adsorption.
Physisorptive processes do not involve structural changes on the sorbent surface and are usually fully reversible. Chemisorption is characterized by strong chemical interactions with high binding energies, which are typical for covalent bonding between adsorbate and adsorbent. The formation of covalent bonds often requires overcoming high activation energies and, therefore, chemisorption mainly occurs at elevated temperatures. Due to the specific chemical adsorbate/sorbent interactions, the adsorption is restricted to one single adsorbate layer. In contrast to physisorption, chemisorptive processes are usually irreversible at lower temperatures and could lead to profound changes in the structure of the sorbent surface.

5.4.2 Gas Sorption Measurements

Nowadays, gas sorption analysis is the method of choice for the characterization of porous materials, especially for pores in the meso- and micropore region. The adsorption of different adsorptive gases on the outer and inner surfaces of a respective porous sample provides detailed information about its surface area and pore structure. A more detailed description of pore structure and porosity in porous materials could be found in section 5.1.

The two most frequently used gas adsorption methods are volumetric and gravimetric methods.[60,375] The two methods differ in the determination of the adsorbed gas amounts. While volumetric methods calculate the gas uptake from the amount of gas removed from the gas phase, the gravimetric methods directly measure the gas uptake from the mass change of the sorbent during the adsorption process.[60] Further details on the different adsorption techniques could be found in the literature.[60,375]
For gas sorption measurements at low temperatures, e.g. nitrogen at 77 K or argon at 87 K, which are usually applied for surface area and pore size characterization, the volumetric method is regarded to be advantageous.[53] The gas sorption isotherms are usually measured by volumetric methods and evaluated by plotting the adsorbed gas volume V_{ads} against the relative pressure p/p_0, where p is the actual pressure in the sample cell and p_0 is the vapor saturation pressure of the adsorptive at working temperature.

The adsorbed gas volumes are by convention converted to standard conditions (T_{st} = 273.15 K, p_{st} = 760 Torr) to obtain a standard adsorbed volume V_{STP} (STP = Standard Temperature and Pressure), facilitating the calculation of the adsorbate weight or the adsorbed molar gas amounts.[375]
It should always be kept in mind that the exact determination and quantification of the amount of material adsorbed in the adsorbate phase is rather difficult.[60] The application of the so-called Gibbs surface excess amount assumes a completely two-dimensional adsorption to a given surface, the Gibbs dividing surface (GDS), which - in case of gas sorption - limits the volume available for the respective adsorptive gas.[60] The difference between the amount of gas in the adsorptive gas in equilibrium with the adsorbate phase on the one hand and the total amount of adsorptive introduced to the system on the other hand determines the surface excess amount.[60] In fact, volumetric or gravimetric gas sorption experiments provide the value for the Gibbs surface excess amount. According to the literature, the difference between the surface excess amount and the actual amount of material adsorbed in the adsorbate phase could be regarded as equal if (i) the adsorption process takes place under pressures of 0.1 MPa and (ii) the assumption of the GDS for the calculation of the surface excess amount is sufficiently accurate to the actual adsorbent surface.[60]

Prior to the measurement the exact volume of the empty measuring chamber has to be determined at working temperature in order to perform a proper calibration of the measuring device.[60] The sample has to be degassed at very low pressures, eventually at elevated temperatures, to remove any pre-adsorbed gases from the sample surface and pores. In the actual gas sorption experiment distinct amounts of adsorptive gas are released stepwise into the measuring chamber and sample cell, starting at low relative pressures.[375] At each step, the adsorptive gas is adsorbed on the sample surface causing a pressure decrease in the sample cell until adsorbate and adsorptive are in a state of equilibrium.[375] The quantity of adsorbed gas can be calculated from the difference of the gas amount applied in the measurement apparatus on the one hand and the present amount of gas filling the free space volume in the system on the other hand by applying the general gas equation.[375]
Additionally, the volume of the empty cell and the free cell volume are required. The free volume is the volume in the sample cell that is not occupied by the sample. It can be obtained by subtracting the volume occupied by the sample from the volume of the empty measuring chamber. It should be stated clearly that the accurate determination of the volumes in the measurement apparatus (including manifold, sample cell, etc.) is essential for the quantification of the adsorbed gas amount on the sorbent. Established methods and techniques to perform appropriate volume determinations prior to gas sorption measurements could be found in the literature.[375]

After the adsorption process is complete, the desorption curve is recorded by withdrawing adsorptive gas from the measuring chamber in several consecutive steps. The shape of the complete sorption isotherm reveals information about various important properties of the porous sample, like specific surface area, pore volume and pore size distribution and depends essentially on the applied adsorptive gas.

5.4.3 Adsorptive Gases

Nitrogen at its boiling temperature around 77 K has been established as a standard adsorptive for gas sorption analysis.[60] The cost-efficiency and the broad availability turn out to be the biggest advantages for the usage of liquid and gaseous nitrogen serving as a coolant and adsorptive at the same time. While the characterization of meso- and micropores has been proven, the applicability of nitrogen gas as an adsorptive is limited when observing ultramicroporous materials.[53,60] The decreased adsorptive diffusion rates at 77 K and the quadrupolar moment of the nitrogen molecules (Table 1) lead to a slow filling of narrow micropores at low relative pressures.[60] For example, the initial stage of physisorption in many zeolites and MOFs takes place at very low relative pressures of about 10^{-7}.[60] As a result the equilibration times in this pore region are comparatively long and could lead to extended measuring times sometimes up to several days.

Table 1: *Kinetic diameters and quadrupole moments of different adsorptive molecules.*[13,376,377]

adsorptive	kinetic diameter (Å)	quadr. moment (C m^2)
N_2	3.64	$4.7 \cdot 10^{-40}$
Ar	3.40	0
CO_2	3.30	$13.4 \cdot 10^{-40}$

Argon is more and more considered as potential alternative to nitrogen as adsorptive for gas sorption studies of microporous materials. The working temperature of 87 K allows argon to fill micropores at higher relative pressures than nitrogen, because the higher kinetic energy of the argon atoms provides accelerated equilibration processes and more efficient penetration of pores in the ultramicropore range.[378,379] Argon sorption measurements at 77 K, however, are considered to be less reliable than nitrogen measurements at the same temperature.[60] At 77 K, argon is approximately 6.5 K below its bulk triple point, and therefore, the actual state might differ from the bulk reference state.[60] Additionally, compared to nitrogen or carbon dioxide, the absence of a quadrupole moment significantly reduces the adsorption potential of the argon atoms, especially when adsorbed

on polar or functionalized pore walls (Table 1).[53] Due to the absence of these disturbing interactions, the pore filling pressure of argon sorption measurements could be regarded as more reliable in these cases compared to carbon dioxide and nitrogen measurements.[380]
Although argon fills micropores at higher relative pressures than nitrogen, suitable vacuum equipment, e.g. turbomolecular pump, is still required to obtain sufficiently low relative pressures (pressure range for argon micropore filling in zeolites: $10^{-5} < p/p_0 < 10^{-3}$).[53] In both cases, the low gas diffusion rates at 87 K (argon) and 77 K (nitrogen) are responsible for extended measurement times up to several days for microporous samples.

Carbon dioxide gas, however, is able to enter even the narrowest micropores at ambient temperatures. The high saturation pressure of CO_2 (35.2 bar at 273 K) allows measurements at far higher temperatures, typically around 273 K, compared to nitrogen and argon sorption experiments.[375] The higher operating temperatures also enable higher kinetic energies of the probe molecules and significantly increase the rate of diffusion in contrast to cryogenic conditions.[380] Additionally, the high saturation pressure of CO_2 provides very low relative pressures during the sorption measurements even without using a turbomolecular pump.[380] These features are beneficial to probe even the narrowest micropores in a porous sorbent material.
Theoretical calculations based on the NLDFT and the Grand Canonical Monte Carlo (GCMC) method assigned the lower sensitivity limit of nitrogen and argon to pores of a width of 5.1 Å and 4.0 Å, respectively.[379] It is also reported, that CO_2 is able to pass pores with a minimum diameter of 3 Å even at 273 K.[379] For the determination of pore volumes and specific surface areas by CO_2 sorption, conventional gas sorption analyzers with a maximum working pressure of 1 bar limit the observable pore sizes to values of just below 15 Å.[379] Jagiello *et al.* report the upper sensitivity limit for pore size distributions from CO_2 sorption isotherms at 10 Å. Pores with a larger diameter become undistinguishable, due to the linear dependence of the respective CO_2 sorption isotherms.[379,381,382]
Therefore, CO_2 sorption measurements reveal a clear difference to argon and nitrogen sorption measurements where a full scale characterization over the whole pore size range - down to the respective lower sensitivity limit - could be performed.
Although, CO_2 might be the best choice for the characterization of micropores, it should be mentioned that the quadrupolar moment of the CO_2 molecule could lead to significant interactions with the pore walls of the sorbent, especially when polar sites are present.[60] As a consequence, the calculated results, e.g. pore size distributions and specific surface areas, might be influenced and should be regarded carefully.[60]

A comparison of evaluation methods based on gas sorption analysis with N_2, Ar and CO_2 has recently been published by Weber *et al.*[130] Therein, the pore structure of two different microporous organic polymer networks has been characterized by applying NLDFT, QSDFT and GCMC methods on the respective gas sorption isotherms.

The results in this report clearly show that the different evaluation methods do not always provide consistent results. Therefore, when pore volumes, specific surface area and pore size distributions are calculated from gas sorption measurements, their values should always be reported in combination with the applied adsorptive gas and the evaluation method. A detailed discussion on the NLDFT and QSDFT method can be found in chapter 5.4.6.

5.4.4 Sorption Isotherms

The shape of a sorption isotherm is closely related to the pore structure of a porous material and on the sorption mechanism of the adsorptive on the sorbent surface. The adsorption mechanism in a pore depends on its diameter and, in consequence, on the occurring adsorption energy potential. The different adsorption potentials for macro-, meso- and micropores are outlined in Figure 5-27.

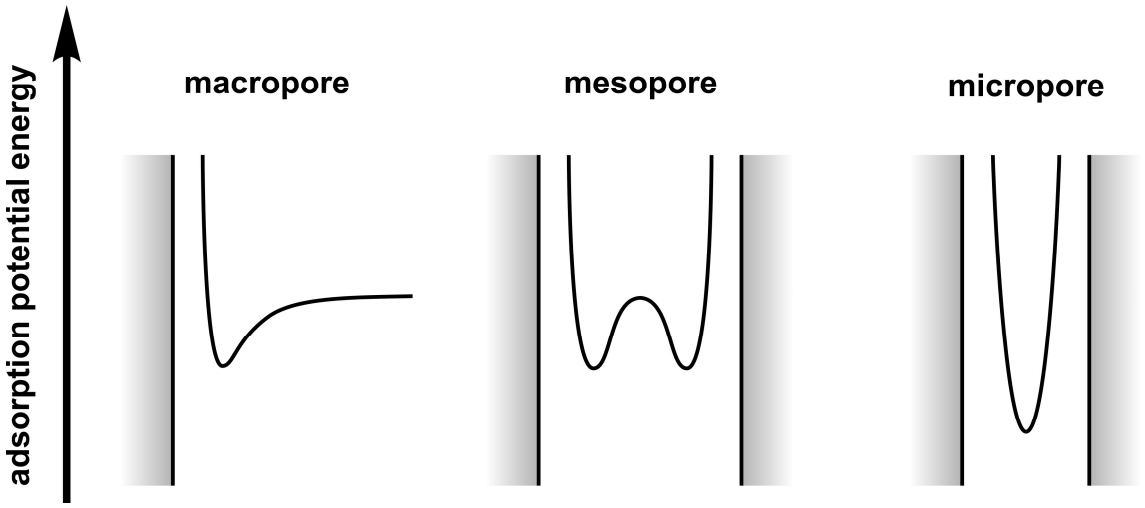

Figure 5-27: *Schematic illustration of the adsorption potential in macropores (left), mesopores (middle) and micropores (right).*

The adsorption mechanism in macropores can be considered as similar to the conventional adsorption of particles on outer surfaces. A given particle with a sufficiently low kinetic energy adsorbs on the sorbent surface in an exothermic process. The depth of the adsorption potential mainly depends on the specific interactions between the adsorptive and the sorbent material.

The adsorption in mesopores is mainly characterized by pore condensation. Hereby, the adsorptive gas condenses in the mesopores at pressures below the saturation pressure of the bulk gas. The pore condensation is closely related to the capillary condensation phenomenon and depends on specific adsorbate/sorbent attraction as well as on specific

molecular adsorptive/adsorbate interactions (e.g. surface tension of the liquid-like adsorbate phase). For pores with uniform shape and width, e.g. cylindrical or slit-like mesopores, the pore condensation phenomenon can be described by the applying the Kelvin equation.[53] Regarding the adsorption potential, the adsorption in mesopores is different from macropore adsorption. While adsorption in macropores is dominated by occurring adsorptive/sorbent interactions, mesopore adsorption depends on both, attractive adsorbate/sorbent interactions and considerable attractive interactions between the adsorbate particles.

The filling of micropores with pore diameters below 2 nm occurs at very low relative pressures. Different from the sorption behavior in mesopores, micropore filling is dominated by the attraction forces between the adsorbate molecules and the pore walls. The confined space within micropores effectively prevents condensation of the gas molecules. The very short wall-to-wall distance leads to an overlap of the two adsorption potentials of both pore walls and in consequence to a significantly lowered total adsorption potential in micropores (Figure 5-27). Hence, the energetically favored adsorption of suitable adsorptive molecules in a given micropore explains the micropore filling mechanism typically occurring at very low relative pressures.
The different kinds of sorption isotherms are commonly used for the characterization of broad variety of porous materials. Information on the composition and structure of a porous or non-porous material is achieved from the shapes of the sorption isotherms and hysteresis loops. The shape of a gas sorption isotherm in a distinct relative pressure region is related to several different factors, e.g. pore size and pore geometry of the sorbent, temperature, chemical and physical properties of the adsorptive.
In 1985, the IUPAC published a number of model adsorption isotherms typically occurring in gas sorption measurements (Figure 5-28).[59] Recently, Thommes *et al.* extended and refined the physisorption isotherms and associated hysteresis loop according to the original IUPAC classifications (Figure 5-28).[60]
According to IUPAC classification, type I isotherms occur when the observed materials are strictly microporous.[59] The isotherm exhibits a very steep increase at low relative pressures until a limiting plateau has been reached. The high gas uptake at low pressures is characteristic for micropore filling due to the high adsorption potential in the micropores. A semi-logarithmic plot of the sorption isotherm is often useful to gain detailed information on the pore structure of microporous sorbents. Especially in physisorptive adsorption processes the limiting plateau in the adsorption branch could be regarded as the total micropore volume, but not as the inner surface area of the sorbent.

The updated classification further distinguishes between type I(a) and type I(b) isotherms.[60] For argon and nitrogen sorption experiments, type I(a) isotherms are typical for microporous materials with mainly narrow micropores showing pore widths of about

1 nm and lower.[60] Type I(b) isotherm appear for materials with a slightly broader pore size distribution exhibiting pore sizes in the range of large micropores or even small mesopores with diameters of approximately 2.5 nm and below.[60]

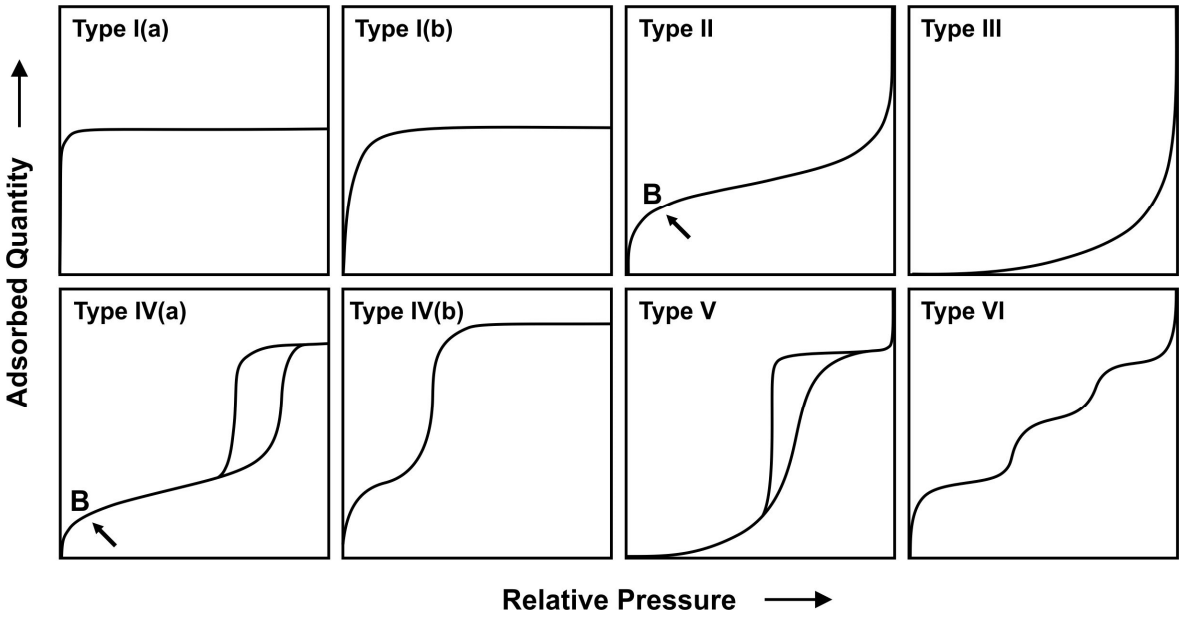

Figure 5-28: *IUPAC classification of different sorption isotherm types according to Sing* et al. *and Thommes* et al.[59,60]

Type II isotherms are typical for non-porous or macroporous adsorbents.[59] The initial gas uptake at low relative pressure is concave to the abscissa and can be attributed to the adsorption of adsorptive molecules on the unoccupied sorbent surface. A steep increase of the adsorption curve in this region indicates considerable attraction between the adsorptive and the sorbent. At the beginning of the linear part of the isotherm (point B in Figure 5-28) the monolayer formation is complete and multilayer adsorption occurs.[59] At relative pressures near the saturation pressure the shape of isotherm is convex relative to the abscissa and characterizes interparticular condensation of the adsorptive gas.

Type III isotherms do not show a rapid gas uptake at low relative pressures.[59] The convex shape relative to the pressure axis indicates weak sorbent/adsorbate interactions, while, especially at high relative pressures, adsorbate/adsorbate attraction is dominant. Examples for this rare isotherm type are the adsorption of nitrogen on collagen and water adsorption on graphite.[383,384]

Type IV isotherms are characteristic for mesoporous materials.[59,60] The occurring monolayer formation in the low-pressure region is similar to the initial stage of a type II isotherm. At higher relative pressures, capillary condensation of the adsorptive gas in the pores causes a rapid gas uptake until mesopore filling is complete. The saturation plateau formed after mesopore filling at high relative pressures is a characteristic feature of type IV

isotherms. The characteristic adsorption behavior of mesoporous materials is closely related to sorbent/sorptive interactions, but also to interactions between the particles in the condensed state within the mesopores.[60]
The original IUPAC characterization of type IV isotherms has recently been subdivided by Thommes et al. in two more specific types, designated as type IV(a) and type IV(b) isotherms.[59,60] The characteristic hysteresis loop for type IV(a) isotherms is formed when the respective steep decrease in the desorption isotherm takes place at significantly lower relative pressures compared to adsorption. The appearance of hysteresis can be observed, when the respective pores exceed a certain critical width depending on the applied experimental parameters, e.g. adsorptive, pore shape, operation temperature, etc.[60]
Materials with pores below the critical pore width show completely reversible type IV(b) isotherms.[60] The absence of the hysteresis loop is characteristic for this type of isotherm. According to Thommes *et al.*, type IV(b) isotherms appear for sorbent materials with conical and cylindrical mesopores which are closed at the tapered end.[60]

Type V isotherms show an adsorption behavior similar to type III isotherms at low relative pressures.[59] At higher relative pressures the characteristic formation of a hysteresis loop can be observed. Type V sorption isotherms are characteristic for mesoporous materials with weak adsorbate/sorbent interactions. Although this isotherm shape is quite uncommon, it is typical for water sorption on activated carbon fibers.[385]

Type VI isotherms occur when adsorptive molecules adsorb in a series of consecutive adsorbate monolayers on a highly uniform non-porous sorbent. The sharpness of the steps observed in the isotherm depends on the adsorption system and the temperature.[59] The uptake capacity of each layer can be determined from the height of the respective step in isotherm.[60] Type VI isotherms have been observed when argon or krypton are adsorbed on non-porous graphitized carbons at 77 K.[386-388]

Hysteresis loops are generally associated with capillary condensation in porous materials. The hysteresis loops appearing in type IV sorption isotherms provide additional information on the nature of the investigated sorbent material. Therefore, the IUPAC has originally recommended four different hysteresis types, types H1 to H4, to be applied for further characterization of (partially) mesoporous materials (Figure 5-29).[59] In 2015, Thommes *et al.* further extended the number of characteristic hysteresis types by adding a new type H5 isotherm and splitting type H2 isotherms in two further sub-classes, type H2(a) and type H2(b) (Figure 5-29).[60]

Type H1 hysteresis loops are typical for ordered mesoporous materials with a narrow pore size distribution. This type of hysteresis has been reported for MCM-41, with an ordered hexagonal cylindrical pore system and for ordered mesoporous silica spheres.[389]
Porous materials showing type H2 hysteresis loops possess highly disordered pore systems

and broad pore size distributions.[59] Type H2(a) show a characteristic steep desorption branch while the gradient of the gas uptake during adsorption is significantly flatter. Thommes *et al.* ascribe the isotherm shape to the presence of either pore-blocking/ percolation effects in a narrow range of pore neck widths or to cavitation-induced evaporation.[60] Type H2(b) isotherms with a steep increase of the adsorption branch and a less steep desorption are also associated with pore blocking effcts.[60] However, in contrast to type H2(a) isotherms, the size distribution of available pore neck widths is significantly broader.[60]

The shapes of Type H3 hystereses are typical for interparticular porosity of large disordered plate-like particles and do not show a plateau limiting the adsorption at high relative pressures.[59]

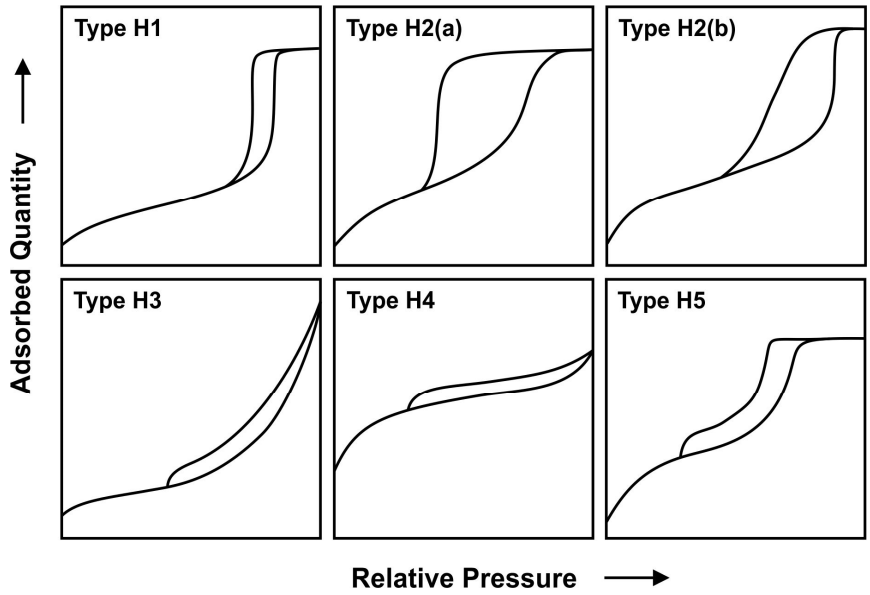

Figure 5-29: *IUPAC classification for hysteresis loops according to Sing* et al. *and Thommes* et al.[59,60]

Type H4 hystereses show considerable gas uptakes in the micropore region and have been reported for samples containing narrow slit pores in combination with a significant amount of mesopores.[59,60] The uncommon but distinctive shape of type H5 isotherms can be observed from porous materials containing both open and partially blocked mesopores.[60]

Additionally, uncommon isotherm shapes have been reported for nitrogen and argon sorption on amorphous polymers like PIMs and porous polyimide networks.[129,362-365,372,390,391] These sorption isotherms usually show a steep increase in the low pressure region similar to type I isotherms, but do not form the typical plateau. The continuous, almost linear increase of the adsorption branch up to high relative pressures and a slow decrease of the desorption branch are characteristic features of the sorption isotherms.

The hystereses could be very large as they do not close until the desorption branch reaches low relative pressures. The difference between the adsorption and the desorption branch might result from structural changes in the polymer network structure during the adsorption process. A reasonable explanation for this unusual isotherm shape is the presence of the so called dual-mode sorption model describing a dynamic system where two different sorption mechanisms are dominant.[130,392] At low relative pressures the adsorption isotherm is dominated by a Langmuir-like shape, representing the micropore filling mechanism known from microporous materials.[392] With increasing pressure, however, the isotherm does not form a plateau, but shows a constant almost linear increase up to high relative pressures.[392] This part of the adsorption isotherm follows Henry´s law and can be explained by a "swelling" of the polymer network as the pressure increases.[362]

5.4.5 Determination of the Specific Surface Area

The determination of the surface area is essential for many potential applications of porous materials. To date, however, no single experimental technique available is capable of providing the true surface area of porous materials.[53]
Nonetheless, two kinetic adsorption models, Langmuir and BET, are frequently used to determine the apparent specific surface area from gas sorption isotherms. Basically, in both theories the surface area of a sorbent is obtained by assuming a complete adsorbate monolayer on the sorbent surface. From the amount of adsorbed material on the surface and the knowledge of the cross-sectional area of one single adsorbate molecule or particle the specific surface area of the sorbent could theoretically be calculated. However, it should be mentioned that the determination of the actual cross-sectional area to be occupied on a given sorbent by a certain adsorptive molecule is rather difficult and depends on several factors like the type of adsorbent and adsorption temperature.[393] For reasons of consistency, fixed values have been recommended for every type of adsorptive at a given sorption temperature which can be found in the literature.[375,393]

Although the total surface area basically refers to the internal and external surface of material, the contribution of the external surface to the total surface area in meso- and microporous materials is very low. However, is should be pointed out that specific surface areas derived from gas sorption experiments do not show the true or absolute surface area of a given sorbent material. Therefore, surface areas determined from gas sorption isotherm should be denoted as apparent or equivalent specific surface areas.[60]

5.4.5.1 The Langmuir Adsorption Model

The Langmuir adsorption theory, developed by Irving Langmuir in 1918, is a comparably simple approach to treat adsorption phenomena on surfaces.[394] It assumes the adsorption of particles on a given sorbent surface with a constant number of energetically equal adsorption sites per unit area. Thus, the adsorbed amount of particles increases until a limiting value is reached, indicating that all available adsorption sites are occupied. The model also assumes an absence of interactions between the adsorptive particles in the adsorbate layer, and thus, limiting the adsorption on the sorbent surface to one single adsorbate monolayer. The linear form of the Langmuir-equation is known as

$$\frac{p}{V_{ads}} = \frac{1}{V_M}p + \frac{1}{KV_M} \tag{5.2}$$

where p stands for the adsorptive pressure, V_{ads} for adsorbed volume, V_M for the volume of a complete adsorbate monolayer and K for a constant in a phase equilibrium between adsorption and desorption processes.[394] When p/V_{ads} is plotted against p, the values for V_M and K can be calculated from the slope and the intercept of the resulting linear graph. The surface area is calculated from the number of adsorbed particles and the cross-sectional area occupied by one single particle on the sorbent surface. A more detailed derivation of the Langmuir-equation based on the Langmuir adsorption theory can be found in the appendix section (chapter 8.1).

In practice, the applicability of the Langmuir theory to characterize porous materials could be regarded as very limited. The Langmuir theory has originally been developed for chemisorptive adsorption systems, where the adsorption energy exceeds the adsorbate/adsorbate interactions by far and the application of the Langmuir-equation might provide reasonable results.[395] In physisorptive systems the formation of only one single monolayer without adsorbate/adsorbate condensation is rather unlikely. If multilayer formation is expected within an adsorption system the calculated Langmuir surface area will exceed the actual surface area of the observed material significantly. Hence, especially for physisorptive adsorption in micropores, the Langmuir-equation might not provide reliable results for the calculation of the specific surface area.

For strictly microporous materials, the limiting plateau in type I isotherms rather describes the micropore volume than the actual surface area.[59,395]

5.4.5.2 The Brunauer-Emmett-Teller (BET) Adsorption Model

The adsorption theory developed by Brunauer, Emmett and Teller (BET) in 1938 extends the Langmuir adsorption theory by including multilayer adsorption.[396] The BET model assumes that an already formed adsorbate layer could act as a sorbent itself, enabling the

formation of a theoretically infinite number of consecutive layers with increasing pressure.[395] The BET model adapts the assumptions described in the Langmuir adsorption theory and additionally considers interactions between neighboring adsorbate layers, which allows a proper description of multilayer formation.[396] However, similar to the Langmuir theory, interactions between particles of the same adsorbate layer are still neglected.[395] It is further assumed that the adsorption energy for the first adsorbate layer, which adsorbs on the sorbent surface, is higher than the adsorption energy for the second and higher adsorbate layers.[396] The adsorption energy between the different layers is treated as constant and equivalent to the condensation energy of the bulk adsorptive phase.

In principle, an evaluation of the specific surface area S_{BET} based on the BET theory can be divided into two main steps.
In the first step, the monolayer volume V_m has to be determined by applying the linearized form of the BET-equation

$$\frac{p}{V_{ads}(p_0 - p)} = \frac{1}{CV_M} + \frac{C-1}{CV_M}\frac{p}{p_0} \tag{5.3}$$

to the experimental sorption isotherm. When $p/(V_{ads}(p_0-p))$ is plotted against p/p_0 the observed graph describes a linear region usually in the range $0.05 < p/p_0 < 0.3$.[59] A linear fit of this region yields the values for the monolayer volume V_M and the C-constant from the slope and the intercept of the linear fit. The C-constant is a specific parameter for a given adsorbent/adsorptive pair roughly characterizing their degree of interaction. For reliable results, the C-constant should exhibit values not less than 100. At values less than 20, the BET equation is regarded to be not applicable due to a considerable overlap of mono- and multilayer adsorption in the system.[52] The BET-equation can be derived from a dynamic equilibrium between the adsorptive or vapor phase with the liquid-like adsorbate phase. A detailed description can be found in chapter 8.2.
In the second step, the specific surface area is calculated from equation (5.4)

$$S_{BET} = \frac{V_M N_A \sigma_0}{V_0} \tag{5.4}$$

by applying V_M and the cross-sectional area σ_0 of a respective adsorbate molecule on the sorbent surface. However, the expression “monolayer volume” might be misleading to some extent, as in an adsorption system based on physisorption the formation of exactly one completely filled adsorbate monolayer is very unlikely. The values N_A and V_0 are the Avogardro’s number and the molar gas volume at given conditions, respectively. An example for the calculation of the specific BET surface area can also be found in chapter 8.3 in the appendix section.

5.4.5.3 Specific Surface Area of Microporous Materials

The BET theory works very well for meso- and macroporous materials with sufficiently high *C*-constants (about 100). Such materials usually describe type II and type IV sorption isotherms and provide linearity in the BET relevant relative pressure region $0.05 < p/p_0 < 0.3$.

Despite the fact that some of the assumptions in the BET theory, like the unrestricted formation of adsorbate multilayers, are not fulfilled for confined geometries in narrow mesopores and micropores, the BET method is still one of the most popular characterization methods for all kinds of porous (and also non-porous) materials. A conventional evaluation of the BET plot of microporous materials ,however, leads to a significant underestimation of the actual surface area because of the occurrence of micropore filling processes in or even below the BET relevant relative pressure range.[378,397] Additionally, the BET plot often does not exhibit a linear behavior in the conventional relative pressure region between 0.05 and 0.3, which is essential for a reliable calculation of the specific surface area from the BET equation. A low-quality linear fit within the BET relevant pressure range would provide inaccurate values for monolayer volume V_M and *C*-constant.

As the BET theory does not consider the confined geometries in micropores and narrow mesopores, the determined value should not be considered as the actual specific surface area of the sample accessible to the respective probe material.[53,60] Especially, the specific surface area derived from type I isotherms by conventional analysis does not provide reliable results.[60] Nonetheless, the BET method is frequently used to characterize porous materials over the whole pore size range. When regarding microporous materials or materials containing a considerable amount of micropores, recent reports by Thommes *et al.* recommend to denote the surface areas derived from the respective BET evaluation as *apparent* or *BET equivalent* specific surface areas.[53,60] It must be stated clearly that the BET equivalent specific surface are does not provide realistic values of the true surface area of microporous materials and thus should be treated as a kind of "fingerprint".[60]

The applicability of the BET method for the determination of the surface of microporous materials has recently been investigated in detail by Rouquerol *et al*.[395] According to this report, it is suggested to perform the linear fit at relative pressures in a region below the conventional BET pressure range to guarantee a sufficient degree of linearity, which is most important for the BET equation to be valid. In order to identify an appropriate pressure region for the linear fit two additional criteria have been postulated.[395] First, the intercept of the linear fit must be positive. A negative value for the *C*-constant, representing the attractive forces between adsorbate and sorbent, would be physically unreasonable. For the second criterion the term $V_{ads}(p_0-p)$ in the rearranged BET-equation

$$V_{ads}(p_0 - p) = \frac{V_M p_0 C}{1 + \frac{p}{p_0}(C-1)} \frac{p}{p_0} \tag{5.5}$$

has to increase steadily over the linear pressure region. A reasonable explanation for the second consistency criterion is given by Bae et al.[397] For a continuous increase the first derivative of equation (5.5) with respect to x = p/p$_0$, the expression

$$\frac{d(V_{ads}(p_0 - p))}{dx} = \frac{V_M p_0 C}{(1 + x(C-1))^2} \tag{5.6}$$

must be positive. The saturation pressure p_0 and the adsorbate monolayer volume V_M are always positive. The *C*-constant must be positive in order to fulfill the first consistency criterion. Hence, when $V_{ads}(p_0\text{-}p)$ is plotted against p/p_0 the curve consequently increases steadily in a valid relative pressure region.

An example for the determination of a proper relative pressure region for a reasonable calculation of the specific BET surface area is displayed in Figure 5-30. In the conventional relative pressure range between 0.05 and 0.3 the linearity of the adsorption data is very poor (Figure 5-30a). Applying the BET-equation in this region yields a negative BET *C*-constant and thus violates the first consistency criterion for microporous materials as described above.

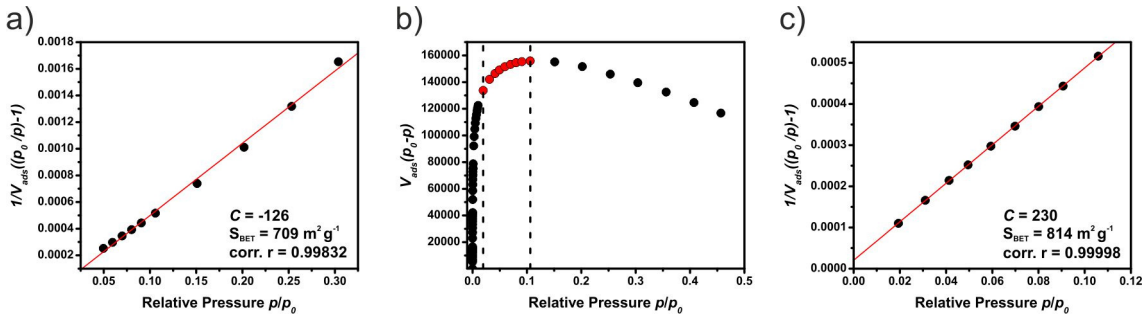

Figure 5-30: *a) BET-plot of a microporous material in the conventional pressure region. The linear fit of this region provides a negative C-constant and a BET surface area of 709 m² g⁻¹. b) Procedure for the determination of the correct pressure region for the BET-plot according to Rouquerol et al.[395] The maximum value is at a relative pressure p/p$_0$ = 0.11. Data points at higher relative pressures are not taken into account for the improved BET-plot. c) Improved BET-plot in the adapted pressure region (between the dashed lines in b)) provides a positive C-constant and an equivalent BET surface area of 814 m² g⁻¹.*

Hence, the obtained specific BET surface area of 709 m^2 g^{-1} might not be trustworthy and an alternative pressure range satisfying both consistency criteria has to be defined. According to the second consistency criterion, Rouquerol *et al.* suggested to limit the pressure range to a region where the term $V_{ads}(p_0\text{-}p)$ increases steadily when plotted

against p/p_0.[395] The respective plot in Figure 5-30b clearly shows that an application of the BET-equation to data points above a relative pressure of 0.11 would not be consistent with the second consistency criterion. As a consequence, the maximum value of $V_{ads}(p_0-p)$ denotes the upper boundary for relative pressure range of an improved BET-plot.
For a reliable multi-point BET evaluation at least five consecutive data points should be selected. Here, nine consecutive data points (red dots in Figure 5-30b) in the relative pressure range between 0.02 and 0.1 have been chosen for the linear fit (Figure 5-30c). The data points in the new pressure region provide a very good linear fit and a positive *C*-constant. The resulting equivalent BET specific surface area is 814 m^2 g^{-1}.

When reagarding the evaluation method of Rouquerol *et al.*, the calculation of the specific BET surface area could be adapted to be applied for microporous materials.[378,395] Recently, the specific surface area of several microporous MOF and zeolite materials have been calculated by GCMC methods and compared with the respective BET specific surface areas.[397,398] Both reports describe and underestimation of the specific surface area when calculated from the conventional BET relative pressure range between 0.05 and 0.3. However, when the calculation of the equivalent BET specific surface area is performed according to the consistency criterion, the obtained values are consistent with the surface areas calculated by GCMC methods. Hence, both reports recommend and adaption of the relative pressure range when applying the BET-equation to microporous materials.[397,398]

5.4.6 Pore Volume and Pore Size Distribution

The pore volume of porous materials usually describes the total volume of all pores below a certain pore diameter. When applying gas sorption techniques the total pore volume is determined only those pores being accessible to the respective adsorptive molecules are considered in the calculation. In the last decades a number of calculation methods to estimate the pore volumes of porous materials have been developed.[375]

The most straightforward approach for the calculation of the pore volume of a porous material is the Gurvich method, where the pore volume is directly calculated from the adsorbed gas volume by assuming the density of the adsorbate phase as equal to the density of the bulk liquid phase of the adsorptive.[60,378]
The total pore volume of a porous material can be determined from adsorption isotherms exhibiting a plateau at relative pressures near unity (p/p_0 = 0.9).[60] If the isotherm is not horizontal at relative pressures near unity, the total pore volume should not be evaluated.[60] However, it should be mentioned that the assumption of bulk-like properties for the adsorbate in micropores and narrow mesopores does probably not reflect the actual

physical conditions in such confined geometries.[60] Therefore, when regarding micro- or very small mesopores, the pore volumes derived from the Gurvich method should be regarded as a rough estimation.[60]

In the past decades the classical macroscopic methods, e.g. Horvath-Kawazoe (HK)[399], Saito-Foley (SF)[400], Dubinin-Radushkevich (DR),[401] Dubinin-Astakhov (DA)[402] or Barrett-Joyner-Halenda (BJH)[403], have been extensively used to estimate the pore volumes and pore size distributions of meso- and microporous materials. However, these methods treat the liquid-like adsorbate phase in the pores as a bulk liquid with conventional thermodynamic properties.[53] The reliability of the data obtained from these methods could be doubted in case of microporous samples, due to the neglected influence of the confined space on the physical properties of the condensed phase.[60,404-406]

A more accurate way to get access to the micropore volume is the t-plot method reported by Lippens et al. by plotting the adsorbed gas volume against a statistical layer thickness *t*.[407] The micropore volume is obtained from the intercept of the resulting linear plot. However, for a correct determination of the parameter *t* a reference isotherm of a non-porous material with similar adsorptive/adsorbent interactions is required.

Since a few years ago, not least because the steadily increasing computer performance, the development of microscopic methods based on statistical mechanics has enabled a more accurate and realistic description of pore structures and sorption phenomena. The most frequently applied methods for a comprehensive investigation of the pore size and structure are based on the NLDFT and the GCMC approach. From these statistical methods a number of different properties like the pore volume and the pore size distribution could be determined by simulating the local behavior of atoms or molecules adsorbed on a sorbent surface.[60] As the fluid-solid interactions strongly depend on the applied pore model, it is necessary to choose a model with sufficient accuracy to determine reasonable values for adsorbate-adsorbate and adsorbate-wall interactions.[60] By applying a suitable model to a given pore system it is possible to describe the whole system by simulating individual adsorption isotherms for a distinct pore size in the size range of micro- and mesopores. A series of individual isotherms is calculated from the equilibrium density profiles of the simulated fluid in the respective uniform size pores.[53] The simulated isotherms are collected and summarized in a so-called kernel, which enables the calculation of the pore size distribution from the Generalized Adsorption Isotherm (GAI) equation

$$N(p/p_0) = \int_{w_{min}}^{w_{max}} N(p/p_0, w)\, f(w) dw \qquad (5.7)$$

where $N(p/p_0)$ is the data obtained from the experimental isotherm, w is the pore width, $N(p/p_0,w)$ is the used kernel and $f(w)$ is the pore size distribution function.[60]

It is important to note that every kernel is sensitive to a number of system parameters like the nature of the sorbent (e.g. carbonaceous, zeolitic or silica surface) and the adsorptive, the pore geometry (slit-shaped, cylindrical or spherical) and the experimental working temperature.[53] Therefore the choice of a suitable kernel is essential for the generation of reliable results. The pore size distribution of a porous material is calculated according to the GAI equation by fitting a theoretical isotherm based on a suitable kernel to the experimental sorption isotherm.[60] A major advantage of the NLDFT model lies in the wide range of observable pores of sizes from about 0.5 to 50 nm, in some cases up to 100 nm.[375]

Most of the NLDFT kernels have been developed for nitrogen, carbon dioxide and argon on carbonaceous or silica-based surfaces.[379,382,408-411] As they are implemented in commercial pore analysis software, the calculation of the pore size distribution from the raw data of the sorption measurement can be performed within minutes. After selecting a kernel for the analysis it is reasonable to check the quality of the fit between the experimental and the theoretical isotherm generated by the program. If the obtained fitting errors lie below a certain confidence limit, e.g. 1% (better < 0.5%), the kernel should provide consistent results.
Unfortunately, for porous materials containing geometric (e.g. disordered, amorphous structure) and chemical (e.g. functionalization of the pore walls) heterogeneities the applicability of the conventional NLDFT model is limited.[53,412] As the model has originally been developed for homogeneous and ordered pore structures, a steep increase can be found in the calculated isotherm at certain relative pressures.[53] This artificial step in the theoretical isotherm results from the assumed completion of an adsorbate monolayer in the respective pressure region.[379,412] This model related steep increase would lead to an overestimation of the pores filled in the respective relative pressure region. In order to eliminate this overestimation in the pore size distribution, the contribution of the affected pores is reduced. For highly disordered or heterogeneous materials, where a distinct formation of consecutive adsorbate layers is not realistic, such a reduction causes an artificial gap around 9-10 Å in the pore size distribution (Figure 5-31).[53,379,412] A number of examples for this “prominent” gap can be found in the literature.[130,379]

The QSDFT approach, which has been developed recently, provides a more accurate description of the pore structure of amorphous and disordered materials as it considers surface roughness and structural inhomogeneities in the pore walls.[412] Indeed, the quality of the QSDFT-based isotherm fits of such highly disordered materials is significantly improved compared to the respective NLDFT fit (Figure 5-31).[53,60] The characteristic steep increase in the NLDFT mode at relative pressures around 10^{-3} (black arrow in Figure 5-31) is no more present in the QSDFT fit.

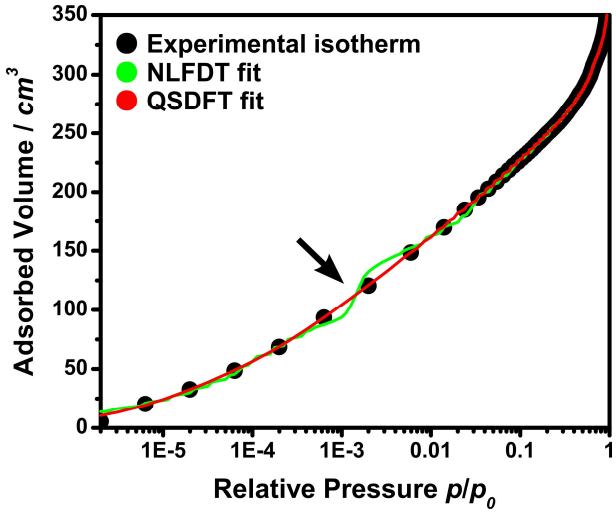

Figure 5-31: *Fitting comparison on the argon sorption isotherm of material TPI-6 (see section 6.4.5) using NLDFT and QSDFT kernels (slit-pore model for argon adsorption at 87 K on carbon surface). The black arrow denotes the region where the NLDFT model describes the completion of the first monolayer.*

Consequently, the prominent gap in the pore size distribution does not occur when using the QSDFT model.[379,412] Therefore the QSDFT model can be regarded as the method of choice when analyzing disordered porous materials.[53]

However, it should be mentioned that the application of both NLDFT and QSDFT models only provide reasonable results, if the experimental conditions and the observed sample material are compatible with the selected kernel. Therefore, in order to obtain reliable results from DFT calculations, a thorough analysis of the structural composition of the investigated porous material is inevitable.

5.5 Carbon Dioxide Adsorption in Porous Organic Polymers

5.5.1 General Considerations

Porous organic polymers have extensively been studied regarding their potential towards an application as CO_2 sorbent materials in order to finally reduce the overall emission of anthropogenic CO_2. Therefore, a significant number of different porous network materials have been investigated over wide range of temperatures and pressures. For a thorough characterization of the CO_2 sorption properties of the respective porous materials most of the reports in the literature consider the conditions of either pre- or post-combustion environments (Table 2).[13]

When regarding current literature, three main fields can be regarded as industrially relevant for CO_2 separation operations. The separation of CO_2 from natural or landfill gas aims at sorbents with high sorption selectivity for CO_2 over CH_4. In gas power plants, the

purification of fuel hydrogen gas requires sorbent materials with high CO_2/H_2 selectivity ratio. Both separation processes take place under elevated pressures. In contrast, the separation of CO_2 from post-combustion flue gases, regarding the CO_2/N_2 sorption selectivity, is usually conducted at lower pressures at about 1 bar. The gas separation experiments within this thesis focus on the separation of CO_2/N_2 gas mixtures at pressures up to 1 bar.

Basically, an efficient adsorption of CO_2 on a sorbent material surface mainly depends on two essential characteristics: (i) High CO_2 uptake combined with (ii) sufficient adsorption selectivity for CO_2 over other potentially competing sorbate species at the given operating conditions. Among several synthesis concepts, the increase of the specific sorbent surface, an increase of the interaction between adsorbent and adsorbate, e.g. by surface functionalization, and pore size engineering to provide an ideal pore size for the CO_2 molecule have been regarded to be most beneficial for the efficiency of POPs as CO_2 sorbent materials.[18]

Table 2: *Typical conditions for pre- and postcombustion processes.*[13]

	precombustion[a]	**postcombustion**
gas composition		
CO_2	35.5 %	15-16 %
N_2	0.25 %	70-75 %
H_2O	0.2 %	5-7 %
H_2	61.5 %	-
O_2	-	3-4 %
CO	1.1 %	20 ppm
H_2S	1.1 %	-
SO_X	-	< 800 ppm
NO_X	-	500 ppm
conditions		
Temperature	40 °C	50-75 °C
Pressure	30 bar	1 bar

[a] after water-gas shift reaction

In any case, the choice of the respective adsorbent material, however, strongly depends on the desired field of application. For instance, the network PAF-1 exhibits an ultrahigh specific surface area of 5600 $m^2\ g^{-1}$ and high excess CO_2 uptake of 29.54 mmol g^{-1} at 298 K and 40 bar, whereas at atmospheric pressure the CO_2 uptake (1.09 mmol g^{-1} at 298 K) is relatively low.[47,306] The values indicate that PAF-1 might be suitable for

precombustion applications, but for postcombustion CO_2 capture other materials, even with considerably lower specific surface areas, will be preferred when regarding the respective operation conditions (Table 2). In general, materials with high specific surface areas and high CO_2 uptakes at elevated pressures tend towards application in precombustion processes, whereas at postcombustion conditions with pressures of about 1 bar, pore structure and interactions between sorbate and sorbent surface gain more influence and can dominate the uptake properties.[117] Thus, for postcombustion applications, structure and chemical composition of a porous network sorbent might be more important than the mere accessible surface area.

Regarding postcombustion CO_2 capture by applying solid sorbent materials, some challenges must be overcome in order to establish an effective separation process. The composition of typical flue gas streams could vary slightly, however, the CO_2 volume concentration within the stream remains comparably low (Table 2). Additionally, the flue gas will be emitted at almost atmospheric pressure, and thus, the partial pressure of CO_2 is also low. A few years ago, the National Energy Technology Laboratory (NETL) in the US postulated an assembly of reasonable guidelines for recommended properties of adsorbent materials for postcombustion CO_2 capture:[20,413] (1) The performance target for a sorbent CO_2 capture process is a reduction of at least 30-50% of the energy required for a respective wet monoethanolamine-based process; (2) The sorbent material should have a CO_2 delta loading between adsorption and desorption of at least 3.0 mmol g^{-1} under operating conditions; (3) The adsorption and desorption of CO_2 must be performed at atmospheric pressure within a narrow temperature window of 40 to 110 °C in the presence of water; (4) The sorbent remains stable at operating conditions and retains its CO_2 capture capacity over multiple adsorption and regeneration cycles; (5) The sorbent must be durable within the plant operating conditions; (6) The sorbent must perform and be stable in the presence of water and other flue gas constituents.

It is obvious that high thermal and hydrolytic stability of potential sorbent materials are required to satisfy the given targets. Additionally, the materials shall provide high surface affinity for CO_2 in order to achieve a high selectivity for CO_2 over other relevant flue gas components. In 2011, Bae and Snurr developed five criteria to evaluate the applicability of potential sorbent materials for CO_2 separation processes.[14] The respective five parameters for adsorbent evaluation are described as

(1) CO_2 uptake under adsorption conditions N_{ads} (mmol g^{-1})

(2) Working CO_2 capacity $\Delta N = N_{ads} - N_{des}$

(3) Regenerability $R = (\Delta N_1 / N_1^{ads}) \times 100$ (%)

(4) Selectivity under adsorption conditions $\alpha_{12}^{ads} = (N_1^{ads}/N_2^{ads})\ (y_2/y_1)$

(5) Sorbent selection parameter $S = (\alpha_{12}^{ads})^2/(\alpha_{12}^{des})(\Delta N_1/\Delta N_2)$

where N stands for the adsorbed amount and y for the molar fraction in the respective gas phase. Subscript 1 denotes the strongly adsorbed component, usually CO_2, while

subscript 2 indicates the weakly adsorbent counterpart, usually CH_4 or N_2. The superscripts *ads* and *des* label adsorption and desorption conditions, respectively.
It should be mentioned that the original evaluation criteria by Bae and Snurr are primarily focusing on MOF materials. However, in a few recent reports the evaluation criteria have also been applied to porous organic polymers and compared to selected MOF structures.[343,344,352]

The following paragraphs will highlight characteristic parameters to identify porous organic polymers suitable for CO_2 capture and separation applications. They include CO_2 sorption capacity, CO_2 sorption selectivity and isosteric enthalpy of adsorption. A summary of the parameters of porous organic networks that have been investigated under conditions relevant for potential postcombustion applications could be found in appendix chapter 8.4.

5.5.2 CO_2 Sorption Capacity

The CO_2 sorption capacity or CO_2 uptake of a material can be determined from the CO_2 adsorption isotherm. The CO_2 uptake capacity is one of the relevant properties of a material to be suitable for CO_2 capture and separation applications. Therefore, the comparison of the CO_2 uptakes of different materials and different methods is common practice.
The applicability of solid sorbents in CO_2 capture could be assessed by comparing the performance of the materials with applied amine scrubbing technology. Considering the energy penalty compared to a wet process, the performance target for the working capacity of solid CO_2 sorbent materials has been determined at values of 3.0 mmol g^{-1} or greater.[20,30,413]

However, it should be mentioned that the values are referring to sorbents carrying immobilized amines. For sorbent systems with weaker sorbent/sorbate binding energies the energy penalty might be lower and probably reduce the performance target significantly. According to Drage *et al.* the working capacity $[CO_2]_{working}$ is defined as

$$[CO_2]_{working} = [CO_2]_{ads} - [CO_2]_{des} \tag{5.8}$$

where $[CO_2]_{ads}$ stands for the maximum adsorption capacity of CO_2 under process adsorption conditions and $[CO_2]_{des}$ for the minimum capacity of the adsorbent under process desorption (regeneration) conditions.[20] Under operating conditions, the ideal values for the upper and lower boundaries of an adsorption/desorption cycle, meaning the

maximum equilibrium capacity for $[CO_2]_{ads}$ and zero for $[CO_2]_{des}$, will probably not be reached. Especially for dynamic processes with short gas contact times and/or materials with low CO_2 adsorption rates the ideal and actual values might differ significantly.

5.5.3 CO_2 Sorption Selectivity

The gas sorption selectivity is an important characteristic of sorbent materials especially in gas separation. It describes the affinity of certain gas molecules in a gas mixture to be adsorbed on the surface of a given sorbent material. For an efficient CO_2 separation in flue gas streams, for instance, the sorbent material should have high adsorption selectivity for CO_2 molecules over all other components. Otherwise, the competing gas molecules would occupy the available adsorption sites and, thus, prevent the adsorption of CO_2. Consequently, for postcombustion applications in flue gas steams, where CO_2 is highly diluted, a high affinity of the sorbent material towards CO_2 could be regarded as a key feature.

When discussing about adsorption selectivities, the occurrence of different types of interaction between sorbent and one or more sorbates has to be considered.[29] One of these mechanisms is the so called size exclusion selectivity, where the dominating pore size of the sorbent defines the sorption behavior significantly. In detail, a sorbent with very small pore sizes could limit or even prevent the diffusion of certain gas molecules with kinetic diameters above a certain value, while other gas molecules with smaller kinetic diameters are able to pass. In consequence, the accessible surface area is higher for gases with lower kinetic diameters, which leads, in theory, to higher uptake capacities.
The adsorption selectivity also depends on the physical and chemical properties of the sorbent surface on the one hand and the nature of the gas molecules to be adsorbed on the other hand. Characteristic properties like polarizability, dipole and quadrupole moments or the presence of certain functionalities on the sorbent surface could significantly influence the sorbent/sorbate interaction, e.g. by inducing Lewis acid-base interactions or hydrogen bonding. As a consequence, gas molecule species might be preferentially adsorbed on the sorbent surface. When MOFs are used as sorbent materials the presence of exposed metal sites could also influence the adsorption selectivities.[29]
The majority of studies on pre- and postcombustion gas adsorption and separation are focusing on CO_2/CH_4 and CO_2/N_2 gas mixtures. To determine the respective gas adsorption selectivities three different evaluation methods have been applied very frequently.[29]

5.5.3.1 Direct Estimation from Single-Component Isotherms

One of the simplest methods to get an idea of the sorption selectivity of a porous material is to estimate the gas sorption selectivity directly from the experimental gas adsorption isotherms of the single components. The selectivity factor *S* is defined as the molar ratio of the adsorbed gas amounts at the respective partial pressures.[29] The selectivity factor *S* is calculated by

$$S = \frac{q_1/q_2}{p_1/p_2} \tag{5.9}$$

where q_i is the adsorbed amount of component 1 or 2 at the respective partial pressure p_i. For instance, in a typical simulated gas mixture for postcombustion CO_2 capture the partial pressures for CO_2 and N_2 could be 0.15 and 0.75 bar, respectively. The related adsorbed gas amounts can be directly taken from the adsorption isotherms. Of course, this very simple approach might be regarded as a raw estimation as it does not consider the effect of competing sorbate molecules on available adsorption sites. However, it is a fast and simple method to conduct a first comparison of the performance of different sorbent materials.[241,337]

5.5.3.2 Initial Slope or Henry´s Law Method

The gas sorption selectivity of a sorbent can also be determined from the ratio of the slopes in the initial region of the single-component adsorption isotherms of the respective adsorbate gases, e.g. CO_2 and N_2. In the initial region of an adsorption isotherm, where the pressures are low and number of unoccupied adsorption sites on the sorbent is rather high ("blank" surface), the amount of gas adsorbed on a given sorbent surface is proportional to applied pressure. The resulting linear adsorption can be expressed as Henry adsorption isotherm.

The gas adsorption selectivity *S* for two gases *i* and *j* can be calculated from

$$S = \frac{m_i}{m_j} \tag{5.10}$$

where *m* is the slope of the linear region in the initial part of the respective single-component adsorption isotherm. However, the selectivity determined by the initial slope method does not consider several selectivity-relevant factors in a real binary gas mixture, for instance, the competition of different gas molecules for adsorption sites.[336] Nevertheless, the initial slope method has been used very frequently in several reports in the past.[216,218,240,255,336,341,352]

5.5.3.3 Ideal Adsorbed Solution Theory (IAST)

The Ideal Adsorption Solution Theory (IAST) developed by Myers and Prausnitz has been widely used to calculate the adsorption selectivity of binary gas mixtures on several different sorbent materials.[29,216,240,337] The IAST concept has originally been developed by Myers and Prausnitz to predict the sorbent/sorbate adsorption behavior from the single-component adsorption isotherms of the constituents of the real gas stream by fitting every isotherm with an appropriate model, e.g. the single-site or dual-site Langmuir model.[414]
The single-site Langmuir model can be expressed as

$$q = \frac{q_{sat} b p}{1 + bp} \tag{5.11}$$

while the dual-site Langmuir model is described by the equation

$$q = q_A + q_B = \frac{q_{sat,A} b_A p}{1 + b_A p} + \frac{q_{sat,B} b_B p}{1 + b_B p} \tag{5.12}$$

where q is the total molar loading of adsorbate, q_{sat} is the saturation loading of adsorbate and b is the Langmuir adsorption parameter of the pure component. The subscripts A and B denote two different adsorption sites. Finally, the IAST adsorption selectivity S for a binary gas mixture can be determined from the equation

$$S = \frac{q_1/q_2}{p_1/p_2} \tag{5.13}$$

where q_1 and q_2 are the molar loadings and p_1 and p_2 the partial pressures of gas components 1 and 2.

Alternatively to the fits based on the Langmuir equation the single-component adsorption isotherms can also be fitted by applying the Langmuir-Freundlich equation.[297,328,415]

5.5.4 Isosteric Enthalpy of Adsorption

The isosteric enthalpy of adsorption is a characteristic parameter to describe the interaction of an adsorbate molecule with a given sorbent surface. The enthalpy of adsorption denotes the affinity of the sorbent surface towards a given gas molecule and could probably influence the potential of a given material for a certain type of application. The enthalpy of adsorption of CO_2 on a given sorbent surface, for instance, is considered to be crucial when evaluating the potential of the sorbent material for CO_2 capture applications.[29] If the

binding energy between CO_2 and the sorbent material is high, the energy efforts to remove the molecules during the regeneration process would lower the efficiency of the whole process. On the other hand, a too low binding energy between CO_2 and sorbent surface would increase the competition with other gas molecules beside CO_2 for available adsorption sites and significantly lower the sorbent material's gas selectivity towards CO_2. Consequently, the capture of CO_2 at low gas selectivities would lead to an increased quantity of sorbent material and again influence the cost-efficiency of the process.

The isosteric enthalpy of adsorption Q_{st} describes the average enthalpy for a gas molecule adsorbed on a given sorbent surface at specific surface coverage.[29] The values for Q_{st} could be calculated from the slope of the Clausius-Clapeyron equation[29,303]

$$(\ln p)_N = -\frac{Q_{st}}{R}\frac{1}{T} + C \tag{5.14}$$

where T is the temperature of the adsorption measurement, R is the universal gas constant, C is a constant, p is the pressure and subscript N refers to the adsorbed gas quantity at pressure p.

In order to achieve reliable results from the Clausius-Clapeyron equation at least three adsorption isotherms measured at slightly different temperatures are required.[416] For CO_2 capture and separation applications, adsorption enthalpies between 25 and 50 kJ mol^{-1} are regarded to be a good balance between selectivity and reversibility.[19]

6 Results and Discussion

6.1 Towards a Functionalization of Covalent Triazine-based Frameworks

6.1.1 Polymer Networks synthesized from 1,4-Dicyanobenzene and Derivatives

6.1.1.1 Synthesis and Characterization of CTF-1

High thermal and chemical stability are desirable properties for potential sorbent materials in CO_2 capture and separation applications. Covalent triazine-based frameworks (CTFs) combine both features with high porosities and their potential application as CO_2 sorbent materials are currently investigated. Certainly, an introduction of functional groups into the pore structure of CTF materials would be recommended to broaden the field of potential applications significantly, e.g. influence the CO_2 sorption selectivity at low pressures. However, CTFs are often synthesized under high synthesis temperature which might limit the successful introduction of certain functional groups significantly.

The following chapter focuses on the functionalization of the inner pore walls and the investigation of their structure and properties of CTFs or related triazine-based porous polymer networks. The porous network material CTF-1 reproted by Kuhn *et al* has been chosen to act as a reference substance for the work on covalent trianzine frameworks within this chapter, containing most of the basic features of a porous highly cross-linked triazine network structure.[45]

Therefore, as a first step, CTF-1 was synthesized according to the original protocol by Kuhn *et al.* from 1,4-DCB in molten zinc(II) chloride at a temperature of 400 °C. [45] The synthesis scheme and the results of the characterization of the synthesized CTF-1 material are shown in Figure 6-1 and are in good agreement with the results presented in the literature. [45] Similar to the original report, the material could be obtained from the synthesis as a black powder in almost quantitative yield.[45]

In the presented ionothermal approach, molten zinc(II) chloride plays an important role as it simultaneously acts as solvent and catalyst for the cyclotrimerization reaction of the nitrile groups.[45] A possible mechanism for $ZnCl_2$-mediated triazine formation has been postulated by Berger *et al*. recently.[417] A Zn^{2+}-induced polarization of the nitrile triple-bond enables the nucleophilic attack of a second nitrile group. The addition of a third

nitrile group, by attacking another carbon atom with positive partial atomic charge, leads to the formation of the triazine ring, due to a significant energy benefit from the generation of an aromatic ring system.[417] The postulated mechanism Zn-catalyzed addition reaction is illustrated in Figure 6-2.

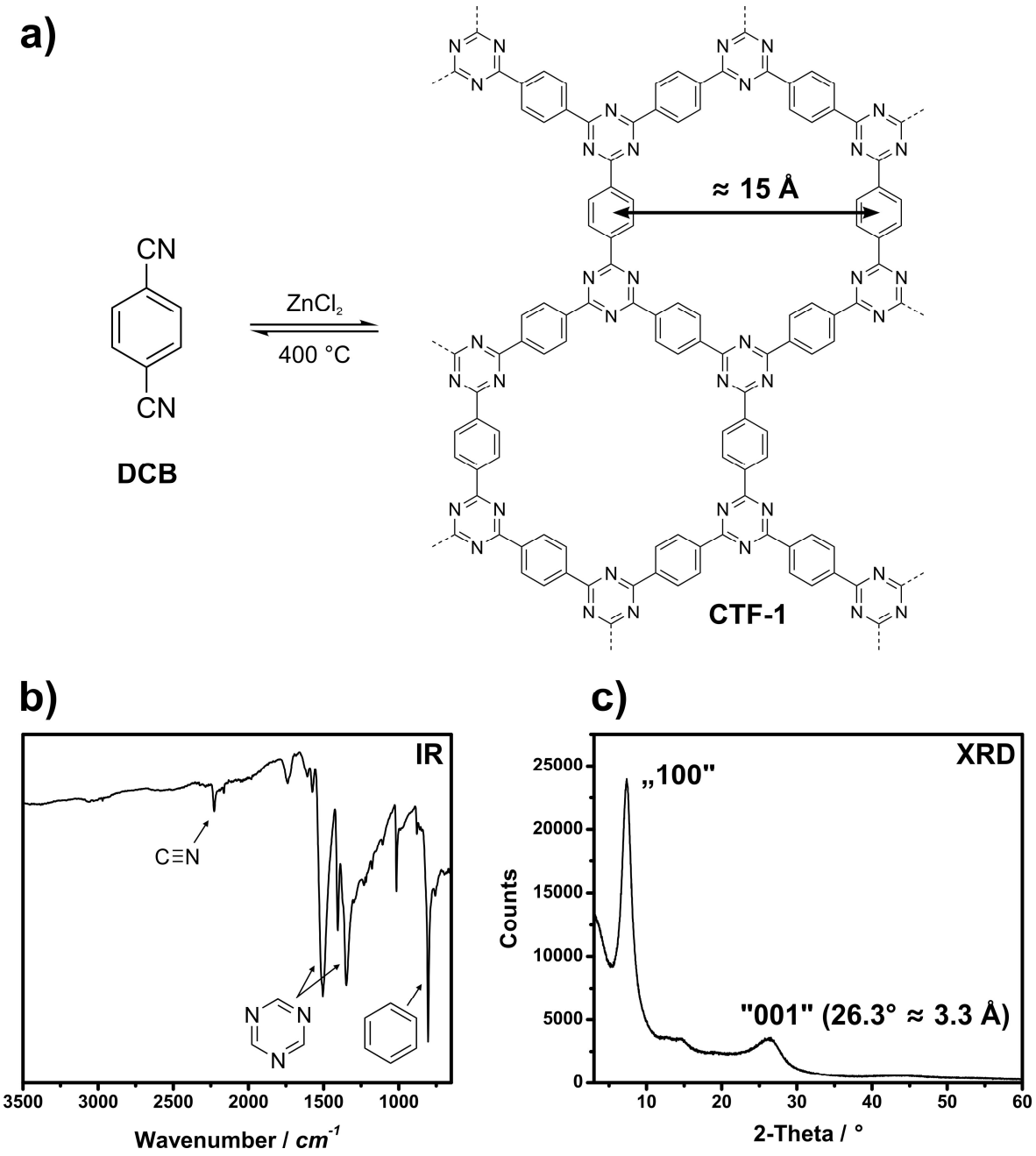

Figure 6-1: *a) Synthesis of CTF-1, b) Infrared spectrum of CTF-1, c) XRD pattern of CTF-1.*

The infrared spectrum of CTF-1 reveals four characteristic bands confirming the formation of the desired polymeric network (Figure 6-1b). The weak band at 2228 cm^{-1} can be attributed to a small amount of unreacted nitrile groups in the polymer network. The strong characteristic bands of the triazine in-plane stretching vibration at 1505 and 1350 cm^{-1} provide evidence for a successful nitrile cyclotrimerization reaction.

The strongest absorption band at 804 cm^{-1} can be attributed to out of plane C-H vibrations of the 1,4-disubstituted phenyl unit.

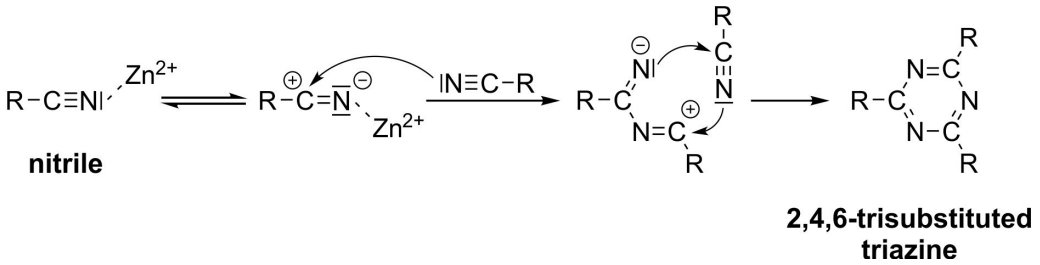

Figure 6-2: *Postulated reaction mechanism for Zn^{2+}-catalyzed cyclotrimerization of nitrile groups.*[417]

The measured powder XRD pattern of CTF-1 shows two characteristic reflections at angles of approximately 7° and 26° (Figure 6-1c). The calculated distances for lattice planes of approximately 15 Å and 3.3 Å can be attributed to the distance between the pore centers of two adjacent hexagonal pores and the stacking distance of CTF-1 layers in *c*-direction. Kuhn *et al.* index the diffraction peak at lower diffraction angles as *(100)* and the peak at higher diffraction angles as *(001)* on the basis of a simulated diffraction pattern.[45] The simulated model describes an array of hexagonal pores in two-dimensional sheets, consisting of alternating triazine and phenyl units.[45] An eclipsed stacking pattern of the individual sheets generates a hexagonal dense packing of cylindrical pores.[45] However, the broad reflections found in the X-ray diffraction pattern are a clear sign of limited long-range order in the CTF-1 network structure.

The ^{13}C MAS NMR spectrum of CTF-1 contains four characteristic peaks (Figure 6-3a). The signal at 170 ppm can be assigned to the carbon atoms in the triazine unit. The phenyl unit provides two different aromatic carbon signals at 139 ppm and 128 ppm, respectively.

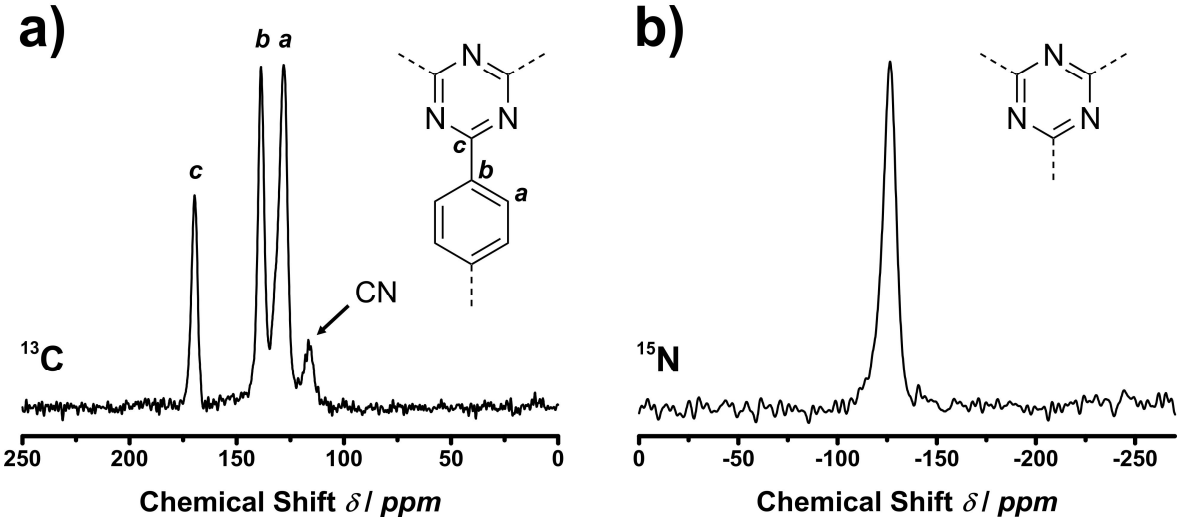

Figure 6-3: *a) ^{13}C MAS NMR spectrum of CTF-1, b) ^{15}N MAS NMR spectrum of CTF-1.*

A small amount of unreacted nitrile groups could be identified through the weak signal at approximately 117 ppm. The absence of side products or starting materials in the carbon spectrum confirms a high purity of the synthesized materials. The presence of small amounts of unreacted nitrile groups has already been confirmed by infrared spectroscopy measurements within this paragraph. The ^{15}N MAS NMR spectrum shows only one single signal from the triazine nitrogen atoms at -127 ppm (Figure 6-3b).
A C/N ratio of 3.3 provided by elemental analysis of the synthesized CTF-1 network also shows good accordance with a theoretical C/N ratio of 4.0 and an experimental C/N ratio of 4.4 reported in the literature at similar reaction conditions.[45]

The argon sorption isotherm of CTF-1 at 87 K shows a rapid gas uptake at low relative pressures, as it is typical for microporous materials (Figure 6-4a). However, the sorption isotherm does not describe a typical type I isotherm. The adsorption and desorption isotherms form a small hysteresis loop down to low relative pressure regions most likely due to "swelling" of the porous network (see section 5.4.4).

The BET equivalent specific surface area of the synthesized CTF-1 has been calculated from a linear region in the BET-plot of the argon sorption isotherm according to the requirements for microporous materials (see section 5.4.5.3). The BET-plot is shown in Figure 6-4b. However, the estimated surface area of 530 $m^2\ g^{-1}$ is significantly lower than the value of 791 $m^2\ g^{-1}$ reported by Kuhn *et al.* at similar synthesis conditions.[45] The reason for the significant difference, however, could not be determined.

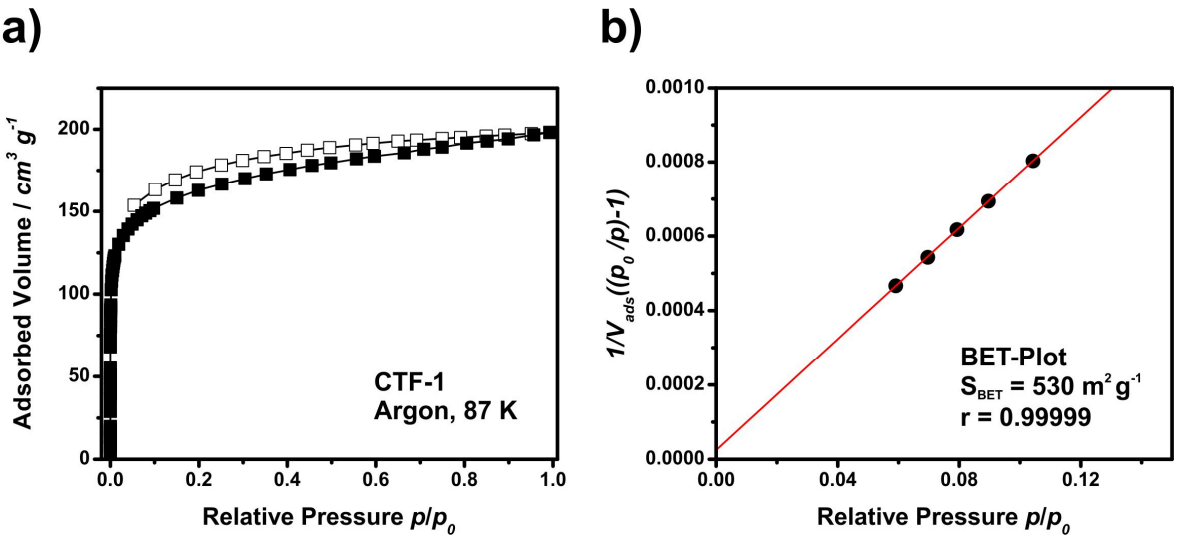

Figure 6-4: *a) Argon sorption isotherm of CTF-1, b) BET-plot of CTF-1.*

Prior to the calculation of the pore size distribution of CTF-1, it is necessary to choose a suitable DFT kernel in order to obtain reasonable results. However, it should be mentioned that most of the available kernels to characterize porous materials have been designed for inorganic materials or activated carbons.

A DFT kernel designed to characterize porous organic polymers is not available at present. For the characterization of the pore structure of CTF-1 the kernel for carbonaceous surfaces has been applied as it is expected to show the closest match among the available kernels due to a certain comparability of surface properties of activated carbons and porous organic polymers.

The structure model proposed by Kuhn *et al.* describes CTF-1 as an array of cylindrical pores in a hexagonal eclipsed AA stacking pattern.[45] Therefore, an application of a kernel based on a cylindrical pore model could be regarded as reasonable. However, the limited long-range order in the polymer structure indicated by XRD measurements might as well be a good argument for the presence of a significant amount of slit pores, typical for disordered porous materials. The pore size distribution of CTF-1 has been calculated by using a series of NLDFT- and QSDFT-based kernels for carbonaceous surfaces (Figure 6-5). The results from DFT calculations performed with the Quantachrome ASiQ software package (see Experimental Section) also including the total pore volume V_p and the specific surface area S_{DFT} are summarized in Table 3.

It should be mentioned that all of the kernels in Table 3 have been applied to the adsorption branch of the sorption isotherm of CTF-1 to minimize a possible influence of swelling effects on the DFT calculations, indicated by the occurring large hysteresis down to low relative pressures. For all applied kernels the fitting errors between the theoretical and the experimental adsorption isotherms are below 1%. Therefore, the obtained data could be regarded as trustworthy regarding the respective pore and surface model. While the calculated values for the total pore volume V_p are quite uniform for all models, the values of the specific surface areas differ significantly (Table 3).

Table 3: *DFT calculations of CTF-1 by applying different pore models for carbonaceous surfaces.*

model	kernel	pore geometry	fitting error	V_p (cm^3 g^{-1})	S_{DFT} (m^2 g^{-1})
1	NLDFT	cylindrical	0.16%	0.25	750
2	NLDFT	slit	0.72%	0.24	612
3	QSDFT	cylindrical	0.23%	0.25	655
4	QSDFT	cylindrical/spherical	0.23%	0.25	653
5	QSDFT	slit	0.14%	0.25	619

For comparison, a pore volume of 0.25 cm^3 g^{-1} has been calculated for the synthesized CTF-1 network from single point evaluation at a relative pressure of 0.99 by applying the Gurvich method. The results confirm good comparability of Gurvich and DFT methods for CTF-1.

Similar to the specific BET surface area, the pore volume of the synthesized CTF-1 network is also significantly lower compared to the values reported in the literature.[200] The differences between the two CTF-1 networks might result from a considerable amount of pores that are inaccessible to the adsorptive gas. It should be noted that the calculated surface areas obtained from DFT methods seem to depend on the applied pore model and should be regarded carefully.

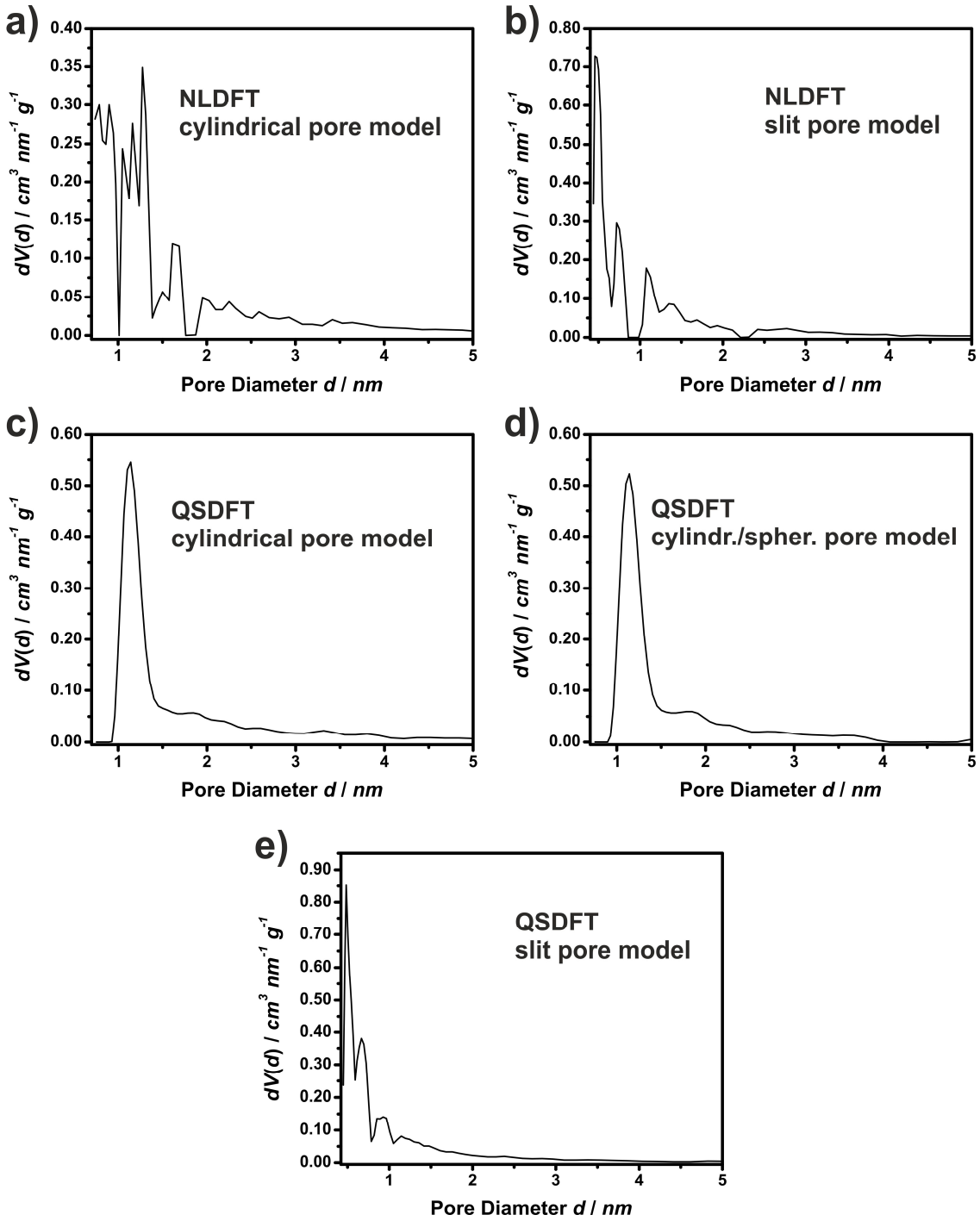

Figure 6-5: *Pore size distributions calculated from the argon adsorption branch of CTF-1 using different NLDFT and QSDFT kernels. a) NLDFT kernel based on a cylindrical pore model, b) NLDFT kernel based on a slit pore model, c) QSDFT kernel based on a cylindrical pore model, d) QSDFT kernel based on a model for cylindrical and spherical pores, e) QSDFT kernel based on a slit pore model.*

However, it is interesting that despite a relatively large variance, the specific surface areas derived from DFT calculations are considerably higher compared to the surface area obtained from BET method. The difference in the obtained specific surface areas significantly depends on the applied method of determination.
The pore size distributions (PSD) for the CTF-1 polymer derived from the five NLDFT and QSDFT kernels in Table 3 are displayed in Figure 6-5. The PSDs based on NLDFT calculations (Figure 6-5a and b) indicate that the majority of the pores in the system possess pore diameters below 2 nm. Interestingly, the cylindrical pore model displays a broad multimodal distribution up to a pore diameter of about 1.4 nm (Figure 6-5a), whereas the slit pore model denotes very high volume fractions to pores with a distinct diameter of 0.5 nm and 0.7 nm (Figure 6-5b), respectively. It should be noted, that the cylindrical pore model is only capable of classifying pores with diameters above 0.7 nm. Both pore size distributions calculated from NLDFT models show the characteristic artificial gap for pore sized around 1 nm (see section 5.4.6).
The PSDs derived from the QSDFT-based cylindrical pore model (Figure 6-5c and d), however, differ significantly from the NLDFT approach. The almost identical distributions provide a sharp maximum at pore diameters of 1.3 nm, which is in good agreement with the values reported in the literature and the results from the XRD measurements.[45] The sharpness and intensity of the peak in both PSDs supports the argument of an ordered structure with cylindrical pores of a distinct diameter. According to Figure 6-5a and b, the contribution of pores with diameters larger than 1.5 nm to the total pore volume is rather low. The results obtained from the slit pore QSDFT model are quite similar to those from the respective NLDFT calculations. Accordingly, the main pore volume fraction is situated in the diameter range between 0.5 and 0.7 nm. However, as already reported in chapter 5.4.6, the artificial gap around 1 nm does not appear in the QSDFT approach.

The evaluation of the pore size distribution of CTF-1 reveals remarkable discrepancies between the different evaluation models. One important reason might be that all applied pore models have been developed for materials with purely carbonaceous surfaces, e.g. activated carbons, which do not contain significant amounts of heteroatoms. Another reason is that neither the cylindrical nor the slit pore model might be capable of describing the complex structure of the present porous framework correctly. All of the applied kernels show very low fitting errors and comparable pore volumes. However, the calculated PSDs differ significantly. Therefore, it is most important for the evaluation to discuss not only the PSD of the investigated material itself, but also the applied pore model, applied kernel and calculation method.

The results for CTF-1 obtained from the QSDFT kernel for cylindrical and cylindrical/spherical pore shapes are in good agreement with the structural model reported in the literature.[45] Compared to the respective NLDFT kernel, the QSDFT approach does

not show the artificial gap at pore sizes of about 1 nm and delivers a more uniform PSD with a peak at roughly 1.5 nm. Therefore, in case of heterogeneous pore surfaces like porous covalent triazine networks the application of QSDFT kernels seems to yield more reliable results compared to the respective NLDFT kernel.

6.1.1.2 Cyclotrimerization of 2-Methylterephthalonitrile

The introduction of functional groups in the network structure is an ambitious challenge in the synthesis of porous materials. By incorporating various functional groups in the pore structure, the tunable structural and chemical properties of the synthesized porous materials might be useful for a broad spectrum of different applications.

Polar functional groups are believed to have a considerable influence on the gas sorption properties of such materials,[2] especially when regarding interactions with polar gases like CO_2.[13]

A straightforward approach for the synthesis of methyl-functionalized CTF networks is the cyclotrimerization of 2-methylterephthalonitrile by using the synthesis protocol of CTF-1. The following paragraph determines the applicability of the synthesis method and the influence of the reaction conditions on the structure of the functionalized polymer. During the work on this thesis, the cyclotrimerization of 2-methylterephthalonitrile has been investigated under supervision in the bachelor thesis of Christian Fremerey.[418]

Similar to the synthesis of CTF-1, 2-methylterephthalonitrile was polymerized in an equimolar amount of zinc(II) chloride to obtain methyl-functionalized covalent triazine frameworks (MeCTFs) at varying temperatures and reaction times (Figure 6-6a, see experimental section) in a sealed glass ampoule. The monomer unit is commercially available at comparatively low prices and the methyl group of the molecule should provide an intense signal in the ^{13}C MAS NMR spectrum to facilitate the detection of present methyl groups in the polymer network and thus verify a successful functionalization.

When regarding the ^{13}C MAS NMR spectrum of 2-methylterephthalonitrile the signal of the methyl group can be clearly identified at 21 ppm (Figure 6-6b). The applied reaction temperature of 370 °C was slightly lower than the original synthesis temperature of 400 °C. The lower reaction temperature should prevent decomposition reactions of the organic framework structure even over extended reaction times.

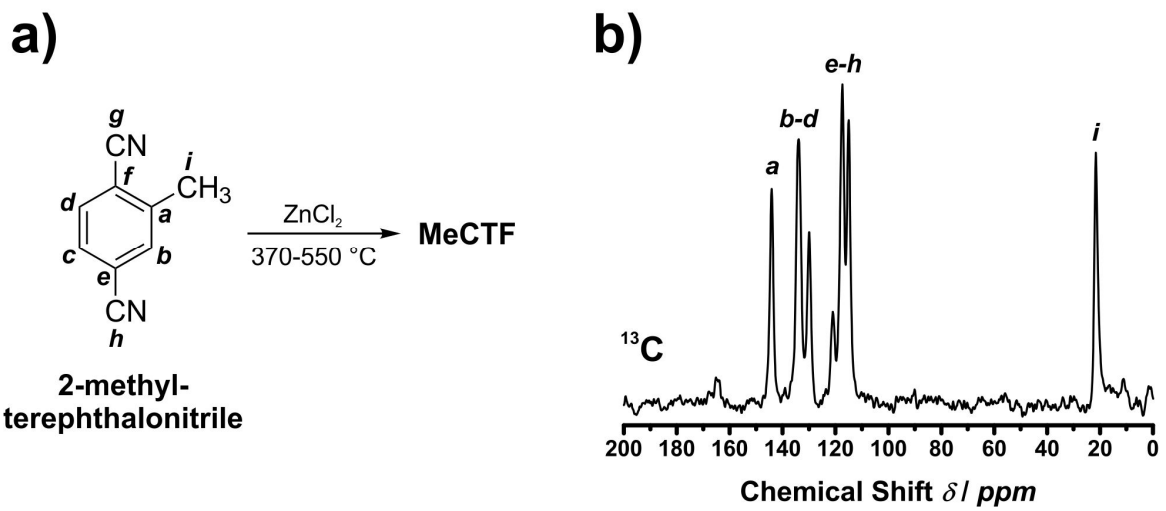

Figure 6-6: *a) Reaction scheme for the synthesis of MeCTFs. b) Solid state ^{13}C MAS NMR spectrum of 2-methylterephthalonitrile. The assignments for the ^{13}C NMR signals in b) are displayed in a).*

Attempts to synthesize CTF networks below 370 °C, even over extended heating periods, did not provide polymeric products, most likely due to incomplete dissolution of the starting material in the zinc(II) chloride melt.

The ^{13}C MAS NMR spectrum of MeCTF-1 is displayed in Figure 6-7a. The characteristic peak at 170 ppm indicates the successful formation of the triazine unit, its intensity, however, is unexpectedly low. The low-intensity signal at 19 ppm suggests that only a small amount of methyl groups is still present in the network. The peak at about 129 ppm is attributed to a heavy overlap of various aromatic carbon signals. In contrast to CTF-1, a separated signal of residual unreacted nitrile groups at approximately 117 ppm could not be identified. The broad and indistinguishable signals of the carbon atoms indicate a high degree of disorder in the polymer structure. Powder XRD measurements confirm the amorphous texture of MeCTF-1.

A small amount of unreacted nitrile groups can be identified in the infrared spectrum of MeCTF-1 (Figure 6-7b). Similar to the infrared spectrum of CTF-1, the weak nitrile absorption band at 2222 cm^{-1} is visible. The characteristic absorption bands for the triazine ring at 1512 and 1350 cm^{-1} are also present. Interestingly, an absorption band caused by residual methyl groups at about 3000 cm^{-1} could not be detected. However, it should be mentioned that the overall absorption level of the infrared spectrum of MeCTF-1 has been very low and hence the displayed intensities might be misleading to some extent.

Nitrogen sorption measurements of MeCTF-1 show very low gas uptakes at 77 K indicating the absence of considerable porosity in the polymeric structure. The lack of porosity in the samples could be ascribed to an insufficient formation of triazine units and, in consequence, to an insufficient degree of cross-linking in the polymer network.

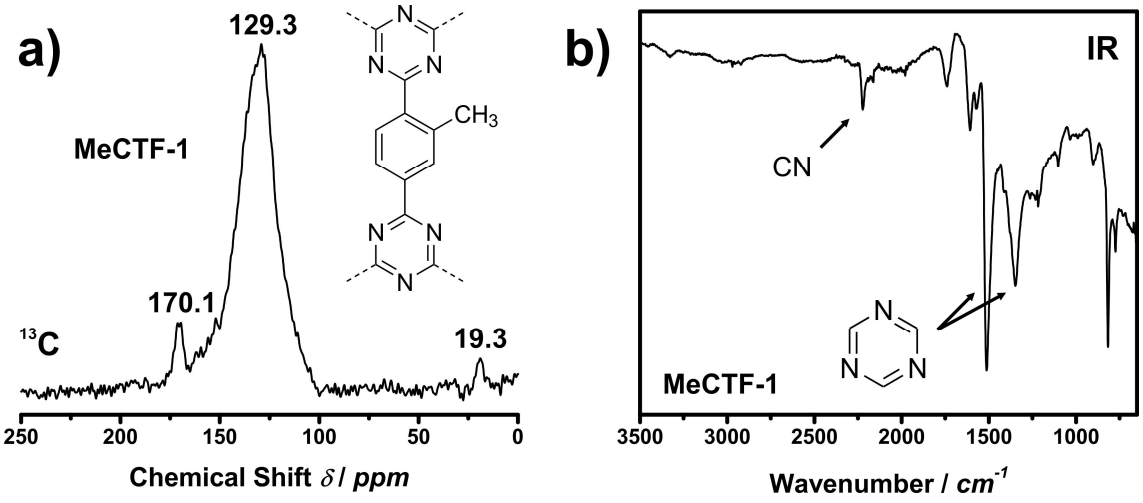

Figure 6-7: *a) ^{13}C MAS NMR spectrum of MeCTF-1.[418] b) Infrared spectrum of MeCTF-1.*

The formation of the triazine rings might be affected by steric hindrance caused by the neighboring *ortho*-methyl groups in 2-methylterephthalonitrile. The partial formation of triazine units can be explained with the reduced steric hindrance for nitrile groups in *meta*-position to the methyl groups. Interestingly, elemental analysis of MeCTF-1 reveals a significant difference of the experimental (6.8) from the calculated C/N ratio (4.5). The difference between the ratios is obviously caused by decomposition of the triazine units or nitrile groups, that has already been observed in the ^{13}C MAS NMR spectra.

For the synthesis of MeCTF-2 the synthesis conditions are almost identical to the conditions applied for MeCTF-1. The heating time was extended to 140 h in order to investigate the influence of the reaction time on triazine formation. The reaction temperature remained unchanged to minimize the impact of occurring decomposition reactions.
The ^{13}C MAS NMR spectrum of MeCTF-2 shows a lower intensity of the triazine peak compared to MeCTF-1 (Figure 6-8a). The signal intensity of the methyl group is close to the lower detection limit still indicating almost complete decomposition over prolonged heating periods. Elemental analysis of MeCTF-2 shows a higher C/N ratio of 7.2 compared to 6.8 for MeCTF-1 and confirms an ongoing loss of nitrogen when increasing the reaction time. X-ray diffraction experiments detect an amorphous structure for MeCTF-2. The obtained results point out, that an increase of the reaction time at a temperature of 370 °C does not increase the triazine content in the final product compared to MeCTF-1. Furthermore, it is also not possible to maintain a sufficient amount of methyl groups in the polymer under the given reaction conditions.

As expected, the amount of methyl and triazine units in the polymeric network decreases upon extended reaction times. Noteworthy, at synthesis temperatures of 550 °C and a reaction time of 140 h for MeCTF-3, still a small amount of nitrogen has been detected by

elemental analysis. However, it is not possible to identify a triazine signal from the ^{13}C MAS NMR spectrum (Figure 6-8b). The broad peak with maximum at 129 ppm is characteristic for highly disordered carbonaceous materials and results from an overlap of several aromatic carbon signals. Based on the analytical results, MeCTF-3 could be described as amorphous nitrogen doped carbonaceous material.

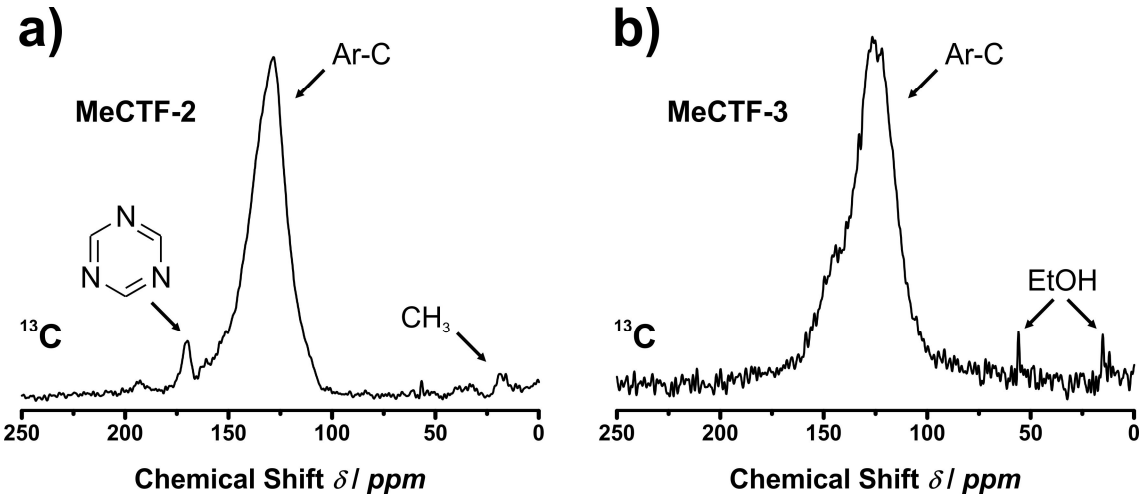

Figure 6-8: *a) ^{13}C MAS NMR spectra of MeCTF-2 and b) MeCTF-3.*[418]

The obtained results from the analysis of the three polymers MeCTF-1, MeCTF-2 and MeCTF-3 show that the synthesis route based on the cyclotrimerization of nitrile groups in molten zinc(II) chloride does not provide functionalized porous covalent triazine frameworks. In the temperature range between 370 °C and 550 °C and over a heating period between 40 and 140 h, it was not possible to synthesize a porous framework material similar to CTF-1 described in the previous chapter. The nitrogen contents in the obtained products determined by elemental analysis were below the calculated values and powder XRD could not detect long-range order in the polymer structure.

6.1.2 Polymer Networks from 4,4'-Dicyanobiphenyl and Derivatives

6.1.2.1 Cyclotrimerization of 4,4'-Dicyanobiphenyl in molten Zinc(II) Chloride

A framework material synthesized from 4,4′-dicyanobiphenyl (DCBP) with a theoretical structure motif similar to CTF-1 has also been reported recently.[45,200] The substitution of one of the aromatic hydrogen atoms in meta-position to each of the nitrile groups of the monomer should provide a functionalized porous material.

When using *meta*-functionalized monomers nitrile cyclotrimerization should not be affected by steric hindrance effects. Prior to functionalization, a detailed characterization of the non-functionalized DCBP-based network has been performed.

The synthesis of DCBP has been performed by cobalt catalyzed biaryl homocoupling reaction from *p*-bromobenzonitrile according to the synthesis protocol reported by Moncomble *et al*. (Figure 6-9).[419]

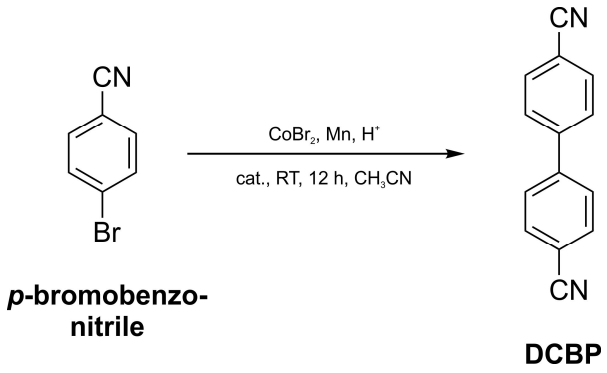

Figure 6-9: *Synthesis of DCBP according to Moncomble* et al.[419]

The reaction was conducted under mild reaction conditions in acetonitrile at room temperature. The *in situ* formation of the active Co-catalyst requires the addition of *N,N'*-bis(2,6-dimethylphenyl)-1,2-ethanediimine as ligand and catalytic amounts of trifluoroacetic acid. The ligand was synthesized according to a synthesis protocol reported by Turkmen *et al.*[420] The synthesis route provides good product yields of about 80% after purification.

The cyclotrimerization of DCPB was carried out in a sealed quartz ampoule at a temperature of 400 °C in molten zinc(II) chloride (Figure 6-10a). The two components were added to the ampoule in a glovebox in a monomer/$ZnCl_2$ ratio of 1:10. After removing zinc chloride from the reaction mixture the reaction product DCBP-polymer 1 was obtained as a black powder. X-ray diffraction measurements confirm an amorphous structure of the material.

The ^{13}C MAS NMR spectrum of DCBP-polymer 1 shows two characteristic peaks at 141 and 127 ppm (Figure 6-10b). The peak at 127 ppm can be attributed to overlapping aromatic C-H-carbons and the peak at 141 ppm is typical for aromatic quaternary carbon atoms. The triazine signal in the chemical shift region at approximately 170 ppm could not be detected. The small shoulder at 150 ppm might result from carbon atoms directly linked to aromatic nitrogen atoms. Such nitrogen-containing aromatic systems could theoretically be formed by Diels-Alder addition between biphenyl units and a terminal nitrile groups.[197]

The infrared spectrum of DCBP-polymer 1 is shown in Figure 6-10c. The bands at 1603 cm^{-1} and 754 cm^{-1} can be attributed to the aromatic C-C stretching vibration and the out-of-plane vibration of the phenyl units, respectively. The weak band at 3061 cm^{-1} is characteristic for aromatic C-H stretching vibrations. In the range of 1200-1500 cm^{-1} a heavy overlap of different absorption bands is visible. The characteristic absorption bands for triazine units at approximately 1500 and 1360 cm^{-1} could not be identified clearly. The absence of triazine units in the structure is also visible in the low nitrogen contents obtained from elemental analysis (see section 7.2.1.3).

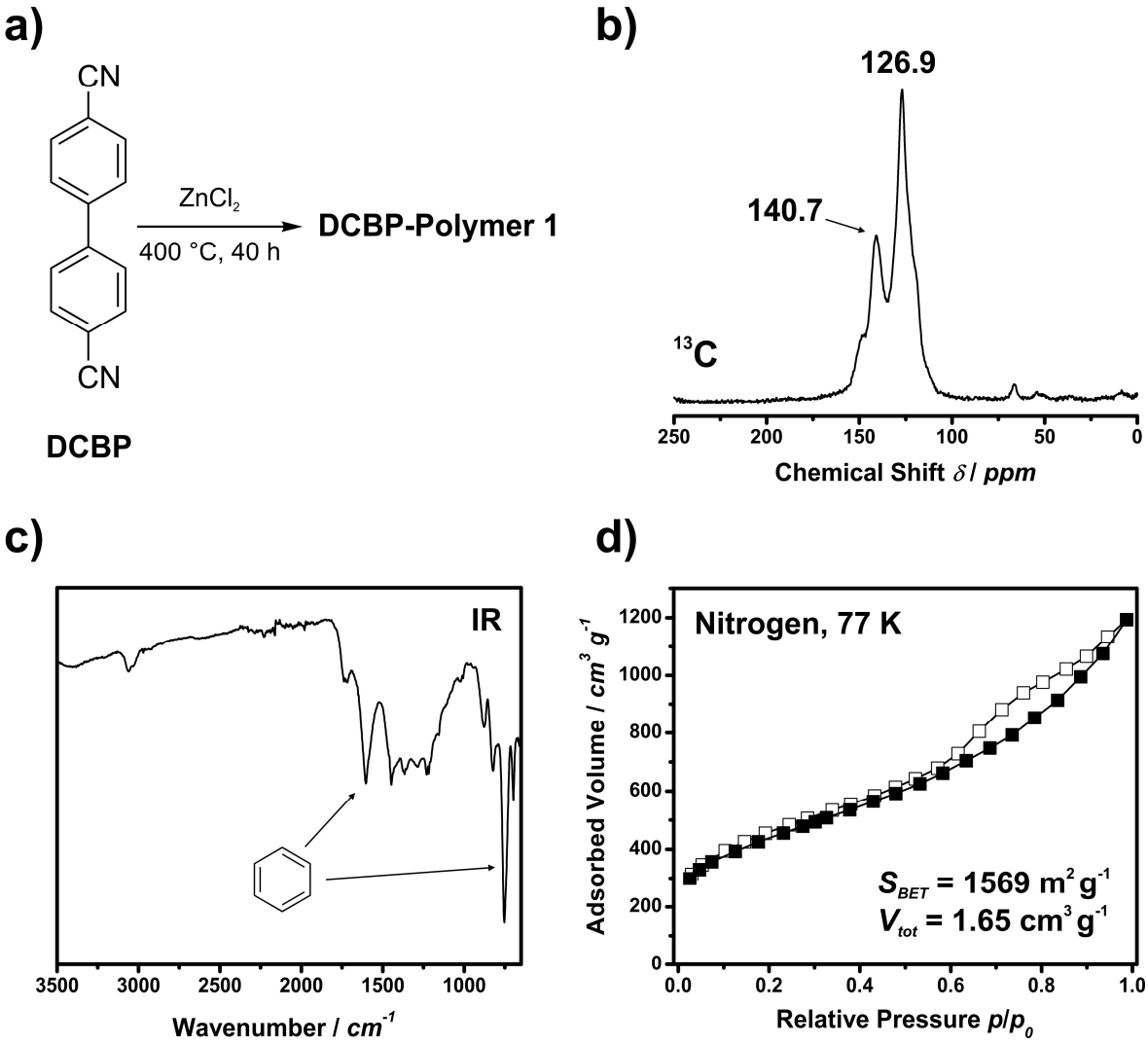

Figure 6-10: *a) Synthesis of DCBP-polymer 1 , b) ^{13}C MAS NMR spectrum of DCBP-polymer 1, c) Infrared spectrum of DCBP-polymer 1, d) Nitrogen sorption isotherms of DCBP-polymer 1. Pore volume has been determined by applying a NLDFT slit pore model.*

Nitrogen sorption measurements at 77 K show a mixture of meso- and micropores in the structure of DCBP-polymer 1 (Figure 6-10). The obtained specific BET surface area of 1569 m^2 g^{-1} is substantially higher than the surface area calculated for CTF-1 and is comparable to the specific BET surface areas of the DCBP-based polymer materials

synthesized by Kuhn *et al.*[197,200] The total pore volume V_{tot} of DCBP-Polymer 1, however, is higher than the reported total pore volume, while the micropore volume V_{mic} is slightly decreased (Figure 6-11a).[197] The pore size distributions from of DCBP-Polymer 1 calculated from NLDFT and QSDFT slit pore models both indicate a large amount of micropores but also a considerable fraction of pores with sizes of 4-8 nm (Figure 6-11a and b).

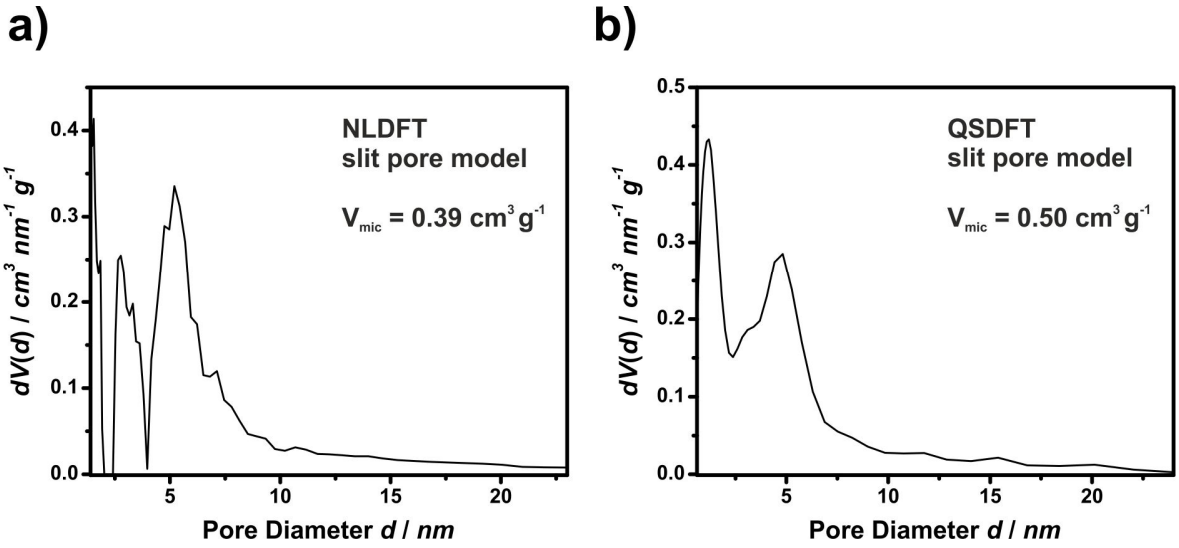

Figure 6-11: *Pore Size Distribution calculated from NLDFT and QSDFT by applying a model for N_2 adsorption on carbonaceous surfaces.*

The high specific surface areas and the presence of mesopores might be explained by the decomposition of the triazine units after the buildup of the polymer network. The obtained results are consistent with the so-called "foaming" phenomenon, where temperature induced decomposition of the triazine units of CTF and CTF-like materials generates additional hollows in porous structures.[218] The effect of foaming on the pore volume of fluorene-based CTF materials has been discussed recently.[218] According to the reported V_{mic}/V_{tot} ratio, the micropore volume of the presented materials decreases relative to the total pore volume. The behavior would strengthen the argument of triazine decomposition at elevated reaction temperatures. Therefore, it might not be correct to speak of a covalent triazine framework in this case. Similarly, due to a low nitrogen content in the samples and an absence of triazine signals in infrared and solid state NMR spectra, it might be more reasonable to describe DCBP-polymer 1 as a nitrogen-doped carbonaceous material.

6.1.2.2 Cyclotrimerization of 4,4'-Dicyanobiphenyl in Chlorosulfuric Acid

A different synthesis concept of triazine containing polymers based on the DCBP monomer has already been reported by Anderson *et al.* in 1966.[421] The resulting network polymer should act as a reference material for a better understanding of the structure of

DCBP-polymer 1. The polymeric material DCBP-polymer 2 has been prepared according to the synthesis protocol of Anderson *et al.* by adding DCBP to neat chlorosulfuric acid (Figure 6-12a).[421]

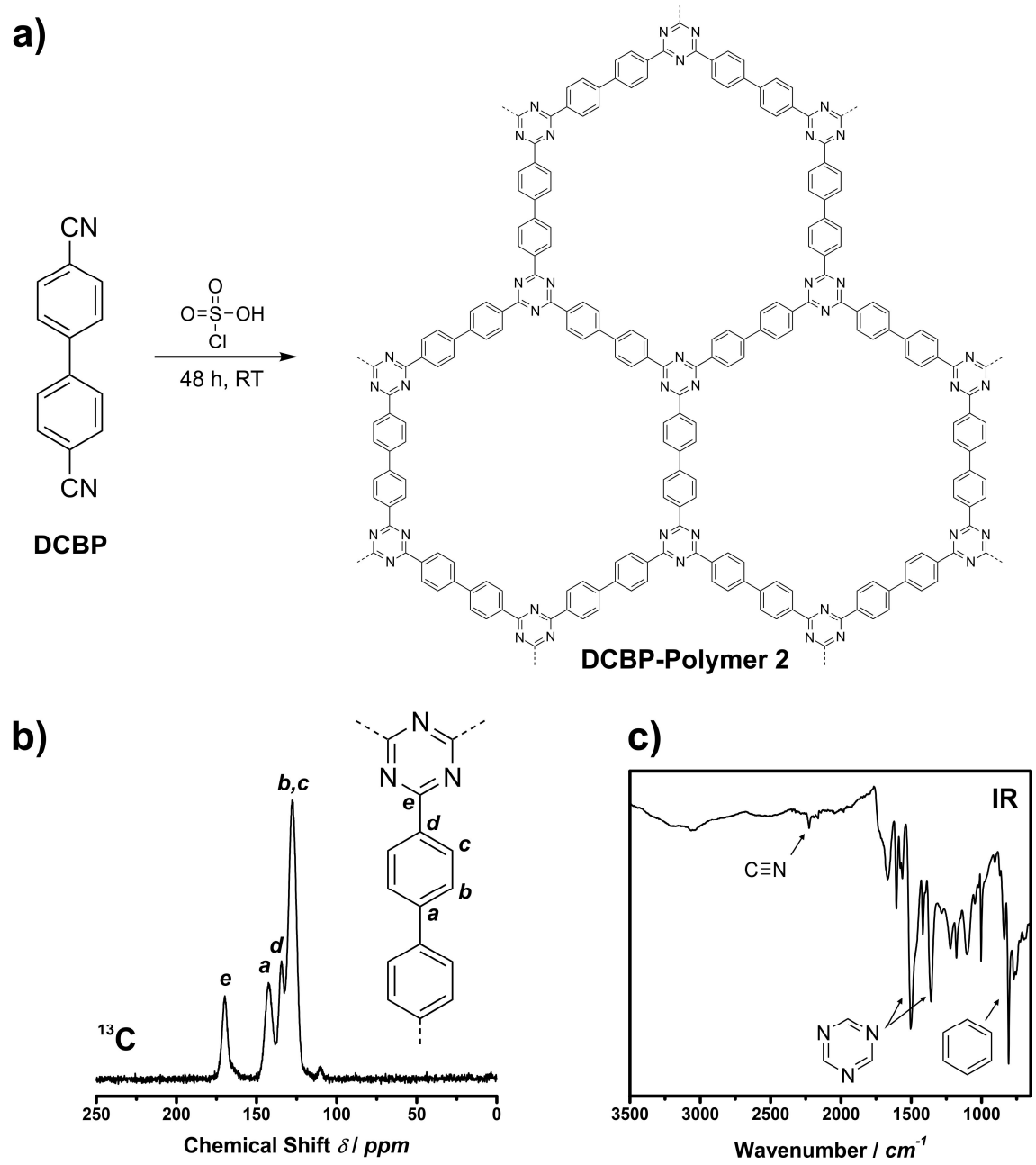

Figure 6-12: *a) Synthesis conditions and ideal structure of DCBP-polymer 2, b) ^{13}C MAS NMR spectrum of DCBP-polymer 2 and c) infrared spectrum of DCBP-polymer 2.*

Chlorosulfuric acid acts as solvent and cyclotrimerization catalyst in this reaction. After two days at room temperature the amorphous and non-porous product DCBP-polymer 2 has been obtained as a yellowish powder in quantitative yields.

Despite both polymers are based on DCBP as starting material, the ^{13}C MAS NMR spectra of DCBP-polymer 1 and DCBP-polymer 2 show significant differences. The sharper peaks in the spectrum of DCBP-polymer 2 point to an increased structural homogeneity compared to DCBP-polymer 1. The most striking difference might be the sharp peak at approximately 170 ppm indicating the presence of considerable amount of triazine units in the polymer network. The three distinctive peaks at 143 ppm, 134 ppm and 127 ppm could be ascribed to the carbon atom of the biphenyl unit according to the assignments in Figure 6-12b. The weak signal at 111 ppm represents a small amount of unreacted terminal nitrile groups.
The triazine unit can also be identified in the infrared spectrum of DCBP-polymer 2 by two characteristic absorption bands at 1504 cm^{-1} and 1360 cm^{-1}. These two bands have already been discussed for CTF-1 in section 6.1.1.1. XRD confirms an amorphous morphology of DCBP-polymer 2, which has been expected due to the contortion of the two phenyl rings in the biphenyl units.[422]
According to nitrogen sorption measurements, the material did not show any considerable nitrogen uptake and could be regarded as non-porous. The high degree of disorder within the material might lead to pore blocking preventing the nitrogen molecules from entering the inner surfaces of the material.
Elemental analysis measurements determine the C/N ratio (7.3) in DCBP-polymer 2 very close to the calculated C/N ratio (7.0) for an ideal polymer according to Figure 6-12a.

A comparison between DCBP-polymer 1 and DCBP-polymer 2 indicates that the chemical structure of the two polymeric materials differs significantly. In case of DCBP-polymer 2, elemental analysis, ^{13}C MAS NMR and infrared measurements confirm the presence of triazine units in the polymer network. However, the applied low-temperature synthesis catalyzed by chlorosulfuric acid is obviously not suitable for the generation of porous materials. Recently, Ren *et al.* reported a successful cyclotrimerization of DCBP in trifluoromethane-sulfonic acid and chloroform and obtained a porous material with a specific BET surface area of 776 $m^2\ g^{-1}$.[205] The reaction could also be carried out under microwave irradiation, however, total pore volume and specific BET surface area are slightly decreased in this case.[205]

6.1.2.3 Cyclotrimerization of 2,2'-dimethyl-4,4'-dicyanobiphenyl in molten Zinc(II) Chloride

An alternative approach to synthesize functionalized porous networks *via* the ionothermal route in molten zinc(II) chloride was performed by using 2,2'-dimethyl-4,4'-dicyanobiphenyl (Me_2DCBP) as starting material. Due to its low melting point at 113 °C, the high thermal stability and the good detectability of the methyl groups by MAS

CP-NMR experiments, the Me_2DCBP monomer should be a promising candidate to perform a successful introduction of methyl groups in a porous organic polymer network. Furthermore, both methyl groups are attached in meta-position to the nitrile groups in 4- and 4'-position and though, contrary to the MeCTF polymers already discussed above (see section 6.1.1.2), their influence on triazine formation by nitrile cyclotrimerization should be negligible.

The synthesis conditions for Me_2DCBP-polymer were similar to those of MeCTF-1 (Figure 6-13a). The synthesis of monomer Me_2DCBP was performed similarly to the synthesis of DCBP described above (Figure 6-9). Slow heating of zinc(II) chloride and Me_2DCBP to 370 °C provided a homogeneous slightly brown reaction mixture. After purification, the reaction product was obtained as black powder. Similar to all biphenyl-containing networks, Me_2DCBP-polymer shows an amorphous texture. The ^{13}C MAS NMR spectrum of Me_2DCBP-polymer is displayed in Figure 6-13b.

The characteristic broad signal with a maximum at 129 ppm results from a heavy overlap of several different aromatic carbon signals and is typical for highly disordered materials. As already observed in the ^{13}C MAS NMR spectrum of DCBP-polymer 1 there is no evidence for the presence of triazine units in the polymer structure. The weak signal at 19 ppm can be ascribed to the presence of methyl groups. However, the low intensity of the signal suggests considerable decomposition of the methyl groups most likely because of the high synthesis temperature. A similar type of decomposition has been observed for MeCTF polymers (see section 6.1.1.2).

The infrared spectrum of Me_2DCBP-polymer stresses the preceding argument (Figure 6-13c). Again, triazine bands could not be detected in the spectrum. The dashed lines in Figure 6-13c represent the approximate positions of triazine bands in CTF-1 (see chapter 6.1.1.1). The observed average signal intensity of the infrared spectrum is very poor, most likely due to the high degree of disorder in the material. The heavy overlap of the bands and their low intensity prevent a distinct assignment.

The specific BET equivalent surface area and the total pore volume of Me_2DCBP polymer calculated from nitrogen sorption isotherms are comparable to the respective data determined for DCBP-polymer 1 (Figure 6-13d). The H2 type hysteresis between the adsorption and the desorption isotherm is typical for highly disordered mesoporous materials. High gas uptake at very low relative pressures also indicates a considerable amount of micropores in the polymer structure.
The multimodal pore size distribution calculated from NLDFT methods describes a maximum for pore sizes of approximately 3.8 nm (Figure 6-14). The calculated total pore volume of 1.27 $cm^3\ g^{-1}$ is lower than the total pore volume of DCBP-polymer 1.

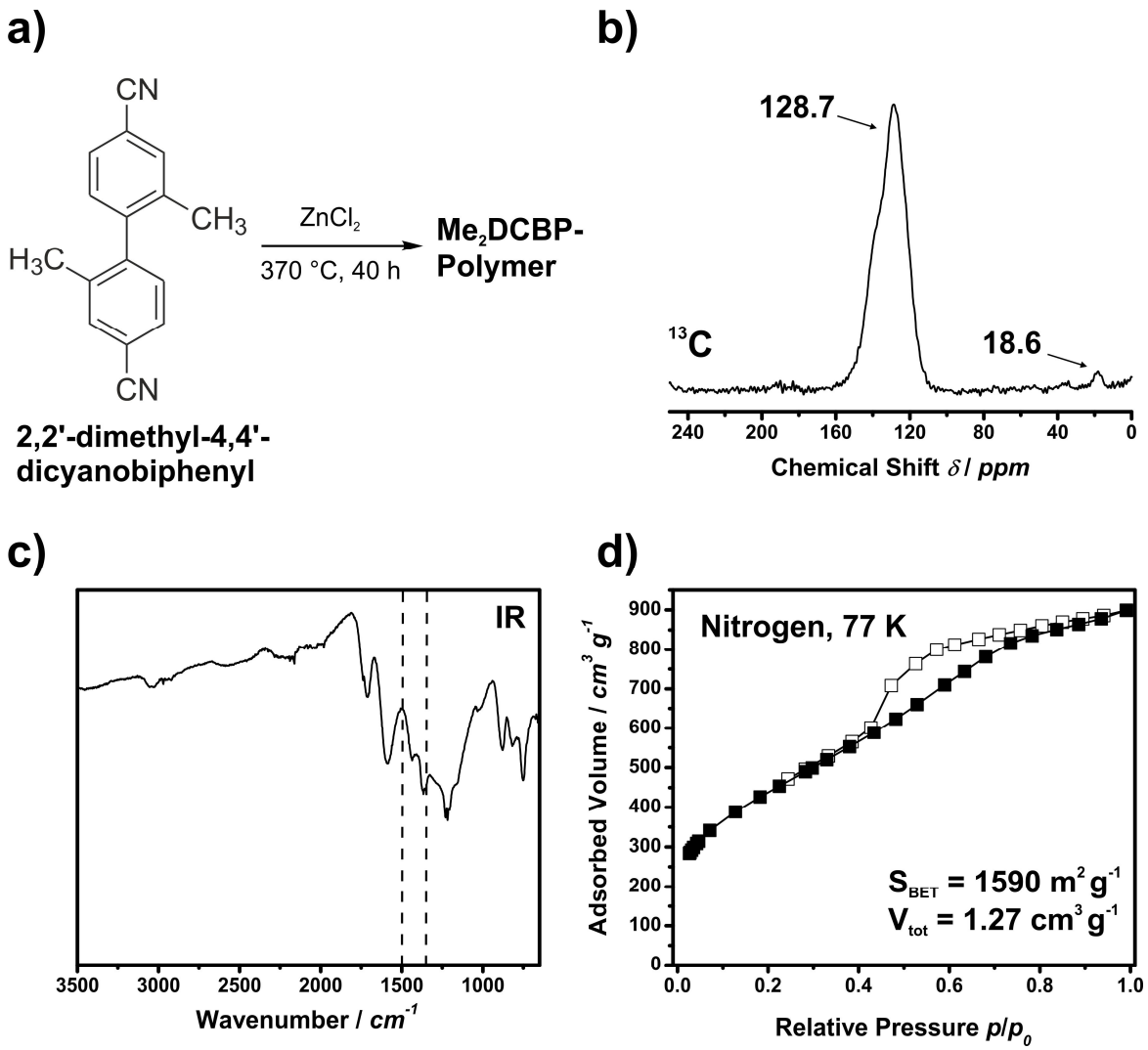

Figure 6-13: *a) Synthesis of Me_2DCBP-polymer, b) ^{13}C MAS NMR spectrum of Me_2DCBP-polymer, c) infrared spectrum of Me_2DCBP-polymer (dashed lines represent the approximate positions of triazine bands in CTF-1), d) nitrogen sorption isotherms of Me_2DCBP-polymer; V_{tot} has been determined at $p/p_0 = 0.99$.*

The total pore volume obtained by QSDFT methods is slightly higher. The bimodal shape of the pore size distribution diagram from QSDFT also differs from the respective NLDFT diagram (Figure 6-14) and describes two dominating pore sizes of 1.2 and 3.4 nm.

The obtained results show that the methyl functionalization of a triazine based framework based on Me_2DCBP could not be achieved *via* the ionothermal route in molten zinc(II) chloride. The relatively high reaction temperatures induce an extensive decomposition of triazine and methyl units providing a predominantly carbonaceous material where low amounts of nitrogen are present. A reduction of the reaction temperature below 370 °C yielded non-porous materials containing large amounts of unreacted nitrile groups that were at least partially soluble in organic solvents like THF and methanol.

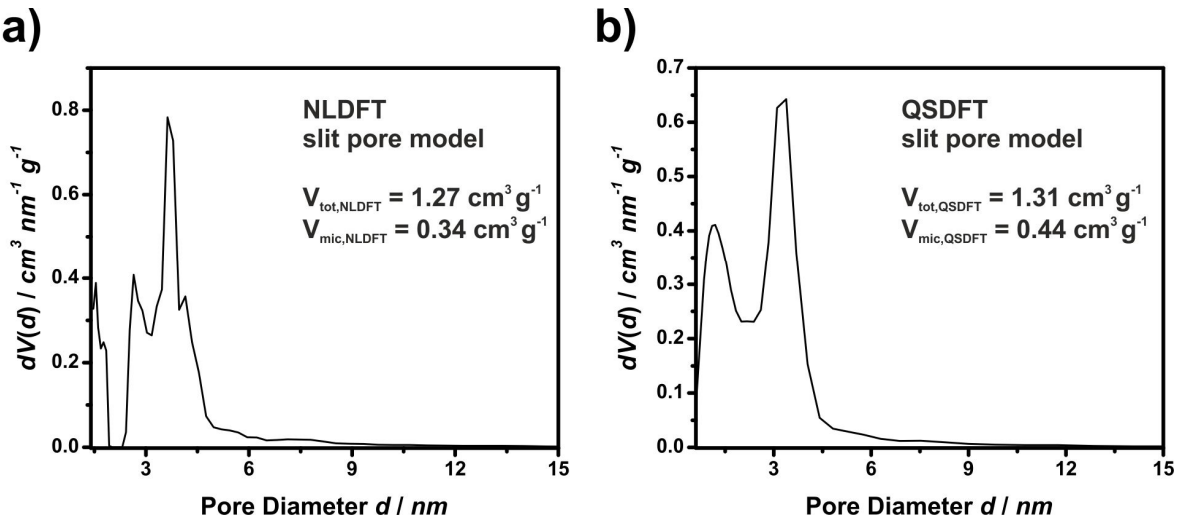

Figure 6-14: *Pore size distribution of Me_2DCBP-polymer calculated from a) NLDFT and b) QSDFT kernel.*

An important challenge for a successful synthesis is the reduction of undesired decomposition reactions in the functionalized CTF polymers. Unfortunately, the number of suitable and chemically stable building blocks for temperatures above 350 °C is rather low and a successful nitrile cyclotrimerization using zinc(II) chloride could probably be performed only at temperatures clearly above the melting point. Based on the results obtained so far and as already assumed in the literature, the harsh reaction conditions seem to prevent a functionalization of the polymer networks.[116] Due to these reasons, no further experiments in molten zinc(II) chloride have been performed.

6.2 Autoclave Syntheses of Covalent Triazine-based Polymers

6.2.1 Piperidine/Metal Salt-catalyzed Syntheses of Triazine-based Polymers

An interesting approach potentially suitable for the low-temperature synthesis of covalent triazine frameworks has been reported by Forsberg *et al.*[423,424] As reported in the study the formation of triazine ring could be achieved by a cyclotrimerization of nitrile groups catalyzed by lanthanide(III) salts and ammonia at a temperature of 200 °C and elevated pressures in a closed reaction vessel (Figure 6-15). When using benzonitrile as starting material, yttrium triflate and equimolar amounts of liquid ammonia catalyze triazine formation and provide 2,4,6-triphenyl-1,3,5-triazine (TPT) in quantitative yields. In a possible reaction mechanism, an yttrium-induced polarization of the nitrile group facilitates the nucleophilic attack of ammonia to form benzamidine. The further addition of two benzonitrile molecules completes the formation of the triazine ring. Regarding a

possible synthesis of functionalized triazine frameworks, the comparatively low reaction temperature should prevent a decomposition of present functional groups in the polymer network. In this thesis, the metal salt catalyzed synthesis of triazine-based polymer networks starting from 1,4-DCB at moderately high temperatures has been studied. Another important goal was to evaluate the influence of different catalyst systems on the nitrile cyclotrimerization reaction.

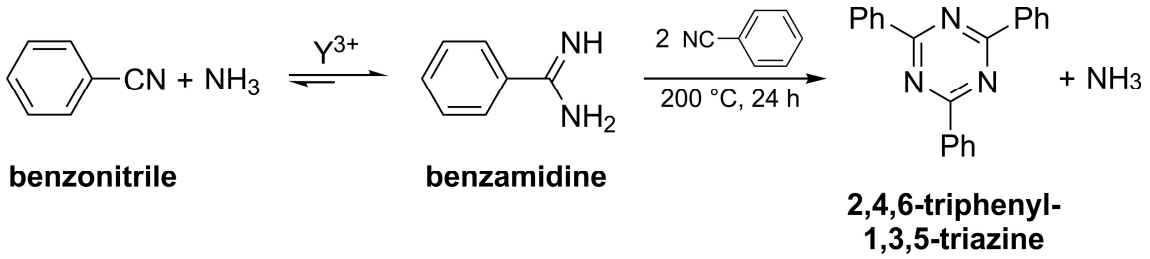

Figure 6-15: *Synthesis of TPT according to Forsberg* et al.[424]

The piperidine-mediated autoclave syntheses of the triazine polymers (ATP-P) were conducted in a steel autoclave with PTFE inset according to the report of Díaz-Ortiz *et al.* with some slight modifications.[425] Contrary to the original protocol of Forsberg *et al.*, Díaz-Ortiz and coworkers applied piperidine instead of ammonia to induce nitrile cyclotrimerization.[424,425]

The cyclotrimerization of 1,4-DCB by using piperidine and three different triflate salts has been studied. Besides yttrium triflate (ATP-P 1), also zinc triflate (ATP-P 2) and lanthanum triflate (ATP-P 3) have been applied to induce nitrile cyclotrimerization under mild reaction conditions. During the work on this thesis, the metal-catalyzed cyclotrimerization of nitriles has also investigated under supervision in the bachelor thesis of Christina Herrmann.[426] The synthesis concept is displayed in Figure 6-16.

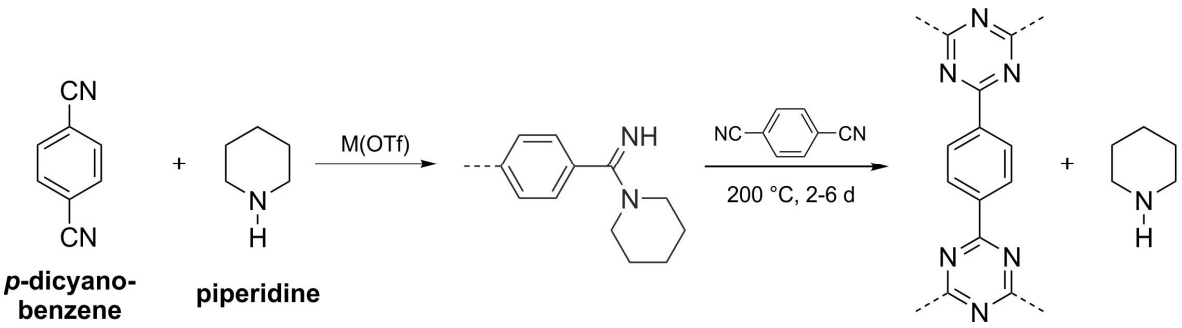

Figure 6-16: *Synthesis route for piperidine-catalyzed syntheses of ATP-P polymers. $M(OTf)_x$ = $Y(OTf)_3$ (ATP-P 1), $Zn(OTf)_2$ (ATP-P 2) or $Ln(OTf_3)$ (ATP-P 3).*

The resulting triazine polymers appear as off-white or yellowish powders and are insoluble in organic solvents like THF, cyclohexane, methanol, DMF and DMSO. It has been found that the obtained product yields strongly depend on the applied reaction times. For reaction times up to 2 d only product yields below 10% were obtained. In contrast, the product yields were almost quantitative for reaction times of more than 5 d. It should be mentioned that in some cases the determined amount of product exceeded the theoretical amount calculated from the applied starting material. This might be explained by the addition of small amounts of piperidine to terminal nitrile groups.

The infrared spectra of the synthesized ATP-P polymers are shown in Figure 6-17a. The dominating features in all three spectra are the characteristic aromatic triazine bands at 1500 cm^{-1} and 1360 cm^{-1} and the phenyl band around 800 cm^{-1}, which have already been discussed for CTF-1 (see section 6.1.1.1). The low intensity of the nitrile band at 2200 cm^{-1} results from a small amount of residual unreacted nitrile groups in the polymer network. Two weak bands in the range between 2800 and 3000 cm^{-1} can be identified in the spectra of ATP-P 2 and 3. The respective bands might be caused by the symmetric and asymmetric C-H stretching vibrations in the aliphatic piperidine ring and would confirm the presence of residual piperidine in the polymer networks.
The XRD patterns of ATP-P 1, ATP-P 2 and ATP-P 3 reveal the amorphous texture of the polymers (Figure 6-17b). The reflections are broad and have low intensity which is a typical feature of materials with a lack of long range order. The only sharp reflection is provided at an angle of 26.7° corresponding to a distance of 3.3 Å. Noteworthy, the (*001*)-reflection of CTF-1 has an almost similar position in the respective powder XRD pattern and indicates a regular stacking of two-dimensional planes in the polymer. The decreased long range order of the ATP-Ps compared to CTF-1 might result from the lower synthesis temperature.

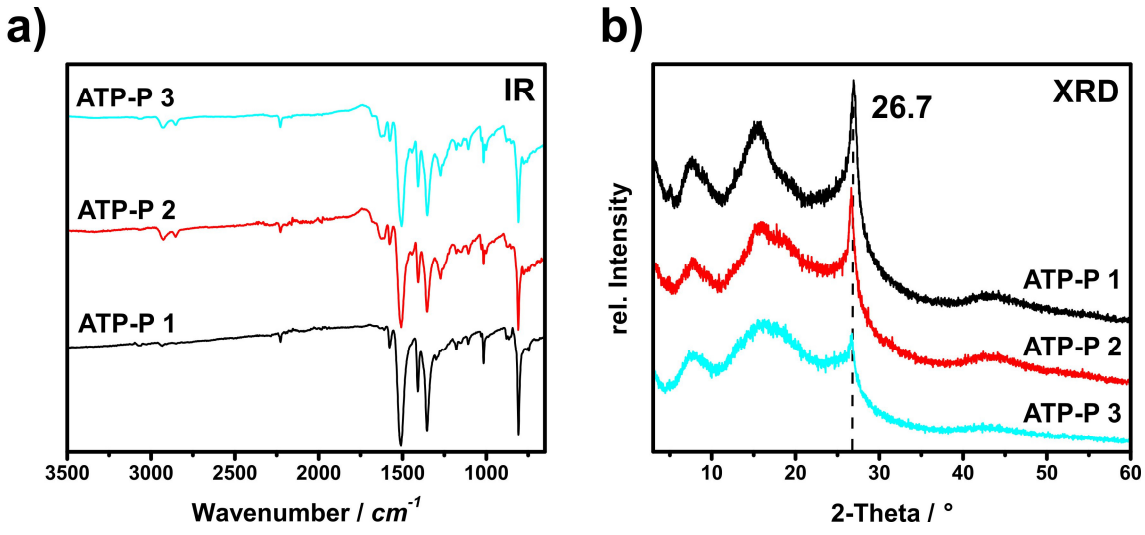

Figure 6-17: *a) Infrared spectrum of ATP-P polymers, b) XRD pattern of ATP-P polymers.*

While CTF-1 has been synthesized under reversible conditions to form a thermodynamically stable network, the triazine polymer synthesis at 200 °C obviously exhibits no reversibility and provides a kinetically stable and amorphous reaction product. The ^{13}C MAS NMR experiments conducted with the ATP-P polymers also provide comparable results for all three candidates (Figure 6-18a and b). The peak positions and the assignment of the signals to the respective carbon atoms can be performed similar to CTF-1. An exception is the signal at 26 ppm most probably caused by the aliphatic carbon atoms of the piperidine moieties included in the polymer structure. The presence of the piperidine signal underlines the attachment of piperidine moieties to the polymer network.

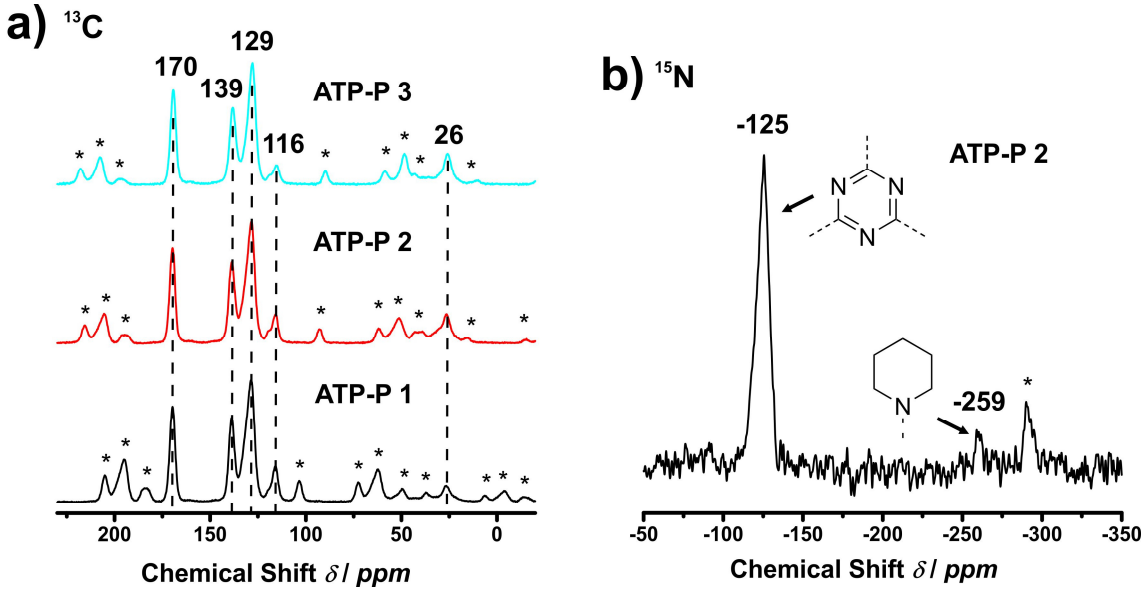

Figure 6-18: *a) ^{13}C MAS NMR spectra of ATP-P polymers. Asterisks (*) denote rotational sidebands ATP-P 1was recorded at a rotation frequency ν_{rot}=5.8 kHz, ATP-P 2 and 3 were recorded at a rotational frequency ν_{rot}=6.0 kHz, b) ^{15}N MAS NMR spectrum of ATP-P 2.*

The ^{15}N MAS NMR spectrum of ATP-P 2 in Figure 6-18b is representative for all three ATP-P polymers (Figure 6-18b). Two different nitrogen sites can be identified from the ^{15}N spectrum. The very intensive peak at -125 ppm is characteristic for present triazine units in the polymer. The second signal in the spectrum at -259 ppm represents the nitrogen atom in the piperidine moieties. The signals caused by the aromatic carbon atoms in the ^{13}C and the triazine signals in the ^{15}N NMR spectrum are comparable to the signals in the respective NMR spectra of CTF-1. The NMR spectra of the ATP-P polymers, however, contain additional signals that could be attributed to residual piperidine in the polymer structure.

The results obtained for the ATP-P polymers confirm that the formation of an extended triazine network by various piperidine/metal salt catalysis can be accomplished under the given reaction conditions. Nitrogen sorption measurements, however, label the three

polymer networks as non-porous. One reason for the absence of porosity might be a lack reversibility of the cyclotrimerization reaction as already described for the kinetically controlled triazine network DCBP-polymer 2 in chapter 6.1.2. Another possible explanation are residual amounts of piperidine incorporated in the network preventing an effective cross-linking and facilitating a dense packing of the polymer structure.

6.2.2 Ammonium Chloride/Metal Salt-catalyzed Syntheses of Triazine-based Polymers

The successful synthesis of a triazine network catalyzed by piperidine and a suitable metal triflate at moderate reaction temperature has been demonstrated in the previous chapter. However, it has been shown, that a considerable amount of residual piperidine remained in the final product, which might prevent an effective cross-linking in the polymer structure. With an insufficient degree of cross-linking the generation of porosity in the polymer network would be very unlikely. Therefore, an alternative approach has been tested replacing piperidine for ammonium chloride as co-catalyst. The respective experiments were conducted as solvent-free reactions under similar inert reaction conditions in a steel autoclave.

Although, the experiments conducted for this thesis have clearly shown, that ammonium chloride catalyzes the formation of 1,3,5-triazines, the mechanism of the cyclotrimerization reaction under these conditions has not been resolved yet. A possible mechanism for the formation of amidine/amidinium chloride is reported in the literature.[427] According to the report by Schaefer and Krapcho, the nitrile group might be activated by protonation to increase the electrophilicity of the nitrile carbon atom.[427] The proton would be provided by gaseous HCl from the gas/solid equilibrium of ammonium chloride at elevated temperatures.[427] In a second step gaseous ammonia might perform a nucleophilic attack on the nitrilium intermediate to form an amidine. The basic amidine should be protonated by present HCl to form amidinium chloride. In the last step amidine or amidinium compounds might react with two additional activated nitrile groups to form a triazine ring similar to Figure 6-15.

The addition of two further nitrile groups completes the triazine formation. It should be mentioned that the initial polarization of the nitrile group might also be caused by the metal salt cation according to the report of Forsberg *et al.* (Figure 6-15).[423,424] Despite the fact, that the role of the catalysts in the reaction mechanism is not clear in full detail, the presence of both compounds, metal salt and ammonium chloride, in the reaction vessel is essential for effective triazine formation.

The syntheses of the ammonium chloride-mediated triazine polymers (ATP-A) were conducted in a steel autoclave with PTFE inset similar to the syntheses of the ATP-P polymers (section 6.2.1) where the applied catalyst piperidine has been exchanged by ammonium chloride. The polymer networks ATP-A 1, ATP-A 2 and ATP-A 3 were isolated as off-white powders in moderate yields. Infrared spectroscopy measurements reveal three almost identical spectra of all three polymers (Figure 6-19a). Beside the dominating triazine and phenyl bands at 1510 cm^{-1}, 1360 cm^{-1} and 810 cm^{-1}, the absorption band at 2225 cm^{-1} indicates a considerable amount of unreacted nitrile groups.

The powder XRD patterns for ATP-A 1, ATP-A 2 and ATP-A 3 could be regarded as rather similar (Figure 6-19b). The diffractograms indicate a distinct long-range order for the three polymers with dominant reflections at angles of 7.9°, 14.9° and 27.1°. Even though the respective intensities differ, these reflections can also be found in the XRD pattern of CTF-1 at comparable positions. However, the poor crystallinity of the samples prevented a further analysis of the crystal structure of the polymeric materials.

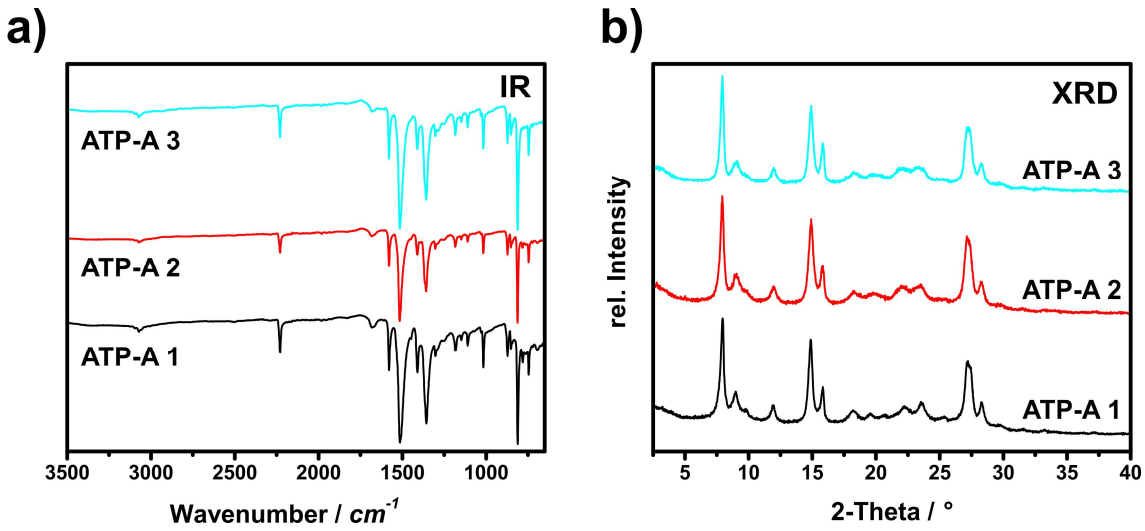

Figure 6-19: *a) Infrared spectra of ATP-A polymers, b) XRD patterns of ATP-A polymers.*

The ATP-A polymers have additionally been analyzed by CP MAS NMR spectroscopy. The ^{13}C MAS NMR spectra show several peaks with high intensity at similar positions compared to the ATP-P polymers (Figure 6-20a). The characteristic sharp peak at 169 ppm confirms the formation of triazine units in the polymers. The different carbon atoms of the phenyl units produce a heavy overlap in the typical chemical shift region between 125 and 140 ppm. The nitrile group peak at 115 ppm shows a quite uncommon signal shape with two small shoulders towards higher chemical shifts. The shape might be explained by the presence of nitrile groups in slightly different chemical environments in the polymer structure causing minor variations in the chemical shifts. The ^{15}N MAS NMR spectrum of ATP-A 1 is representative for all three ATP-A polymers (Figure 6-20b). The very intense

signal at -123 ppm attributed to the triazine units, whereas the neighboring smaller peak at -118 ppm again indicates the presence of residual nitrile groups. No other nitrogen signals could be identified in the spectrum.

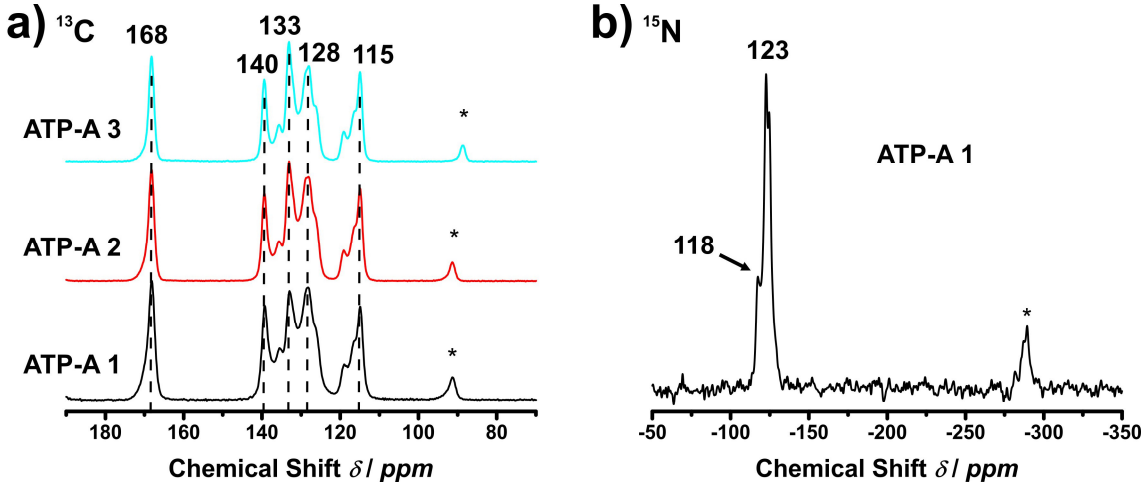

Figure 6-20: *a) ^{13}C MAS NMR spectra of ATP-A polymers, b) ^{15}N MAS NMR spectrum of ATP-A 1 representative for ATP-A polymers. Asterisks (*) denote rotational sidebands.*

A ^{13}C direct excitation NMR experiment was conducted to gain additional information on the structure of the crystalline ATP-A polymer. The direct excitation technique allows a quantification of the carbon atoms in the material by integrating the respective signals in the NMR spectrum. The ^{13}C direct excitation NMR spectrum of ATP-A 1 is shown in Figure 6-21a. There are three characteristic integrated signal regions to be separated in the spectrum. The signal at 169 ppm marks the triazine carbons (red), whereas the nitrile carbons and the neighboring aromatic quaternary carbon atom generate the broad signal with a maximum intensity at 118 ppm (green integral). The third region (blue) represents the remaining aromatic carbon atoms in the phenyl rings.

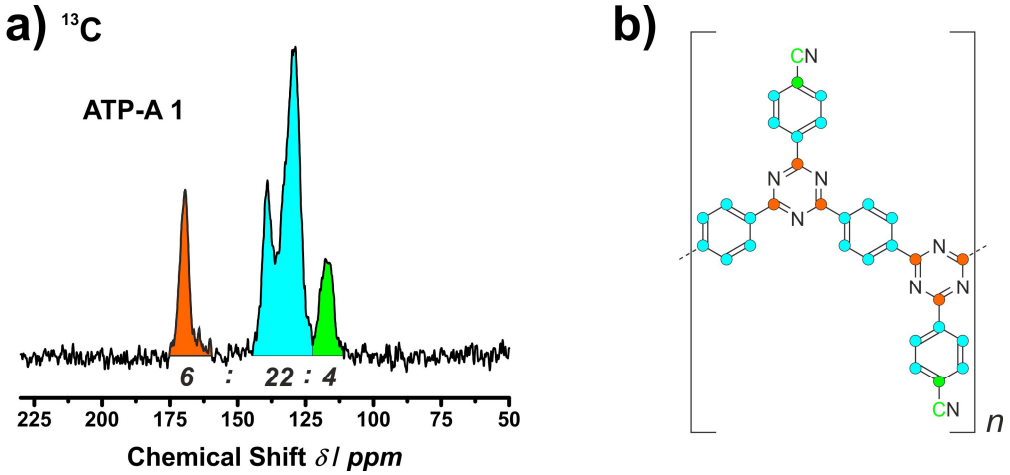

Figure 6-21: *a) ^{13}C direct excitation spectrum of ATP-A 1. b) Hypothetical structure of ATP-A 1. Red, blue and green carbons can be assigned to the respective signal in a).*

The relative amount of different carbon atoms in the polymeric material can be determined from the integration of the respective signal regions. In the present case the ratio of the integrated signal regions was 6 (red) : 22 (blue) : 4 (green) as displayed below. Based on the obtained analytical results a hypothetical linear polymeric structure has been postulated (Figure 6-21b). The colors in the repeating unit of the polymer in Figure 6-21b mark the carbon atoms included in the respective signal regions in Figure 6-21a. The postulated polymer structure is characterized by a backbone of alternating triazine and phenyl units. Additionally, every triazine ring is linked to phenyl units carrying nitrile groups in *para*-position. The assignments of the carbon atoms in the linear polymer are consistent with simulated NMR data.
The results from the NMR experiments for the ATP-A materials are consistent with those obtained from infrared spectroscopy. The ATP-A polymers show a certain long range order with reflections of high intensity in their powder XRD patterns. Although there is a certain resemblance to the XRD patterns of CTF-1, performed attempts to index the unit cell of the polymeric ATP-A materials from the respective XRD patterns have not been successful.
It is worth mentioning that similar to ATP-P networks, nitrogen sorption measurements did not detect any porosity in the structure of ATP-A 1, 2 and 3. A reason for the lack of porosity might be insufficient cross-linking of the polymers under the given reaction conditions, stressed by the presence of considerable amounts of residual nitrile groups in all final products. Another plausible explanation would be a poor degree of polymerization due to diffusion limitations in the reaction vessel caused by an insufficient solvatization of starting materials and oligomers. This argument would also explain the presence of numerous unreacted nitrile groups in the polymers.

The results reported in this paragraph confirm a successful triazine synthesis by applying ammonium chloride/metal salt catalysis. The three ATP-A polymers synthesized by using different metal triflates, $Y(OTf)_3$, $Zn(OTf)_2$ and $Ln(OTf)_3$, as catalysts seem to have similar structures. Only minor differences between ATP-A 1, ATP-A 2 and ATP-A 3 have been detected in IR, NMR and XRD measurements. However, the structure of the synthesized polymers could not be solved during the work on this thesis.

6.3 Triazine Syntheses in Zinc(II) Chloride-containing Salt Melts

The previous results show that a successful synthesis of extended triazine-based networks can be achieved by different routes. However, the synthesis of porous polymer networks

was restricted to reactions in zinc(II) chloride salt melts at relatively high synthesis temperatures. Due to the limited thermal stability of most organic compounds, the elevated synthesis temperatures prevent an introduction of functional groups into the polymer networks. Unfortunately, the application of zinc(II) chloride as solvent and catalyst is limited to temperatures above its melting point of about 320 °C. The experiments performed for this thesis have shown that even higher temperatures of more than 350 °C are required to ensure an efficient mixing of the reaction compounds.

A promising attempt to lower the reaction temperature might be the use of eutectic salt melts containing a high amount of zinc(II) cations. Various mixtures of zinc(II) chloride and various alkali salts have been tested in order to determine a suitable system to act as a catalyst/solvent system for the cyclotrimerization of DCB. In the literature several reports on the thermal behavior of the salt mixture $LiCl/ZnCl_2$ can be found, however, the published results differ significantly.[428,429] The difference might result from a difficult handling of $ZnCl_2$ due to its low stability against hydrolysis. Some of the published eutectic melts have been examined, but the reported mixtures did not melt below 300 °C.[429] Due to the high melting points, which are almost as high as the melting temperature of neat zinc(II) chloride, $LiCl/ZnCl_2$ salt mixtures have not been taken into account for cyclotrimerization experiments with 1,4-DCB.

In 1941, Nikonova *et al.* presented a study on various salt mixtures consisting of NaCl, KCl and $ZnCl_2$.[430] Two of the reported mixtures, a binary $KCl/ZnCl_2$ mixture and a ternary mixture of NaCl, KCl and $ZnCl_2$, possess eutectic points at 228 °C and 203 °C, respectively. Due to the low melting points and the comparatively high zinc(II) chloride content, these two eutectic mixtures were chosen as promising candidates for the synthesis of triazine networks at moderate temperatures.

Within this thesis, the salt melts SM-1 (60 mol% $ZnCl_2$, 20 mol% NaCl, 20 mol% KCl) and SM-2 (54 mol% $ZnCl_2$, 46 mol% KCl) have been tested for their application as solvent/catalyst system for the cyclotrimerization of 1,4-DCB. The synthesis route for SMP-1 and SMP-2 is displayed in Figure 6-22a. Upon heating the pure salt melts appear as clear liquids with remarkably low viscosity. At temperatures around 230 °C when using SM-1 and 260 °C when using SM-2 considerable amounts of starting material dissolve in the melts and a homogeneous mixture is formed in both cases. The polymerization of 1,4-DCB in the respective salt melt provides good yields for SMP-1 and for SMP-2 at about 300 °C. At significantly lower reaction temperatures the product yields decrease significantly and the obtained products are almost completely soluble in hot methanol suggesting an oligomerization, if any, but no complete polymerization of 1,4-DCB. At sufficiently high reaction temperatures SMP-1 and SMP-2 were obtained as yellowish powders. The residual salt melts were removed in 1M HCl. The polymers are insoluble in water, hydrochloric acid and common organic solvents like methanol, ethanol, THF, acetone and DMSO. Gas sorption measurements did not detect any significant porosity.

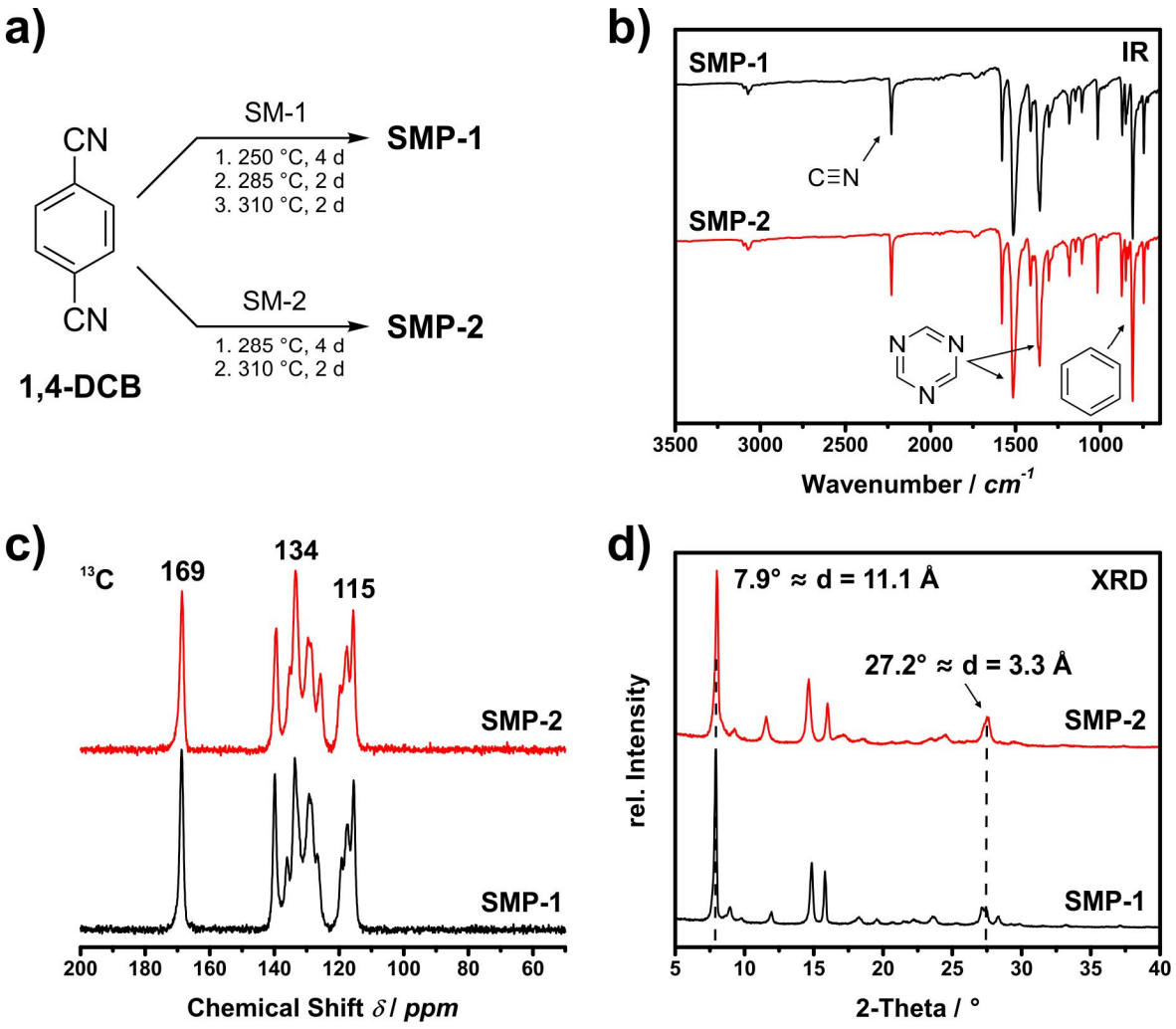

Figure 6-22: *a) Synthesis route for polymers SMP-1 and SMP-2. Characterization of SMP-1 and SMP-2 by (b) infrared spectroscopy, c) ^{13}C MAS NMR spectroscopy and d) powder X-ray diffraction.*

Infrared spectra of the polymers SMP-1 and SMP-2 are very similar (Figure 6-22b). Again the absorption bands at 2230 cm^{-1} denote a considerable amount of nitrile groups in both SMP polymers. The most dominant bands in both spectra can be found at 1510 cm^{-1}, 1360 cm^{-1} and 810 cm^{-1}. They are characteristic for the presence of large amounts of triazine and phenyl units in the polymeric structures and have already been discussed in detail for preceding infrared spectra in this chapter. As expected ^{13}C MAS NMR measurements confirm the successful formation of triazine units in both cases by showing the characteristic triazine signal at 169 ppm in the spectra of SMP-1 and SMP-2 (Figure 6-22c). In the region between 120 and 140 ppm aromatic carbon atoms show a number of distinct signals of variable intensity. The quite sharp signals in both spectra point to a certain degree of order in the materials SMP-1 and SMP-2. Similar to preceding polymer materials in this chapter, the overlapping carbon signals in the region between 115 and 120 ppm can be attributed to terminal nitrile groups and their adjacent aromatic carbon atom, respectively. It should be noticed that for SMP polymers the signals in both ^{13}C MAS NMR spectra in general appear significantly sharper compared to the preceding ATP

polymers and point to the presence of ordered domains in the SMP structure. This argument is strengthened by powder XRD measurements where a number of sharp reflections have been detected in the diffractograms of both materials SMP-1 and SMP-2 (Figure 6-22d).

Although the two powder XRD diffractograms seem to be very similar, minor differences in the reflection positions of SMP-1 and SMP-2 have been identified, specifically at 2-theta angles between 13° and 17°. The most intense reflection can be found for both polymers at a reflection angle of 7.9° representing a distance of 11.1 Å. Noteworthy, the characteristic *100*-reflection of CTF-1 can be found at comparable reflection angles for both polymers, SMP-1 and SMP-2.[45] This might be a hint to structural similarities between these polymers. However, it was not possible to index the diffraction patterns in Figure 6-22d. The measurements were performed on a diffractometer with reflection geometry and yielded diffraction patterns with comparably poor reflection intensities for SMP-1 and SMP-2. In a comparable measurement on a diffractometer using transmission geometry the obtained results differ significantly, at least for SMP-1. The respective powder XRD pattern is shown in Figure 6-23.

The powder diffraction pattern of SMP-1 has been be indexed successfully by using TOPAS, yielding a number of potential unit cells with monoclinic or orthorhombic crystal system.[431] Indexing and profile fit with TOPAS has been performed by Dr. Thomas Martin, Chair of Inorganic Chemistry I, University of Bayreuth. The unit cell yielding the highest Goodness of Fit (GoF) are displayed in Table 4. The Pawley fit and the respective experimental X-ray diffraction pattern of SMP-1 are displayed in Figure 6-23. It should be noticed that the shape of the experimental pattern is very similar to the diffraction patterns of the ATP-A polymers (see Figure 6-19).

Table 4: *Unit cells with highest GoF from indexing run of SMP-1 using TOPAS software.*

rank	space group	crystal system	GoF	a	b	c	α	β	γ
1	P2	monoclinic	5.87	9.9461	22.5035	4.3770	90.000	90.310	90.000
2	P2	monoclinic	5.85	9.9498	22.5044	4.3740	90.000	90.339	90.000
3	P2	monoclinic	5.79	9.9495	22.5023	4.3732	90.000	89.652	90.000
4	P2	monoclinic	5.60	10.8994	22.5093	4.3744	90.000	113.942	90.000
5	F222	orthorhombic	5.58	45.0482	19.9838	8.7789	90.000	90.000	90.000
6	P2	monoclinic	5.37	10.8905	22.4866	4.3792	90.000	113.931	90.000
7	F222	orthorhombic	5.36	45.0642	19.9867	8.7751	90.000	90.000	90.000
8	P2	monoclinic	5.24	9.9545	22.5071	4.3764	90.000	89.724	90.000
9	F222	orthorhombic	5.21	45.0738	19.9875	8.7734	90.000	90.000	90.000
10	P2	monoclinic	5.18	10.8647	22.4917	4.3759	90.000	113.514	90.000

However, the reflections measured in the diffraction pattern of SMP-1 are considerably sharper than those found in the patterns of ATP-A polymers, clearly indicating a more ordered microstructure in the first case.

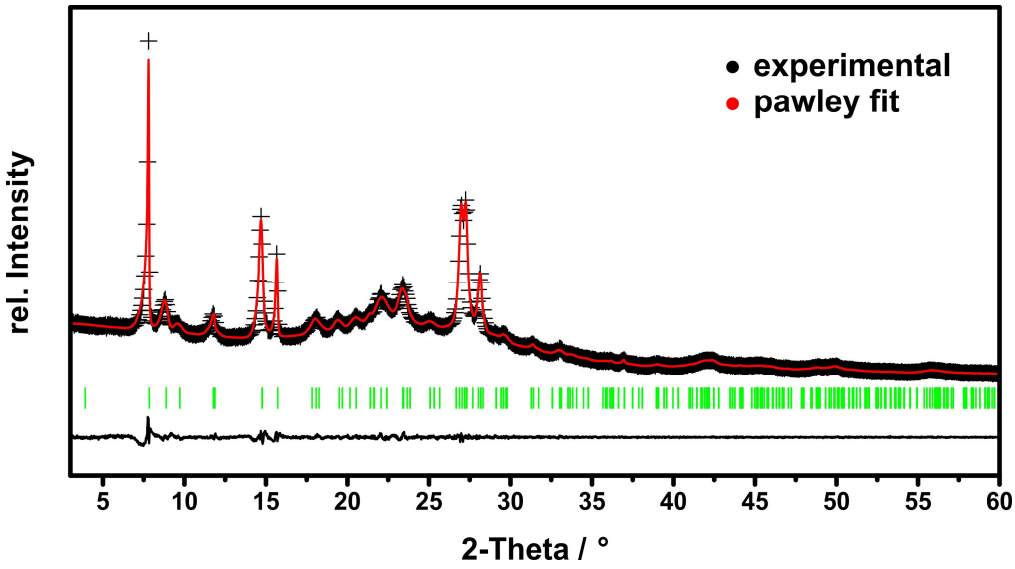

Figure 6-23: *Pawley fit of the powder XRD diffractogram of SMP-1 measured on STOE Stadi P device.*

The unit cell data are summarized in Table 5. Pawley refinement of the indexed powder diffractogram yielded a monoclinic unit cell at a weighted profile factor R_{wp} of 2.066.

Table 5: *Data from Pawley fit applied to SMP-1 powder diffractogram.*

	SMP-1
refinement	Pawley
diffractometer	STOE STADI P
λ [Å]	1.5406 (Cu $K\alpha_1$)
crystal system	monoclinic
space group	P2
lattice constants [Å]	a = 22.539
	b = 4.4036
	c = 9.9457
	β = 89.961
V [Å^3]	987.13
R_p	1.432
R_{wp}	2.066
R_{exp}	0.887

A chain-like polymer structure as displayed in Figure 6-21b might be in accordance with the analytical results so far. The dominant reflection at a 2-theta angle of 7.8° represents a distance of approximately 11.2 Å, which might be in the range of the length along the polymer backbone of the repeating unit in Figure 6-21b. The number of repeating units in the unit cell based on the determined unit cell volume has been approximated in a range between 1.2 and 1.4.
However, the structure of the material could not be solved from the results obtained during the work on this thesis.

6.4 Porous Polyimide Materials

6.4.1 General Considerations

In previous chapter porous triazine frameworks have been synthesized by cyclotrimerization of nitrile monomers at high temperatures. Unfortunately, high reaction temperatures often limit the introduction of functional groups in the network structures due to thermal decomposition. In an alternative synthesis approach presented in this chapter functionalized porous triazine-based networks have been generated by connecting triazine nodes with imide linkers at moderate reaction temperatures. By applying monomer units carrying more than two amine or anhydride moieties it is possible to directly synthesize cross-linked porous polyimide networks. This chapter aims at the synthesis and characterization of porous functionalized polyimide networks and evaluates their applicability for CO_2 storage and separation. The results of the work on porous triazine-based polyimides (TPIs) presented in this chapter have already been published.[46]

6.4.2 Synthesis Concepts of Polyimide Materials

Polyimides are known as high performance polymers showing excellent thermal, chemical and mechanical properties. Due to the commercial availability of many suitable building blocks and the development of various different synthesis methods, a large number of linear polyimides have been investigated extensively in the past decades. Some commercially available polyimides are used as coating materials and high performance moldings in automotive and aerospace industry.[432,433] Especially aromatic polyimides play an important role as key materials in aerospace industry, microelectronics, and optoelectronics industries due to their excellent thermal and chemical stability.[357,358,434]

However, aromatic polyimide materials often show limited solubility in common organic solvents combined with high melting points. In some cases aromatic polyimide materials do not melt below the respective decomposition temperatures at all. These properties could be disadvantageous as they might lead to poor processability and limited applicability of the respective materials.[357,435]

The structural backbone of linear polyimides consists of aromatic or aliphatic monomers linked by imide bridges. Due to their limited conformational flexibility, polyimide chains synthesized from aromatic monomer units are more rigid compared to aliphatic polyimides. However, when regarding porous network materials a certain degree of stiffness is required and desirable to avoid a collapse of the porous network structure and maintain permanent porosity.

6.4.2.1 Synthesis of Polyimides

The essential step in the synthesis of linear polyimides is the formation of the five-membered imide ring by polycondensation of tetracarboxylic dianhydrides and diamines. The choice of the monomers is supposed to determine the chemical and physical properties of the final polyimide material. Due to high glass transition and melting points, a large number of the different polyimides decompose before melting. Therefore, the processing of polyimide polymers could be rather challenging in some cases.

Currently, most of the polyimides might be synthesized in a two-step process. The first step involves the formation of a soluble poly(amic acid) precursor polymer. Commonly, polar aprotic solvents, e.g. DMAc, DMSO, DMF, NMP, are used for polymerization, however, the reaction is not limited to this class of solvents.[433-436] As the resulting poly(amic acid) polymer is still soluble in the solvent, the polymer could easily be processed at this stage of the reaction (e.g. film casting). Various parameters like temperature, concentration of the poly(amic acid) solution and the presence of moisture seem to have a considerable influence on the stability of the solution by reducing the molecular weight of the solvated polymer chains.[437,438] The final polyimide is formed in a second step from the poly(amic acid) solution either by thermal or chemical imidization.

Exemplarily, the synthesis of the polyimide poly-*N,N'*-(oxydi-*p*-phenylene)pyro-mellitimide, also known as Kapton™, is illustrated in Figure 6-24.[437]

The first step in the synthesis of Kapton™ starts with a nucleophilic attack of the terminal amino group of 4,4'-oxydiphthalic anhydride on a carbonyl carbon of anhydride group of PMDA, causing an opening of the five-membered anhydride ring. The ring opening reaction leads to the formation of amide bonds, the backbone of the poly(amic acid) polymer, with adjacent carboxylate groups in *ortho*-position. A major driving force of the reaction is a strong acid-base interaction between the carboxylic acid group and the lewis-

basic solvent.[439] Beside the *trans*-isomer (Figure 6-24) carrying linking groups in *para*-position, the formation of the respective *cis*-isomer with linking amide groups in *meta*-position as a side reaction is also possible.

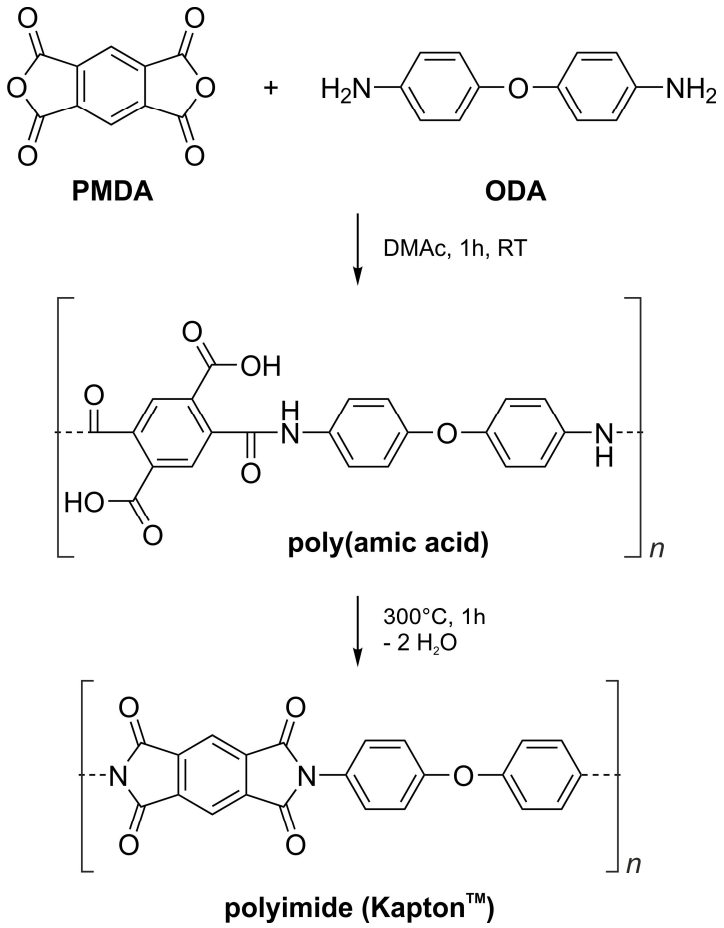

Figure 6-24: *Synthesis route of Kapton™ polyimide according to Sroog et al.*[437]

An efficient polymerization to poly(amic acid) strongly depends on the presence of water in the reaction vessel. Dianhydrides are known as potent dehydrating agents and react even with traces of water by forming *ortho*-dicarboxylic groups.[439] Due to the low reactivity of *ortho*-dicarboxylic acid groups the formation of amic acid groups is highly unfavored at this stage. The carboxylic acid groups are further stabilized by acid-base interactions if the reaction is carried out in Lewis-basic dipolar solvents.[439] The presence of undesired moisture might result from impure solvent or starting materials, but also from a partial conversion of amic acid groups to imide even at ambient conditions.[433] According to a report by Frost *et al.* poly(amic acids) are hydrolyzed even at ambient conditions resulting in a lower molecular weight of the obtained polymer.[440]

In polyimide synthesis the stoichiometry of the applied monomers influences the properties of the final polymer. An excess of anhydride groups in the reaction vessel, for instance, could also decrease the molecular weight of the final product significantly.[438] Some

dianhydride building blocks are able to convert amic acid groups to imide groups by dehydration.[439] The formal addition of water to the dianhydride group yields *ortho*-dicarboxylic acid groups as unreactive chain ends. The respective dehydration reaction is illustrated in Figure 6-25. When using Lewis-basic solvents the present carboxylic acid groups are additionally stabilized by acid-base interactions.

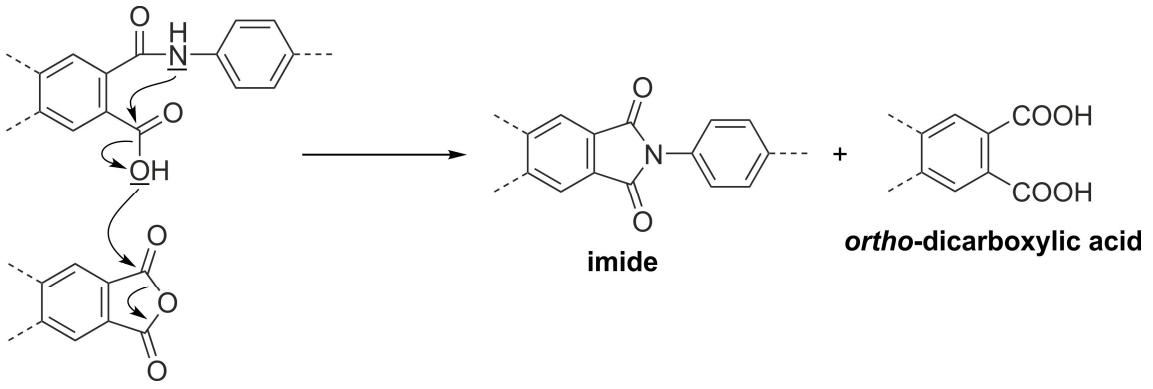

Figure 6-25: *Formation of imide and ortho-dicarboxylic acid groups by dehydration of amic acid.*[439]

As a consequence, the mode of monomer addition obviously seems to influence the final product, as the decrease of molecular weight has not been observed when dianhydride monomers are added to a solution with excess diamine content.[433,438,439]
After the formation of the poly(amic acid) precursors is complete, the final polyimide polymer is formed in a second reaction step called imidization. Therein, the five-membered imide ring is formed by an intramolecular nucleophilic attack of the nitrogen atom of the amide group on the neighboring carboxylate group and the following condensation reaction with one equivalent of water as leaving group.
The ring closing reaction can be achieved by two different methods. Thermal imidization, as performed in Kapton™ synthesis described above, involves heating at moderate rates up to temperatures of about 300 °C and holding the temperature until imidization is completed.[433,437,438] The second method known as chemical imidization introduces dehydrating agents (e.g. acetic anhydride, propionic anhydride) to the poly(amic acid) solution and shifts the reaction equilibrium towards imide formation.[433,434]

As an alternative to the established two-step method for polyimide synthesis, the formation of poly(amic acid) and subsequent imidization can also be performed in a one-step reaction. Here, the final polyimide material can be obtained from the stoichiometric mixture of the corresponding diamine and dianhydride monomers.[435] Kaneda *et al.* used solvents with high boiling points (e.g. phenol, *m*-cresol) to conduct poly(amic acid) and polyimide formation consecutively in the same reaction vessel.[441] Inoue *et al.* compared the one-step and the two-step method by synthesizing a polyimide from 3,3',4,4'-biphenyl-tetracarboxylic dianhydride and 4,4'-oxydianiline in *m*-cresol.[442] Interestingly, the

resulting polyimide materials did not show significant differences in molecular weight and mechanical properties.[442] However, it should be mentioned that the one-step method only yielded similar results to the two-step method, if the final polyimides are sufficiently soluble in the respective reaction solvents. A precipitation of the polymer in the reaction solvent has been found to have a tremendous effect by decreasing the molecular weight of the final product.[441]

In several studies various amines, e.g. pyridine, isoquinoline and lutidine, are added to the reaction solution of one-step syntheses acting as accelerators or catalysts in polyimide synthesis.[435,443-446] In an early study, Endrey postulated that amines might catalyze the imide cyclization reaction by activating the anhydride compound.[447,448] The polyimide syntheses during the work on this thesis have been performed by applying a one-step synthesis protocol. In general, stoichiometric amounts of the respective monomers have been dissolved in a *m*-cresol/isoquinoline solvent system and converted to polyimide by increasing the temperature in several subsequent steps.

6.4.2.2 Synthesis of Porous Polyimide Networks

Porous polyimide materials with predominating pore sizes in meso- and micrometer scale could generally be divided in two classes. In the first class, e.g. polymers of intrinsic microporosity (PIMs), porosity is generated by insufficient packing of the polymer chains due to the high rigidity and the specific geometry of the applied monomers.[119-123] In the second class of porous organic polymer (POP) networks, which is discussed predominantly in this thesis, porosity is generated by effective cross-linking of rigid building blocks, where at least one of the monomer units carries more than two of the respective functionalities.

This chapter puts a focus on porous polyimides synthesized from amine and dianhydride monomers. In principle, the applied synthesis methods following an A_n+B_m (with $n \geq 2$ and $m \geq 3$) reaction scheme are similar to those for conventional linear polyimides described above. However, there are certain requirements concerning the applied reaction conditions and the used dianhydride and amine monomer units. In order to avoid a collapse of the pores in the dry or non-solvated state, it is necessary to build up a cross-linked network possessing sufficient structural rigidity and stability. Therefore, in general, porous polyimides mainly consist of aromatic building blocks, due to the higher rigidity compared to their aliphatic counterparts.

The majority of the reported porous polyimide structures have been synthesized by following a one-step synthesis protocol introduced in the preceding paragraph. Similarly to the two-step synthesis, poly(amic acid) synthesis and imidization are carried out consecutively in high-boiling solvents. Due to the cross-linking mechanism of the three-

dimensional networks, an early agglomeration and precipitation of the polymers is more likely compared to linear polyimide chains if the synthesized polyimide does not exhibit sufficient solubility in the chosen solvent. Therefore, low total monomer concentration below 10% of weight is characteristic for the synthesis of porous polyimides, in order to avoid precipitation at low temperatures.

In the following paragraph, the synthesis procedures of selected literature reports will be discussed in detail in order to obtain a better understanding of the implementation of one-pot polyimide network synthesis. The experimental details within these reports form the basis for the synthesis of TPI polymer networks later in this thesis.

In a study by Weber *et al.* the porous polyimide PI1 has been synthesized from 2,2',7,7'-tetraamino-9,9'-spirobifluorene and PMDA by applying a *m*-cresol/isoquinoline solvent system in almost quantitative yield (Figure 5-19a).[362] Despite a relatively high monomer concentration of about 20 wt% and a moderate reaction time, the resulting networks exhibit specific BET surface areas of nearly 1000 m^2 g^{-1}.[362] The contorted structural motif of the spirobifluorene moiety and the rigidity of both monomer units prevent an effective dense packing of the polymer network and seem to promote the formation of large inner surfaces.[362]

Wang *et al.* synthesized two different porous polyimide polymers by linking PMDA (PI-1) and NTDA (PI-2) with tetrahedral-shaped TAPM combined in an A_4+B_2 reaction system (Figure 5-19b).[363] Again, the condensation has been performed as an isoquinoline-catalyzed one-step polymerization reaction in *m*-cresol. Low monomer concentrations and ice bath temperature provide the formation of poly(amic acid) chains at low reaction rates, while at the same time imidization is suppressed. The chosen conditions prevent a rapid gelation of the reaction mixture, which would decrease the mobility of residual unreacted end groups and, as a consequence, avoid an efficient cross-linking of the final polyimide network.[363] In the following the temperature has been increased very slowly in several consecutive heating steps. Both polyimide networks were obtained in quantitative yields showing very high specific BET surface areas.

Recently, Wang et al. reported four porous polyimide structures based on trigonal linking nodes.[365] The networks have been formed by combination of the amine monomers TAPB and TAPA with PMDA and NTDA by applying the *m*-cresol/isoquinoline solvent system (Figure 5-20). As already described for similar syntheses, the temperature during the reaction has been increased slowly in several consecutive steps to enable a proper orientation of the network structure. Although, the amorphous polyimide networks were obtained in quantitative yields, the specific BET surface areas between 232 cm^3 g^{-1} and 818 cm^3 g^{-1} do not reach the values reported for comparable materials containing tetrahedral nodes.[363]

An interesting synthesis concept has been reported by Farha *et al.* (Figure 5-21).[366] The porous polyimide network introduced in this study was synthesized from the same starting materials, namely TAPM and NTDA, as the network polymer PI-2 by Wang *et al.*, which has already been described above.[363] However, the two synthesis protocols differ significantly from each other in some points. Farha *et al.* used a mixture of DMF and propionic acid as solvent in a one-pot reaction to obtain a porous polyimide network, where the reaction temperature was kept constantly at 170 °C throughout the entire reaction process. Although the absolute yields have not been stated, the authors suggest a complete conversion due to the absence of amine signals in the respective infrared spectra.[366] It is worth mentioning that the condensed water has obviously not been removed from the reaction vessel, as the reaction has been carried out under reflux conditions. However, the obtained specific BET surface area of the final polyimide (750 m^2 g^{-1}) calculated from the nitrogen adsorption isotherm is by far lower than the surface area of the structurally similar PI-2 (1407 m^2 g^{-1}) by Wang *et al.*[363,366]

Recently, Rao *et al.* presented two porous polyimide networks containing the uncommon 3,4,9,10-perylene diimide linker (Figure 5-22).[368] The difference between the described polyimide networks Tr-PPI and Td-PPI lies in the applied amine building blocks. The network material Tr-PPI has been synthesized by a condensation reaction from 3,4,9,10-perylenetetracarboxylic acid dianhydride and the trigonal TAPA, while the tetragonal TAPM has been used in the synthesis of Td-PPI. Both materials were synthesized in a solvent mixture of DMAc and imidazole in quantitative yields. Due to the high melting point of imidazole, the amine compounds have been added at temperatures above 150 °C. Tr-PPI and Td-PPI exhibit specific BET surfaces of 400 m^2 g^{-1} and 2213 m^2 g^{-1}, respectively.

6.4.3 Preparation of Monomer Units for the Synthesis of Triazine-based Polyimides

For the synthesis of polyimides by polycondensation, an equimolar amount of amine and anhydride groups is essential for a high molecular weight and, in case of porous polymers, for an efficient cross-linking. Additionally, as described above, the presence of impurities could easily lead to undesired side or chain termination reactions. Therefore, it is important to apply starting materials of high purity in these polycondensation reactions.

The synthesis concepts of porous polyimides discussed in this thesis are based on polyimide formation between bifunctionalized dianhydrides on the one hand and amine building block carrying three amine functionalities on the other hand. While several

suitable dianhydride monomers are commercially available at moderate prices, the situation concerning the respective amines is different. Usually, the amine building blocks have to be synthesized in reactions involving several synthesis steps. Therefore, the development of efficient synthesis protocols to gain access to amine building blocks at reasonable efforts is important for the whole reaction process to be competitive. The work on this thesis involves the synthesis, purification and detailed characterization of amine and dianhydride monomers for the synthesis of TPIs.

6.4.3.1 Synthesis and Purification of Dianhydride Monomers

Nowadays, a large number of different aromatic dianhydrides can be purchased "off the shelf" from various chemical compound suppliers. However, dianhydrides have a tendency to hydrolyze very easily, and therefore, a purification of the dianhydride compounds prior to application in polycondensation reactions is highly recommended.
One of the most popular methods to purify anhydrides is sublimation at reduced pressure. However, during the work on this thesis, the purification of aromatic dianhydrides by sublimation has not been effective in all cases. Only 3,3',4,4'-benzophenonetetrcarboxylic dianhydride, NTDA and 4,4'-(hexafluoroisopropylidene)diphthalic anhydride (HIDA) can be obtained in sufficient amounts within a reasonable time frame.

The dehydration of at least partly hydrolyzed dianhydride monomers in acetic anhydride turned out to be a more effective way to obtain pure dianhydrides in sufficient purity. Exemplarily, the dehydration of 1,2,4,5-benzenetetracarboxylic acid at elevated temperatures in acetic anhydride to yield PMDA is illustrated in Figure 6-26.

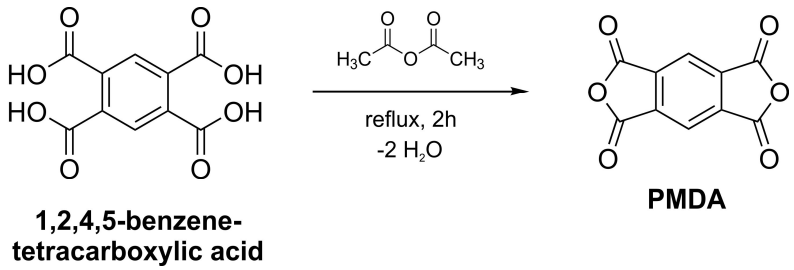

Figure 6-26: *Synthesis of PMDA by dehydration of 1,2,4,5-benzenetetracarboxylic acid in acetic anhydride.*

Acetic anhydride is able to promote the intramolecular cyclization to aromatic anhydride by reacting with leaving water molecules to acetic acid. The formation of acetic acid is not reversible under the given reaction conditions. It is worth noting that all dianhydrides used for the synthesis of TPI polymers have been purified by applying this method in quantitative yield (see experimental section).

6.4.3.2 Synthesis of 1,3,5-Tris(*p*-aminophenyl)benzene

The triamine 1,3,5-tris(*p*-aminophenyl)benzene (TAPB) has been applied in several studies as triangular building unit for the synthesis of porous polyimide structures.[232,365,372] Among the published reports, the synthesis of TAPB from *p*-aminoacetophenone catalyzed by *p*-toluenesulfonic acid yielded good results.[449] According to literature, TAPB has been obtained in one-pot reaction from *p*-aminoacetophenone in neat *p*-toluenesulfonic acid at an isolated yield of 71%.[449] However, when performing the reaction under similar reaction conditions for this thesis, only yields of isolated TAPB around 20% could be achieved. Gattuso *et al.* also confirm a deviation to the yields reported by Zhao *et al.*[449,450]

The synthesis pathway reported by Bao *et al.* should also provide TAPB in acceptable yields and high purity.[451] The synthesis of TAPB during the work on this thesis confirmed the findings in the respective literature report.[451] First, the central benzene ring is formed by acid-catalyzed cyclotrimerization of *p*-nitroacetophenone using $SiCl_4$.[452,453] The yielded 1,3,5-tris(*p*-nitrophenyl)benzene has been directly used for the next reaction step without further purification. After catalytic reduction of the nitro groups by treatment with hydrazine monohydrate and Pd/C the monomer TAPB can be obtained after recrystallization at a yield of 64%.

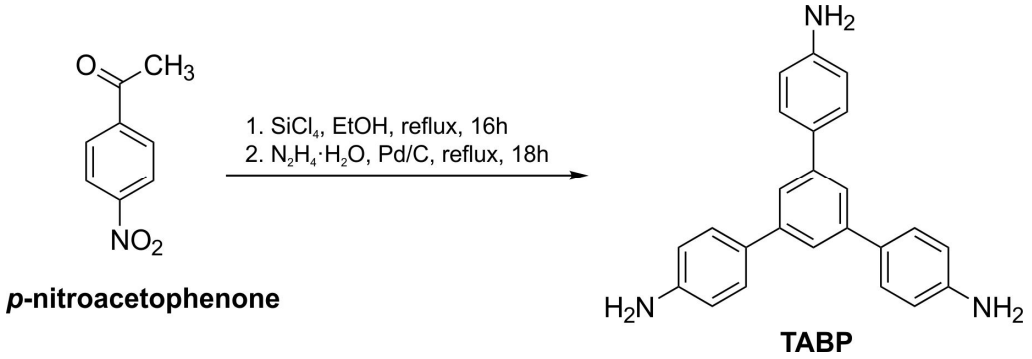

Figure 6-27: *Synthesis of TAPB according to Bao* et al.[451]

Elmorsy *et al.* claimed that the described cyclization reaction can be conducted by applying substituted acetophenone derivatives carrying either electron donating or electron withdrawing groups.[454] However, attempts to synthesize TAPB directly from *p*-amino-acetophenone in reasonable yields during the work on this thesis have not been successful.

6.4.3.3 Synthesis of Tris(*p*-aminophenyl)amine

One of the monomers for disordered, amorphous polyimide networks is the triamine tris(*p*-aminophenyl)amine (TAPA).[365,368,372] Due to the free electron pair situated in the sp^3-orbital of the central nitrogen atom its molecular structure does not exhibit a planar triangular, but a pyramidal geometry.[365,368] However, the amount of energy required to

invert the pyramidal geometry is regarded as relatively low.[455] Thus, the occurring nitrogen inversion provides an increased flexibility in the structure of the final polymer networks which might influence the rigidity of the network structure and facilitate an at least partial collapse of pores.

During the lab work on this thesis, the synthesis of TAPA has been performed in two steps. In the first step the precursor molecule *N,N*-bis(*p*-nitrophenyl)-1,4-phenylenediamine has been synthesized in high yields of about 90% by K_2CO_3-catalyzed S_NAr reaction between 1,4-phenylenediamine and *p*-fluoronitrobenzene in DMSO according to Gattuso *et al.* (Figure 6-28).[450]

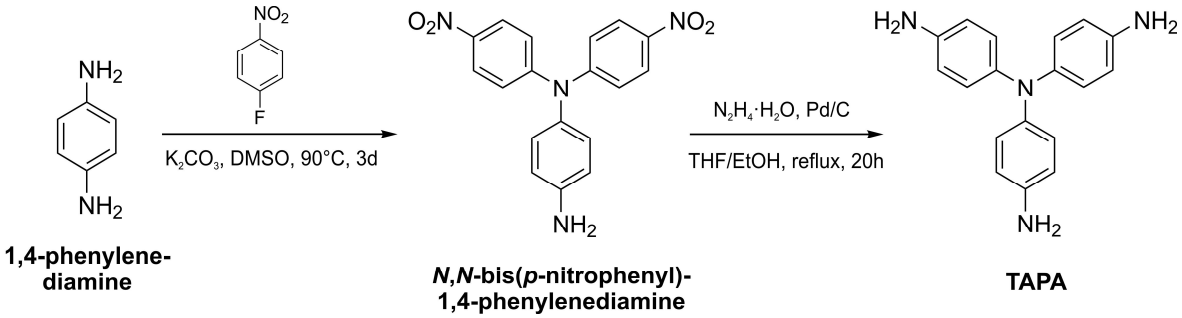

Figure 6-28: *Synthesis of TAPA according to Gattuso* et al.[450]

The reaction is catalyzed by K_2CO_3, as the nucleophilicity of aromatic amines would not be sufficient to perform a nucleophilic attack. A possible mechanism for the activation process has been suggested by Gorvin, where the formation of hydrogen-bonds between carbonate and amine group should increase the nucleophilicity of the amine significantly (Figure 6-29).[456] According to the report, diarylamines were expected to be even more reactive due to the formation of nitranions after deprotonation.[456]

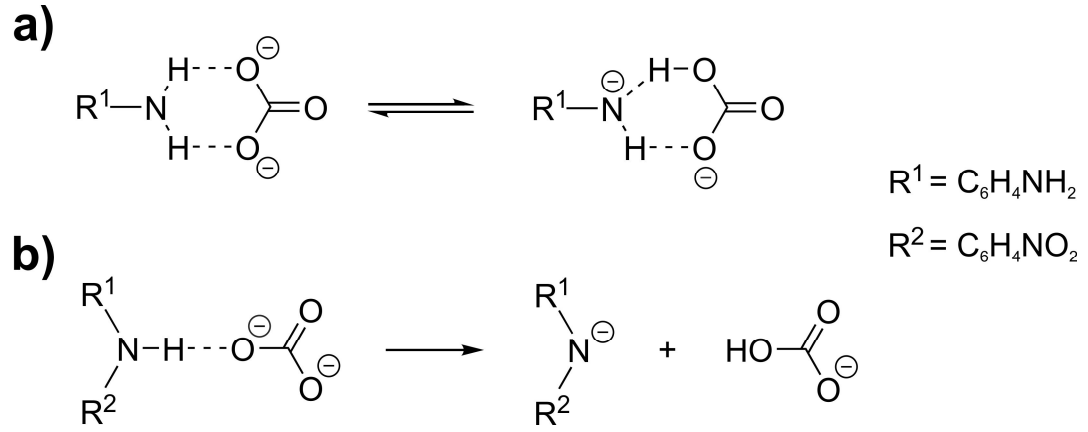

Figure 6-29: *Suggested activation mechanism of a) primary and b) secondary arylamine groups in presence of carbonate anions.*[450,456]

Furthermore, the negative charge occurring after the nucleophilic attack is stabilized by delocalization in the aromatic system and the electron-withdrawing effect of the nitro group in *para*-position. The energetically favored rearomatization of the phenyl ring facilitates an elimination of the fluoride anion and the subsequent formation of potassium fluoride.
In a second step TAPA has been obtained by hydrazine-mediated catalytic reduction of *N,N*-bis(*p*-nitrophenyl)-1,4-phenylenediamine in satisfactory yields of 20%. However, the high yields reported by Gattuso *et al.* and Rao *et al.* for this synthesis have not been reached.[368,450]

6.4.3.4 Synthesis of 2,4,6-Tris(*p*-aminophenyl)-1,3,5-triazine

Compared to the triangular amines TAPB and TAPA, the precursor molecule 2,4,6-tris(*p*-aminophenyl)-1,3,5-triazine (TAPT) is rarely used for the synthesis of porous network materials.[240,248] In contrast to the contorted phenyl units in TAPB the aromatic rings in TAPT are arranged in one plane due to the absence of hydrogen atoms in at the central ring (see section 6.5). Recently, a study by Ren *et al.* revealed a significantly higher CO_2 sorption capacity of porous polymer networks linked by triazine moieties compared to similar network materials linked by phenyl units.[50] The reason for the increased CO_2 sorption capacity might be dedicated to the Lewis-basic nature of the triazine ring having a higher affinity towards the acidic CO_2 compared to the analogous phenyl unit.

The synthesis of TAPT has been conducted starting with an acid-catalyzed cyclotrimerization of *p*-bromobenzonitrile in dry chloroform (Figure 6-30).[50,457,458] The intermediate molecule 2,4,6-tris(*p*-bromophenyl)triazine (TBPT) could be obtained from a one-pot reaction at reasonable yields. A scale-up of the reaction did not affect the yield significantly. It is worth noting that the attempt to obtain sufficient ^{13}C-NMR data for TBPT has been successful in bromobenzene-d_5 at 353 K.

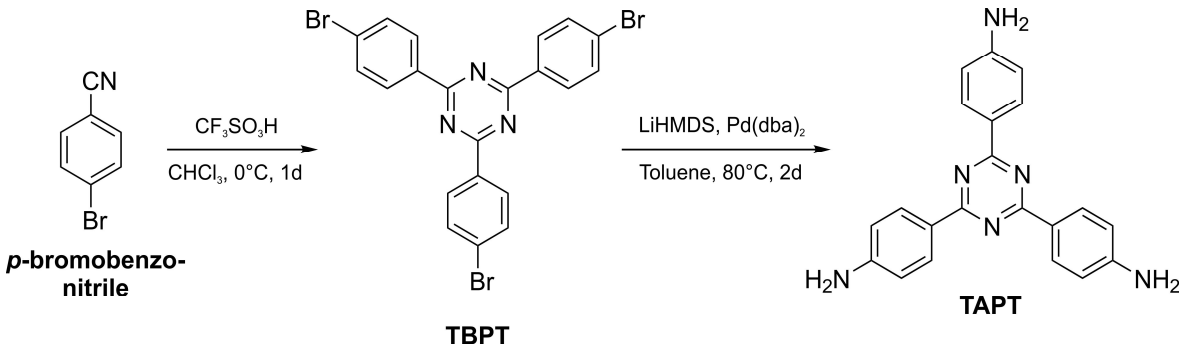

Figure 6-30: *Synthesis of TAPT according to Ishi-i* et al.[459]

To the best of the author`s knowledge, it has been the first report of ^{13}C-NMR data of TBPT to date. The following amination of TBPT has been performed by using a method developed by Ishi-i *et al*. (Figure 6-30).[459] The C-N bond is formed through a metal-catalyzed reaction between aryl bromide and lithium bis(trimethylsilyl)amide (LiHMDS). The active Pd-catalyst in this reaction is formed *in situ* from $Pd(dba)_2$ and $P(t\text{-}Bu)_3$.[460]
The resulting structure TAPT has been synthesized at an isolated yield of about 58%. The compound has been applied as amine monomer in the syntheses of all TPI polymers presented in the next paragraph.

6.4.4 Synthesis and Characterization of Triazine-based Polyimides

6.4.4.1 Synthesis of Triazine-based Polyimides

The synthesis of porous triazine-based polyimides (TPIs) in the scope of this thesis has generally been performed in a one-step reaction by coupling the precursor molecule TAPT with various functionalized aromatic tetracarboxylic acid dianhydride monomers. The general synthesis route is illustrated in Figure 6-31.

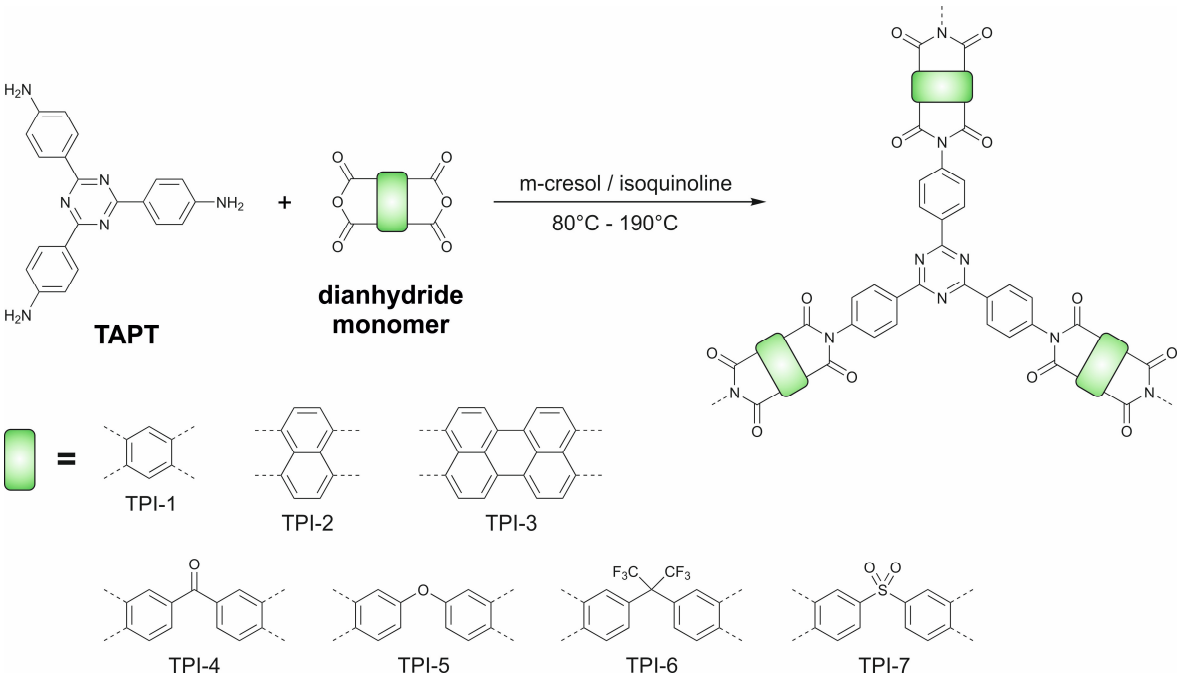

Figure 6-31: *Synthesis route for TPI polymer networks.*

The polymerization reaction is carried out in an *m*-cresol/isoquinoline solvent system in order to enable high reaction temperatures combined with a sufficient solubility of the different reaction compounds to avoid premature precipitation.
In the initial step of the synthesis the respective dianhydride monomer is added to a solution of TAPT in *m*-cresol. Typical for step growth polymerization the stochiometry of the reacting groups considerably influences the molecular weight of the product polymer. As an A_3+B_2 type polycondensation the molar ratio of TAPT and the respective dianhydride monomers has been set to 1:1.5 to provide an equal amount of amine and anhydride groups in the reaction mixture.
Additionally, the solubility of the starting materials in *m*-cresol is critical for the degree of cross-linking and thus for the porosity of the final polymer. If the monomer concentration in the initial stage of the reaction is too high, rapid gelation of the reaction mixture occurs and leads to an incomplete condensation with dramatically reduced specific surface area and gas uptake capacity of the resulting polymer.
An explanation for the drastic influence on the porosity of the TPI networks might be the decreased mobility of TPI oligomers in the gel phase that “freezes” the reaction mixture at an early stage and, in consequence, prevents the formation of cross-linked networks due to incomplete polymerization. Therefore, the total mass fractions of starting materials in *m*-cresol have been adjusted between 1.0 and 5.0 wt% depending on the solubility of the applied dianhydride in the solvent.

The formation of the poly(amic acid) intermediate and the following imidization are carried out in one step by slowly increasing the reaction temperature from 0 °C to 190 °C in several consecutive steps.
The slow temperature increase facilitates kinetic control over the condensation reaction and is also crucial for an efficient cross-linking in the TPI networks. Higher starting temperatures or increased heating rates again could lead to rapid gelation of the reaction mixture and prevent the formation of cross-linked porous networks. A more detailed description of TPI synthesis procedures is given in the experimental section.
When five-membered polyimide rings are formed the reaction mixture darkens at elevated temperatures above 120 °C and an increase of the viscosity can be observed. During the synthesis of TPI-2 and TPI-3, however, the viscosity only slightly increases at reaction temperatures of about 160 °C. This divergent behavior might be ascribed to the lower reactivity of six membered anhydride rings. The condensation reaction is completed by maintaining a temperature of 190 °C for several hours where the crude polyimide materials precipitate in the reaction solution..
After purification all TPI polymer networks appear as fluffy powders which are insoluble in water and common organic solvents (Table 6).

Table 6: *Observed colors and yields of TPI polymers after purification.*

network	color	yield [%]
TPI-1	yellowish	94%
TPI-2	brown	92%
TPI-3	dark red	83%
TPI-4	yellowish	87%
TPI-5	off-white	86%
TPI-6	off-white	88%
TPI-7	off-white	81%

6.4.4.2 Characterization of Triazine-based Polyimides

The synthesized TPI polymers have been characterized by different methods including infrared spectroscopy, MAS NMR spectroscopy, XRD, SEM, elemental analysis and TGA. The infrared spectra of the seven synthesized TPI polymers are displayed in Figure 6-32. The characteristic absorption bands of the symmetric and asymmetric vibrations of the imide carbonyl groups could be found at 1725 cm^{-1} and 1785 cm^{-1} for five-membered and at 1665 cm^{-1} and 1710 cm^{-1} for six-membered polyimide rings, respectively.

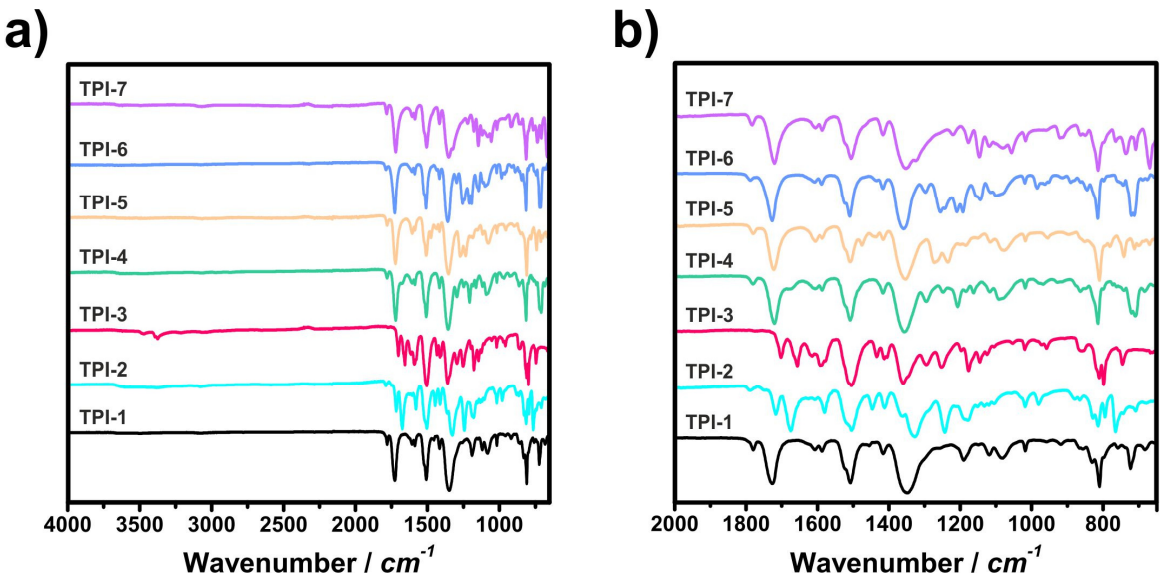

Figure 6-32: *Infrared spectra of TPI polymers at a) full frequency range and b) enlarged frequency range between 650 and 2000 cm^{-1}.*

The broad band in the region between 1350 cm^{-1} and 1360 cm^{-1} results from an overlap of the C-N-C stretching vibration of the imide ring and the in-plane stretching vibration of the triazine ring. The characteristic absorption signal at about 1500 cm^{-1} confirms the

successful formation of the triazine ring in all TPI polymer structures. The absence of characteristic anhydride and poly(amic acid) absorption bands at 1860 cm^{-1} and 1650 cm^{-1} indicate complete imidization for TPI polymers containing five-membered imide rings. Similarly, the signal of the six-membered anhydride ring expected at 1780 cm^{-1} cannot be found in the infrared spectra of TPI-2 and TPI-3. However, the spectrum of TPI-3 contains a weak absorption band 3380 cm^{-1} which is assigned to a small amount of unreacted amine groups in the polymer structure. The SO_2 groups in TPI-7 are clearly identified by the absorption bands of its characteristic symmetric and asymmetric stretching vibration at 1320 cm^{-1} and 1147 cm^{-1}.

The structures of the seven TPI polymers have been characterized by ^{13}C CP MAS NMR spectroscopy (Figure 6-33). A detailed assignment for all ^{13}C signals for all TPI polymers could be found in chapter 8.5 in the appendix section. The characteristic signal of the triazine ring is clearly identified for all TPI polymers at about 170 ppm.[50,202] The successful imidization in all polymer networks is confirmed by the peaks in the range between 162 ppm and 166 ppm referring to the carbon atoms within the five and six-membered imide rings (*Cf*).[365,368]

The aromatic carbon atoms in the polymeric TPI structures show different chemical shifts with signals ranging from 120-140 ppm. Due to the polymeric and disordered structure of the TPI networks a considerable broadening of the NMR signals can be observed. The broadening causes a heavy overlap of the different NMR signals and hampers their assignment significantly.

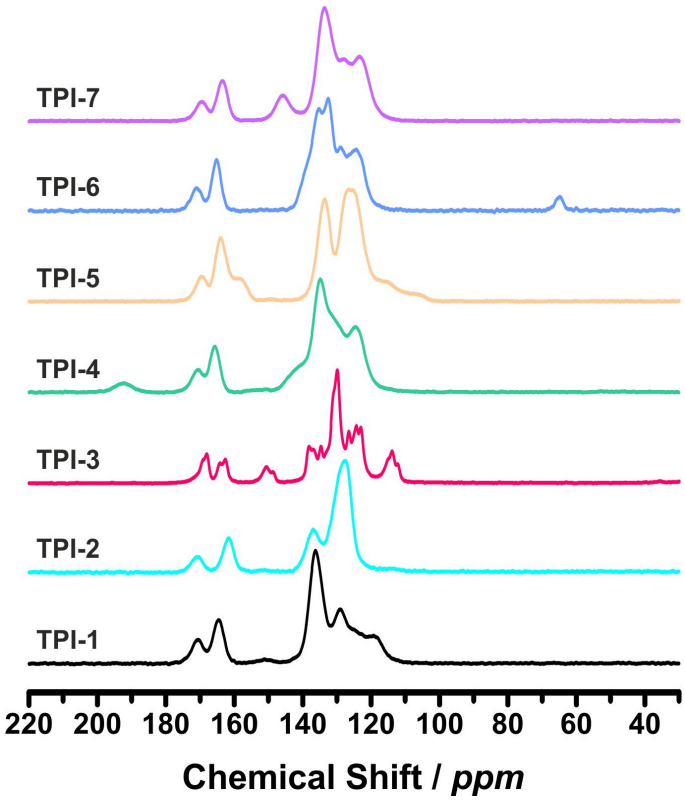

***Figure 6-33**: ^{13}C CP MAS NMR of TPI polymer networks.*

Following the results obtained from IR spectroscopy, a small amount of unreacted amino groups are present in the NMR spectrum of TPI-3. The two signals at 151 ppm and 114 ppm are ascribed to the carbon atom carrying the amino group (C_q) and the adjacent carbon atom in the aromatic ring (C_p), respectively.
The carbonyl group peak in TPI-4 (C_n) is found at 192 ppm, whereas the neighboring carbon atom (C_j) is described by a broad signal at about 141 ppm.
The characteristic resonance at 159 ppm in the spectrum of TPI-5 at about 159 ppm (C_j) identifies the quaternary aromatic carbon atom next to the bridging oxygen atom.
Analogously, for network TPI-7 the peak of the carbon atom next to the bridging sulfone group (C_j) is found at 146 ppm. The bridging aromatic carbon atom (C_n) in TPI-6 carrying two trifluoromethyl moieties is observed at 65 ppm.

As expected from the non-reversible reaction mechanism of polyimide synthesis, XRD measurements do not detect any long range order in TPI polymer networks (see appendix section 8.6). The non-planar nature of the imide linkages most likely prevents long-range order in the network structure.
Additionally, SEM imaging displays highly aggregated platelet-like particles with sizes up to several micrometers (see appendix section 8.12). The images additionally show void spaces of different sizes which would be consistent with the presence of a hierarchical pore system throughout the TPI networks.

Elemental analysis in general yields matching values for calculated and measured CHN contents in almost all TPI samples (see experimental section). Only elemental analysis of TPI-3 reveals a significant difference between the calculated and actually measured C/N ratio. The decreased carbon and increased nitrogen content in the TPI-3 sample can be explained with the presence of a relevant amount of terminal unreacted TAPT moieties in the polymeric structure. The increased hydrogen content in some TPI samples might result from adsorbed water on the surface and in the pores of the networks.

The thermal stability in air is an essential factor when evaluating the applicability of potential sorbent materials for post-combustion CO_2 capture. Thermogravimetric analysis data for TPI polymers are illustrated in Figure 6-34. The decomposition temperatures T_{dec} for each polymer were determined at 10% mass loss under air and are summarized in Table **7**. Therein, the porous networks TPI-2 and TPI-7 possess the highest decomposition temperatures at 456 °C and 450 °C, respectively. The values are in agreement with the exceptionally high thermal stability of conventional polyimide polymers.[444,461,462] The significantly lower decomposition temperature of TPI-3 is attributed to the lower degree of cross-linking in the polymer structure.

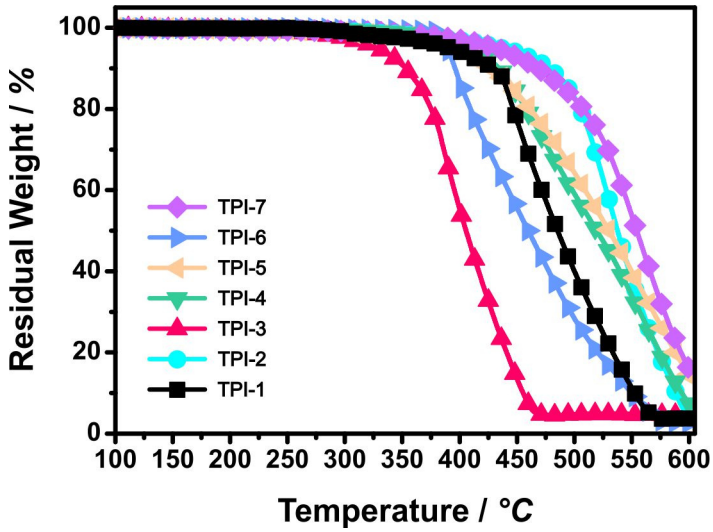

Figure 6-34: *Plot from thermographic analysis of TPI polymers under air.*

Nonetheless, thermogravimetric analysis confirms that the thermal decomposition of TPI polymer networks initiates far above the temperature operating window for postcombustion CO_2 sorption applications. Therefore, the applicability of TPIs for such applications with reference to thermal stability is valid.

Table 7: *Temperatures at 10% decomposition of TPI polymers under air.*

material	T_{dec} (°C)	material	T_{dec} (°C)
TPI-1	419	TPI-5	421
TPI-2	456	TPI-6	396
TPI-3	342	TPI-7	450
TPI-4	427		

6.4.5 Gas Adsorption Properties of TPI Polymers

The porous structure of TPI polymer networks has been analyzed by argon and carbon dioxide sorption measurements. The argon sorption isotherms TPI-1, TPI-2 and TPI-6 show a rapid argon uptake at low relative pressures ($p/p_0 > 0.1$) typical for microporous materials. However, these isotherms do not follow the typical shape of a type-I isotherm according to IUPAC classifications (see chapter 5.4.4).[59]

For all argon adsorption isotherms of TPI polymers, except TPI-7, a large hysteresis loop down to low relative pressures have been observed (Figure 6-35a). The hysteresis has been reported for disordered porous organic network materials and could be ascribed to a

swelling of the network structure.[121,201,362,392] During desorption phase argon molecules are trapped in the swollen network structure leading to a delayed desorption from the sorbent surface and cavities. Alternatively, the occurring hysteresis might also be explained by the presence of a so-called "throat and cavity" type microporosity known from activated carbons.[463] The isotherms of the polymers TPI-3, TPI-4 and TPI-5 show a similar hysteresis, however, the gas uptake at the initial stage is significantly reduced indicating a decreased amount of micropores in the respective network structure.

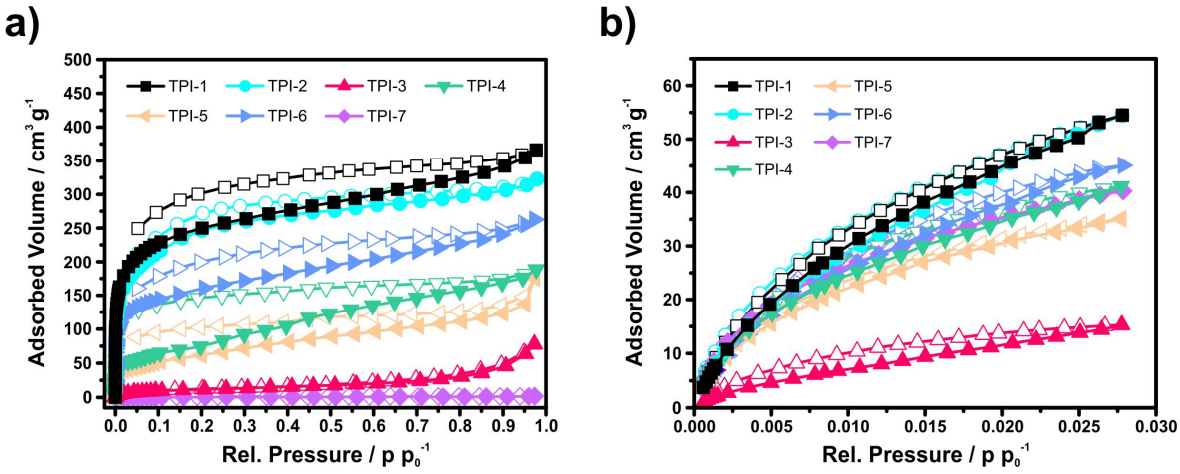

Figure 6-35: *a) Argon and b) CO_2 sorption isotherms of TPI polymer networks measured at 87 K (Ar) and 273 K (CO_2). Adsorption isotherms are illustrated with solid symbols, desorption isotherms are illustrated with open symbols.*

The specific surface areas of TPI networks have been determined from the respective argon and CO_2 sorption isotherms by the BET method and, for comparison, by applying DFT models (Table 8). The BET equivalent specific surface area of each polymer network has been calculated from a linear region in the BET-plot of the argon sorption isotherm according to the requirements for microporous materials, the so-called consistency criterion (see section 5.4.5).[395,397,398]

The networks TPI-1 and TPI-2 exhibit the largest specific BET equivalent surface areas of 809 $m^2\ g^{-1}$ and 796 $m^2\ g^{-1}$, respectively. These values are the highest BET equivalent surface areas of all TPI polymers within this thesis. The specific BET surface areas of TPI-4, TPI-5 and TPI-6 are slightly lower most likely due to the higher flexibility of single bonds in the respective linkers that could lead to a collapse of the pores and reduce the surface area accessible to argon. Nonetheless, TPI-6 still reaches a specific BET equivalent surface area of 510 $m^2\ g^{-1}$. The values of the specific BET surface areas of TPI polymers are in line with those reported for other porous polyimide networks.[49,362,365,366] However, they do not reach the surface areas of Td-PPI (2213 $m^2\ g^{-1}$), PI-1 (1407 $m^2\ g^{-1}$) and MPI-1 (1454 $m^2\ g^{-1}$) which are under the highest reported to date.[363,368,372]

Additionally, the specific surface areas of TPI networks have been calculated from argon (87 K) and CO_2 (273 K) sorption isotherms of all seven TPI networks by applying DFT methods. For DFT surface area and pore structure calculations from argon sorption isotherms the QSDFT kernel has been chosen due to a better performance at inhomogeneous sorbent surfaces compared to a similar NLDFT kernel (for details see section 5.4.6). The QSDFT calculations from argon sorption isotherms have been performed by using the QSDFT equilibrium model assuming slit pores integrated in the Quantachrome ASiQ software package.

Table 8: *Specific surface areas of TPI polymers calculated from Ar (87 K) and CO_2 (273 K) sorption isotherms.*

material	S_{BET} ($m^2\ g^{-1}$)	$S_{DFT,Ar}$ [a] ($m^2\ g^{-1}$)	$S_{DFT,CO2}$ [b] ($m^2\ g^{-1}$)
TPI-1	809	828	573
TPI-2	796	765	558
TPI-3	40	32	147
TPI-4	245	236	419
TPI-5	201	191	326
TPI-6	510	623	437
TPI-7	< 10	< 10	425

[a] from Ar sorption isotherms measured at 87 K assuming slit-pore QSDFT model on carbon, [b] from CO_2 sorption isotherms measured at 273 K assuming NLDFT model on carbon.

In order to avoid possible swelling effects on the calculation only the adsorption branch of the respective argon sorption isotherms has been taken into account. The specific surface areas $S_{DFT,Ar}$ of TPIs calculated from their respective adsorption isotherms are shown in Table 8. In all cases the values are comparable with the determined BET equivalent surface areas.

The specific surface areas calculated from CO_2 sorption isotherms (Figure 6-35b) are illustrated in Table 8. However, they deliver quite different values compared to the argon sorption measurements. The reduced specific surface areas of TPI-1, TPI-2 and TPI-6 can be ascribed to the upper sensitivity limit of CO_2 measurements, where only pores with maximum diameter of 1 nm are considered in the calculation of $S_{CO2,DFT}$.
The CO_2 sorption isotherms of TPI-4, TPI-5 and TPI-7 yield significantly larger specific surface areas $S_{DFT,CO2}$ than the corresponding values from argon sorption $S_{DFT,Ar}$. One reason might be the increased temperature (273 K) during CO_2 sorption measurements. The higher temperature increases the flexibility of the networks and increases the kinetic energy of the probing gas molecules. Both effects might lead to a higher accessible surface

area in the porous structures and, in consequence, to a higher specific surface area. Compared to the other polymer networks TPI-3 shows a significantly decreased gas uptake at both sorption experiments for argon and CO_2. The reduced gas uptake could be explained by insufficient cross-linking in the polymer structure with almost no formation of rigid and stable micropores.

The determination of the pore volume and the PSD are an essential part in the characterization of porous materials. Both parameters give information on the composition of the pore structure of a certain material regarding the inner volume and the dominating sizes of the present pores. At postcombustion conditions the micropore volume could have a crucial influence on total gas uptakes of a sorbent material, even dominating the influence of surface area and total pore volume.[143]
The pore volumes of TPI polymers have been determined from CO_2 and argon sorption isotherms by applying DFT methods (Table 9). Additionally, micropore and total pore volume, $V_{Ar,mic}$ and $V_{Ar,tot}$, have been calculated conventionally from the adsorbed argon volumes by assuming that the density of the adsorbed argon phase is equal to the density of liquid bulk argon. The ratio of $V_{mic,DFT}$ over $V_{tot,DFT}$ has been added as an indicator of the degree of microporosity in the respective TPI polymer.

Table 9: *Calculated pore volumes of TPI polymer networks.*

material	$V_{Ar,mic}$ ($cm^3\ g^{-1}$)[a]	$V_{Ar,mic,DFT}$ ($cm^3\ g^{-1}$)[b]	$V_{Ar,tot}$ ($cm^3\ g^{-1}$)[c]	$V_{Ar,tot,DFT}$ ($cm^3\ g^{-1}$)[d]	$V_{CO2,DFT}$ ($cm^3\ g^{-1}$)[e]	$V_{Ar,mic,DFT}$ / $V_{Ar,tot,DFT}$
TPI-1	0.31	0.31	0.45	0.43	0.15	0.64
TPI-2	0.30	0.31	0.40	0.38	0.15	0.70
TPI-3	-	-	-	-	0.04	-
TPI-4	0.08	0.06	0.22	0.22	0.11	0.41
TPI-5	0.07	0.07	0.17	0.18	0.08	0.41
TPI-6	0.19	0.19	0.32	0.31	0.11	0.59
TPI-7	-	-	-	-	0.11	-

[a] micropore volume calculated at relative pressure $p/p_0 = 0.15$; [b] pore volume of pores with diameters below 2 nm calculated from Ar sorption isotherm at 87 K using QSDFT model; [c] total pore volume calculated at relative pressure $p/p_0 = 0.95$; [d] total pore volume calculated from Ar sorption isotherm at 87 K using QSDFT model; [e] total pore volume of pores with diameters below 1 nm from CO_2 sorption isotherm at 273 K using NLDFT model.

The non-functionalized networks TPI-1 and TPI-2 exhibit the highest total pore volumes derived from argon sorption isotherms (Table 9). For TPI-1 the total pore volume determination yielded 0.45 $cm^3\ g^{-1}$ from single point ($p/p_0 = 0.95$) and 0.43 $cm^3\ g^{-1}$ from QSDFT evaluation. For TPI-2, the respective values are 0.40 $cm^3\ g^{-1}$ (single point) and 0.38 $cm^3\ g^{-1}$ (QSDFT). The more flexible and functionalized polymers TPI-4, TPI-5 and

TPI-6 show considerably lower pore volumes. It should be mentioned, that the pore volume calculations from argon sorption isotherms yield comparable results for both methods. The networks TPI-3 and TPI-7 adsorbed too low amounts of argon to be calculated. The materials TPI-1 and TPI-2 show a high degree of microporosity where 64% of the total pore volume could be assigned to micropores and also TPI-6 reaches a good value of 59%. The fraction of micropores in TPI-4 and TPI-5 with 41% of the total pore volume is slightly lower.

The pore volume calculations obtained from CO_2 sorption isotherms deliver slightly different results. Similar to argon sorption measurements TPI-1 and TPI-2 possess the largest pore volumes of 0.15 $cm^3\ g^{-1}$ of all TPIs. The clear deviation from the pore volumes obtained from argon sorption can be ascribed to the upper sensitivity limit for pore characterization from CO_2 sorption measurements.[379,382] Pore volume calculation from CO_2 sorption isotherms only include pores with a maximum diameter of 1 nm. At ambient pressures larger pores are above the upper sensitivity limit and are not included (see section 5.4.3).[379,382] Contrary to the behavior of TPI-1 and TPI-2, the pore volumes $V_{DFT,CO2}$ for TPI-4 and TPI-5 are slightly higher than the respective pore volumes from argon sorption. This could be explained by a better accessibility of small micropores to CO_2 molecules compared to argon molecules.

The pore size distributions of TPI-1, TPI-2 and TPI-6 determined from argon sorption isotherms show a dominating fraction of pores with pore sizes in the micropore region (Figure 6-36a). For TPI-1 and TPI-6 the main fraction of pores is even smaller than 1 nm. The networks TPI-4 and TPI-5 have a considerable amount of pores in the micropore and in the mesopore region. These observations are consistent with the slightly decreased inner surface areas and the lower micropore volume of TPI-4 and TPI-5 compared to the materials TPI-1, TPI-2 and TPI-6. The PSDs of TPI-3 and TPI-7 could not be evaluated due to an insufficient argon uptake during the sorption experiment.

Additional information about the composition of the different pore sizes in the pore systems of TPIs can be obtained from the pore size distributions from CO_2 sorption isotherms (Figure 6-36b). The slightly smaller kinetic diameter of the CO_2 molecule compared to argon combined with the higher kinetic energy of the probe molecules at 273 K might be beneficial when evaluating even small micropores of about 0.4 nm. However, similar to pore volume calculations the pore size distributions determined from CO_2 sorption isotherms only consider the pores with diameters below the upper sensitivity limit of 1 nm.[379,382]

The main fraction of pores of all TPIs except TPI-3 is located in the size range between 0.45 and 0.7 nm. The networks TPI-1, TPI-2 and TPI-6 additionally have a considerable amount of pores up to 0.85 nm. The PSDs of TPI-4, TPI-5 and TPI-7 reveal only minor amounts of pore with sizes larger than 0.7 nm.

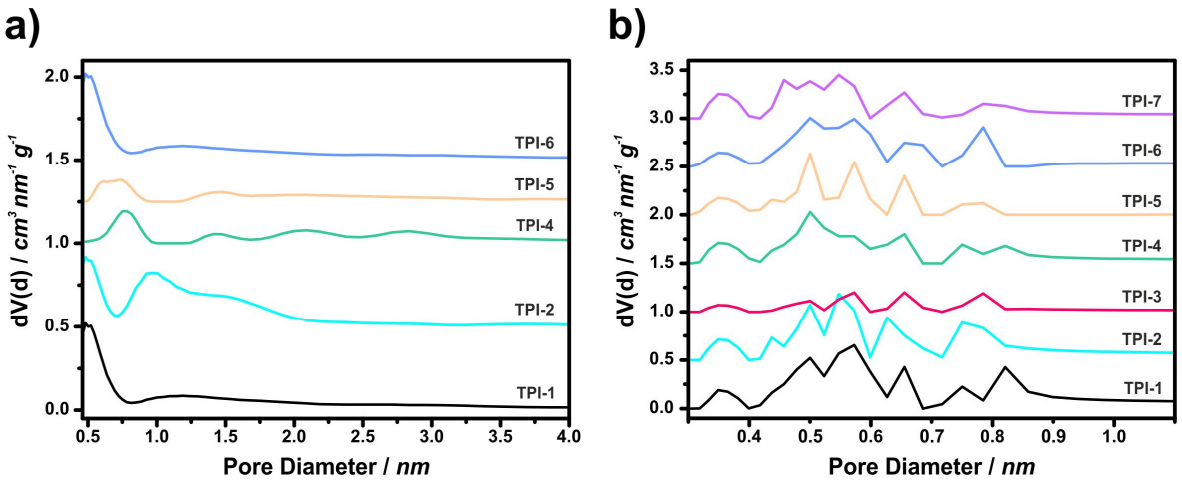

Figure 6-36: *a) Pore size distributions of TPI polymers derived from the respective argon sorption isotherms. The plots for TPI-2, TPI-4, TPI-5 and TPI-6 are shifted vertically by 0.5, 1.0, 1.25 and 1.5 cm^3 nm^{-1} g^{-1}, respectively; b) Pore size distributions of TPI polymers derived from the respective CO_2 sorption isotherms. The plots are shifted vertically in cumulative steps of 0.5 cm^3 nm^{-1} g^{-1}.*

6.4.6 Gas separation properties of TPI polymers

The synthesized TPI polymers have been investigated for their applicability as CO_2 sorbents under postcombustion conditions. Therefore, CO_2 sorption isotherms of all TPIs have been recorded at temperatures of 273 K, 298 K and 313 K at pressures up to 1 bar (Figure 6-37). In order to evaluate the selectivity for CO_2 over N_2 the nitrogen sorption properties of the TPI networks have also been determined at 298 K in the same pressure range. The obtained values for CO_2 uptakes at 273 K, 298 K and 313 K together with the N_2 uptakes at 298 K at an absolute pressure of 1 bar are summarized in Table 10.
The rigid non-functionalized networks TPI-1 and TPI-2 show the highest carbon dioxide uptakes of 2.45 mmol g^{-1} at a pressure of 1 bar and a temperature of 273 K. The functionalized networks TPI-4, TPI-5, TPI-6 and TPI-7 exhibit considerably lower CO_2 uptakes. Obviously, the higher degree of rigidity of TPI-1 and TPI-2 compared to the functionalized networks seems to be beneficial for the CO_2 uptake capacity. As expected, TPI-3 exhibits the lowest CO_2 uptake capacity of all TPIs at all three measured temperatures, most likely due to the incomplete formation of the porous network structure.

The CO_2 uptakes of TPIs at 273 K and 1 bar are also comparable to those reported for other porous sorbent materials like COFs (1.21-3.84 mmol g^{-1}),[160,273] BPL carbon (2.09 mmol g^{-1}),[273] PIs (1.00-1.41 mmol g^{-1}),[229] CMPs (1.60-2.05 mmol g^{-1}),[273,324] BLPs (1.68-2.91 mmol g^{-1}),[195] PAFs (2.05-3.48 mmol g^{-1}),[47] PECONFs (1.86-3.49 mmol g^{-1}),[19] MOPs (1.80-3.86 mmol g^{-1}),[273] and TCMPs (1.22-2.62 mmol g^{-1}).[50]

However, the porous materials with the highest CO_2 uptakes at pressures around 1 bar and a temperature of 273 K reported to date are ALPs (2.5-5.4 mmol g^{-1}),[351,352] BILPs (2.91-5.34 mmol g^{-1}),[342,343,348] STPs (3.67-4.14 mmol g^{-1}),[151] PPFs (2.09-6.07 mmol g^{-1})[243] and POFs (ca. 2.8-4.2 mmol g^{-1}).[146]

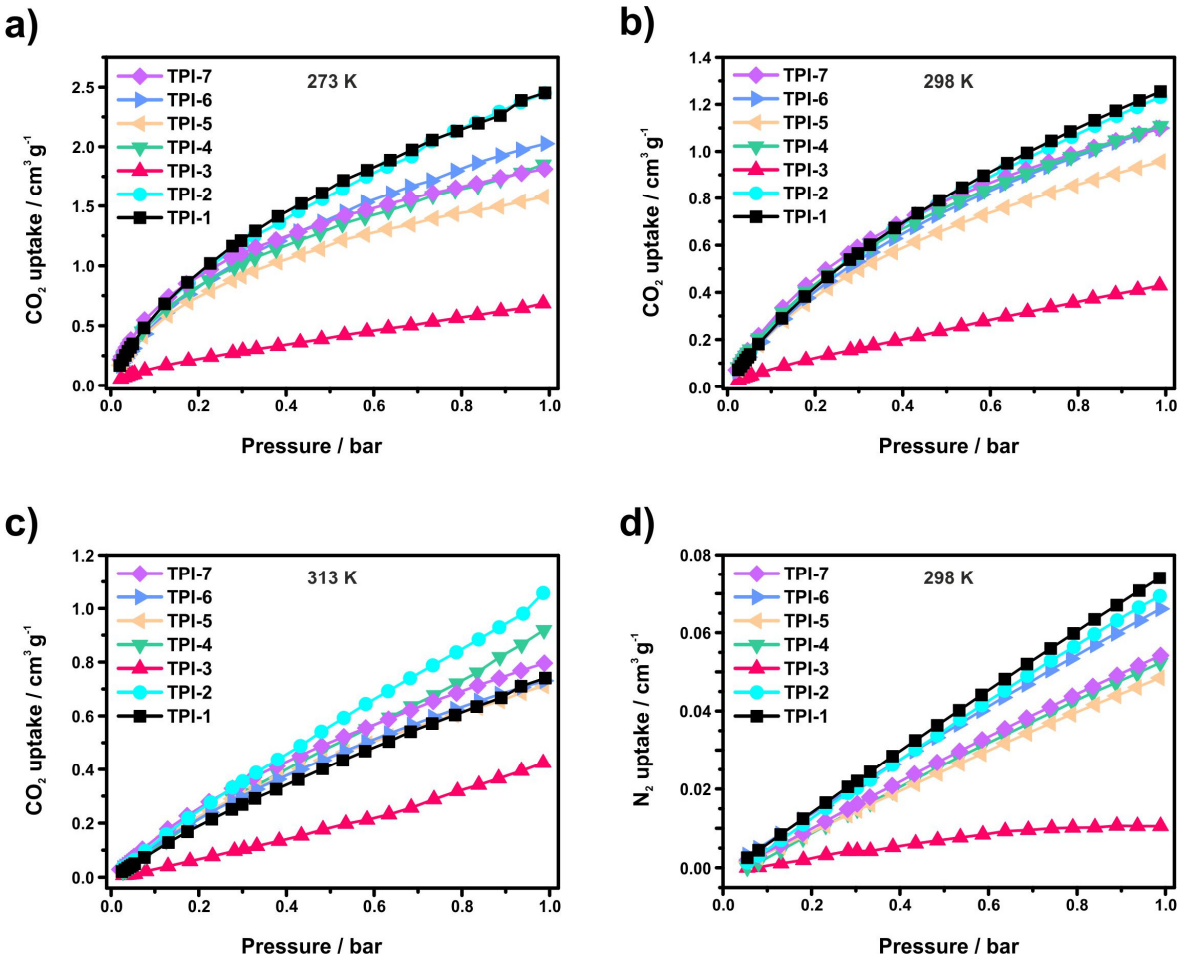

Figure 6-37: *CO_2 adsorption isotherms of TPI networks at a) 273 K, b) 298 K and c) 313 K. d) Nitrogen adsorption isotherms of TPI networks at 298 K.*

When regarding only porous triazine-based materials the highest CO_2 uptakes have been reported for *bipy*-CTFs (5.34 mmol g^{-1} and 5.58 mmol g^{-1}),[216] TBILP-2 (5.18 mmol g^{-1}),[344] FCTFs (4.67-5.53 mmol g^{-1})[217] and CTF-BIs (4.85 mmol g^{-1} and 4.93 mmol g^{-1} for CTF-BI-4 and CTF-BI-11).[219] The uptake capacities of TPI-1 and TPI-2 at 273 K and 1 bar are in the range of other porous triazine-based materials like PAF16 (1.88 mmol g^{-1})[208], PINs (1.06-1.80 mmol g^{-1}),[240] PI networks (0.06-1.66 mmol g^{-1}, 1.13 bar),[370] APOPs (2.27-4.45 mmol g^{-1}),[464] CTFs (0.94-4.22 mmol g^{-1}),[199,205,217] and MCTFs (2.25-3.16 mmol g^{-1}).[220] A comprehensive overview on the CO_2 sorption properties of several porous organic network materials could be found in the appendix section.

Table 10: *CO_2 and N_2 sorption data of TPI polymer networks including CO_2/N_2 sorption selectivity.*

material	CO_2 uptake[a]			N_2 uptake[a]	CO_2/N_2 selectivity	
	273 K	298 K	313 K	298 K	Henry	IAST
TPI-1	2.45	1.25	0.74	0.07	30.9	29
TPI-2	2.45	1.23	1.06	0.07	33.5	31
TPI-3	0.68	0.43	0.42	0.01	35.1	48
TPI-4	1.85	1.11	0.92	0.05	46.2	43
TPI-5	1.57	0.96	0.71	0.05	46.2	38
TPI-6	2.02	1.10	0.73	0.07	33.8	31
TPI-7	1.81	1.10	0.80	0.05	55.5	45

[a] in mmol g^{-1}

The CO_2 uptake capacity of TPIs strongly depends on the operating temperature during the gas sorption measurement. The CO_2 sorption capacity decreases significantly with increasing temperature, however, the relative loss in capacity differs between the TPI sorbent materials. While the loss in total CO_2 sorption capacity of TPI-1 and TPI-2 from 273 K to 298 K at a pressure of 1 bar has been determined at roughly 43%, the relative loss from 273 K to 313 K adds up to 50% for TPI-1 and even 65% for TPI-1. The lowest relative loss of in uptake capacity of about 19% from 273 K to 313 K at a pressure of 1 bar has been observed for TPI-5.

When regarding a potential application as flue gas sorbents the CO_2 uptake capacities at 313 K might be more meaningful compared to the respective values at 273 K. Additionally, in a real flue gas stream the occurring CO_2 is significantly diluted. Therefore, it might be helpful to consider the TPI CO_2 uptakes at partial pressures of 0.15 bar, which might be realistic for the partial pressure of CO_2 in a given flue gas stream. At a pressure of 1 bar the network TPI-2 shows the highest CO_2 uptake of 1.06 mmol g^{-1}, followed by TPI-4 (0.92 mmol g^{-1}) and TPI-7 (0.80 mmol g^{-1}). Interestingly, at a pressure of 0.15 bar and 313 K, the material TPI-7 shows the highest CO_2 uptake of 0.20 mmol g^{-1} and surpasses TPI-2 (0.19 mmol g^{-1}) and TPI-5 (0.18 mmol g^{-1}).

In general, the CO_2 uptake capacity of TPI polymers differs considerably depending on the given operation temperatures and pressures. A clear trend for this behavior could not be identified. For instance, the two TPIs with the highest uptakes at 273 K and 1 bar – both at 2.45 mmol g^{-1} – perform different at 313 K and 0.15 bar. While TPI-2 still adsorbs 0.19 mmol g^{-1} of CO_2 under the latter conditions, the respective uptake capacity of TPI-1 is reduced to only 0.14 mmol g^{-1}.

The interaction between the sorbent surface and the adsorbate gas plays an important role when evaluating the CO_2 uptake capacity of the TPI networks at low pressures. The strength of the interaction is characterized by regarding isosteric enthalpies of adsorption Q_{st}. For all TPI networks the isosteric enthalpies of adsorption have been determined from

the respective CO_2 sorption isotherms at 273 K, 298 K and 313 K (Figure 6-38). At low surface coverage, the networks TPI-1 (34.4 kJ mol^{-1}), TPI-4 (33.6 kJ mol^{-1}) and TPI-7 (32.4 kJ mol^{-1}) exhibit the highest enthalpies of adsorption among the TPIs. However, the enthalpies of TPI-2 (31.4 kJ mol^{-1}), TPI-5 (30.0 kJ mol^{-1}) and TPI-6 (29.2 kJ mol^{-1}) are only marginally lower. Only TPI-3 shows a steep decrease of the adsorption enthalpies starting from 32.8 kJ mol^{-1}. The determined isosteric enthalpies of adsorption of TPIs are characteristic for physisorptive interactions between sorbate and sorbent surface and are in line with a large number of other porous organic networks reported to date. The relatively high values might be ascribed to strong dipolar and quadrupolar interactions between the CO_2 molecules on the one side and the triazine rings and imide moieties within the networks on the other side.

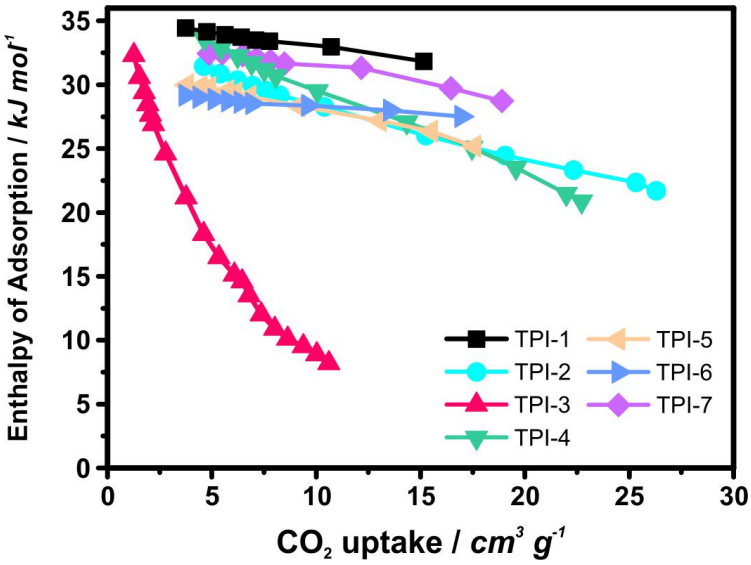

Figure 6-38: *Isosteric enthalpy of adsorption Q_{st} of TPI polymers from CO_2 sorption isotherms at 273 K, 298 K and 313 K.*

The sorption selectivity of CO_2 over N_2 is an important criterion for potential sorbent materials to be applied in CO_2 capture from flue gas streams. The CO_2/N_2 sorption selectivities of all TPI polymer networks have been determined by the initial slope method and IAST method (see chapter 5.5.3).[337,414] The selectivities have been calculated at a temperature of 298 K and for IAST calculations a simulated flue gas stream with a CO_2/N_2 ratio of 15:85 derived from the respective single component sorption isotherms has been applied. Therefore, a possible competitive sorption effect of CO_2 and N_2 molecules on the present sorption sites has not been considered. Additionally, it should be noted that both methods neglect the possible effect of the presence of water vapor in the gas stream, e.g. flue gas streams under real conditions (see chapter 5.5.1).[264] Generally, if the competitive adsorption of water molecules on the sorbent surface severely lowers the CO_2/N_2 sorption selectivity, a removal of water prior to CO_2 removal should be taken into account.

However, an additional water separation step could have negative effects on the cost efficiency of the whole process. The results of the CO_2/N_2 sorption selectivity calculations for TPI polymer networks are summarized in Table 10. The CO_2/N_2 sorption selectivities of the networks TPI-1, TPI-2, TPI-3 and TPI-6 derived from the initial slope or Henry´s law method range from 30.9 to 33.8. Except for TPI-3 (48), the respective IAST selectivities for TPI-1, TPI-2 and TPI-6 show values (29 for TPI-1 and 31 for TPI-2 and TPI-6) comparable to the initial slope method. Interestingly, the CO_2/N_2 sorption selectivities from the initial slope method increase significantly when oxygen containing linker molecules are used. The initial slope method applied to network polymers TPI-4, TPI-5 and TPI-7 yields sorption selectivities of 46.2, 46.2 and 55.5. The respective IAST selectivities of 43 (TPI-4), 38 (TPI-5) and 45 (TPI-7) follow the tendency towards increased selectivity compared to networks with non-oxygen containing linkers. However, the values calculated from initial slope and IAST method show noticeable differences. The increased selectivity of TPI-7 of 55.5 might be ascribed to the high CO_2 affinity of the bridging sulfone unit which has already been observed in other framework materials.[49,]
The values of CO_2/N_2 sorption selectivities of TPI polymer networks at 298 K, especially TPI-4, TPI-5 and TPI-7, are in accordance with the values of other porous organic materials like ALPs (27-48 (Henry) and 26-56 (IAST)),[340,342,345] CTFs (27-61 (Henry) and 24-42 (IAST)),[216,218] MOPIs (33-78 (Henry) and 26-65 (IAST)),[49] APOPs (20-32 (Henry)),[464] TBILPs (40-63 (Henry) and 43-62 (IAST)),[344] PECONFs (41-51 (Henry))[19] and PI-NO_2-1 (33 (Henry) and 18 (IAST)).[373] However, the TPI selectivities are considerably lower than the values for the best performing materials to date including Azo-COP-2 (142 (Henry) and 131 (IAST)),[349] CTF-BI-4 (103 (Henry, 303 K)),[219] PAF-1-450 (209 (IAST, 273 K)),[307] PN-101 (199 (IAST, 273 K))[347] and PPN-6 (196 (Henry, 313 K) and 150-796 (IAST, at temperatures from 295 to 313 K)).[335-337]

When regarding the CO_2/N_2 selectivities of TPI-polymers even the examples synthesized from non-functionalized linkers provide good values around 30 at both calculation methods. These quite high selectivities can be ascribed to the presence of microporosity in the network structure, but also to the Lewis basic character of the polyimide and triazine groups within the network structure. The Lewis basic sites might be beneficial for the interaction with Lewis acidic molecules like CO_2 and favor the adsorption of such molecules against others with lower interaction potential.

It has been demonstrated that a further functionalization of porous polyimide networks, e.g. with polar sulfone or carbonyl groups, has a significant influence on the sorption selectivities of the respective sorbent. As a consequence, the functionalization of porous organic sorbents might also influence the sorption selectivity ratios when applying different gas mixtures at different temperatures and pressures. Therefore, beside the evaluation of CO_2/N_2 sorption selectivities, an investigation of the sorption behavior of

porous organic polymer networks whin applying other gas mixtures, e.g. CO_2/CH_4 or CO_2/H_2, is necessary. However, when regarding the sorption properties not only the kind of functionalization of the sorbent but also the nature of the actual pore system and the accessible surface area have to be taken into account. A varation of the synthesis conditions might enable synthetic control over structure and properties of a given porous network.
Another subject to be evaluated is the competitive adsorption of CO_2 and other polar gas molecules, e.g. water, on a given sorbent, which might be of relevance if the sorbent is applied in moist flue gas streams. Unfortunately, a possible coadsorption of water and CO_2 molecules on a given sorbent surface cannot be predicted reliably even if polyimides, for instance, are generally regarded as hydrophobic polymers.[337,466,467]

However, in a recent study on gas sorption properties of porous polyimides the results clearly indicate considerable water uptake in some cases.[49] As the water uptakes could differ significantly between the different polymers, a profound discussion on CO_2/H_2O coadsorption in porous organic polymer networks might require sorption data from real gas streams.

6.5 Crystal structures of Trisubstituted 1,3,5-Triazines

To date, the determination of crystal structures of organic compounds by XRD methods is an important and frequently used method to gain access to detailed information structural and chemical properties. However, the determination of the molecular structure from single crystal XRD is only practical for molecules forming single crystals of sufficient size. Data sets obtained from neutron scattering or synchrotron would facilitate structure determination, however, access to these radiation sources is rather limited. Numerous materials do not develop single crystals of sufficient size for single crystal XRD. The crystal structures of these microcrystalline materials can be solved from powder X-ray diffraction data.

6.5.1 Crystal Structure of 2,4,6-Triphenyltriazine

Prior to the structure determination of TBPT and TAPT the applied analysis strategy has been tested on model compound 2,4,6-triphenyl-1,3,5-triazine (TPT). The crystal structure of the model compound has been published by Damiani *et al.* in 1965.[468] The synthesis of the compound 2,4,6-triphenyl-1,3,5-triazine is illustrated in Figure 6-39.

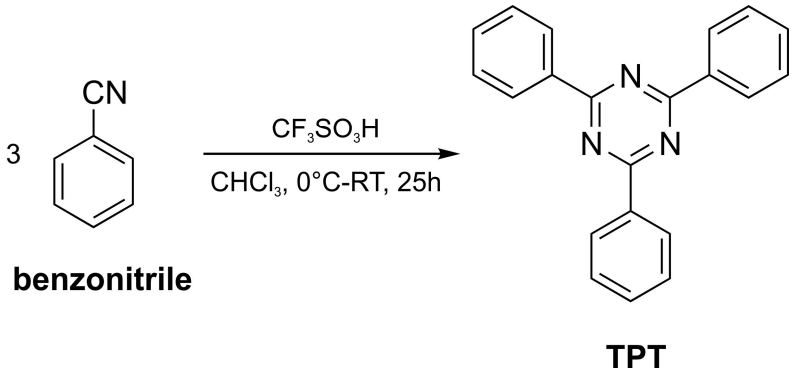

Figure 6-39: *Synthesis scheme for TPT.*

After synthesis of TPT its crystal structure should be confirmed by evaluating the data obtained from powder XRD. The respective diffractogram measured with Cu-Kα_1-radiation is displayed in Figure 6-40. For the determination of the crystal structure the phenyl rings were allowed to rotate freely around the linking bond to the triazine ring. The triazine and phenyl rings were treated as rigid bodies. Rietveld refinement of the obtained XRD pattern showed good accordance with the already published data of Damiani *et al.*[468]

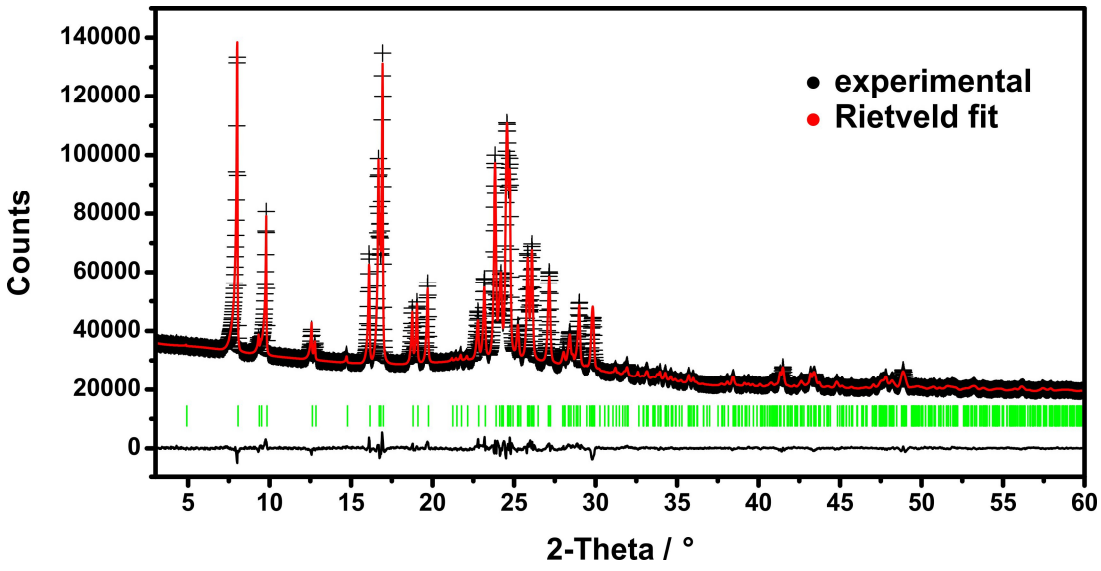

Figure 6-40: *Experimental powder X-Ray diffractograms (black) and Rietveld profile plot (red) of TPT for space group* $P2_1/c$.

The results of the refined unit cell are summarized in Table 11. The lattice constants of the monoclinic crystal system and the determined space group $P2_1/c$ agree with the values reported by Damiani *et al.*[468] The profile fits for the structure solution after Rietveld refinement provided very good values of roughly 2.1% for R_p and 2.9% for R_{wp}. The low values suggest that the applied approach is capable of conducting structure solutions from powder diffraction in good quality, despite the presence of solely "light" atoms in the structure. A view along the a-axis shows that the molecules are arranged in antiparallel paired alignments. These alignments are slightly tilted against each other (Figure 6-41a),

showing dihedral angles of approximately 141°. The crystal structure derived from the structure solution with a view along the b-axis reveals an almost eclipsed arrangement of molecules along this direction (Figure 6-41b). The presence of two different bond angles within the triazine ring (C-N-C angle is 115.5°, N-C-N angle is 124.5°) has also been reported for other triazine structures.[469,470] Damiani *et al.* suggest that the sp^2-hybridization of the triazine-nitrogen lone pair is responsible for the deformation.[468] It should be noted that the molecule itself is not planar despite the formal presence of a conjugated π-system throughout the molecule. The torsion angles between the central triazine ring and the phenyl units vary between 4.7° and 10.1°. The contortion might result from an intramolecular steric hindrance standing against the energetically favored formation of an extended conjugated π-system.

Table 11: *Crystallographic data of triphenyl triazine obtained from XRD (Figure 6-40).*

	$C_3N_3(C_6H_5)_3$
structure refinement	Rietveld
diffractometer	STOE STADI P
λ [Å]	1.5406 (Cu $K\alpha_1$)
crystal system	monoclinic
space group	$P2_1/c$ (No. 14)
GoF[431]	3.448
lattice constants [Å, °]	a = 10.9631(3)
	b = 3.9142(1)
	c = 35.9367(8)
	β = 90.9724(16)
cell volume [Å^3]	1541.88(6)
Z	4
calc. density [g cm^{-3}]	1.333
profile range	$3° \leq 2\theta \leq 60°$
data points	3800
observed reflections	460
R_p	2.128
R_{wp}	2.906
R_{exp}	0.843

A closer look on the phenyl units along the b-axis indicates a slight shift in the stacking order of two superimposed molecules. Aromatic carbon and nitrogen atoms are situated

right above the center of the underlying or superimposed aromatic triazine or phenyl ring (Figure 6-42). This is a strong sign for the presence of π-π-stacking interactions by parallel displacement in the crystal structure. However, the distance of 3.57-3.67 Å between the molecular planes is slightly larger than expected when regarding the Van-der-Waals radii of carbon and nitrogen. The increased distance might be ascribed to the contortion between the aromatic rings towards each other already discussed above.

The good accordance between crystal structure solution from X-ray powder diffraction data and the published structure by Damiani *et al.* proves the validity of the applied method. In the following, a similar approach has been applied to perform the structure solution of TBPT and TAPT from the respective X-ray powder diffraction data.

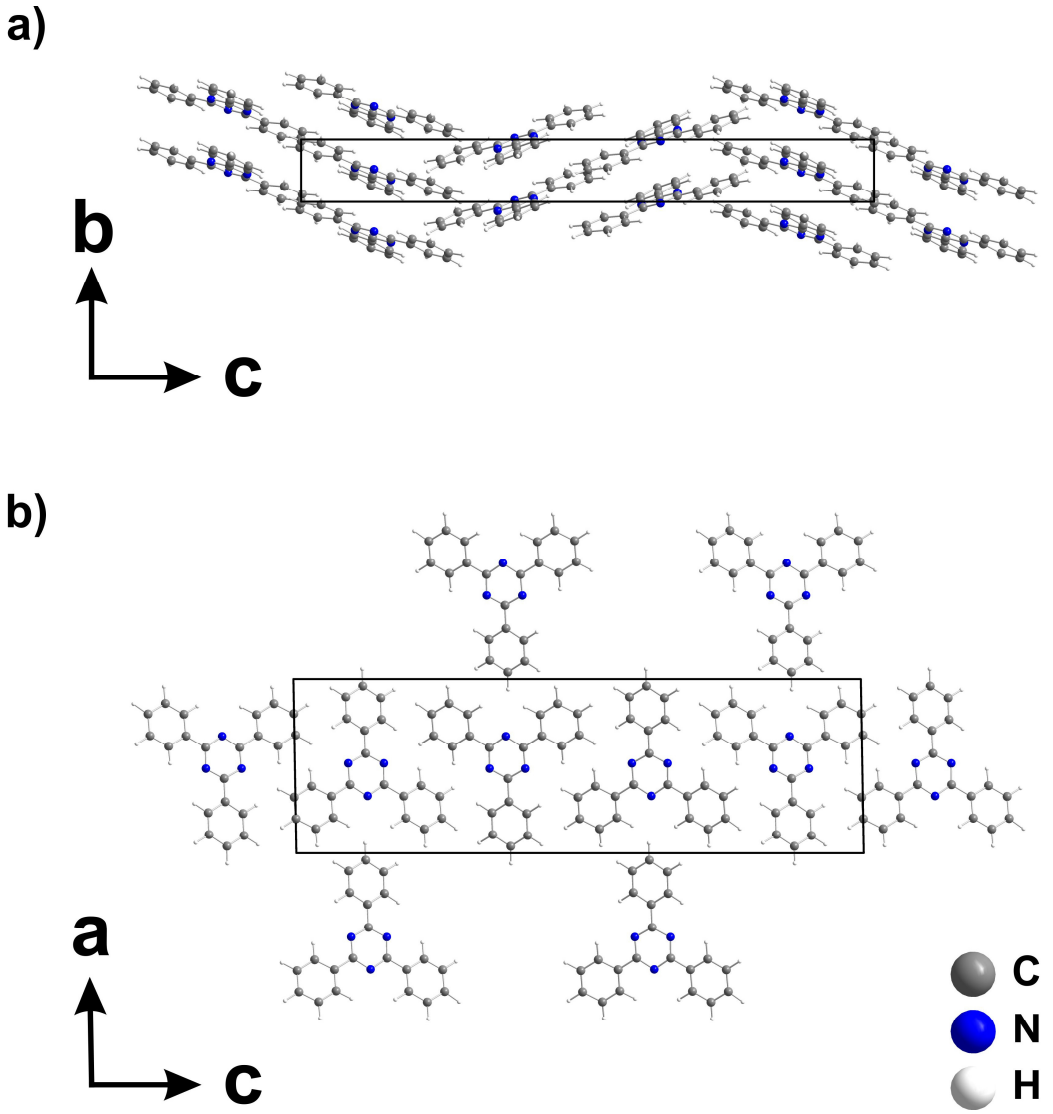

Figure 6-41: *Unit cell of TPT with a view along the a) a-axis and b) b-axis.*

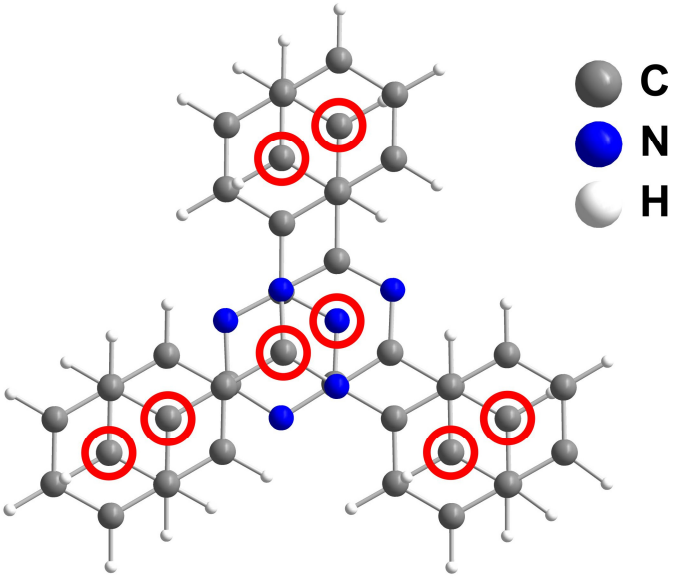

Figure 6-42: *View perpendicular to the molecular planes of two superimposed molecules of TPT. Red circles denote the atoms lying right above or, respectively, below the aromatic rings of the neighboring molecule.*

6.5.2 Crystal Structure of Tris(*p*-bromophenyl)triazine and Tris-(*p*-aminophenyl)triazine

To date, a number of reports on crystal structures of organic metal-free triazine structures can be found in the literarture.[468,470-472] To the best of the authors knowledge the structures of 2,4,6-tris(*p*-bromophenyl)-1,3,5-triazine (TBPT) and 2,4,6-tris-(*p*-amino-phenyl)-1,3,5-triazine (TAPT) have not been reported so far.

The syntheses of both triazine derivatives yielded microcrystalline solids (see section 6.4.3.4). The crystal structures of TBPT and TAPT have been solved by using an approach similar to the crystal structure solution of TPT described above. The crystallographic data of both new structures after Rietveld refinement are summarized in Table 12.

The powder X-ray diffractograms and the respective profile fits after Rietveld refinement of TBPT and TAPT are shown in Figure 6-43 and Figure 6-44. The compound TBPT crystallizes in an orthorhombic crystal system with $P2_12_12_1$ symmetry. The residual values of the applied profile fits after Rietveld refinement R_p and R_{wp} are 3.4% and 4.7%, respectively.

The compound TAPT also crystallizes in an orthorhombic crystal system. However, the determined symmetry with space group *Pbcn* is different to the $P2_12_12_1$ symmetry in TBPT (Table 12).

Table 12: *Crystallographic data for TBPT and TAPT.*

	$C_3N_3(C_6H_4Br)_3$	$C_3N_3(C_6H_6N)_3$
structure refinement	Rietveld	Rietveld
diffractometer	STOE STADI P	STOE STADI P
λ [Å]	1.5406 (Cu $K\alpha_1$)	1.5406 (Cu $K\alpha_1$)
crystal system	orthorhombic	orthorhombic
space group	$P2_12_12_1$ (No. 19)	*Pbcn* (No. 60)
GoF[431]	2.674	2.017
lattice constants [Å]	a = 4.5359(4)	a = 17.7386(6)
	b = 19.7809(11)	b = 12.6142(4)
	c = 21.6744(11)	c = 7.7503(2)
cell volume [Å^3]	1944.70(24)	1734.18(9)
Z	4	4
calc. density [g cm^{-3}]	1.864	1.357
profile range	$3° \leq 2\theta \leq 70°$	$3° \leq 2\theta \leq 70°$
data points	4460	4460
observed reflections	556	380
R_p	3.368	1.436
R_{wp}	4.721	1.962
R_{exp}	1.766	0.973

The Rietveld refinement of the crystal structure yields R_p and R_{wp} values of 1.44% and 1.96%, respectively. These low values are characteristic for an excellent quality of the fit.

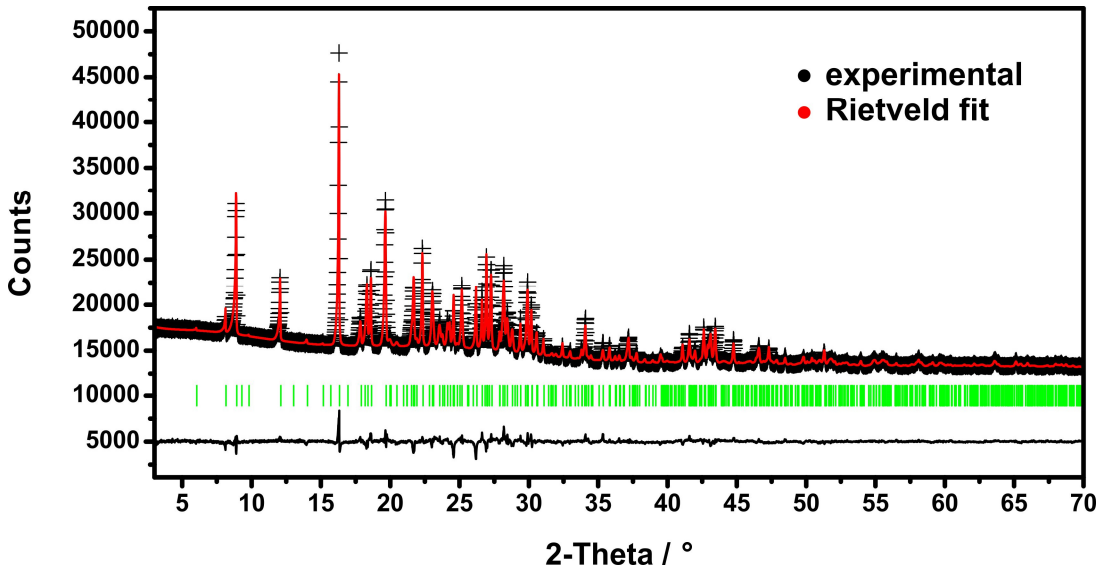

Figure 6-43: *Experimental powder X-Ray diffractograms (black) and Rietveld profile plot (red) of TBPT for space group* $P2_12_12_1$.

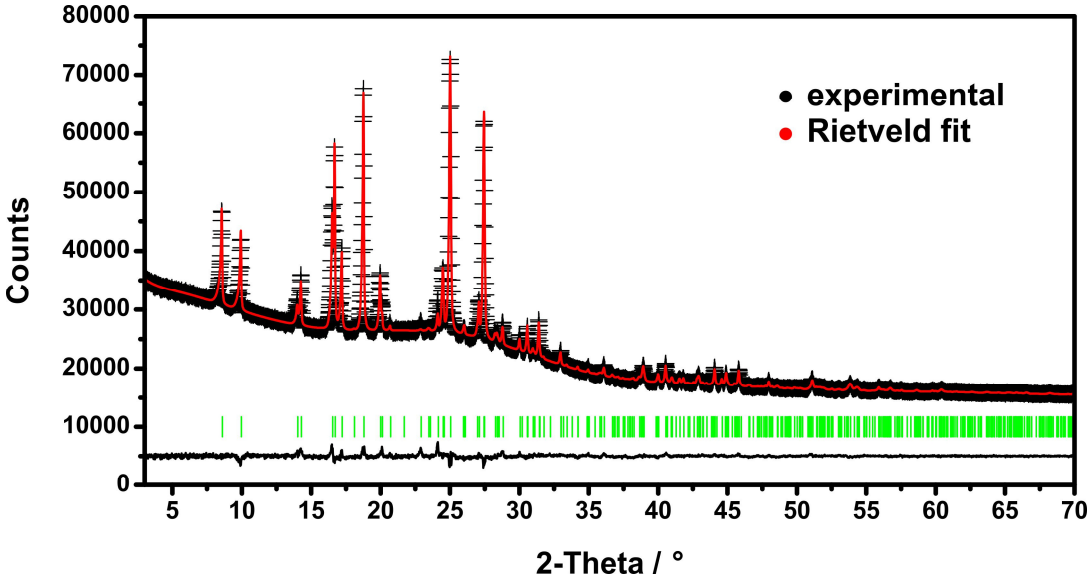

Figure 6-44: *Experimental powder X-Ray diffractograms (black) and Rietveld profile plot (red) of TAPT for space group* Pbcn.

Starting from space group *Pca*2$_1$, the higher symmetric space group *Pbcn* has been identified by using the program PLATON. The determined unit cell of TBPT contains four molecules on general positions (Figure 6-45). A view along the a-axis reveals an eclipsed stacking of molecules (Figure 6-45a).
Similar to the crystal structure of TPT the molecular plane of the central triazine in TBPT is contorted against the planes of the three neighboring phenyl rings with torsion angles ranging from 1.9-7.5° with a zig-zag shaped alignment of molecules along the b-axis (Figure 6-45b). The molecular planes of neighboring molecules are tilted against each other showing dihedral angles of approximately 99° (Figure 6-45b).
A view perpendicular to the molecular plane of TBPT is illustrated in Figure 6-46. Similar to the crystal structure of TPT aromatic carbon atoms can be found right above (blue circle) or below (red circle) the center of the neighboring aromatic ring, phenyl or triazine.

The distance of approximately 3.4 Å between two molecules strongly supports the presence of π-π-stacking interactions by parallel displacement. Similar stacking distances between phenyl and triazine have been reported in the literature.[473] The refined unit cell of TAPT also contains four molecules with half a molecule in the asymmetric unit (Figure 6-47). Five atoms are situated on special positions, all others on general positions. The molecules in the unit cell are almost planar with only small torsion angles of 3.2°-5.0° between the central triazine ring and the three phenyl rings. Similar to the unit cell of TBPT, neighboring molecules along the a-axis are slightly tilted against each other with dihedral angles between the molecular planes (Figure 6-47a). However, the angles of approximately 122° are considerably larger than the comparable dihedral angle found for TBPT.

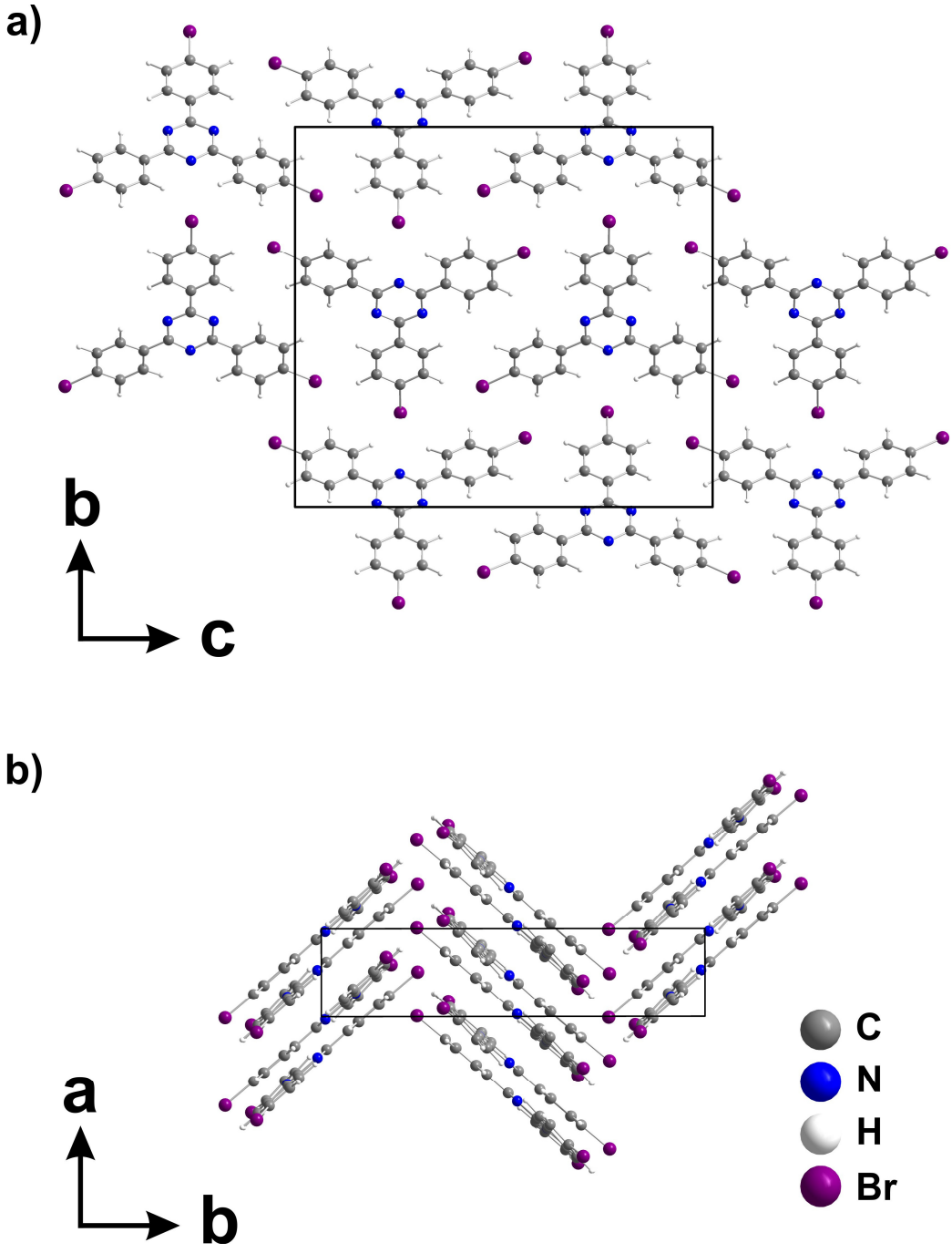

Figure 6-45: *Unit cell of TBPT with a view along the a) a-axis and b) b-axis.*

One explanation for the significant difference might be the different nature of the interactions between the molecules. While in the crystal structure of TBPT π-π-stacking interactions seem to be dominant, there is strong evidence for the presence of considerable hydrogen bonding in the structure of TAPT (Figure 6-48). The N-H···N distance of about 2.34 Å is characteristic for hydrogen bonding and matches similar distances for hydrogen bonding between amino and triazine moieties reported by Mereiter.[474]

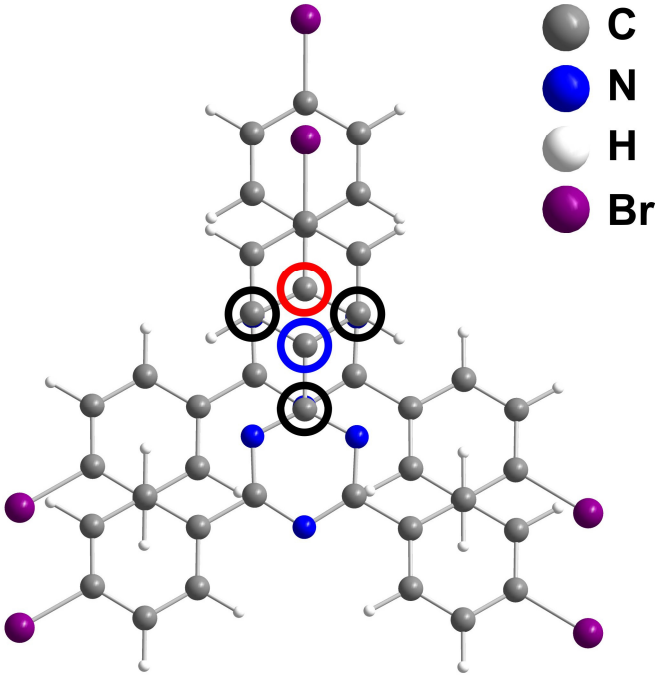

Figure 6-46: *View perpendicular to the molecular plane of two molecules of TBPT. One aromatic carbon atom is situated right above the center of the underlying triazine ring (blue circle), another below the center of a phenyl ring (red circle). The black circles mark three carbon atoms covering the underlying nitrogen atoms of the triazine ring.*

Another interesting feature in the crystal structure of TAPT is revealed when regarding the unit cell along the c-axis (Figure 6-47b). Consecutive molecules arranged along the c-axis are rotated 180° perpendicular to the molecular plane describing a 2_1 screw axis. The distance between the molecular planes has been determined at approximately 3.40 Å. However, contrary to the crystal structure of TBPT, the presence of π-π-stacking interactions could not be identified.

When regarding the unit cell of TBPT, a relatively short distance of 3.39 Å can be found between a Br-atom and one nitrogen atom in the triazine ring (Figure 6-49). However, an interaction could not be identified clearly.

One possible explanation, namely the presence of halogen bonding, where halogen atoms interact as electron acceptors with electron donors (e.g. filled atom or molecular orbitals),[475,476] might be taken into consideration. However, the dihedral angle of 99° between the interacting molecular planes of two potentially interacting molecules could be regarded as too small compared to other examples where halogen bonding has been observed.[477] The direction of the C-Br bond runs almost perpendicular to the orbital containing the nitrogen´s free electron pair which might prevent a considerable electron donor-acceptor interaction.

In the case of efficient halogen bonding the angle C-Hal···Donor would be expected at roughly 180° in order to provide a sufficient overlap of the electron pair donating and the electron pair accepting orbital.[475,477]

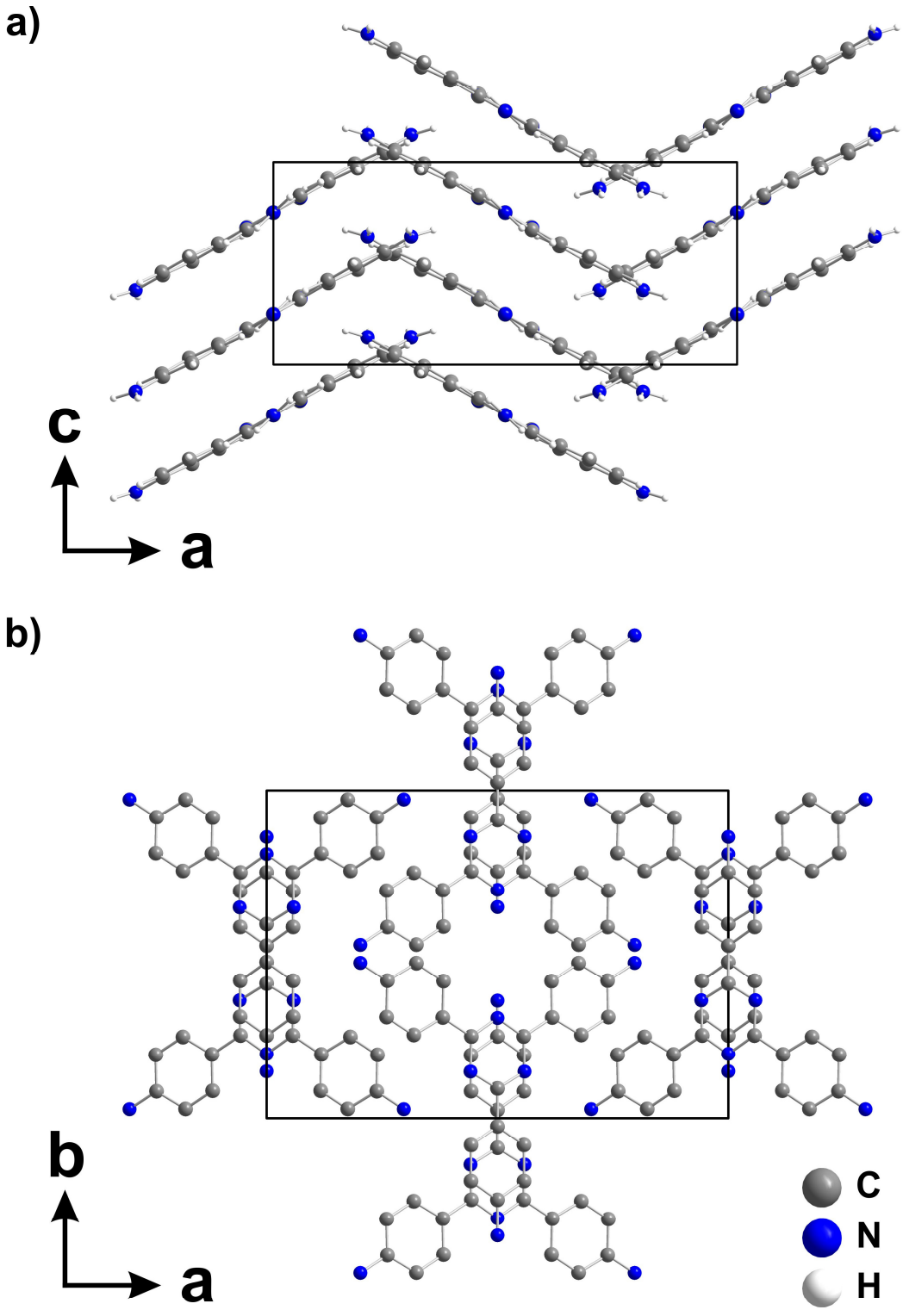

Figure 6-47: *a) Crystal structure of TAPT viewed along the b-axis. b) Crystal structure viewed along the c-axis. Hydrogen atoms have been omitted for clarity.*

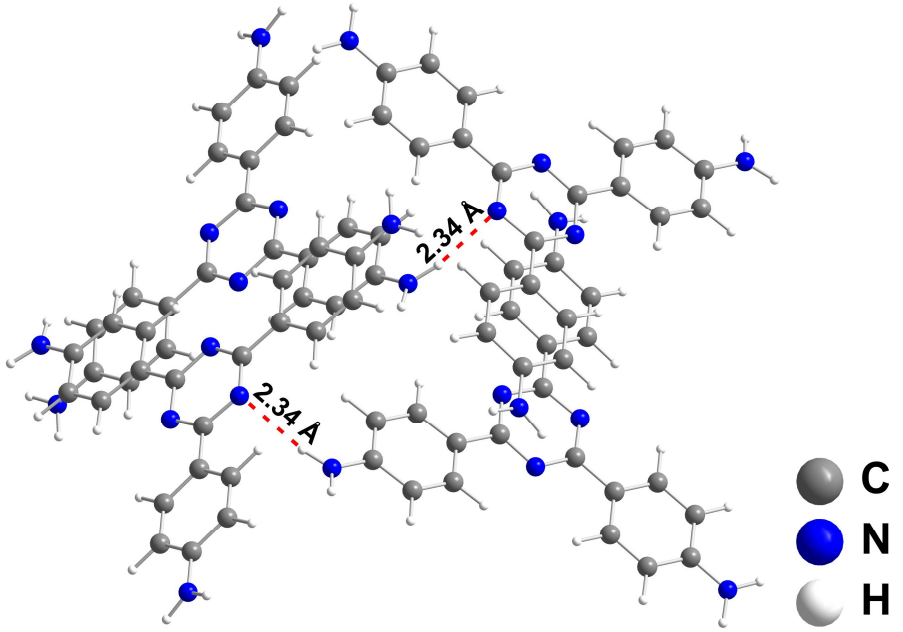

Figure 6-48: *Hydrogen bonds in TAPT (red dotted lines).*

Another stabilizing factor to be considered might be an at least weak donor-acceptor interaction between the Br atom and the aromatic π-electron system of the phenyl rings (Figure 6-49).[477]

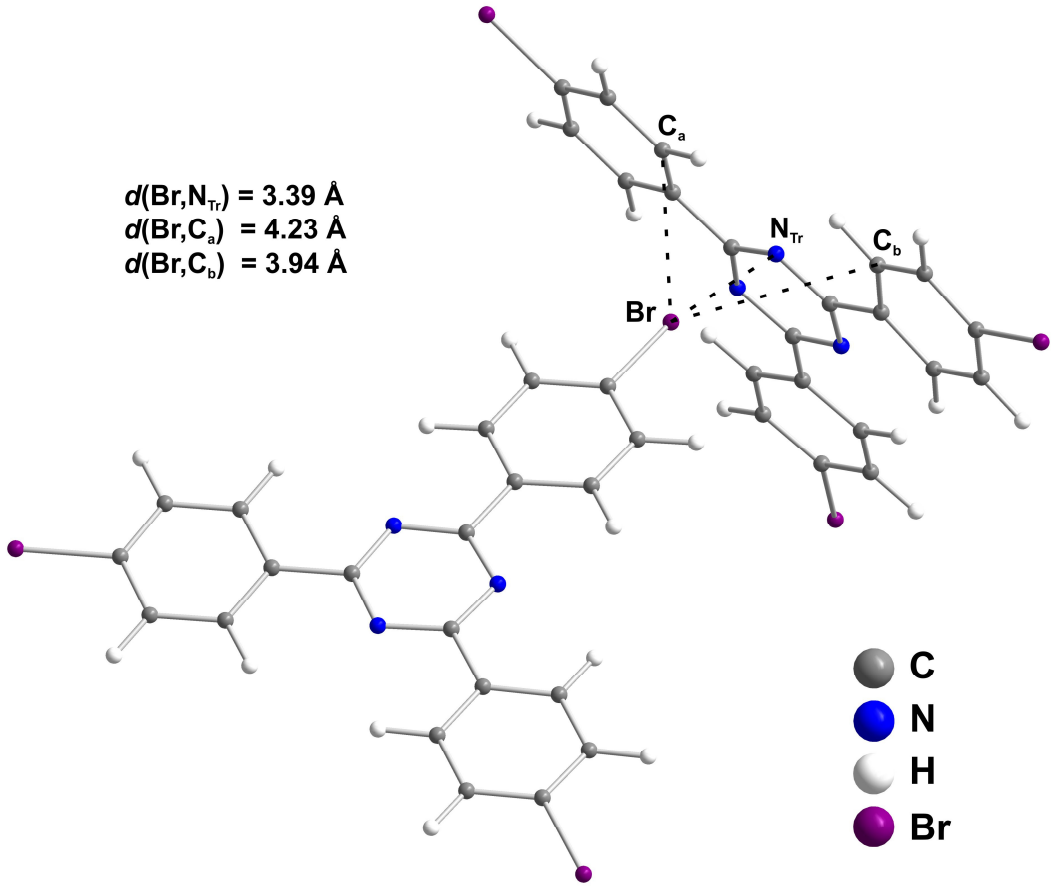

Figure 6-49: *Distances between selected atoms in the crystal structure of TBPT.*

All three crystal structures discussed in this paragraph have been determined by Rietveld refinement of the respective powder XRD patterns. While the crystal structure of TPT and TBPT is dominated by π-π-stacking interaction with parallel displacement of the molecules against each other. In contrast, the crystal structure of TAPT is mainly stabilized by hydrogen bonding between the amino and triazine groups. In summary, the presented approach for the determination of the crystal structure of organic non-metal compounds has been successful.

7 Experimental Part

7.1 Materials and Methods

7.1.1 General Remarks

All experiments with air or moisture sensitive compounds were performed in a dry reaction vessel under argon atmosphere at ambient pressure using standard Schlenk or glove box techniques unless otherwise noted. Argon 4.8 (Riessner Gase) has been passed through three columns containing molecular sieve (3 Å), P_2O_5 and BTS catalyst.

7.1.2 Solvents

All solvents of analytical or reagent grade were used without further purification. All solvents of technical grade were distilled applying solvent-dependent drying agents prior to use. Toluene was distilled from sodium and halogenated solvents (dichloromethane, chloroform) from P_2O_5. Acetonitrile was distilled from P_2O_5 prior to use.
Solvents applied for recrystallization and chromatography (cyclohexane, ethyl acetate) were freshly distilled prior to use. Diethylether was distilled prior to use.
Deuterated solvents for solution NMR spectroscopy (see section 7.1.8) were purchased from Cambridge Isotopes and Eurisotop and used without further purification.

7.1.3 Compounds and Reagents

All commercial compounds were exclusively purchased from ABCR, Acros, Alfa Aesar, Grüssing, Merck, Sigma-Aldrich, TCI and VWR and were used without further purification unless otherwise noted. The compounds *m*-cresol and piperidine were freshly distilled under inert atmosphere prior to use.

Table 13: *Sources and purity of applied chemical compounds.*

name	purity	supplier
Acetic anhydride	99%	Sigma-Aldrich
Acetone	99.8%	Merck
Ammonium chloride	99.5%	ABCR
Benzonitrile	99%	Merck
3,3‘,4,4‘-Benzophenonetetracarboxylic dianhydride	98%	TCI
Bis(dibenzylideneacetone)palladium ($Pd(dba)_2$)	-	ABCR
4-Bromobenzonitrile	98%	ABCR
4-Bromo-3-methylbenzonitrile	98%	ABCR
Chlorosulfuric acid	99%	Alfa Aesar
Cobalt bromide	97%	Alfa Aesar
2,6-Dimethylaniline	99%	Sigma-Aldrich
Dimethylsulfoxide (anhydrous)	99.8%	Sigma-Aldrich
Ethanol	99.8%	VWR
p-Fluoronitrobenzene	98%	ABCR
Glyoxal (aqueous solution)	40% in water	Sigma-Aldrich
4,4’-Hexafluoroisoprpylidenediphthalic anhydride	98%	TCI
Hydrazine monohydrate	80%	Sigma-Aldrich
Hydrochloric acid (conc.)	31-33%	Hedinger
Isoquinoline	95%	TCI
m-Cresol	99%	Sigma-Aldrich
Lanthan trifluoromethanesulfonate	98%	ABCR
Lithium bis(trimethylsilyl)amide (LiHMDS)	1M in hexanes	ABCR
Magnesium sulfate	99%	Grüssing
Manganese (powder)	99.6%	Alfa Aesar
Methanol	99.8%	VWR
N-Methylpyrrolidone (NMP)	99%	Sigma-Aldrich
2-Methylterephthalonitrile	98%	Sigma-Aldrich
Naphthalene-1,4,5,8-tetracarboxylic dianhydride	97%	TCI
p-Nitroacetophenone	98%	Alfa Aesar
4,4’-Oxydiphthalic anhydride	98%	TCI
Palladium	10wt% on carbon	Alfa Aesar
Perylene-3,4,9,10-tetracarboxylic dianhydride	98%	Merck
1,4-Phenylenediamine	99%	Sigma-Aldrich
Piperidine	99%	Merck

name	purity	supplier
Pyromellitic dianhydride	97%	Merck
Potassium carbonate, anhydrous	99%	Alfa Aesar
Potassium chloride	99.5%	Merck
Terephthalonitrile	98%	Alfa Aesar
Tetrahydrofuran	99.5%	Merck
Tri-*t*-butylphosphine	10wt% in hexane	ABCR
Trifluoroacetic acid	99%	Sigma-Aldrich
Trifluoromethanesulfonic acid	98%	ABCR
Silicon tetrachloride	99%	Sigma-Aldrich
Sodium chloride	99%	Fisher
Sodium hydroxide	99%	Merck
4,4'-Sulfonyldiphthalic anhydride	98%	TCI
Yttrium trifluoromethanesulfonate	98%	ABCR
Zinc chloride	98%	Merck
Zinc triflouromethanesulfonate	98%	ABCR

7.1.4 Thin Layer Chromatography

Reaction processes were monitored by TLC using POLYGRAM® SIL G/UV_{254} silica sheets by Macherey-Nagel. The detection of the samples was performed by using UV irradiation (λ=254 nm) or a solution of molybdatophosphoric acid (5% in ethanol).

7.1.5 Column Chromatography

For the purification of chemical compounds by column chromatography *Kieselgel 60* (Macherey-Nagel) with a grain size of 63-200 µm has been applied as stationary phase.

7.1.6 Infrared Spectroscopy

All infrared (IR) spectra were obtained by using a *Spectrum One FT-IR Spectrometer* (Perkin Elmer) equipped with an attenuated total reflectance (ATR) top plate. The

measured absorption values are given in wavenumbers (cm^{-1}). Characterization of the absorption peaks was performed by using the following abbreviations: strong (s), medium (m), weak (w), broad (br), stretching vibration (str), deformation vibration (def).

7.1.7 Mass Spectrometry

All mass spectra were recorded using a *MAT 8500 spectrometer* running on data system *MAT SS 300* (Finnigan). The measurements were conducted by direct injection applying an ionization energy of 70 eV. The detected ions are reported in m/z and their abundance in brackets as a percentage relative to the base peak.

7.1.8 NMR Spectroscopy

Solid state NMR measurements were carried out at ambient temperature on a Bruker *Avance II 300* spectrometer operating at a proton frequency of 300 MHz. Samples for ^{13}C and ^{15}N measurements were contained in 4 mm or 7 mm ZrO_2 rotors and mounted in standard triple resonance MAS probes (Bruker). For all ^{13}C MAS cross polarization (CP) experiments a ramped CP (CPramp) sequence with contact times of 5-32 ms were applied. For all ^{15}N MAS cross polarization (CP) experiments a ramped CP (CPramp) sequence with contact times of 5-10 ms were applied. The spinning frequencies varied between 10 to 11.5 kHz for measurements in 4 mm rotors and 4.5 to 5 kHz for measurements in 7 mm rotors. The ^{13}C and ^{15}N chemical shifts were referenced to TMS and nitromethane, respectively. For all measurements broadband proton decoupling using the SPINAL64 sequence with a nutation frequency of around 80 kHz was applied.[478]

Solution NMR spectroscopy was carried out on a Varian INOVA spectrometer equipped with a temperature unit operating at a proton frequency of 300 MHz. All measurements were carried out at 298 K (chloroform-d_1, acetone-d_6, benzene-d_6 and DMSO-d_6) and at 353 K (bromobenzene-d_5), respectively. Chemical shifts δ are reported in ppm relative to the used deuterated solvent with TMS as internal standard.[479] Coupling constants *J* are reported in Hz. Characterization of the ^{1}H-NMR signals was performed by using the following abbreviations: singlet (s), doublet (d), doublet of doublets (dd), triplet (t), quartet (q), multiplet (m).
The solvent signal of the C-Br carbon of bromobenzene-d_5 (^{13}C) has been determined at 122.26 ppm relative to TMS at 298 K. This solvent signal was used as a reference for measurements in bromobenzene-d_5 at 353 K.

7.1.9 Elemental Analysis

Elemental analysis (EA) was carried out on a Vario Elementar EL III at the Chair of Inorganic Chemisty II, University of Bayreuth.

7.1.10 X-Ray Diffraction

Routine powder X-ray diffraction (XRD) measurements were performed on a Panalytical Xpert-Pro diffractometer (Bragg-Brentano geometry) equipped with an X´Celerator Scientific RTMS detector. Nickel filtered Cu-Kα radiation with a wavelength of 1.54187 Å was used. During measurement the sample was placed on a zero background silicon plate spinning with a rotation frequency of 1 Hz.

For crystal structure determinations, PXRD patterns were recorded on a STOE StadiP diffractometer equipped with a germanium (111) monochromator also using Cu-Kα radiation with a wavelength of 1.54187 Å. The samples were measured in capillary tubes with an inner diameter of 0.5 mm.

The solution of the crystal structures described in this paragraph started by indexing the measured powder X-ray diffractograms using the algorithms developed by Werner, Visser and Louer.[480-482]
The obtained lattice constants were refined by applying the Pawley method.[483] The next step involved the determination of the correct space group by careful analysis of the systematic absences in the X-ray diffractograms searching for space groups possessing the highest possible symmetry. The structure solution has been performed by applying real space methods. The molecules inserted in the unit cell have been geometry optimized using DFT methods (see section 7.1.12) and were treated as rigid bodies.

Rietveld refinement of the structure proposals obtained from real space methods yielded the final crystal structures. Crystal structure solution and Rietveld refinement of the unit cells have been performed by Dr. Thomas Martin, Chair of Inorganic Chemistry I, University of Bayreuth, using the TOPAS Academic software package.[484]

The given R factors are defined as

$$R_p = \sqrt{\frac{\sum |Y_o - Y_c|}{\sum Y_o}} \tag{7.1}$$

$$R_{wp} = \sqrt{\frac{\sum w \cdot (Y_o - Y_c)^2}{\sum w \cdot Y_o^2}} \tag{7.2}$$

$$R_{exp} = \sqrt{\frac{M - P}{\sum w \cdot Y_o^2}} \tag{7.3}$$

$$GOF = chi = \frac{R_{wp}}{R_{exp}} = \sqrt{\frac{\sum w \cdot (Y_o - Y_c)^2}{M - P}} \tag{7.4}$$

with Y_o = observed intensity at data point
Y_c = calculated intensity at data point
w = weighting factor given to data point
M = number of data points
P = number of parameters

7.1.11 Gas Adsorption Measurements

Argon sorption measurements were carried out on a Quantachrome Autosorb-1 pore analyzer at 87 K. The specific BET equivalent surface areas were calculated considering analysis requirements for microporous materials.[395,397,398] For all TPI polymers specific surface areas, pore volumes and pore size distributions from the argon adsorption isotherms were obtained by applying the quenched solid density functional theory (QSDFT) equilibrium pore model for carbon materials with slit pore geometry.
Carbon dioxide and nitrogen sorption measurements were carried out on a Quantachrome Nova surface analyzer. Specific surface areas, pore volumes and pore size distributions from CO_2 isotherms at 273 K were obtained by applying the non-local density functional theory (NLDFT) slit pore model for carbon materials.
The isosteric heats of adsorption were calculated from the CO_2 adsorption isotherms at temperatures of 273 K, 298 K and 313 K up to a pressure of 1 bar.
For all gas sorption analyses the isosteric enthalpies of adsorption have been calculated

based on the Clausius-Clapeyron equation by applying the Quantachrome ASiQ v3.0 software package.[218] All samples were degassed at 433 K for 20 h under vacuum prior to all gas sorption measurements. The equilibration time for Ar, CO_2 and N_2 sorption measurements was set to 120 s.

7.1.12 Computational Calculations

Geometry optimization of the molecular structures was performed by applying DFT methods with the module *DMol3* implemented in the MS Modeling 5.0 software package from Accelrys Software Inc. The geometry minimization was performed by generalized gradient approximation (GGA) using the PBE[485] functional. The applied basis set was DNP (double numerical basis set with polarization).

7.1.13 Melting point Determination

Melting points were determined using a *Büchi Melting Point M-565* apparatus. All values are uncorrected.

7.1.14 Thermogravimetric Analysis

Thermogravimetric analysis (TGA) was conducted with a Linseis T6/DTA (Type L81/077) thermoanalyzer instrument. All samples were heated under air with a heating rate of 5 K min^{-1}.

7.1.15 Scanning Electron Microscopy

Scanning Electron Microscopy (SEM) images were recorded with a high resolution scanning electron microscope (LEO 1530 FESEM) equipped with a field emission cathode at 3 kV. The accessible magnification ranges from 20x to 900000x. All samples were investigated from conductive carbon tabs and sputtered with carbon (20-40 nm) prior to the measurements.

7.2 Synthesis Procedures

7.2.1 Polymer Syntheses *via* Nitrile Cyclotrimerization

7.2.1.1 CTF-1

The compound was prepared by a slight modification of a known procedure.[45] In a glovebox, first 1,4-DCB (0.26 g, 2.0 mmol) and then zinc(II) chloride (0.27 g, 2.0 mmol) were weighted in a glass ampoule in a glovebox. The glass ampoule (d = 10-15 mm) was sealed under vacuum at total length of 120 mm. The ampoule was heated to 400 °C at a heating rate of 10 °C min^{-1} and held at this temperature for 40 h. The resulting black solid was finely ground and afterwards suspended in 1M aqueous HCl (400 mL). After stirring for 20 h at room temperature the black solid was filtered off and washed subsequently with water (100 mL), THF (100 mL) and acetone (50 mL). The title compound was obtained as a black solid.

Yield: 0.25 g (98%);

IR (cm^{-1}): 2228 (w, CN), 1738 (w), 1575 (w, phenyl), 1505 (s, triazine), 1405 (m, phenyl), 1348 (s, triazine), 1015 (m, phenyl), 804 (vs, phenyl);

Elem. Anal. (%): Calcd: C: 74.99, H: 3.15, N: 21.86;

Found: C: 70.77, H: 2.97, N: 19.07;

7.2.1.2 Me-CTF

For the syntheses of MeCTF-1, MeCTF-2 and MeCTF-3, the compounds 2-methyl-terephthalonitrile (0.28 g, 2.0 mmol) and zinc(II) chloride (0.27 g, 2.0 mmol) were weighted in a glass ampoule in a glovebox. The ampoules were sealed analogously to section 7.2.1.1. The different reaction conditions for the syntheses of MeCTF-1, Me-CTF-2 and MeCTF-3 are summarized in Table 14. The resulting black solids were ground finely and afterwards suspended in 1M aqueous HCl (400 mL). After stirring for 20 h at room temperature the black solid was filtered off and washed subsequently with water (100 mL), THF (100 mL) and ethanol (100 mL). MeCTF-1, MeCTF-2 and MeCTF-3 were obtained as black powders.

Table 14: *Reaction conditions for the syntheses of MeCTF-1, MeCTF-2 and MeCTF-3.*

network	catalyst $ZnCl_2$	temp. (°C)	time (h)	heating rate (°C min^{-1})
MeCTF-1	1 eq.	370	40	10
MeCTF-2	1 eq.	370	140	10
MeCTF-3	1 eq.	550	140	10

Yield: MeCTF-1: 82%, MeCTF-2: 73%, MeCTF-3: 68%;

IR (cm^{-1}): MeCTF-1: 2224 (w, CN), 1739 (w), 1608 (w, phenyl), 1573 (w, phenyl), 1512 (vs, triazine), 1347 (s, triazine), 1217 (m, phenyl), 1103 (m), 901 (m, phenyl), 816 (vs, phenyl), 774 (m, triazine);

MeCTF-2: 2222 (w, CN), 1613 (s, phenyl), 1512 (s, triazine), 1343 (s, triazine), 890 (m, phenyl), 818 (s, phenyl);

Elem. Anal. (%): Calcd: C: 76.04, H: 4.25, N: 19.71;

Found: MeCTF-1: C: 57.48, H: 4.86, N: 9.82;

MeCTF-2: C: 69.78, H: 3.76, N: 11.34;

MeCTF-3: C: 60.46, H: 3.67, N: 7.81;

7.2.1.3 DCBP-Polymer 1

In a glovebox, DCBP (0.30 g, 1.47 mmol) and zinc(II) chloride (2.00 g, 14.7 mmol) were weighted in a glass ampoule. The ampoule was sealed analogously to section 7.2.1.1. The ampoule was heated to 400 °C at a heating rate of 10 °C min^{-1} and held at this temperature for 40 h. The resulting black solid was finely ground and afterwards suspended in 1M aqueous HCl (400 mL). After stirring for 20 h at room temperature the black solid was filtered off and washed subsequently with water (100 mL), THF (100 mL) and ethanol (100 mL). The final product was obtained as a black powder.

Yield: 0.25 g (83%);

IR (cm^{-1}): 3061 (w, phenyl), 1737 (w), 1723 (w), 1603 (m, phenyl), 1447 (m, phenyl), 1366 (m, phenyl), 1289 (m), 1231 (m, phenyl), 877 (m, phenyl), 821 (m, phenyl), 754 (vs, phenyl), 698 (m, phenyl);

Elem. Anal. (%): Calcd: C: 82.33, H: 3.95, N: 13.72;

Found: C: 90.04, H: 3.95, N: 2.96;

7.2.1.4 DCBP-Polymer 2

The compound was prepared by a slight modification of a known procedure.[421] A flame-dried 50 mL flask containing DCBP (0.96 g, 4.70 mmol) was placed in an ice bath. At 0 °C chlorosulfuric acid (3.7 mL, 99%) was added dropwise and the reaction mixture was allowed to stand for 48 h. Afterwards, the reaction mixture was poured in cold water (200 mL) under stirring to remove residual chlorosulfuric acid. The precipitate was filtered off and finely ground. Then the mixture was suspended in water (100 mL), filtered off again and washed with acetone (100 mL) and ethanol (100 mL). After drying, the purified polymer was obtained as a yellow solid.

Yield: 0.95 g (99%);

IR (cm^{-1}): 2226 (w, CN), 1666 (m), 1606 (m, phenyl), 1563 (m, phenyl), 1504 (vs, triazine), 1417 (s, phenyl), 1360 (s, triazine), 1218 (s, phenyl), 1178 (s), 1111 (s), 1043 (m), 1003 (s), 839 (s), 807 (vs, phenyl), 772 (s), 697 (m, phenyl);

Elem. Anal. (%): Calcd: C: 82.33, H: 3.95, N: 13.72;

Found: C: 72.24, H: 5.63, N: 11.55;

7.2.1.5 Me_2DCBP-Polymer

In a glovebox, Me_2-DCBP (0.30 g, 1.29 mmol) and zinc(II) chloride (1.76 g, 12.9 mmol) were weighted in a glass ampoule. The ampoule was sealed analogously to section 7.2.1.1. The ampoule was heated to 370 °C at a heating rate of 10 °C min^{-1} and held at this temperature for 40 h. The resulting black solid was finely ground and afterwards suspended in 1M aqueous HCl (400 mL).

After stirring for 20 h at room temperature the black solid was filtered off and washed subsequently with water (100 mL), THF (100 mL) and ethanol (100 mL). The final product was obtained as a black powder.

Yield: 0.22 g (73%);

IR (cm^{-1}): 3020 (w, Ar-CH_3, Ar-H), 1709 (m), 1590 (s, phenyl), 1435 (s, phenyl), 1365 (vs, phenyl), 1231 (vs), 1217 (vs, Ar-CH_3), 1031 (m, phenyl), 880 (s, phenyl), 818 (s, phenyl), 750 (s, phenyl);

Elem. Anal. (%): Calcd: C: 82.73, H: 5.21, N: 12.06;

Found: C: 86.48, H: 3.16, N: 2.17;

7.2.1.6 ATP-P Polymers

In a glovebox, 1,4-DCB (1.28 g, 10 mmol) and the respective metal salt catalyst (0.15 mmol) were weighted in a steel autoclave reactor with PTFE inlet. After removing the autoclave from the glovebox, freshly distilled piperidine (0.96 mL, 10 mmol) was added to the reaction mixture under inert atmosphere. The autoclave was sealed and then heated to 200 °C. After 6 d at 200 °C the heating was turned off and the autoclave was allowed to cool down to room temperature. The reaction conditions are summarized in Table 15. The resulting yellow solids were washed subsequently with water (100 mL), THF (100 mL) and acetone (100 mL). The final products were obtained as a yellowish powders.

Table 15: *Reaction conditions for ATP-P polymer syntheses.*

polymer	catalyst	m(catalyst) (g)	temperature (°C)	reaction time (h)
ATP-P 1	$Y(CF_3SO_3)_3$	0.080	200	148
ATP-P 2	$Zn(CF_3SO_3)_2$	0.053	200	148
ATP-P 3	$La(CF_3SO_3)_3$	0.087	200	148

Yield: ATP-P1: 1.50 g (117%), ATP-P2: 1.60 g (125%), ATP-P3: 122%; Yields above 100%, due to the addition of piperidine to the polymers.

IR (cm^{-1}): ATP-P3: 2927 (w, piperidyl), 2853 (w, piperidyl), 2229 (w, CN), 1625 (w), 1575 (w, amidine), 1505 (vs, triazine), 1407 (s, phenyl), 1352 (vs, triazine), 1272 (s), 1178 (w, phenyl), 1107 (w, phenyl), 1016 (m, phenyl), 808 (vs, phenyl);

ATP-P2: 2927 (w, piperidyl), 2853 (w, piperidyl), 2228 (w, CN), 1627 (w), 1577 (w, amidine), 1507 (vs, triazine), 1406 (s, phenyl), 1353 (vs, triazine), 1272 (s), 1179(w, phenyl), 1107 (w, phenyl), 1016 (m, phenyl), 809 (vs, phenyl);

ATP-P1: 2228 (w, CN), 1577 (w, amidine), 1510 (vs, triazine), 1408 (s, phenyl), 1354 (vs, triazine), 1178(w, phenyl), 1108 (w, phenyl), 1016 (m, phenyl), 879 (w), 808 (vs, phenyl);

Elem. Anal. (%): Calcd: C: 74.99, H: 3.15, N: 21.86;

Found: ATP-P1: C: 70.65, H: 4.45, N: 17.32;

ATP-P2: C: 68.89, H: 5.10, N: 15.24;

ATP-P3: C: 69.96, H: 5.04, N: 16.00;

7.2.1.7 ATP-A Polymers

In a glovebox, terephthalonitrile (1.28 g, 10 mmol), ammonium chloride (0.53 g, 10 mmol) and the respective metal salt catalyst (0.15 mmol) were weighted in autoclave reactor. The autoclave was sealed and then heated to 200 °C. After 6 d at 200 °C the heating was turned off and the autoclave was allowed to cool down to room temperature. The reaction conditions are summarized in Table 16. The resulting yellow solids were suspended in 0.1 M aqueous HCl (400 mL). After stirring for 20 h at room temperature the solids were filtered off and washed subsequently with water (100 mL), THF (100 mL) and acetone (100 mL). The final products were obtained as a yellowish powders.

Table 16: *Reaction conditions for ATP-A Polymer syntheses.*

polymer	catalyst	m(catalyst) (g)	temperature (°C)	reaction time (h)
ATP-A 1	$Y(CF_3SO_3)_3$	0.080	200	148
ATP-A 2	$Zn(CF_3SO_3)_2$	0.053	200	148
ATP-A 3	$La(CF_3SO_3)_3$	0.087	200	148

Yield: ATP-A1: 0.75 g (59%), ATP-A2: 0.62 g (48%), ATP-A3: 1.07 g (83%);

IR (cm^{-1}): ATP-A3: 3072 (w, Ar-H), 2230 (m, CN), 1682 (w), 1579 (m), 1515 (vs, triazine), 1411 (m, phenyl), 1357 (s, triazine), 1303 (w), 1184 (w, phenyl), 1148 (w), 1110 (w, phenyl), 1017 (m, phenyl), 872 (w), 851 (w), 812 (vs, phenyl), 746 (m);

ATP-A2: 3072 (w, Ar-H), 2229 (w, CN), 1684 (w), 1579 (m), 1516 (vs, triazine), 1411 (m, phenyl), 1358 (s, triazine), 1303 (w), 1184 (w, phenyl), 1148 (w), 1110 (w, phenyl), 1016 (m), 872 (w), 851 (w), 812 (vs, phenyl), 746 (m);

ATP-A1: 3072 (w, Ar-H), 2229 (m, CN), 1682 (w), 1579 (m), 1514 (vs, triazine), 1410 (m, phenyl), 1356 (vs, triazine), 1302 (w), 1183 (w, phenyl), 1147 (w), 1110 (w), 1016 (m, phenyl), 872 (w), 851 (w), 811 (vs, phenyl), 746 (m);

Elem. Anal. (%): Calcd: C: 74.99, H: 3.15, N: 21.86;

Found: ATP-A2: C: 71.85, H: 3.17, N: 20.10;

ATP-A3: C: 71.82, H: 3.54, N: 19.63;

7.2.1.8 $ZnCl_2$/NaCl/KCl eutectic salt melt (SM-1)

In a glovebox 8.17 g (60 mmol) anhydrous $ZnCl_2$, 1.17 g (20 mmol) NaCl and 1.49 g (20 mmol) KCl were finely ground and transferred into a 250 ml Schlenk tube. Under a continuous flow of argon the mixture was heated until all solid components are molten. The resulting salt mixture appeared as an off-white powder in quantitative yield.

Melting point (°C): 207-208 (lit. 203 °C);[430]

7.2.1.9 $ZnCl_2$/KCl eutectic salt melt (SM-2)

For preparation of SM-2 3.43 g (46 mmol) anhydrous KCl and 7.36 g (54 mmol) anhydrous $ZnCl_2$ were used. The $ZnCl_2$/KCl eutectic mixture was prepared analogously to 7.2.1.8.

After cooling to room temperature the solid salt mixture appeared as an off-white solid in quantitative yield.

Melting point (°C): 229-231 (lit. 228 °C);[430]

7.2.1.10 SMP-1

In a glovebox, 1,4-DCM (0.30 g, 2.34 mmol) and the eutectic salt mixture SM-1 (0.85 g, 4.68 mmol $ZnCl_2$, see section 7.2.1.8) were weighted in a glass ampoule. The ampoule was sealed analogously to section 7.2.1.1. The ampoule was heated to 250 °C at a heating rate of 10 °C min^{-1} and held at this temperature for 4 d. Then the temperature was raised to 285 °C for 2 d and finally to 310 °C for additional 2 d. The resulting yellowish solid was suspended in 0.1 M aqueous HCl (400 mL) and stirred for 20 h at room temperature. The remaining solid was filtered off and stirred for additional 2 h in methanol (200 mL) at room temperature. Then the solid was filtered off again and washed subsequently with water (100 mL) and THF (100 mL). The final product was obtained as a yellowish powder.

Yield: 0.19 g (63%);

IR (cm^{-1}): 3072 (w, Ar-H), 2229 (m, CN), 1579 (m), 1514 (vs, triazine), 1412 (m, phenyl), 1357 (vs, triazine), 1303 (m), 1184 (m, phenyl), 1148 (w), 1110 (w, phenyl), 1017 (m), 872 (m), 851 (m, phenyl), 811 (vs, phenyl), 745 (m);

Elem. Anal. (%): Calcd: C: 74.99, H: 3.15, N: 21.86;

Found: C: 73.64, H: 3.27, N: 21.22;

7.2.1.11 SMP-2

In a glovebox, 1,4-DCB (0.30 g, 2.34 mmol) and the eutectic salt mixture SM-2 (0.89 g, 4.68 mmol $ZnCl_2$, see section 7.2.1.9) were weighted in a glass ampoule. The ampoule was sealed analogously to section 7.2.1.1. The ampoule was heated to 285 °C at a heating rate of 10 °C min^{-1} and held at this temperature for 4 d. Then the temperature was raised to 310 °C for additional 2 d. The resulting yellowish solid was suspended in 0.1 M aqueous HCl (400 mL) and stirred for 20 h at room temperature. The remaining solid was filtered off and stirred for additional 2 h in methanol (200 mL) at room temperature. Then the solid was filtered off again and washed subsequently with water (100 mL) and THF (100 mL). The final product was obtained as a yellowish powder.

Yield: 0.22 g (73%);

IR (cm^{-1}): 3072 (w, Ar-H), 2229 (m, CN), 1580 (m), 1515 (vs, triazine), 1412 (m, phenyl), 1358 (vs, triazine), 1304 (m), 1183 (m, phenyl), 1147 (w), 1110 (w, phenyl), 1017 (m), 875 (m), 851 (m), 811 (vs, phenyl), 746 (m);

Elem. Anal. (%): Calcd: C: 74.99, H: 3.15, N: 21.86;

Found: C: 74.37, H: 2.71, N: 21.70;

7.2.2 Syntheses of Triazine-based Polyimides

7.2.2.1 General Procedure

In a typical reaction a solution of TAPT in *m*-cresol the respective dianhydride was added in order to provide a molar ratio of 1:1.5 between amine and anhydride functionalities. The amount of dianhydride depended on its solubility in *m*-cresol and was adjusted between 1 to 5 wt%. The mixture was stirred for 10 h at 0 °C, before the ice bath was removed and several drops of isoquinoline were added. After the reaction mixture reached room temperature it was stirred for an additional 12 h. The polymerization was carried out at 80 °C for 4 h, 120 °C for 4 h and 160 °C for 6 h. In the final step the temperature was raised to 190 °C and held for another 18 h. The mixture was cooled down to room temperature before the precipitated polymer was filtered off and washed with toluene (100 mL), dichloromethane (100 mL) and methanol (100 mL) subsequently. Finally the polymer was purified by treatment with THF in a Soxhlet apparatus and dried.

7.2.2.2 TPI-1

PMDA (0.28 g, 1.28 mmol), TAPT (0.30 g, 0.85 mmol) and *m*-cresol (50 mL) were used in this polymerization. The title compound was obtained as a yellowish powder.

Yield: 0.50 g (94%);

IR (cm^{-1}): 1779 (w, imide ring, C=O), 1723 (s, imide ring, C=O), 1606 (w), 1587 (w), 1508 (s, triazine ring), 1415 (m, phenyl), 1352 (vs, imide ring, C-N; triazine ring), 1190 (m, phenyl), 1118 (m, phenyl), 1085 (m), 1017 (m), 830 (m), 810 (vs, phenyl), 723 (s);

Elem. Anal. (%): Calcd: C: 68.90, H: 2.41, N: 13.39;

Found: C: 68.78, H: 3.40, N: 12.46;

7.2.2.3 TPI-2

NTDA (0.34 g, 1.28 mmol), TAPT (0.30 g, 0.85 mmol) and m-cresol (60 mL) were used in this polymerization. The title compound was obtained as a brown powder.

Yield: 0.55 g (92%);

IR (cm^{-1}): 1788 (w, imide ring), 1717 (m, imide ring), 1675 (vs, naphthyl), 1580 (m, naphthyl), 1505 (vs, triazine), 1447 (m), 1412 (m, phenyl), 1362 (m, triazine), 1327 (vs), 1243 (vs, imide ring, C-N), 1178 (m, phenyl), 1018 (m), 980 (m), 813 (s, naphtyl, phenyl), 765 (vs), 708 (m);

Elem. Anal. (%): Calcd: C: 71.90, H: 2.58, N: 11.96;

Found: C: 69.16, H: 3.17, N: 11.40;

7.2.2.4 TPI-3

PTDA (0.50 g, 1.28 mmol), TAPT (0.30 g, 0.85 mmol) and *m*-cresol (75 mL) were used in this polymerization. The title compound was obtained as a dark red powder.

Yield: 0.63 g (83%);

IR (cm^{-1}): 3470 (w), 3375 (w, amine, N-H), 1702 (m, imide ring, C=O), 1656 (m, naphthyl/perylene), 1615 (m, amine), 1592 (m, naphthyl/perylene), 1505 (vs, trazine), 1434 (m), 1413 (m), 1360 (vs, triazine), 1295 (m), 1253 (s, imide ring), 1177 (s, phenyl), 1145 (m), 1019 (m), 958 (m), 860 (m), 811 (vs, phenyl), 798 (vs), 746 (s);

Elem. Anal. (%): Calcd: C: 77.02, H: 2.72, N: 9.46;

Found: C: 71.89, H: 4.19, N: 13.35;

7.2.2.5 TPI-4

BPDA (0.41 g, 1.28 mmol), TAPT (0.30 g, 0.85 mmol) and m-cresol (70 mL) were used in this polymerization. The title compound was obtained as a yellowish powder.

Yield: 0.58 g (87%);

IR (cm^{-1}): 1781 (w, imide ring), 1722 (vs, imide ring), 1607 (w), 1587 (w), 1509 (s, triazine), 1417 (m), 1357 (vs, triazine), 1295 (m), 1248 (m, imide ring), 1207 (m), 1162 (m, phenyl), 1117 (m), 1092 (m), 1018 (w), 863 (w), 814 (vs, phenyl), 720 (s), 710 (s);

Elem. Anal. (%): Calcd: C: 71.26, H: 2.70, N: 10.72;

Found: C: 70.38, H: 2.93, N: 9.98;

7.2.2.6 TPI-5

ODA (0.40 g, 1.28 mmol), TAPT (0.30 g, 0.85 mmol) and m-cresol (65 mL) were used in this polymerization. The title compound was obtained as an off-white powder.

Yield: 0.56 g (86%);

IR (cm^{-1}): 1780 (w, imide ring), 1722 (s, imide ring), 1606 (w), 1587 (w), 1507 (m, triazine ring), 1457 (m), 1416 (w), 1353 (vs, triazine ring), 1272 (s, Ar-O-Ar), 1235 (s, imide ring), 1184 (m, phenyl), 1116 (m), 1077 (m), 1017 (m), 810 (vs, phenyl), 781 (m), 741 (m), 712 (m);

Elem. Anal. (%): Calcd: C: 71.59, H: 2.76, N: 10.98;

Found: C: 69.54, H: 2.93, N: 10.31;

7.2.2.7 TPI-6

HIDA (0.57 g, 1.28 mmol), TAPT (0.30 g, 0.85 mmol) and *m*-cresol (80 mL) were used in this polymerization. The title compound was obtained as an off-white powder.

Yield: 0.72 g (88%);

IR (cm^{-1}): 1788 (w, imide ring), 1727 (vs, imide ring), 1609 (w), 1588 (w), 1510 (s, triazine ring), 1417 (m), 1359 (vs, triazine ring), 1298 (m), 1256 (s, imide ring), 1210 (s, CF_3), 1193 (s, phenyl), 1144 (m, CF_3), 1099 (m), 984 (w), 963 (w), 845 (w), 815 (s, phenyl), 744 (w), 720 (s);

Elem. Anal. (%): Calcd: C: 61.50, H: 2.19, N: 8.69;

Found: C: 61.77, H: 2.22, N: 8.43;

7.2.2.8 TPI-7

SDA (0.46 g, 1.28 mmol), TAPT (0.30 g, 0.85 mmol) and *m*-cresol (70 mL) were used in this polymerization. The title compound was obtained as an off-white powder.

Yield: 0.58 g (81%)

IR (cm^{-1}): 1783 (w, imide ring), 1720 (vs, imide ring), 1605 (w), 1587 (w), 1506 (s, triazine ring), 1416 (m), 1352 (vs, triazine ring), 1325 (vs, SO_2), 1220 (m), 1177 (m, phenyl), 1147 (s, SO_2), 1119 (m), 1080 (m), 1056 (m), 1017 (m), 914 (m), 850 (m), 814 (vs, phenyl), 765 (m), 736 (s), 709 (s), 669 (vs);

Elem. Anal. (%): Calcd: C: 64.51, H: 2.53, N: 10.03;

Found: C: 61.49, H: 3.18, N: 8.78;

7.2.3 Monomer Syntheses

7.2.3.1 *N,N'*-Bis(2,6-dimethylphenyl)-1,2-ethanediimine

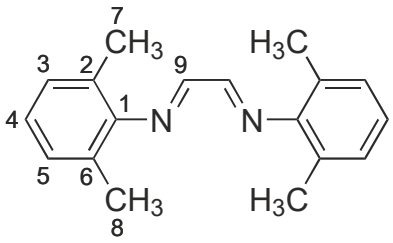

Molecular Formula: $C_{18}H_{20}N_2$

Molecular Weight: 264.16 g mol^{-1}

To a solution of 2,6-dimethylaniline (4.84 g, 40 mmol) in 100 mL ethanol aqueous glyoxal solution (40%, 2.88 g, 20 mmol) was added dropwise and stirred for 16 h at room temperature. After that about 50 mL of the solvent was removed under reduced pressure. The solid crude product was filtered off and recrystallized in methanol. The title compound was obtained as a bright yellow solid.

Yield: 3.33 g (63%);

Melting Point (°C): 154-156;

R_f: 0.63 (cyclohexane/ethyl acetate 4:1);

IR (cm^{-1}): 3023 (w, Ar-H), 2968 (w, Ar-CH_3), 2919 (w, Ar-CH_3), 2853 (w, Ar-CH_3), 1921 (w), 1618 (m, imine, C=N str), 1593 (w, phenyl ring, C=C str), 1472 (m, phenyl ring, C=C str), 1374 (w, phenyl ring, Ar-CH_3 symmetric def), 1184 (m, phenyl ring, C-H in-plane def), 1092 (m, phenyl ring, C-H in-plane def), 1031 (w, phenyl ring, C-H in-plane def), 963 (w, phenyl ring, C-H out-of-plane def), 913 (w, phenyl ring, C-H out-of-plane def), 819 (m, phenyl ring, C-H out-of-plane def), 769 (s, phenyl ring, C-H out-of-plane def), 759 (vs, phenyl ring, C-H out-of-plane def), 675 (m, phenyl ring, out-of-plane ring def);

MS (m/z (%)): 264 (1) $[M]^+$, 250 (100), 132 (39), 117 (10), 105 (13), 77 (11);

^{1}H-NMR ($CDCl_3$): δ (ppm) = 8.13 (s, 2H, H-9), 7.11 (d, 4H, H-3/H-5, $^{3}J_{H,H}$ = 7.6 Hz), 7.05-6997 (m, 2H, H-4), 2.20 (s, 12H, H-7/H-8);

^{13}C-NMR ($CDCl_3$): δ (ppm) = 163.6 (C-9), 150.0 (C-1), 128.4 (C-3/C-5), 126.6 (C-2/ C-6), 124.9 (C-4), 18.4 (C-7/C-8);

Elem. Anal. (%): Calcd: C: 81.78, H: 7.63, N: 10.60;

Found: C: 81.05, H: 6.68, N: 10.48;

7.2.3.2 4,4'-Dicyanobiphenyl (DCBP)

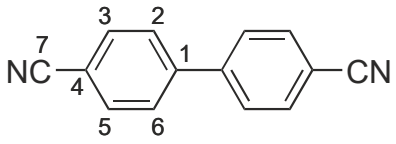

Molecular Formula: $C_{14}H_8N_2$

Molecular Weight: 204.07 g mol^{-1}

To a solution of $CoBr_2$ (10 mol%, 0.5 mmol, 110 mg) and manganese powder (0.82 g, 30 mmol) in acetonitrile (5 mL) 4-bromobenzonitrile (0.91 g, 5 mmol) and trifluoroacetic acid (50 µL, 0.7 mmol) were added at room temperature and stirred for 10 min. Then *N,N'*-bis(2,6-dimethylphenyl)-1,2-ethanediimine (10 mol%, 0.132 mg, 0.5 mmol) was added and the mixture was stirred for 12 h. The reaction mixture was diluted with dichloromethane (200 mL) and filtered. The filtrate was transferred to a separating funnel and hydrolyzed using aqueous hydrochloric acid solution (0.1 M, 100 mL). After drying with $MgSO_4$ the solvent was removed under reduced pressure. The crude product was purified by column chromatography (cyclohexane/ethyl acetate 9:1). The title compound was obtained as an off-white solid.

Yield: 0.40 g (79%);

Melting Point (°C): 234-236;

R_f: 0.50 (cyclohexane/ethyl acetate 2:1);

IR (cm^{-1}): 2225 (s, Ar-CN), 1603 (m, phenyl ring, C=C str), 1490 (m, phenyl ring, C=C str), 1396 (m, phenyl ring, C=C str), 1311 (w, phenyl ring, C-H in-plane def), 1179 (m, phenyl ring,

C-H in-plane def), 1124 (w, phenyl ring, C-H in-plane def), 1005 (w, phenyl ring, C-H in-plane def), 858 (m), 814 (vs, phenyl ring, C-H out-of-plane def), 712 (m, phenyl ring, C-H out-of-plane def);

MS (m/z (%)): 204 (100) $[M]^+$, 177 (17) $[M\text{-}HCN]^+$, 151 (8), 102 (6) $[M\text{-}C_7H_4N]^+$, 75 (10);

^{1}H-NMR (acetone-*d*$_6$): δ (ppm) = 7.98 (d, 4H, C-2/C-6, $^3J_{H,H}$ = 8.7 Hz), 7.92 (d, 4H, C-3/C-5, $^3J_{H,H}$ = 8.7 Hz);

^{13}C-NMR (acetone-*d*$_6$): δ (ppm) = 144.3 (C-1), 133.9 (C-3/C-5), 129.1 (C-2/C-6), 119.2 (C-7), 113.2 (C-4);

Elem. Anal. (%): Calcd: C: 82.33, H: 3.95, N: 13.72;

Found: C: 82.32, H:4.15, N: 13.68;

7.2.3.3 4,4'-Dicyano-2,2'-dimethylbiphenyl (Me$_2$-DCBP)

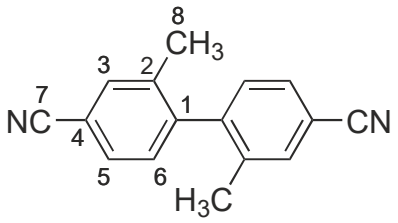

Molecular Formula: $C_{16}H_{12}N_2$

Molecular Weight: 232.28 g mol^{-1}

To a solution of $CoBr_2$ (10 mol%, 0.5 mmol, 110 mg) and manganese powder (0.82 g, 30 mmol) in acetonitrile (5 mL) 4-bromo-3-methylbenzonitrile (0.980 mg, 5 mmol) and trifluoroacetic acid (50 µL, 0.7 mmol) were added at room temperature and stirred for 10 min. Then *N,N'*-bis(2,6-dimethylphenyl)-1,2-ethanediimine (10 mol%, 0.132 mg, 0.5 mmol) was added and the mixture was stirred for 12 h. The reaction mixture was diluted with dichloromethane (200 mL) and filtered. The filtrate was transferred to a separating funnel and hydrolyzed using aqueous hydrochloric acid solution (0.1 M, 100 mL). After drying with $MgSO_4$ the solvent was removed under reduced pressure.

The crude product was recrystallized in methanol. The title compound was obtained as an off-white solid.

Yield: 0.36 g (62%);

Melting Point (°C): 111-112;

R_f: 0.23 (cyclohexane/ethyl acetate 4:1);

IR (cm^{-1}): 3054 (w, Ar-CH_3, Ar-H), 2964 (w, Ar-CH_3, asymmetric str), 2928 (w, Ar-CH_3, symmetric str), 2224 (m, Ar-CN), 1601 (w, phenyl ring, C=C str), 1478 (m, phenyl ring, C=C str), 1443 (w, phenyl ring, C=C str), 1395 (m, phenyl ring, C=C str), 1006 (m, phenyl ring, C-H in-plane def), 907 (m), 884 (m, phenyl ring, C-H out-of-plane def), 835 (s, phenyl ring, C-H out-of-plane def), 822 (vs, phenyl ring, C-H out-of-plane def);

MS (m/z (%)): 232 (98) $[M]^+$, 217 (100) $[M\text{-}CH_3]^+$, 204 (14) $[M\text{-}C_2H_6]^+$, 190 (69), 177 (10), 140 (9), 88 (9);

^{1}H-NMR ($CDCl_3$): δ (ppm) = 7.60 (s, 2H, H-3), 7.56 (d, 2H, H-5, $^3J_{H,H}$ = 7.8 Hz), 7.17 (d, 2H, H-6, $^3J_{H,H}$ = 7.8 Hz), 2.07 (s, 6H, H-8);

^{13}C-NMR ($CDCl_3$): δ (ppm) = 144.6 (C-1), 137.1 (C-2), 133.8 (C-5), 129.8 (C-3/C-6), 129.7 (C-3/C-6), 118.7 (C-7), 112.2 (C-4), 19.7 (C-8);

Elem. Anal. (%): Calcd: C: 82.73, H: 5.21, N: 12.06;

Found: C: 82.71, H: 4.31, N: 12.05;

7.2.3.4 General Synthesis Procedure for Dianhydride Monomers

The respective commercially available (partly) hydrated dianhydride (10 g) was dissolved in boiling acetic anhydride (100 ml). Then the solution was refluxed for 12 h. The reaction was monitored by TLC to ensure a complete conversion to the respective dianhydride. After cooling to room temperature the precipitated dianhydrides were filtered and washed with glacial acetic acid (2×10 ml), transferred to a Schlenk tube, and dried at 50 °C under vacuum. The pure dianhydrides were obtained in almost quantitative yield (>95%).

7.2.3.5 Pyromellitic Dianhydride

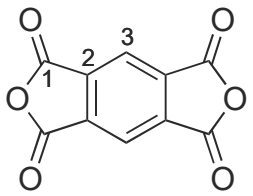

Molecular Formula: $C_{10}H_2O_6$

Molecular Weight: 218.12 g mol^{-1}

Melting Point (°C): 286-288;

R_f: 0.74 (cyclohexane/ethyl acetate 1:1);

IR (cm^{-1}): 1854 (m, C=O str), 1841 (m, C=O str), 1803 (m, C=O str), 1765 (s, C=O str), 1462 (w, phenyl ring, C=C str), 1371 (m, Ar-COOH), 1214 (s, C-O-C str), 1160 (m, C-O-C str), 1074 (m, C-O-C str), 921 (vs, C-O-C str), 911 (vs, C-O-C str), 902 (vs, C-O-C str), 798 (w, phenyl ring, C-H out-of-plane def), 765 (s, phenyl ring, C-H out-of-plane def), 707 (vs, phenyl ring, C-H out-of-plane def);

MS (m/z (%)): 218 (4) $[M]^+$, 174 (100) $[M\text{-}CO_2]^+$, 102 (53) $[M\text{-}C_3O_5]^+$, 74 (33) $[M\text{-}C_4O_6]^+$;

^{1}H-NMR (DMSO-d_6): δ (ppm) = 8.74 (s, 2H, H-3);

^{13}C-NMR (DMSO-d_6): δ (ppm) = 161.4 (C-1), 137.7 (C-2), 121.8 (C-3);

Elem. Anal. (%): Calcd: C: 55.06, H: 0.92;

Found: C: 54.41, H: 1.02;

7.2.3.6 1,4,5,8-Naphthalenetetracarboxylic Dianhydride (NTDA)

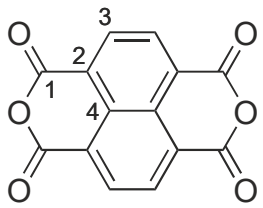

Molecular Formula: $C_{14}H_4O_6$

Molecular Weight: 268.18 g mol^{-1}

Melting Point (°C): 370-372 (dec.);

R_f: 0.74 (cyclohexane/ethyl acetate 1:1);

IR (cm^{-1}): 3119 (w, Ar-H), 3079 (w, Ar-H), 3035 (w, Ar-H), 1760 (s, C=O str), 1744 (m, C=O str), 1578 (m, naphthyl, C=C str), 1515 (w, naphthyl, C=C str), 1436 (w, naphthyl, C=C str), 1292 (s, C-O-C-str), 1231 (s, C-O-C-str), 1156 (m), 1118 (s, C-O-C-str), 1028 (s, C-O-C str), 943 (m), 881 (m, naphthyl rings, C-H out of-plane def), 811 (m), 753 (vs, naphthyl rings, C-H out of-plane def), 695 (s);

MS (m/z (%)): 268 (100) $[M]^+$, 224 (83) $[M\text{-}CO_2]^+$, 180 (32) $[M\text{-}C_2O_4]^+$, 152 (42) $[M\text{-}C_3O_5]^+$, 124 (40) $[M\text{-}C_4O_6]^+$, 98 (16), 74 (27), 62 (36);

^{1}H-NMR (DMSO-*d_6*): δ (ppm) = 8.71 (s, 4H, H-3);

^{13}C-NMR (DMSO-*d_6*): δ (ppm) = 159.4 (C-1), 131.6 (C-3), 128.4 (C-4), 124.6 (C-2);

Elem. Anal. (%): Calcd: C: 62.70, H: 1.50;

Found: C: 61.34, H: 1.63;

7.2.3.7 3,3',4,4'-Benzophenonetetracarboxylic Dianhydride (BPDA)

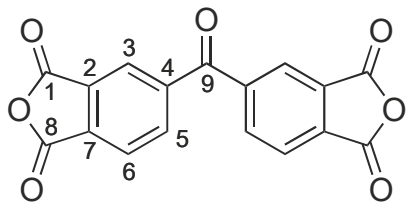

Molecular Formula: $C_{17}H_6O_7$

Molecular Weight: 322.23 g mol^{-1}

Melting Point (°C): 224-226;

R_f: 0.69 (cyclohexane/ethyl acetate 1:1);

IR (cm^{-1}): 3094 (w, Ar-H), 1857 (m, C=O str), 1772 (vs, C=O str), 1666 (m, Ar-CO-Ar), 1618 (m, phenyl ring, C=C str), 1599 (w, phenyl ring, C=C str), 1484 (w, phenyl ring, C=C str), 1426 (w, phenyl ring, C=C str), 1342 (m, Ar-COOH), 1261 (m), 1226 (s, C-O-C str), 1213 (s, C-O-C str), 1157 (m, phenyl ring, C-H in-plane-deformation), 1105 (m, C-O-C str), 1070 (m, phenyl ring, C-H in-plane-deformation), 987 (m), 912 (s, phenyl ring, C-H out-of-plane def), 887 (vs, phenyl ring, C-H out-of-plane def), 817 (s, phenyl ring, C-H out-of-plane def), 735 (m), 709 (vs, phenyl ring, out-of-plane def), 686 (s, phenyl ring, out-of-plane def), 679 (s);

MS (m/z (%)): 323 (25) $[M+1]^+$, 279 (100), 207 (15), 176 (19), 151 (10), 103 (37), 75 (40);

^{1}H-NMR (DMSO-*d_6*): δ (ppm) = 8.31-8.28 (m, 4H, H-3/H-6), 8.27-8.24 (m, 2H, H-5);

^{13}C-NMR (DMSO-*d_6*): δ (ppm) = 192.7 (C-9), 162.5 (C-1/C-8), 162.5 (C-1/C-8), 142.5 (C-4), 136.8 (C-5), 134.4 (C-7), 131.8 (C-2), 125.8 (C-3/C-6), 125.8 (C-3/C-6);

Elem. Anal. (%): Calcd: C: 63.37, H: 1.88;

Found: C: 62.82, H: 2.06;

7.2.3.8 4,4'-Oxydiphthalic Anhydride (ODA)

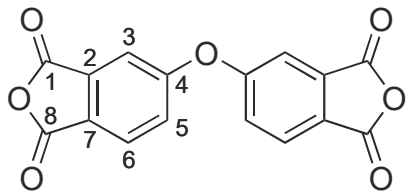

Molecular Formula: $C_{16}H_6O_7$

Molecular Weight: 310.21 g mol^{-1}

Melting Point (°C): 223-225;

R_f: 0.73 (cyclohexane/ethyl acetate 1:1);

IR (cm^{-1}): 3105 (w, Ar-H), 1846 (m, C=O str), 1770 (vs, C=O str), 1606 (m, phenyl ring, C=C str), 1596 (m, phenyl ring, C=C str), 1475 (m, phenyl ring, C=C str), 1445 (m, phenyl ring, C=C str), 1347 (w, Ar-COOH), 1272 (vs, Ar-O-Ar), 1258 (vs, Ar-O-Ar), 1223 (m, C-O-C str), 1156 (m, phenyl ring, C-H in-plane def), 1105 (m, C-O-C str), 1081 (m, phenyl ring, C-H in-plane def), 946 (m), 929 (m), 900 (s, C-O-C str), 875 (vs, phenyl ring, C-H out-of-plane def), 793 (s, phenyl ring, C-H out-of-plane def), 760 (m), 747 (m), 735 (s, phenyl ring, C-H out-of-plane def), 729 (s, phenyl ring, C-H out-of-plane def), 691 (m, phenyl ring, C-H out-of-plane def), 673 (m);

MS (m/z (%)): 310 (41) $[M]^+$, 266 (100) $[M\text{-}CO_2]^+$, 238 (19) $[M\text{-}C_2O_3]^+$, 194 (75) $[M\text{-}C_3O_5]^+$, 166 (32) $[M\text{-}C_4O_6]^+$, 137 (11), 111 (10), 75 (33), 63 (17);

^{1}H-NMR (DMSO-d_6): δ (ppm) = 8.19 (dd, 2H, H-6, $^3J_{H,H}$ = 8.2 Hz, $^5J_{H,H}$ = 0.6 Hz), 7.77 (dd, 2H, H-3, $^4J_{H,H}$ = 2.2 Hz, $^5J_{H,H}$ = 0.6 Hz), 7.74 (dd, 2H, H-5, $^3J_{H,H}$ = 8.2 Hz, $^4J_{H,H}$ = 2.2 Hz);

^{13}C-NMR (DMSO-d_6): δ (ppm) = 162.4 (C-4), 161.5 (C-1/C-8), 161.5 (C-1/C-8), 134.3 (C-2), 128.1 (C-6), 127.0 (C-7), 126.9 (C-5), 115.3 (C-3);

Elem. Anal. (%): Calcd: C: 61.95, H: 1.95;

Found: C: 61.09, H: 2.14;

7.2.3.9 4,4'-(Hexafluoroisopropylidene)diphthalic Anhydride (HIDA)

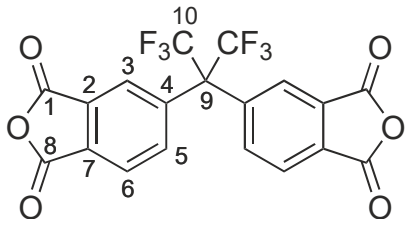

Molecular Formula: $C_{19}H_6F_6O_6$

Molecular Weight: 444.24 g mol^{-1}

Melting Point (°C): 242-244;

R_f: 0.78 (cyclohexane/ethyl acetate 1:1);

IR (cm^{-1}): 1852 (m, C=O str), 1778 (vs, C=O str), 1437 (w, phenyl ring, C=C str), 1340 (w, Ar-COOH), 1255 (s, C-O-C str), 1241 (s, CF_3), 1213 (m, C-O-C str), 1190 (s, CF_3), 1149 (s, CF_3), 1117 (m, phenyl ring, C-H in-plane def), 1103 (m, C-O-C str), 987 (m), 964 (m, phenyl ring, C-H out-of-plane def), 928 (m, phenyl ring, C-H out-of-plane def), 895 (vs, C-O-C str), 864 (w), 848 (m, phenyl ring, C-H out-of-plane def), 837 (m), 734 (m), 717 (vs, phenyl ring, C-H out-of-plane def), 689 (m, phenyl ring, C-H out-of-plane def);

MS (m/z (%)): 444 (39) $[M]^+$, 400 (100) $[M\text{-}CO_2]^+$, 344 (6), 328 (55) $[M\text{-}C_3O_5]^+$, 300 (13) $[M\text{-}C_4O_6]^+$, 231 (31), 178 (28), 115 (16), 75 (20);

^{1}H-NMR (DMSO-*d_6*): δ (ppm) = 8.29 (d, 2H, H-6, $^3J_{H,H}$ = 8.2 Hz), 8.01 (d, 2H, H-5, $^3J_{H,H}$ = 8.2 Hz), 7.85 Hz (s, 2H, H-3);

^{13}C-NMR (DMSO-d_6): δ (ppm) = 162.3 (C-1/C-8), 162.2 (C-1/C-8), 138.5 (C-4/C-5), 137.0 (C-4/C-5), 132.9 (C-2/C-7), 132.6 (C-2/C-7), 126.3 (C-3/C-6), 125.6 (C-3/C-6), 121.2 (C-10), 64.6 (C-9);

Elem. Anal. (%): Calcd: C: 51.37, H: 1.36;

Found: C: 51.22, H: 1.68;

7.2.3.10 4,4'-Sulfonyldiphthalic Anhydride (SDA)

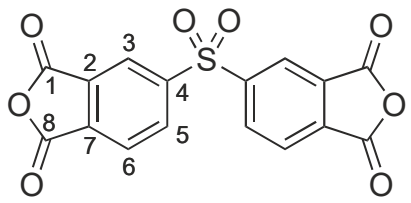

Molecular Formula: $C_{16}H_6O_6S$

Molecular Weight: 358.28 g mol^{-1}

Melting Point (°C): 286-288;

R_f: 0.73 (cyclohexane/ethyl acetate 1:1);

IR (cm^{-1}): 3103 (w, Ar-H), 1861 (m, C=O str), 1814 (m, C=O str), 1788 (m, C=O str), 1774 (vs, C=O str), 1425 (m, phenyl ring, C=C str), 1353 (m, Ar-COOH), 1326 (m, SO_2 asymmetric str), 1251 (s, C-O-C str), 1179 (m, C-O-C str), 1151 (m, SO_2 symmetric str), 1119 (m, phenyl ring, C-H in-plane def), 1104 (m, C-O-C str), 1057 (m, C-O-C str), 911 (vs, C-O-C str), 886 (s, phenyl ring, C-H out-of-plane def), 862 (m), 736 (m, phenyl ring, C-H out-of-plane def), 717 (s, phenyl ring, C-H out-of-plane def), 704 (m), 665 (vs, phenyl ring, C-H out-of-plane def);

MS (m/z (%)): 358 (4) $[M]^+$, 314 (100) $[M\text{-}CO_2]^+$, 242 (6) $[M\text{-}C_3O_5]^+$, 103 (57), 75 (50);

^{1}H-NMR (DMSO-*d*$_6$): δ (ppm) = 8.89 (dd, 2H, H-3, $^{4}J_{H,H}$ = 1.6 Hz, $^{5}J_{H,H}$ = 0.7 Hz), 8.72 (dd, 2H, H-5, $^{3}J_{H,H}$ = 8.0 Hz, $^{4}J_{H,H}$ = 1.6 Hz), 8.33 (dd, 2H, H-6, $^{3}J_{H,H}$ = 8.0 Hz, $^{5}J_{H,H}$ = 0.7 Hz);

^{13}C-NMR (DMSO-*d*$_6$): δ (ppm) = 161.9 (C-1/C-8), 161.7 (C-1/C-8), 146.1 (C-4), 136.3 (C-7), 135.5 (C-5), 133.0 (C-2), 126.8 (C-6), 125.2 (C-3);

Elem. Anal. (%): Calcd: C: 53.64, H: 1.69;

Found: C: 53.09, H: 1.80;

7.2.3.11 1,3,5-Tris(*p*-aminophenyl)benzene (TAPB)

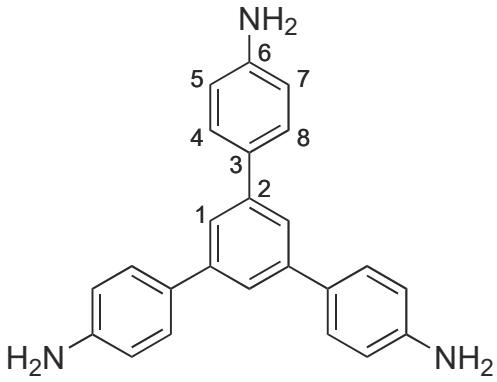

Molecular Formula: $C_{24}H_{21}N_3$

Molecular Weight: 351.44 g mol^{-1}

In a 250 mL flask $SiCl_4$ (20 mL, 0.18 mol) was added dropwise to a solution of 4-nitroacetophenone (10.0 g, 60 mmol) in absolute ethanol (50 mL) at 0 °C. In the following the mixture was refluxed for 16 h. After cooling to room temperature, saturated ammonium chloride solution (100 mL) was added and the mixture was stirred for an additional 30 min. The yellow precipitate was filtered and washed twice with water (2×30 mL) and dried. Afterward the yellow solid was added to a suspension of Pd/C (10 wt%, 800 mg) in absolute ethanol (100 mL). After heating the mixture to reflux hydrazine monohydrate (98%, 20 mL) was added carefully to the hot solution. Then the suspension was refluxed for an additional 18 h. The mixture was filtrated hot (Caution!), the obtained filtrate was cooled to room temperature.

The off-white crude product was filtered off and recrystallized in absolute ethanol. The title compound was obtained as a yellowish solid.

Yield: 4.50 g (64%);

Melting Point (°C): 220-222 (dec.);

R_f: 0.36 (cyclohexane/ethyl acetate 1:4);

IR (cm^{-1}): 3433 (m, Ar-NH_2), 3354 (m, Ar-NH_2), 3028 (w, Ar-H), 1620 (s, phenyl ring, C=C str), 1606 (s, phenyl ring, C=C str), 1514 (vs, phenyl ring, C=C str), 1448 (m, phenyl ring, C=C str), 1406 (w, phenyl ring, C=C str), 1279 (s, phenyl ring, C-H in-plane def), 1241 (m, phenyl ring, C-H in-plane def), 1176 (s, phenyl ring, C-H in-plane def), 1127 (m, phenyl ring, C-H in-plane def), 871 (m, central phenyl ring, C-H out-of-plane def), 822 (vs, phenyl ring, C-H out-of-plane def), 730 (m, phenyl ring, C-H out-of-plane def), 706 (s, central phenyl ring, out-of-plane ring def);

MS (m/z (%)): 351 (100) $[M]^+$, 288 (8), 251 (12);

^{1}H-NMR (DMSO-d_6): δ (ppm) = 7.47 (s, 3H, H-1), 7.46 (d, 6H, H-4/H-8, $^3J_{H,H}$ = 8.6 Hz), 6.67 (d, 6H, H-5/H-7, $^3J_{H,H}$ = 8.6 Hz), 5.19 (s, 6H, NH_2);

^{13}C-NMR (DMSO-d_6): δ (ppm) = 148.4 (C-6), 141.6 (C-2), 128.1 (C-3), 127.5 (C-4/C-8), 120.4 (C-1), 114.3 (C-5/C-7);

Elem. Anal. (%): Calcd: C: 82.02, H: 6.02, N: 11.96;

Found: C: 79.99, H: 5.54, N: 11.97;

7.2.3.12 *N,N*-Bis(*p*-nitrophenyl)-1,4-phenylenediamine

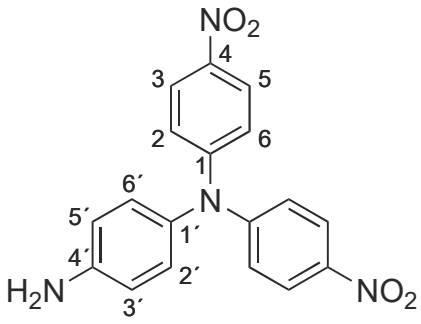

Molecular Formula: $C_{18}H_{14}N_4O_4$

Molecular Weight: 350.33 g mol^{-1}

To a solution of 1,4-phenylenediamine (2.16 g, 20 mmol) in anhydrous DMSO (50 mL) 4-fluoronitrobenzene (5.64 g, 40 mmol) and anhydrous K_2CO_3 (11.06 g, 80 mmol) were added and the mixture was stirred at 90 °C for 3 d. After cooling to room temperature the mixture was poured into water (500 ml). The dark red precipitate was collected by filtration and dissolved in ethyl acetate (500 ml). The organic phase was washed twice with saturated sodium chloride solution (2×100 ml) and dried with anhydrous $MgSO_4$. After evaporation of the solvent the dark red crude product was purified by column chromatography (cyclohexane/ethyl acetate 1:1). The title compound was obtained as a dark red solid.

Yield: 6.15 g (88%);

Melting Point (°C): 232-234;

R_f: 0.4 (cyclohexane / ethyl acetate 1:1);

IR (cm^{-1}): 3472 (w, Ar-NH_2), 3380 (w, Ar-NH_2), 3071 (w, Ar-H), 2923 (w, Ar-H), 1619 (w, phenyl ring, C=C str), 1600 (m, phenyl ring, C=C str), 1575 (s, Ar-NO_2, asymmetric NO_2 str), 1489 (s, phenyl ring, C=C str), 1338 (s, center N, C-N str), 1324 (s, Ar-NO_2, symmetric NO_2 str), 1306 (s, Ar-NH_2, C-N str), 1266 (vs, phenyl ring, C-H in-plane def), 1179 (s, phenyl ring, C-H in-plane def), 1107 (vs, Ar-NO_2, C-N str), 1005 (m, phenyl ring, C-H in-plane def), 917 (w), 836 (s, phenyl ring, C-H out-of-plane def), 749 (s, Ar-NO_2), 723 (m, phenyl ring, C-H out-of-plane def), 694 (m);

MS (m/z (%)): 350 (100) $[M]^+$, 304 (17) $[M\text{-}NO_2]^+$, 258 (25) $[M\text{-}N_2O_4]^+$;

^{1}H-NMR (DMSO-*d*$_6$): δ (ppm) = 8.15 (d, 4H, H-3/H-5, $^3J_{H,H}$ = 9.3 Hz), 7.17 (m, 4H, H-2/H-6, $^3J_{H,H}$ = 9.3 Hz), 6.92 (d, 2H, H-3′/H-5′, $^3J_{H,H}$ = 8.7 Hz), 6.65 (d, 2H, H-2′/H-6′, $^3J_{H,H}$ = 8.7 Hz), 5.41 (s, 2H, NH_2);

^{13}C-NMR (DMSO-*d*$_6$): δ (ppm) = 152.0 (C-1), 148.4 (C-4′), 141.3 (C-4), 131.9 (C-1′), 128.8 (C-2′/C-6′), 125.4 (C-2/C-6), 121.3 (C-3/C-5), 115.2 (C-3′/C-5′);

Elem. Anal. (%): Calcd: C: 61.71, H: 4.03, N: 15.99;

Found: C: 62.10, H: 4.42, N: 15.32;

7.2.3.13 Tris(*p*-aminophenyl)amine (TAPA)

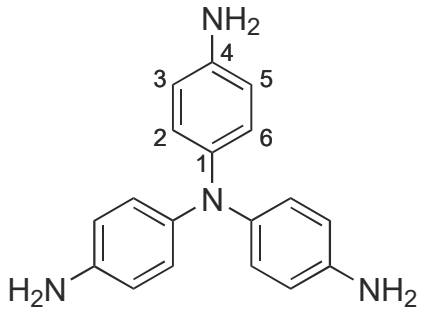

Molecular Formula: $C_{18}H_{18}N_4$

Molecular Weight: 290.36 g mol^{-1}

To a solution of *N,N*-bis(*p*-nitrophenyl)-1,4-phenylenediamine (0.210 g, 0.60 mmol) in THF/EtOH (2:1, 10 ml) a small amount of Pd/C (10 wt.%, 0.015 g) was added. After the addition of hydrazine monohydrate (0.15 mL) the mixture was refluxed for 20 h. After cooling to room temperature the mixture was filtered through a celite pad. After the filtrate was concentrated to dryness the solid residue was recrystallized in ethanol. The title compound was obtained as blue grey crystals.

Yield: 0.035 g (20%);

Melting Point (°C): 241-243 (dec.);

R_f: 0.22 (cyclohexane/ethyl acetate 1:4);

IR (cm^{-1}): 3405 (w, Ar-NH_2), 3336 (m, Ar-NH_2), 3032 (w, Ar.-H), 3004 (w, Ar-H), 1618 (m, phenyl ring, C=C str), 1498 (vs, phenyl ring, C=C str), 1328 (s, center N, C-N str), 1305 (m, Ar-NH_2, C-N str), 1256 (vs, phenyl ring, C-H in-plane def), 1174 (m, phenyl ring, C-H in-plane def), 1121 (m, phenyl ring, C-H in-plane def), 1082 (w), 1009 (w, phenyl ring, C-H in-plane def), 911 (w), 825 (vs, phenyl ring, C-H out-of-plane def), 719 (s, phenyl ring, C-H out-of-plane def);

MS (m/z (%)): 290 (100) $[M]^+$, 198 (8) $[M-C_6H_6N]^+$, 182 (8), 145 (6);

^{1}H-NMR (DMSO-d_6): δ (ppm) = 6.59 (s, 6H, H-3/H-5), 6.43 (d, 6H, H-2/H-6, $^3J_{H,H}$ = 8.5 Hz), 4.69 (s, 6H, NH_2);

^{13}C-NMR (DMSO-d_6): δ (ppm) = 143.2 (C-4), 138.5 (C-1), 124.1 (C-2/C-6), 114.8 (C-3/C-5);

Elem. Anal. (%): Calcd: C: 74.46, H: 6.25, N: 19.30;

Found: C: 74.63, H: 6.18, N: 19.33;

7.2.3.14 2,4,6-Tris(*p*-bromophenyl)-1,3,5-triazine (TBPT)

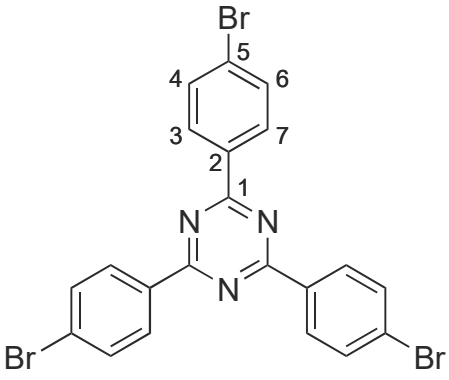

Molecular Formula: $C_{21}H_{12}Br_3N_3$

Molecular Weight: 542.86 g mol^{-1}

A flame dried 500 mL-flask was equipped with a magnetic stirrer and dry chloroform (150 mL). After cooling the solvent to 0 °C with an ice bath trifluoromethanesulfonic acid

(10.0 g, 66.7 mmol) was added carefully under vigorous stirring. Then 4-bromobenzonitrile (6.00 g, 33.0 mmol) was added in small portions. The reaction mixture was stirred at 0 °C for 1 h and afterwards for further 24 h at room temperature. Then water (200 mL) was added to the reaction mixture and a white precipitate formed. After stirring for additional 3 h the suspension was filtered and the resulting white solid was washed twice with water and afterwards with ethanol and diethyl ether. The crude product was recrystallized in toluene and dried. The title compound was obtained as a white solid.

Yield: 3.90 g (65%);

Melting Point (°C): 361-363;

R_f: 0.79 (cyclohexane/ethyl acetate 4:1);

IR (cm^{-1}): 1590 (w, phenyl ring, C=C str), 1579 (s, phenyl ring, C=C str), 1541 (w, phenyl ring, C=C str), 1512 (vs, triazine ring, in-plane str), 1486 (m, phenyl ring, C=C str), 1401 (m, triazine ring in-plane str), 1369 (m), 1354 (s, triazine ring, in-plane str), 1172 (w, phenyl ring, C-H, in-plane def), 1067 (m, Ar-Br, str), 1009 (s, phenyl ring, C-H, in-plane def), 842 (m, triazine ring, out-of-plane bend), 805 (vs, phenyl, out-of-plane def);

MS (m/z (%)): 545 (100) $[M]^+$, 283 (7), 181 (85), 155 (7), 102 (77), 75 (18), 52 (8);

^{1}H-NMR ($CDCl_3$): δ (ppm) = 8.61 (m, 6H, H-3/H-7), 7.71 (m, 6H, H-4/H-6);

^{13}C-NMR (C_6D_5Br): δ (ppm) = 171.0 (C-1), 134.9 (C-2), 131.8 (C-4/C-6), 130.5 (C-3/C-7), 127.7 (C-5);

Elem. Anal. (%): Calcd: C: 46.19, H: 2.22, N: 7.70;

Found: C: 46.04, H: 2.69, N: 7.72;

7.2.3.15 2,4,6-Tris(*p*-aminophenyl)-1,3,5-triazine (TAPT)

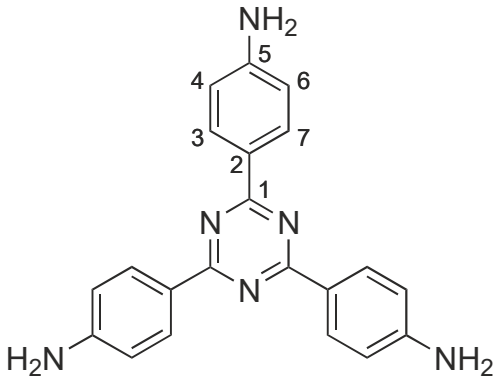

Molecular Formula: $C_{21}H_{18}N_6$

Molecular Weight: 354.16 g mol^{-1}

Under argon atmosphere $Pd(dba)_2$ (403 mg, 0.70 mmol) and $P(t\text{-}Bu)_3$ (10 wt% in hexane, 0.70 mmol, 2.08 mL) were added to 35 mL dry toluene at room temperature. After stirring the mixture for 10 min a solution of LiHMDS in hexanes (1.0 M, 23.1 mL, 23.1 mmol) and TBPT (3.82 g, 7.00 mmol) were added. The mixture was stirred for 48 h at 80 °C before it was quenched with aqueous hydrochloric acid (1.0 M, 30 mL) and diluted with water (50 mL). The viscous suspension was filtered and washed with aqueous hydrochloric acid (1.0 M, 50 mL), water (150 mL) and ethyl acetate (10 mL). The filtrate was transferred to a separating funnel. The separated organic phase was washed once with 1.0 M hydrochloric acid (50 mL). The aqueous phases were combined and washed three times with diethyl ether (50 mL). The separated aqueous dark yellow phase was treated carefully with sodium hydroxide solution (1.0 M) until a precipitate was formed. The pale yellow solid was collected by filtration, recrystallized in NMP and dried overnight at 100 °C. The title compound was obtained as a yellow solid.

Yield: 1.44 g (58%);

Melting Point (°C): 376-378 (dec.);

R_f: 0.55 (cyclohexane/ethyl acetate 1:4);

IR (cm^{-1}): 3459 (w, Ar-NH_2, asymmetric str), 3320 (m, Ar-NH_2), 3030 (w, Ar-H), 1631 (m), 1604 (s, phenyl ring, C=C str), 1578 (m, triazine ring, in-plane str), 1486 (vs, phenyl ring, C=C str), 1429 (s, phenyl ring, C=C str), 1363 (vs, triazine ring, in-plane str), 1293 (s, phenyl ring, C-H in-plane def), 1176 (s,

phenyl ring, C-H in-plane def), 1145 (s), 1129 (m, phenyl ring, C-H in-plane def), 1009 (w, phenyl ring, C-H in-plane def), 851 (w, triazine ring, out-of-plane def), 810 (vs, phenyl ring, C-H out-of-plane def);

MS (m/z (%)): 354 (100) $[M]^+$, 339 (19), 235 (5), 177 (7), 118 (94), 91 (11);

^{1}H-NMR (acetone-*d*$_6$): δ (ppm) = 8.50 (m, 6H, H-3/H-7), 6.81 (m, 6H, H-4/H-6), 5.32 (s, 6H, NH_2);

^{13}C-NMR (acetone-*d*$_6$): δ (ppm) = 171.2 (C-1), 153.5 (C-5), 131.3 (C-3/C-7), 125.7 (C-2), 114.4 (C-4/C-6);

Elem. Anal. (%): Calcd: C: 71.17, H: 5.12, N: 23.71;

Found: C: 70.93, H: 4.48, N: 22.63;

7.2.3.16 2,4,6-Triphenyl-1,3,5-triazine (TPT)

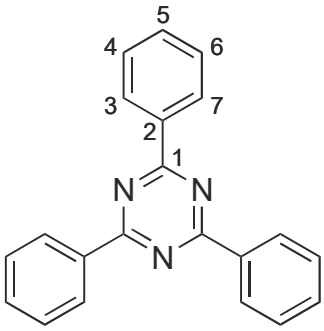

Molecular Formula: $C_{21}H_{15}N_3$

Molecular Weight: 309.36 g mol^{-1}

In a 500 mL flask 10.0 g trifluoromethane sulfonic acid (66.7 mmol) were added quickly to 150 ml dry Chloroform at 0 °C. Then benzonitrile (3.4 g, 33 mmol, 3.37 mL) was added dropwise and the mixture was stirred for 1 h at 0 °C. Afterwards the ice bath was removed and the mixture was stirred for additional 24 h. After adding water (200 mL) the mixture was stirred vigorously for 1 h and then transferred to a separating funnel. The organic phase was treated with saturated potassium carbonate solution (Caution! Gas evolution (carbon dioxide)!) until the aqueous phase reacted neutral. The organic phase was washed twice with water before it was dried with anhydrous $MgSO_4$. The solvent was removed

with a rotary evaporator and the resulting off-white solid was recrystallized in toluene. The title compound was obtained as white crystals.

Yield: 2.45 g (72%);

Melting Point (°C): 236-238;

R_f: 0.68 (cyclohexane/ethyl acetate 4:1);

IR (cm^{-1}): 3059 (w, Ar-H), 3029 (w, Ar-H), 1589 (m, phenyl ring, C=C str), 1516 (vs, triazine ring, in-plane str), 1444 (s, phenyl ring, C=C str), 1364 (vs, triazine ring, in-plane str), 1299 (m, phenyl ring, C-H in-plane def), 1173 (m, phenyl ring, C-H in-plane def), 1145 (m, phenyl ring, C-H in-plane def), 1067 (m, phenyl ring, C-H in-plane def), 1027 (m, phenyl ring, C-H in-plane def), 1001 (w, m, phenyl ring, C-H in-plane def), 839 (s, triazine ring, out-of-plane def), 741 (vs, phenyl ring, out-of-plane def), 679 (vs, phenyl ring, out-of-plane def);

MS (m/z (%)): 309 (66) $[M]^+$, 103 (100) $[M\text{-}C_7H_5N]^+$, 76 (18);

^{1}H-NMR (C_6D_6): δ (ppm) = 8.90-8.82 (m, 6H, H-3/H-7), 7.39-7.27 (m, 9H, H-4/H-5/H-6);

^{13}C-NMR (C_6D_6): δ (ppm) = 172.0 (C-1), 136.9 (C-2), 132.6 (C-5), 129.5 (C-4/C-6), 128.8 (C-3/C-7);

Elem. Anal. (%): Calcd: C: 81.53, H: 4.89, N: 13.58;

Found: C: 80.77, H: 4.59, N: 13.32;

8 Appendix

8.1 Langmuir Adsorption Theory

The adsorption of a particle on the sorbent surface depends on the partial pressure p and the fraction of unoccupied sorbent surface area θ_0. The number of gas molecules adsorbing on the sorbent surface N_{ads} is

$$N_{ads} = k_{ads} p \theta_0 \tag{8.1}$$

where k_{ads} is the constant for the adsorption rate and includes the probability of a gas molecule adsorbing on the sorbent surface. Analogously the number of molecules desorbing from the sorbent surface can be written as

$$N_{des} = k_{des} \theta_1 e^{\frac{-E}{RT}} \tag{8.2}$$

where θ_1 is the surface fraction occupied by the adsorbate layer, E stands for the adsorption energy, R is the universal gas constant and T the temperature of the system. Desorption constant k_{des} and term $e^{-E/RT}$ describe the probability of a particle in the adsorbate layer desorbing from the surface.

The Langmuir adsorption model is able to predict the surface area of a specific sorbent by the number of adsorbed molecules in a single adsorbate monolayer.[394] Therefore, if the cross-sectional area σ_0 of one adsorbed molecule on the sorbent surface is known, the sorbent surface area S_0 is calculated by

$$S_0 = N_M \sigma_0 = \frac{V_M N_A \sigma_0}{V_0} \tag{8.3}$$

where V_m is the volume of the adsorbate monolayer, V_0 is the adsorbate molecular volume, N_A is Avogardro´s number and σ_0 is the cross-sectional area of one single adsorbate particle occupied on the sorbent surface. By assuming a constant number of energetically equal adsorption sites and neglecting an interaction between the adsorptive molecules, the equilibrium state between adsorption (8.1) and desorption processes (8.2) is described as

$$k_{ads} p \theta_0 = k_{des} \theta_1 e^{\frac{-E}{RT}} \tag{8.4}$$

For the Langmuir model, where only one adsorbate layer can be formed and the term $\theta_0 = 1\text{-}\theta_1$ is valid, a rearrangement of equation (8.4) gives

$$k_{des}\theta_1 e^{\frac{-E}{RT}} = k_{ads}p - k_{ads}p\theta_1 \tag{8.5}$$

and then

$$\theta_1 = \frac{k_{ads}p}{k_{des}e^{\frac{-E}{RT}} + k_{ads}p} \tag{8.6}$$

When assuming a constant energy of adsorption E and introducing K as

$$K = \frac{k_{ads}}{k_{des}e^{\frac{-E}{RT}}} \tag{8.7}$$

equation (8.6) can be rewritten as

$$\theta_1 = \frac{N_{ads}}{N_M} = \frac{Kp}{1 + Kp} \tag{8.8}$$

Equation (8.8) is known as the Langmuir equation. By setting

$$\theta_1 = \frac{N_{ads}}{N_M} = \frac{V_{ads}}{V_M} \tag{8.9}$$

where V_{ads} is the volume of the adsorbed particles and V_M is the monolayer volume, the Langmuir equation is transferred to its linear form

$$\frac{p}{V_{ads}} = \frac{1}{V_M}p + \frac{1}{KV_M} \tag{8.10}$$

By plotting p/V against p, the values for K and V_M can be calculated from the slope and the intercept of the linear graph. The surface area of the sample is calculated by inserting the value of V_M in equation (8.3).

8.2 The BET Adsorption Theory

The BET adsorption theory extends the Langmuir adsorption theory to the formation of multiple adsorbate layers on the sorbent surface. The BET theory is able to handle adsorption and desorption mechanisms based on physisorptive interactions, where the uppermost adsorbate layer is in a state of dynamic equilibrium with the adsorptive phase.[375,396] For a unified total surface area, the addition of the surface fractions of all occurring adsorbate layers is given as

$$\sum_{i=0}^{\infty} \theta_i = 1 \tag{8.11}$$

where θ_i represents the surface fractions on the sorbent that are occupied by exactly i layers of adsorbed molecules. The adsorption principle of equation (8.11) is explained in Figure **8-1**, displaying the surface fractions for three adsorbate layers.

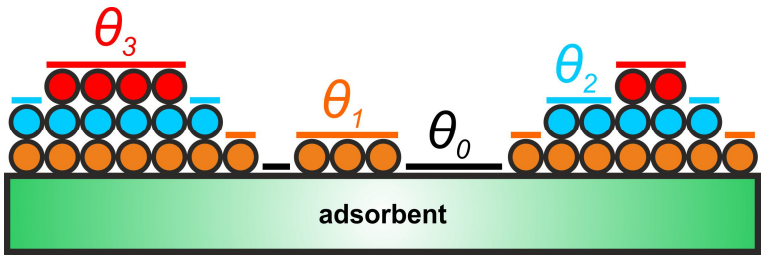

Figure 8-1: *Schematic representation of the first three adsorbate layers on a sorbent surface with the respective surface fractions*

Alternatively, the fraction of unoccupied surface θ_0 can also be expressed as

$$\theta_0 = 1 - \sum_{i=1}^{\infty} \theta_i \tag{8.12}$$

A state of equilibrium between the sorbent surface and the first adsorbate layer is described similarly to equation (8.4) as

$$k_{ads,1} p \theta_0 = k_{des,1} \theta_1 e^{\frac{-E_1}{RT}} \tag{8.13}$$

Accordingly, if two adsorbate layers are formed, the equilibrium for the second layer is described as

$$k_{ads,2} p \theta_1 = k_{des,2} \theta_2 e^{\frac{-E_2}{RT}} \tag{8.14}$$

and for the third layer as

$$k_{ads,3} p \theta_2 = k_{des,3} \theta_3 e^{\frac{-E_3}{RT}} \tag{8.15}$$

Theoretically, the formation of an infinite number of adsorbate layers is possible and for the *i*-th adsorbate layer the equilibrium is given as

$$k_{ads,i} p \theta_{i-1} = k_{des,i} \theta_i e^{\frac{-E_i}{RT}} \tag{8.16}$$

The BET theory does not consider a possible polarization effect on the adsorbate layers and assumes *E,* k_{ads} and k_{des} as constant for the second and higher layers.[375,396] Therefore, it is only necessary to distinguish between the sorbent/adsorbate interactions for the sample surface and the first adsorbate layer and the adsorbate/adsorbate interactions for the second and higher layers. For the first case $i = 1$ equation (8.12) is rewritten as

$$\frac{\theta_1}{\theta_0} = \frac{k_{ads,1} p}{k_{des,1} e^{\frac{-E_1}{RT}}} = y \tag{8.17}$$

whereas for the latter case ($i > 1$)the term

$$\frac{\theta_2}{\theta_1} = \frac{\theta_i}{\theta_{i-1}} = \frac{k_{ads,2} p}{k_{des,2} e^{\frac{-E_2}{RT}}} = x \tag{8.18}$$

is valid. The relation between the terms *x* and *y* is described by the *C*-constant as

$$y = Cx \tag{8.19}$$

On the basis of the equations (8.17), (8.18) and (8.19) the *C*-constant can be defined as

$$C = \frac{k_{ads,1} k_{des,2}}{k_{ads,2} k_{des,1}} e^{\frac{E_1 - E_2}{RT}} \tag{8.20}$$

For the calculation of the total number of adsorbed particles N_{ads}, the number of occurring adsorbate layers *i* is multiplied with the fraction of a complete monolayer N_M of the

respective adsorbate phase. When considering the underlying adsorbate layers, the total amount of adsorbed adsorptive particles N_{ads} is obtained from

$$N_{ads} = N_M\theta_1 + 2N_M\theta_2 + \cdots + iN_M\theta_i = N_M\sum_{i=1}^{\infty} i\theta_i \tag{8.21}$$

Regarding (8.17), (8.18) and (8.19), the surface fraction of every occurring adsorbate layer can be expressed as a term of θ_0, giving

$$\theta_1 = y\theta_0 = Cx\theta_0 \tag{8.22}$$

$$\theta_2 = x\theta_1 = Cx^2\theta_0 \tag{8.23}$$

$$\theta_3 = x\theta_2 = Cx^3\theta_0 \tag{8.24}$$

and in the general form

$$\theta_i = x\theta_{i-1} = Cx^i\theta_0 \tag{8.25}$$

Substitution θ_i in equation (8.21) yields

$$N_{ads} = N_M\sum_{i=1}^{\infty} iCx^i\theta_0 = N_MC\theta_0\sum_{i=1}^{\infty} ix^i \tag{8.26}$$

where for $x < 1$ the geometric series on the right side can be written as

$$\sum_{i=1}^{\infty} ix^i = \frac{x}{(1-x)^2} \tag{8.27}$$

and accordingly yields

$$\frac{N_{ads}}{N_M} = \frac{Cx\theta_0}{(1-x)^2} \tag{8.28}$$

For $x = 1$ the term N_{ads}/N_M would become infinite. This behavior would be physically reasonable for applied pressures equal to the vapor pressure p_0 of the pure adsorbate, where the adsorptive condenses at the sample surface.[375] Hence, similar to (8.18) one can write

$$\frac{k_{ads,2}}{k_{des,2}e^{\frac{-E_2}{RT}}}p_0 = 1 \tag{8.29}$$

or

$$\frac{1}{p_0} = \frac{k_{ads,2}}{k_{des,2}e^{\frac{-E_2}{RT}}} \tag{8.30}$$

The combination of equations (8.18) and (8.30) yields

$$\frac{1}{p_0} = \frac{k_{ads,2}}{k_{des,2}e^{\frac{-E_2}{RT}}} = \frac{x}{p} \tag{8.31}$$

and then

$$x = \frac{p}{p_0} \tag{8.32}$$

where $x < 1$, if the applied pressure p lies below the vapor pressure p_0 of the adsorptive gas. This also validates the expression in equation (8.27).

Returning to equation (8.28), θ_0 is substituted. According to (8.12) and (8.25), θ_0 is

$$\theta_0 = 1 - \sum_{i=1}^{\infty}\theta_i = 1 - \sum_{i=1}^{\infty} C\,x^i\theta_0 \tag{8.33}$$

and can be rewritten as

$$\theta_0 + C\theta_0\sum_{i=1}^{\infty}x^i = 1 \tag{8.34}$$

Again, for $x < 1$ the geometric series can be expressed as

$$\sum_{i=1}^{\infty} x^i = \frac{x}{1-x} \tag{8.35}$$

which is substituted into (8.34), yielding

$$\theta_0 + \frac{C\theta_0 x}{1-x} = 1 \tag{8.36}$$

or

$$\theta_0 = \frac{1}{1+\frac{Cx}{1-x}} = \frac{1-x}{1+x(C-1)} \tag{8.37}$$

At this point term N/N_M in (8.28) can be expressed by only using the parameters C and x. Now (8.28) is

$$\frac{N_{ads}}{N_M} = \frac{Cx(1-x)}{(1-x)^2(1+x(C-1))} = \frac{Cx}{(1-x)(1-x+Cx)} \tag{8.38}$$

and can be rearranged to

$$\frac{1}{N_{ads}}\left(\frac{x}{1-x}\right) = \frac{1}{CN_M} + \frac{C-1}{CN_M}x \tag{8.39}$$

By considering $x = p/p_0$ from (8.32) and $N_{ads}/N_M = V_{ads}/V_M$ from (8.9), the linear form of the BET equation is obtained as

$$\frac{p}{V_{ads}(p_0-p)} = \frac{1}{CV_M} + \frac{C-1}{CV_M}\frac{p}{p_0} \tag{8.40}$$

The values for C and V_M are obtained directly from the slope and the intercept of the linear function. As an example, the calculation of the surface area of TPI-6 from the experimental data is described in the following chapter.

It should be mentioned, that the BET theory assumes the possible formation of an almost infinite number of consecutive adsorbate layers on the sorbent surface. Without this assumption, equations (8.27) and (8.35) would not be valid. Especially for confined geometries in micro- and narrow mesopores, this assumption must be regarded critically. A more detailed discussion on this issue can be found in the literature.[396]

8.3 Calculation of the BET Specific Surface Area

In this chapter, an example of a calculation of the specific surface area of TPI-6 is displayed. For a better understanding, the consecutive calculation steps starting from the original data of the adsorption measurement are shown in detail.

The specific BET surface area is calculated by using a rearranged form of the BET equation (8.40):

$$\frac{1}{V_{ads}\left(\frac{p_0}{p}-1\right)} = \frac{1}{CV_M} + \frac{C-1}{CV_M}\frac{p}{p_0} \tag{8.41}$$

Before calculating the BET specific surface area, it is necessary to obtain the values for the *C*-constant and the monolayer volume V_M. They can be derived directly from the slope and the intercept of the linear BET plot of TPI-6 (Figure 8-2) using the raw analysis data from the sorption measurement in Table 17.

Table 17: *Analysis data for the BET plot of TPI-6.*

data point #	p/p_0[a]	V_{ads} $(cm^3\ g^{-1})$[a]	$1/W_{ads}((p_0/p)-1)$[a]	p_0/p	$1/V_{ads}((p_0/p)-1)$
1	0.05906	134.4227	0.26199	16.9315	4.6695e-04
2	0.06962	136.9739	0.30479	14.4393	5.4323e-04
3	0.07924	139.4442	0.34628	12.6196	6.1718e-04
4	0.08954	141.7086	0.38937	11.1685	6.9398e-04
5	0.10423	144.7738	0.45093	9.59444	8.0370e-04

[a] extracted from the .qps-file of TPI-6 using Quantachrome ASiQ software package

From the slope

$$m = \frac{C-1}{V_M C} \tag{8.42}$$

and the intercept

$$t = \frac{1}{V_M C} \tag{8.43}$$

of the linear fit one can calculate the parameters $C = 278.3$ and $V_M = 133.8$ cm^3 g^{-1}.

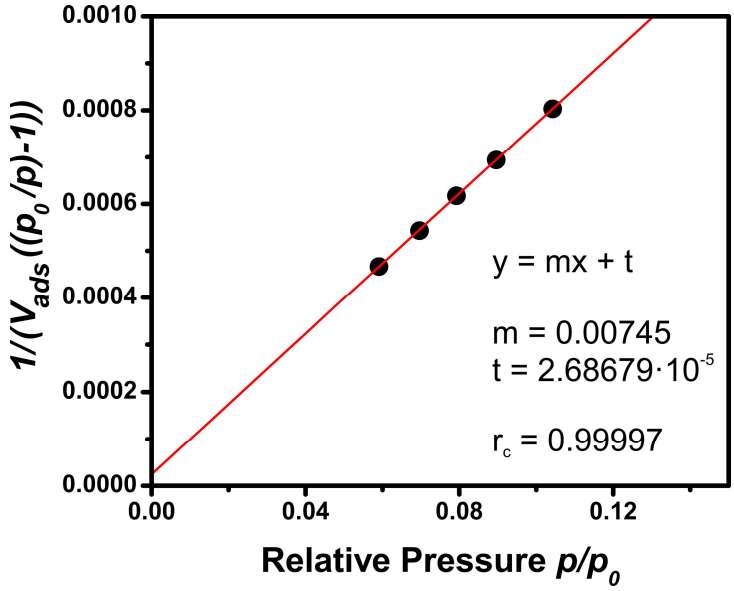

Figure 8-2: *BET plot from the argon adsorption isotherm of TPI-6. The correlation coefficient r_c is displayed.*

Finally, the specific BET surface area of TPI-6 could be obtained from (8.3), by inserting V_M:

$$S_{BET,TPI-6} = \frac{V_M N_A \sigma_0}{V_0} \tag{8.44}$$

$$= \frac{1.337 \cdot 10^{-4} m^3 \cdot 6.022 \cdot 10^{23} mol^{-1} \cdot 1.420 \cdot 10^{-19} m^2}{0.0224 \frac{m^2}{mol}}$$

$$= 510.4 m^2$$

For comparison, the specific BET surface area calculated by the Quantachrome ASiQ software package was 510.1 m^2.[375]

8.4 Selected POP Sorbents for Postcombustion Applications

material	S_{BET} ($m^2\ g^{-1}$)	CO_2 uptake ($mmol\ g^{-1}$)	T (K)	p (bar)	CO_2/N_2 selectivity		Q_{st} ($kJ\ mol^{-1}$)	reference
					Henry	IAST		
ACOF-1	1176	4.02	273	1	40	-	27.6	Li et al.[255]
ALP-1	1235	5.4	273	1	35	40 (15:85)	29.2	Arab et al.[351]
		3.3	298	1	27	28 (15:85)		
ALP-2	1065	4.8	273	1	29	34 (15:85)	27.9	Arab et al.[351]
		2.4	298	1	27	26 (15:85)		
ALP-3	975	3.8	273	1	43	44 (15:85)	29.6	Arab et al.[351]
		2.3	298	1	35	35 (15:85)		
ALP-4	862	3.5	273	1	30	35 (15:85)	28.2	Arab et al.[351]
		1.8	298	1	28	26 (15:85)		
ALP-5	801	4.5	273	1	51	60 (10:90)	325	Arab et al.[352]
		2.9	298	1	41	47 (10:90)		
ALP-6	698	3.4	273	1	46	45 (10:90)	28.6	Arab et al.[352]
		2.2	298	1	47	48 (10:90)		
ALP-7	412	2.5	273	1	47	52 (10:90)	30.7	Arab et al.[352]
		1.5	298	1	43	56 (10:90)		
ALP-8	517	3.0	273	1	48	51 (10:90)	29.4	Arab et al.[352]
		2.0	298	1	48	44 (10:90)		
APOP-1	1298	4.26	273	1	23.8	-	26.6	Song et al.[464]
		2.69	298	1	20.3	-		
APOP-1-OH	875	2.89	273	1	35.1	-	30.0	Song et al.[464]
		1.86	298	1	26.0	-		
APOP-1-ONa	760	2.89	273	1	36.7	-	30.6	Song et al.[464]
		1.71	298	1	29.2	-		
APOP-1-F	724	3.07	273	1	43.4	-	33.3	Song et al.[464]
		2.02	298	1	31.8	-		
APOP-2	906	2.27	273	1	24.3	-	31.7	Song et al.[464]
		1.30	298	1	20.2	-		
APOP-3	1402	4.45	273	1	27.5	-	27.5	Song et al.[464]
		2.59	298	1	26.0	-		
APOP-4	833	2.70	273	1	35.8	-	30.7	Song et al.[464]
		1.64	298	1	23.3	-		
Azo-CMP1	1146	3.72	273	1.13	42.1	79.9 (15:85)	≈ 30	Wang et al.[333]
Azo-CMP2	898	3.17	273	1.13	44.4	66.5 (15:85)	≈ 30	
Azo-COP-1	635	2.44	273	1	73	63.7 (15:85)	29.3	Patel et al.[349]
		1.48	298	1	113	96.6 (15:85)		
Azo-COP-2	729	2.55	273	1	124	109.6 (15:85)	24.8	Patel et al.[349]
		1.53	298	1	142	130.6 (15:85)		
Azo-COP-3	493	1.93	273	1	98	78.6 (15:85)	32.1	Patel et al.[349]
		1.22	298	1	122	95.9 (15:85)		
Azo-POF1	712	2.98	273	1	69	52 (15:85)	27.5	Lu et al.[354]
		1.88	298	1	46	37 (15:85)		

material	S_{BET} ($m^2 g^{-1}$)	CO_2 uptake ($mmol\ g^{-1}$)	T (K)	p (bar)	CO_2/N_2 selectivity Henry	CO_2/N_2 selectivity IAST	Q_{st} ($kJ\ mol^{-1}$)	reference
Azo-POF2	439	1.92	273	1	76	55 (15:85)	26.6	Lu et al.[354]
		1.25	298	1	54	42 (15:85)		
BILP-1	1172	4.27	273	1	70	-	26.7	Rabbani et al.[340]
		2.98	298	1	36	-		
BILP-2	708	3.39	273	1	113	-	28.6	Rabbani et al.[342]
		2.36	298	1	71	-		
BILP-3	1306	5.11	273	1	59	-	28.6	Rabbani et al.[345]
		3.30	298	1	31	-		
BILP-4	1135	5.34	273	1	79	-	28.7	Rabbani et al.[342]
		3.59	298	1	32	-		
BILP-5	599	2.91	273	1	95	-	28.8	Rabbani et al.[342]
		1.98	298	1	36	-		
BILP-6	1261	4.80	273	1	63	-	28.4	Rabbani et al.[345]
		2.75	298	1	39	-		
BILP-7	1122	4.39	273	1	62	-	27.8	Rabbani et al.[342]
		2.77	298	1	34	-		
BILP-10	787	4.02	273	1	111	-	38.2	Sekizkardes et al.[343]
		2.52	298	1	59	57 (10:90)		
BILP-11	658	3.09	273	1	103	-	32.0	Sekizkardes et al.[343]
		2.00	298	1	55	56 (10:90)		
BILP-12	1497	5.07	273	1	56	-	27.6	Sekizkardes et al.[343]
		3.18	298	1	31	31 (10:90)		
BILP-13	677	2.57	273	1	103	-	26.7	Sekizkardes et al.[343]
		1.80	298	1	38	32 (10:90)		
BILP-101	536	2.43	298	1	80	-	33.0	Sekizkardes et al.[348]
BLP-1(H)	1360	1.68	273	1	-	-	25.3	Jackson et al.[195]
		0.93	298	1	-	-		
BLP-12(H)	2244	2.73	273	1	-	-	25.2	Jackson et al.[195]
		1.68	298	1	-	-		
BLP-10(Cl)	924	2.70	273	1	-	-	28.3	Reich et al.[194]
		1.41	298	1	16	< 12 (5:95)		
COF-1	750	2.32	273	1	-	-		Furukawa et al.[160]
COF-5	1670	1.34	273	1	-	-		Furukawa et al.[160]
COF-6	750	3.84	273	1	-	-		Furukawa et al.[160]
COF-8	1350	1.43	273	1	-	-		Furukawa et al.[160]
COF-10	1760	1.21	273	1	-	-		Furukawa et al.[160]
COF-102	3620	1.56	273	1	-	-		Furukawa et al.[160]
COF-103	3530	1.70	273	1	-	-		Furukawa et al.[160]
CTF-0	2011	4.22	273	1	-	-		Katekomol et al.[199]
CTF-1	746	2.47	273	1	-	-	≈ 28	Zhao et al.[217]
		1.41	298	1	-	20 (10:90)		
CTF-1-600	1553	3.82	273	1	-	-	≈ 30	Zhao et al.[217]
		2.25	298	1	-	13 (10:90)		

material	S_{BET} ($m^2\ g^{-1}$)	CO_2 uptake ($mmol\ g^{-1}$)	T (K)	p (bar)	CO_2/N_2 selectivity Henry	CO_2/N_2 selectivity IAST	Q_{st} ($kJ\ mol^{-1}$)	reference
***bipy*-CTF500**	1548	5.34	273	1	-	-	34.2	Hug et al.[216]
		3.07	298	1	61	42 (15:85)		
***bipy*-CTF600**	2479	5.58	273	1	-	-	34.4	Hug et al.[216]
		2.95	298	1	37	24 (15:85)		
***fl*-CTF350**	1350	4.28	273	1	-	-	32.7	Hug et al.[218]
		2.29	298	1	35	37 (15:85)		
***lut*-CTF500**	1680	5.04	273	1	-	-	38.2	Hug et al.[216]
		2.58	298	1	27	27 (15:85)		
CTF-BI-4	1025	4.85	273	1	44.0	-	≈ 32	Tao et al.[219]
		2.46	303	1	102.7	-		
CTF-BI-11	1549	4.93	273	1	34.3	-	≈ 34	Tao et al.[219]
		2.37	303	1	34.9	-		
CTF-P6	1152	3.36	273	1	-	16.1 (15:85)		Ren et al.[205]
CTF-P6M	947	4.17	273	1	-	14.2 (15:85)		Ren et al.[205]
DHATab-COF	1480	3.48	273	1	-	-		Kandambeth et al.[242]
FCTF-1	662	4.67	273	1	-	-	35	Zhao et al.[217]
		3.21	298	1	-	31 (10:90)		
FCTF-1-600	1535	5.53	273	1	-	-	≈ 32	Zhao et al.[217]
		3.41	298	1	-	19 (10:90)		
Fe-POP-1	875	4.30	273	1	-	-		Modak *et al.*[325]
ILCOF-1	2723	1.36	273	1	-	-		Rabbani et al.[247]
MCTF-300	640	2.25	273	1	-	-	24.6	Liu et al.[220]
		1.41	298	1	-	-		
MCTF-400	1060	2.37	273	1	-	-	25.4	Liu et al.[220]
		1.58	298	1	-	-		
MCTF-500	1510	3.16	273	1	-	-	26.3	Liu et al.[220]
		2.26	298	1	-	-		
MOP A-B1	378	2.67	273	1	-	68 (15:85)	30.0	Xu et al.[241]
MOP A-B2	614	2.71	273	1	-	56 (15:85)	33.4	Xu et al.[241]
MOP A-B3	589	2.24	273	1	-	65 (15:85)	28.4	Xu et al.[241]
MOPI-I	206	3.3	273	1	-	-	39	Klumpen et al.[49]
		2.2	298	1	78	65.3 (15:85)		
MOPI-II	644	2.9	273	1	-	-	32	Klumpen et al.[49]
		1.9	298	1	51	36.4 (15:85)		
MOPI-III	443	3.0	273	1	-	-	32	Klumpen et al.[49]
		1.8	298	1	50	50.2 (15:85)		
MOPI-IV	660	3.8	273	1	-	-	31	Klumpen et al.[49]
		2.3	298	1	52	43.4 (15:85)		
MOPI-V	921	2.9	273	1	-	-	13	Klumpen et al.[49]
		1.6	298	1	33	26.4 (15:85)		
MPI-1	1454	3.82	273	1	102	-	35	Li et al.[372]
MPI-2	814	3.14	273	1	71	-	30	Li et al.[372]
MPI-3	586	2.25	273	1	41	-	31	Li et al.[372]

material	S_{BET} ($m^2\ g^{-1}$)	CO_2 uptake ($mmol\ g^{-1}$)	T (K)	p (bar)	CO_2/N_2 selectivity Henry	CO_2/N_2 selectivity IAST	Q_{st} ($kJ\ mol^{-1}$)	reference
NPAF	1790	3.64	273	1	-	88 (15:85)	19	Demirocak et al.[296]
		2.32	298	1	-	48 (15:85)		
NPOF-1-NH_2	1535	1.07	298	0.15	-	25 (10:90)	32.1	Islamoglu *et al.*[334]
		3.77	298	1	-	-	-	
NPTN-1	1187	3.02	273	1	-	45 (15:85)	34	Wu et al.[486]
NPTN-2	1558	3.18	273	1	-	22 (15:85)	37	Wu et al.[486]
NPTN-3	1055	2.23	273	1	-	25 (15:85)	30	Wu et al.[486]
PAF-1	5600	2.07	273	1	-	-	15.6	Ben *et al.*[47]
			298	1	-	-		
PAF-3	2932	3.48	273	1	-	-	19.2	Ben *et al.*[47]
		1.82	298	1	-	-		
PAF-4	2246	2.43	273	1	-	-	16.2	Ben *et al.*[47]
		1.16	298	1	-	-		
PAF-1-450	1191	4.50	273	1	-	209 (15:85)	27.8	Ben et al.[307]
PECONF-1	499	1.86	273	1	109	-	29	Mohanty et al.[19]
		1.34	298	1	51	-		
PECONF-2	637	2.85	273	1	74	-	31	Mohanty et al.[19]
		1.98	298	1	44	-		
PECONF-3	851	3.49	273	1	77	-	26	Mohanty et al.[19]
		2.47	298	1	41	-		
PECONF-4	-	2.95	273	1	83	-	34	Mohanty et al.[19]
		1.96	298	1	51	-		
PI-ADPM	868	3.32	273	1	-	-	34.4	Shen et al.[364]
PI-NO_2-1	286	4.03	273	1	33	18 (15:85)	43.3	Shen et al.[373]
		2.02	298	1	-	-		
PN-101	1096	5.14	273	1	-	199 (15:85)		Zhang et al[347]
POF1B	917	4.19	273	1	-	-		Katsoulidis et al.[146]
		2.14	298	1	-	-		
PON-1	1422	2.48	298	1	-	-		Jeon et al.[330]
PPF-1	1740	6.07	273	1	-	14.5	25.6	Zhu et al.[243]
PPF-2	1470	5.54	273	1	-	15.4	29.2	Zhu et al.[243]
PPF-3	429	2.09	273	1	-	20.4	21.8	Zhu et al.[243]
PPF-4	726	2.59	273	1	-	15.0	25.1	Zhu et al.[243]
PPN-4	6461	48.20	295	50	-	-		Yuan et al.[309]
PPN-6	4023	1.16	295	1	-	≈ 7 (15:85)	17	Lu et al.[335]
PPN-6-SO_3H	1254	3.6	295	1	-	150 (15:85)	30.4	Lu et al.[335]
PPN-6-SO_3Li	1186	3.7	295	1	-	414 (15:85)	35.7	Lu et al.[335]
PPN-6-SO_3NH_4	593	2.8	313	1	196	796 (15:85)	40	Lu et al.[336]
PPN-6-CH_2DETA	555	4.3	295	1	-	442 (15:85)	56	Lu et al.[337]
SMPI-0	574	2.53	273	1	29.5	-	36	Yang et al.[371]
		1.43	298	1	-	-		
SMPI-10	112	3.15	273	1	32.1	-	33	Yang et al.[371]
		1.87	298	1	-	-		

material	S_{BET} ($m^2\ g^{-1}$)	CO_2 uptake ($mmol\ g^{-1}$)	T (K)	p (bar)	CO_2/N_2 selectivity Henry	CO_2/N_2 selectivity IAST	Q_{st} ($kJ\ mol^{-1}$)	reference
SMPI-50	44	2.96	273	1	48.0	-	30	Yang et al.[371]
		1.61	298	1	-	-		
SMPI-100	23	2.82	273	1	57.6	-	30	Yang et al.[371]
		1.87	298	1	-	-		
SNU-C1-va	595	3.49	273	1	-	-	34.9	Xie et al.[303]
		2.31	298	1	-	-		
SNU-C1-sca	1990	4.38	273	1	-	-	31.2	Xie et al.[303]
		3.14	298	1	-	-		
STP-I	1305	3.67	273	1.13	-	-		Zhang et al.[151]
STP-II	1990	4.14	273	1.13	-	-		Zhang et al.[151]
TBILP-1	330	2.66	273	1	-	-	29	Sekizkardes et al.[344]
		1.55	298	1	40	43 (10:90)		
TBILP-2	1080	5.18	273	1	-	-	35	Sekizkardes et al.[344]
		3.32	298	1	63	62 (10:90)		
TB-MOP	694	4.05	273	1	-	-	29.5	Zhu et al.[487]
		2.57	298	1	51	-		
TDCOF-5	2497	2.09	273	1	-	-	21.8	Kahveci et al.[174]
		≈ 1.23	298	1	-	-		
Td-CPI	210	5.00	195	1	-	-		Rao et al.[369]
Td-PPI	2213	7.00	195	1		-		Rao et al.[369]
			298		25	-		
Tr-CPI	130	5.68	195	1	-	-		Rao et al.[369]
Tr-NPI	567	11.4	195	1	-	-		Rao et al.[369]
			298		22	-		
Tr-PPI	400	10.2	195	1	-	-		Rao et al.[369]
			298		12	-		
TRITER-1	716	13.38	273	5	-	-	38.1	Gomes et al.[248]
		3.11	298	5	-	-		

[a] IAST selectivities derived from the single component sorption isotherms. The values in brackets denote the applied CO_2:N_2 ratio of the simulated gas mixtures.

8.5 Solid State NMR Spectroscopy of Porous Triazine-based Polyimides

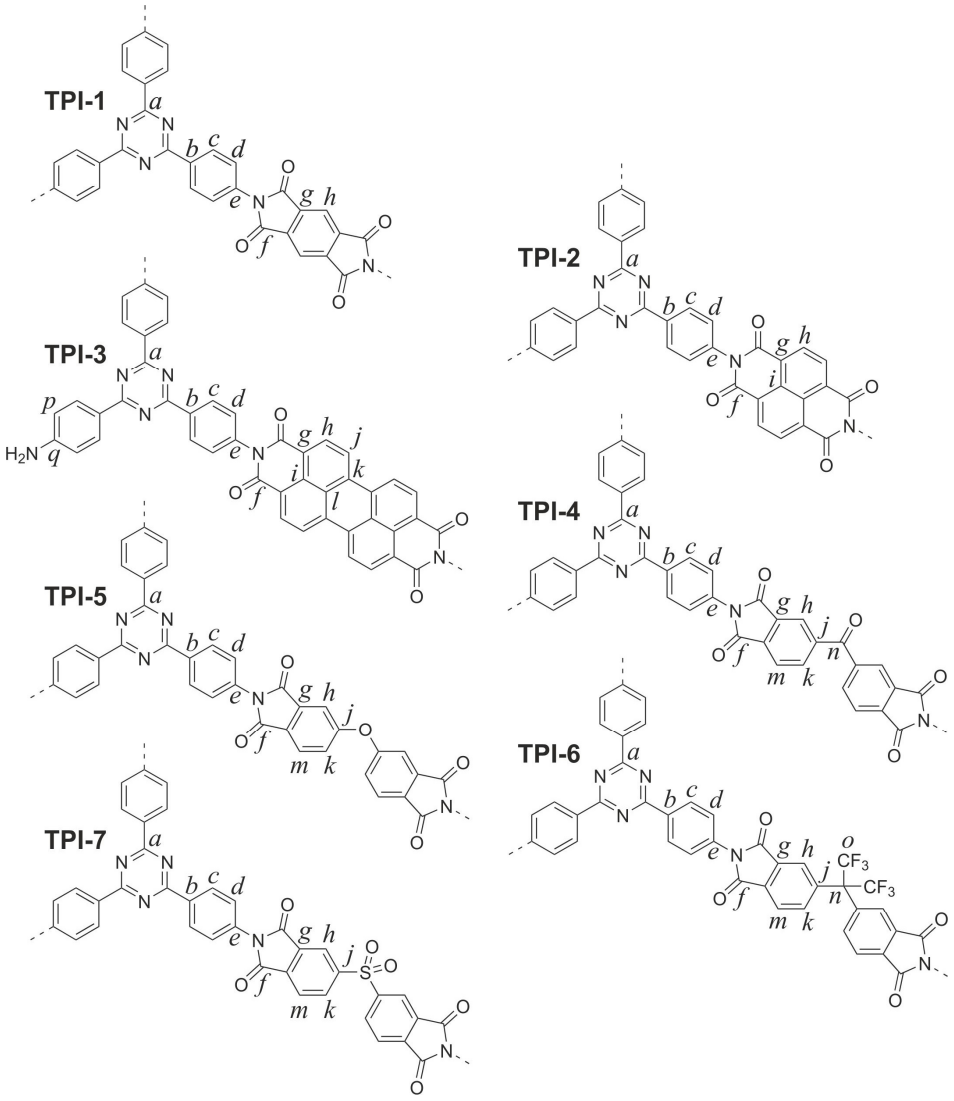

Figure 8-3: *TPI structures and assignments in NMR spectra.*

Table 18: *Assignments for NMR signals in ppm.*

polymer network	*a*	*b*	*c*	*d*	*e*	*f*	*g*	*h*	*i*	*j*	*k*	*l*	*m*	*n*	*o*	*p*	*q*
TPI-1	171	136	136	129	136	165	136	119	-	-	-	-	-	-	-	-	-
TPI-2	171	137	137	128	137	162	128	128	128	-	-	-	-	-	-	-	-
TPI-3	168	135	130	130	138	163	123	131	130	131	138	130	-	-	-	114	151
TPI-4	171	135	135	130	135	166	135	125	-	141	135	-	125	192	-	-	-
TPI-5	169	134	134	127	134	164	134	115	-	159	125	-	125	-	-	-	-
TPI-6	171	135	133	129	135	165	135	125	-	135	135	-	125	65	125	-	-
TPI-7	169	134	134	128	134	163	135	123	-	146	134	-	124	-	-	-	-

8.6 X-Ray Diffraction Patterns of Porous Triazine-based Polyimides

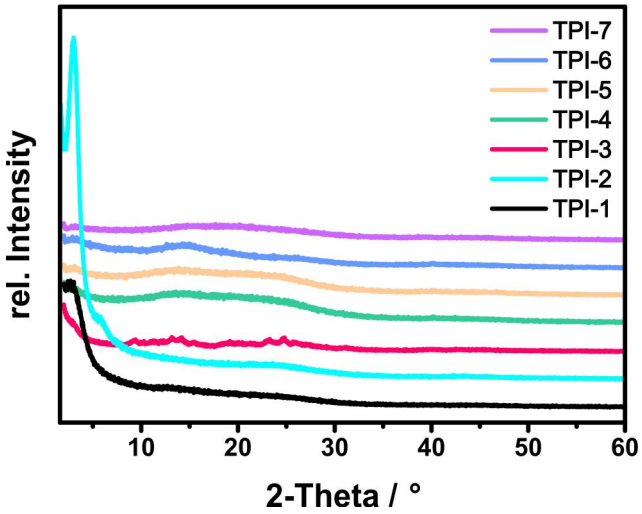

Figure 8-4: *XRD patterns of porous triazine-based polyimides.*

8.7 BET-Plots of Porous Triazine-based Polyimides

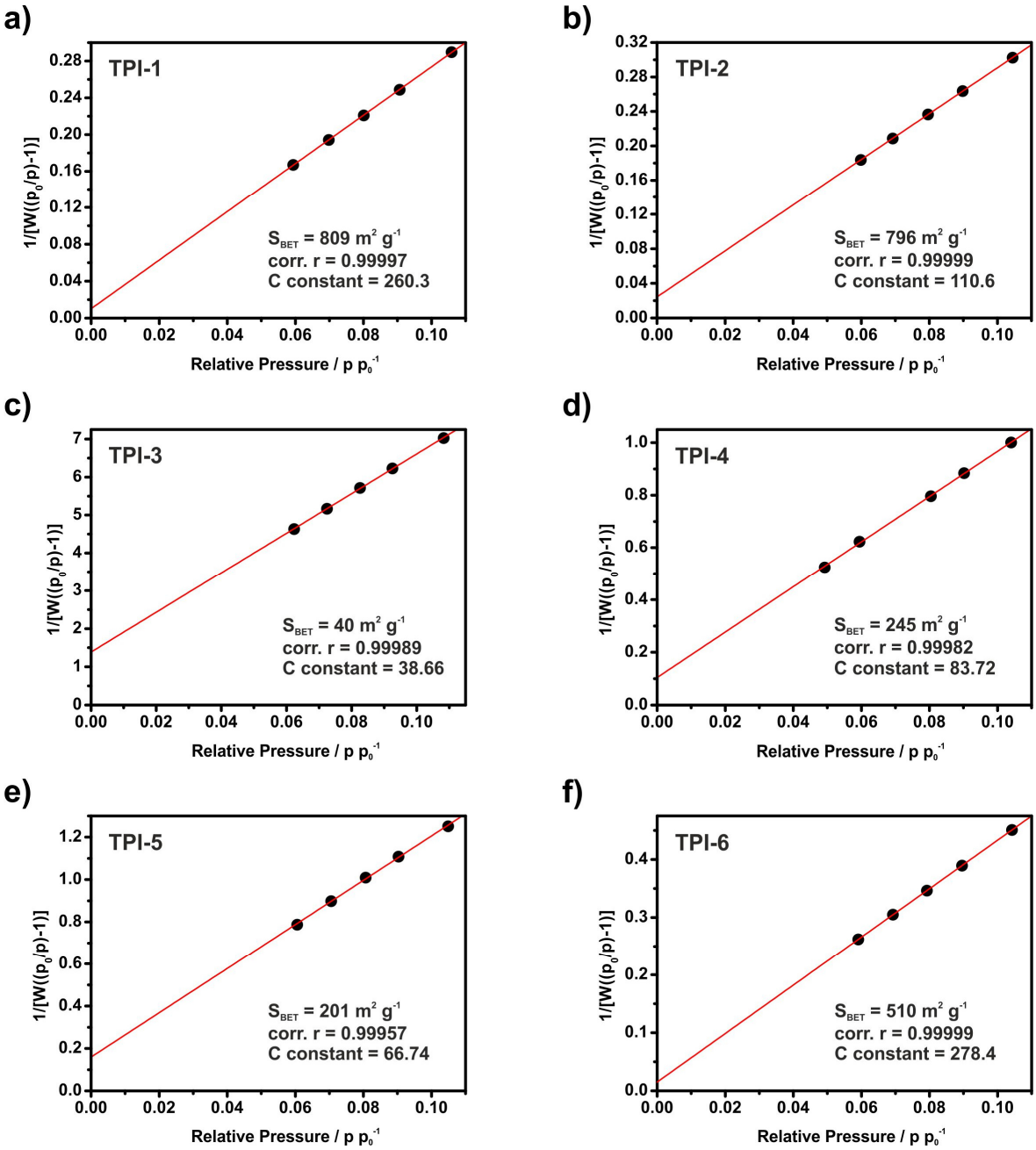

Figure 8-5: *BET-plots of TPI polymers. BET-plot of TPI-7 is not displayed due to insufficient argon uptake during argon sorption measurements.*

8.8 Fitting Comparison of Ar Sorption Isotherms of Porous Triazine-based Polyimides

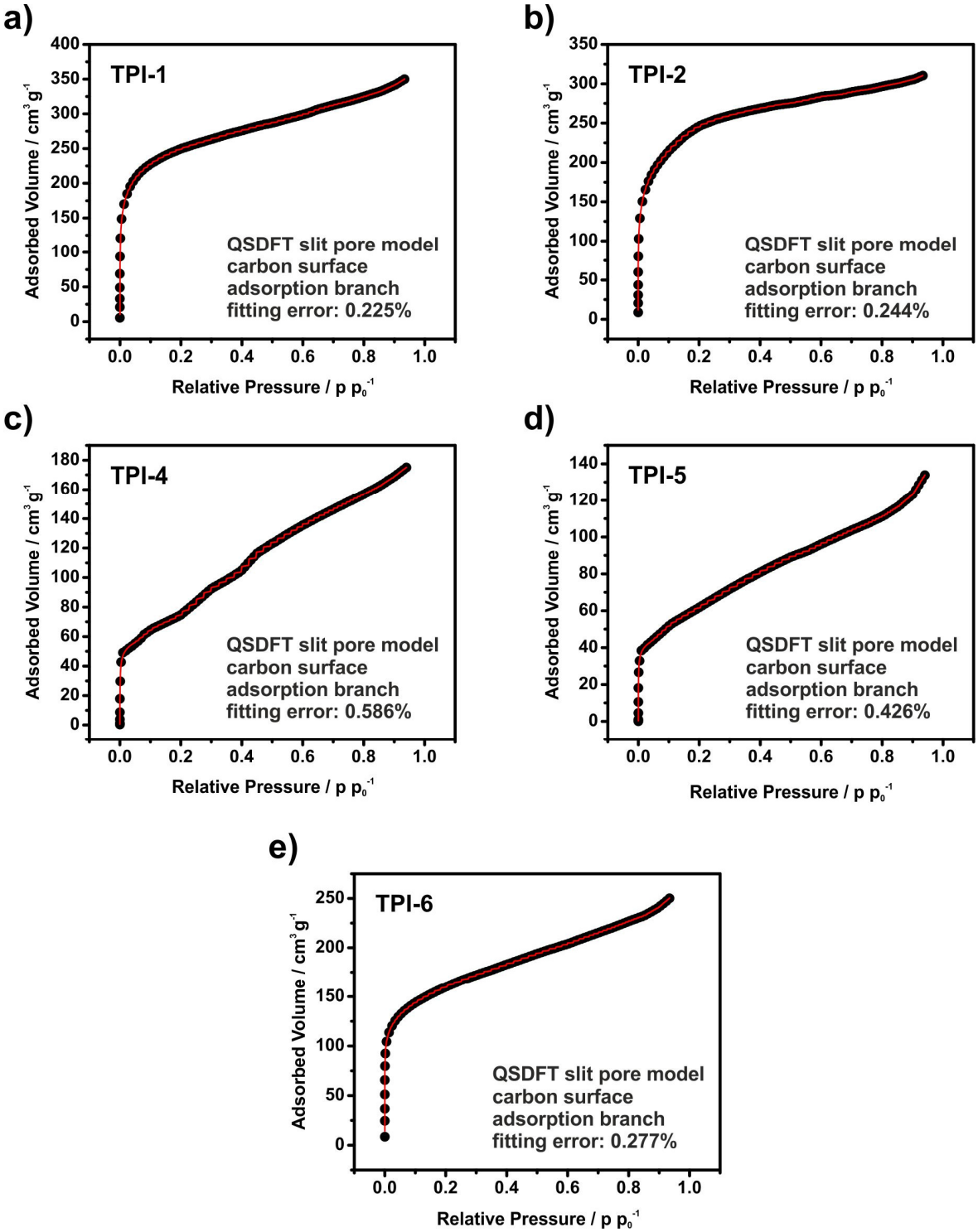

Figure 8-6: *Fitting Comparison of argon sorption isotherms of TPI polymer networks.*

8.9 Fitting Comparison of CO_2 Sorption Isotherms of Porous Triazine-based Polyimides

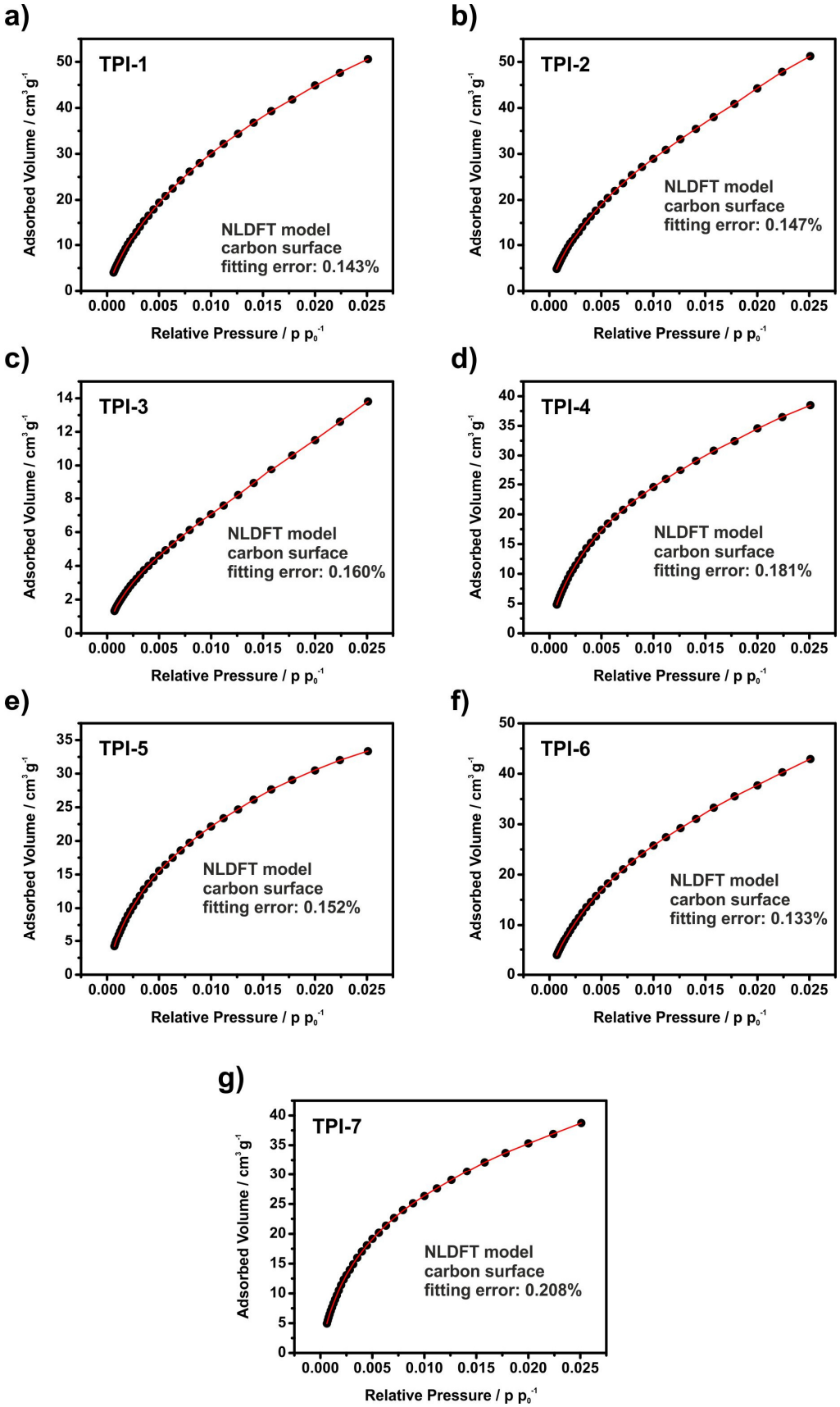

Figure 8-7: *Fitting comparison of CO_2 sorption isotherms of TPI polymer networks.*

8.10 Initial Slope Fits of CO_2 and N_2 Sorption Isotherms of Porous Triazine-based Polyimides

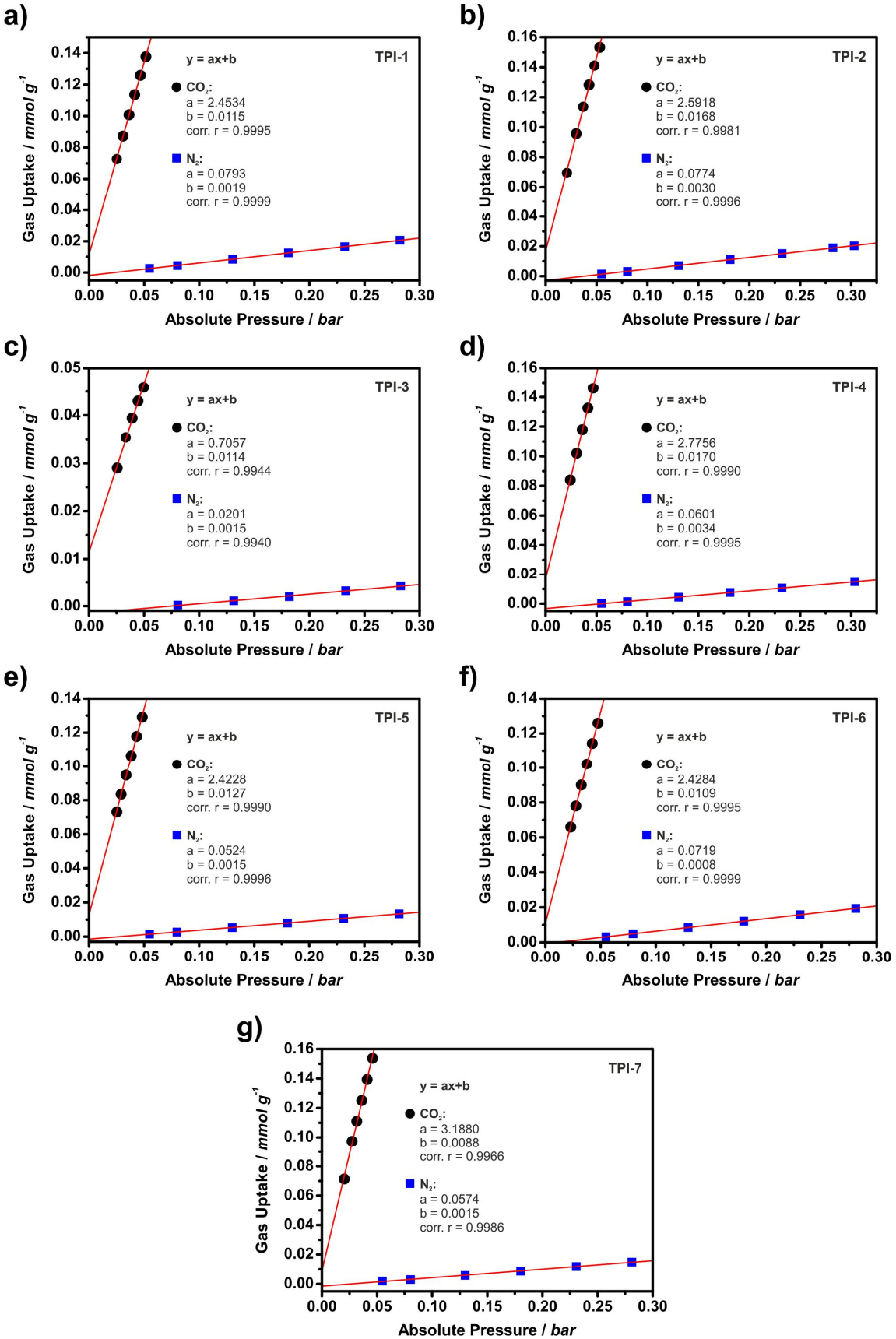

Figure 8-8: *Initial slope fits of CO_2 and N_2 sorption isotherms of TPI polymers.*

8.11 IAST Selectivity of Porous Triazine-based Polyimides from CO_2 and N_2 Adsorption Isotherms

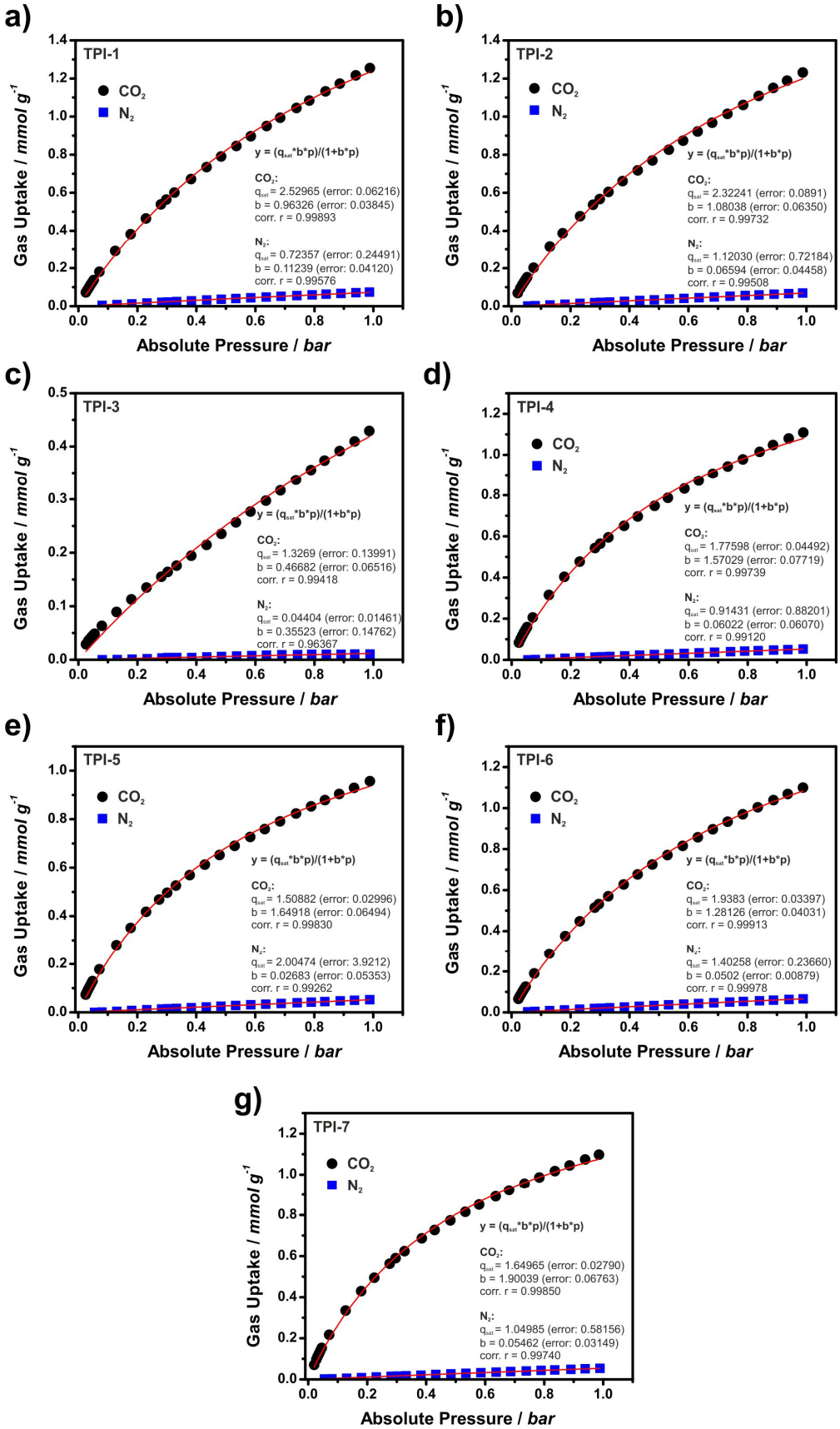

Figure 8-9: *Single site Langmuir fits of CO_2 and N_2 adsorption isotherms of TPIs.*

Table 19: *Data calculated from single site Langmuir fits of CO_2 and N_2 sorption isotherms of TPI polymers for CO_2/N_2 gas mixtures of 15:85 and 25:75.*

material	$q_{sat,CO2}$	b_{CO2}	$q_{sat,N2}$	b_{N2}	p_{CO2}	p_{N2}	IAST Selectivity CO_2/N_2
TPI-1	2.52965	0.96326	0.72357	0.11239	0.15	0.85	29
	2.52965	0.96326	0.72357	0.11239	0.25	0.75	26
TPI-2	2.32241	1.08038	1.12030	0.06594	0.15	0.85	31
	2.32241	1.08038	1.12030	0.06594	0.25	0.75	28
TPI-3	1.32690	0.46682	0.04404	0.35523	0.15	0.85	48
	1.32690	0.46682	0.04404	0.35523	0.25	0.75	44
TPI-4	1.77598	1.57029	0.91431	0.06022	0.15	0.85	43
	1.77598	1.57029	0.91431	0.06022	0.25	0.75	38
TPI-5	1.50882	1.64918	2.00474	0.02683	0.15	0.85	38
	1.50882	1.64918	2.00474	0.02683	0.25	0.75	33
TPI-6	1.93830	1.28126	1.40258	0.05020	0.15	0.85	31
	1.93830	1.28126	1.40258	0.05020	0.25	0.75	28
TPI-7	1.64965	1.90039	1.04985	0.05462	0.15	0.85	45
	1.64965	1.90039	1.04985	0.05462	0.25	0.75	39

8.12 SEM Images of Porous Triazine-based Polyimides

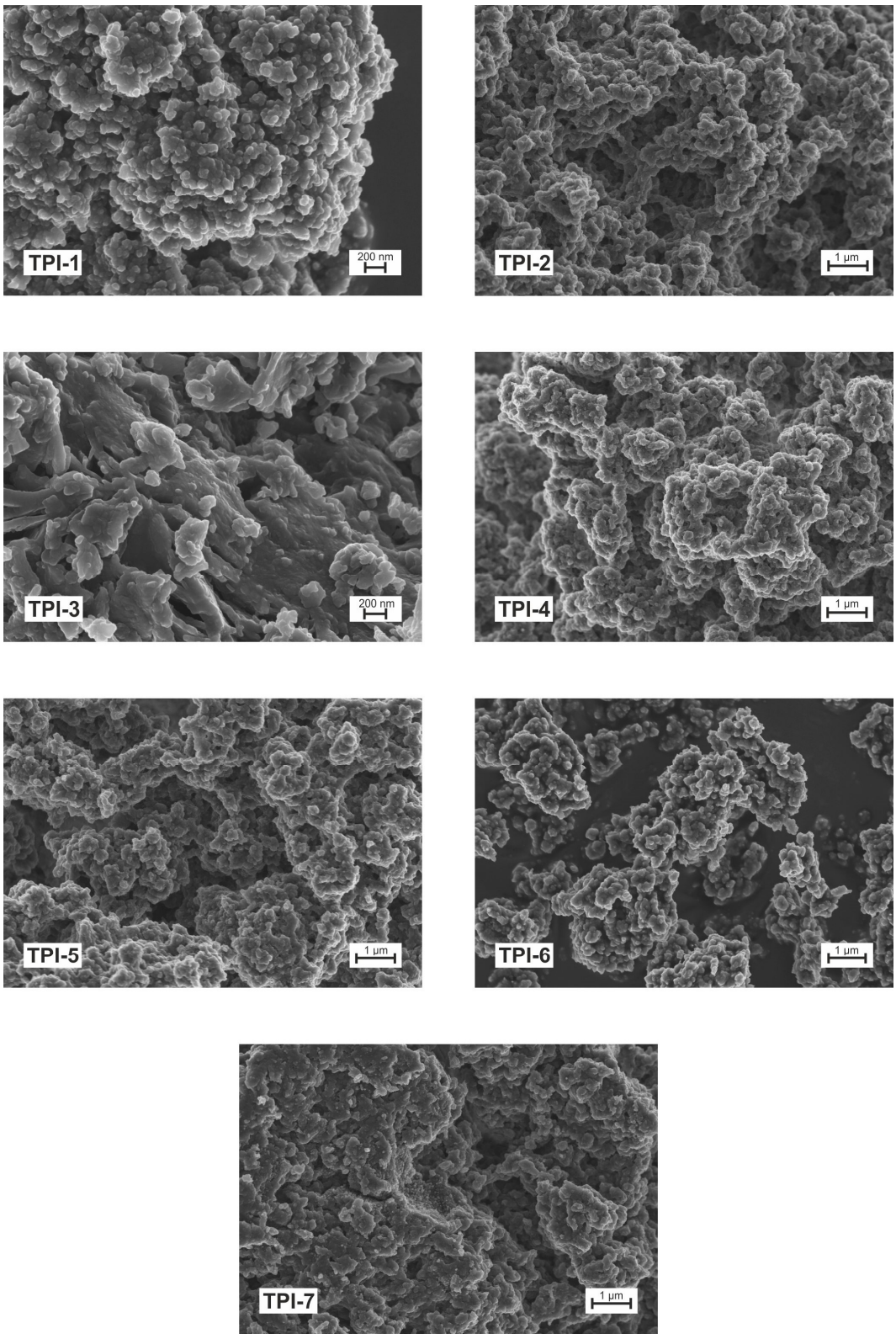

Figure 8-10: *SEM Images of TPI polymers.*

8.13 Single molecule ^{13}C and ^{1}H NMR spectra

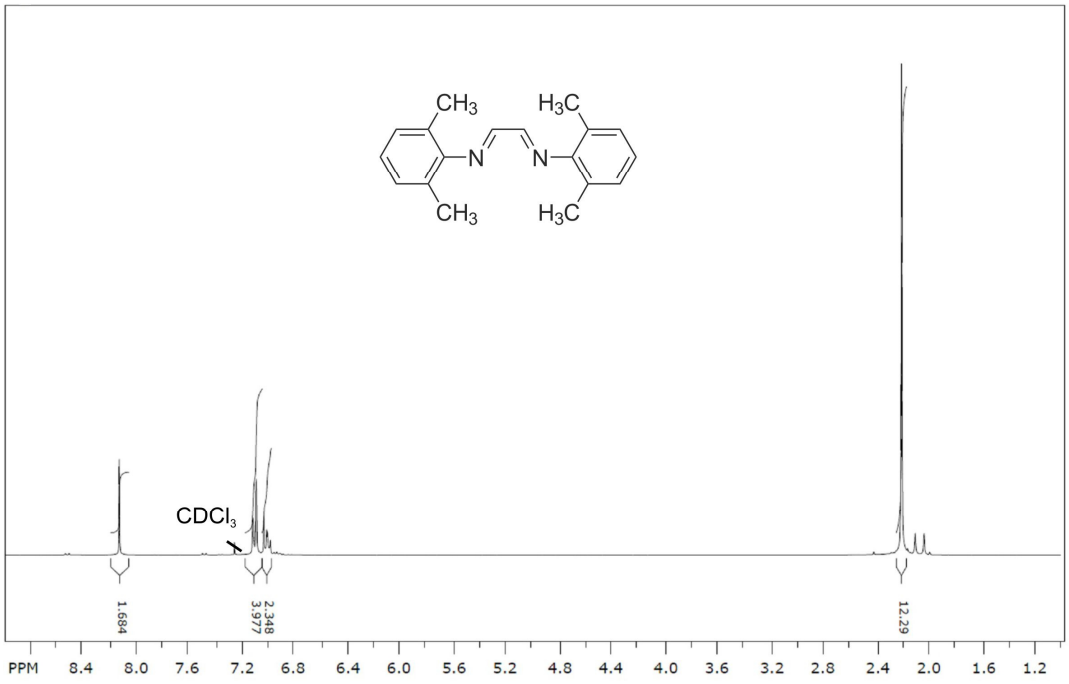

Figure 8-11: *^{1}H NMR spectrum of* N,N-*bis(2,6-dimethylphenyl)-1,2-ethanediimine.*

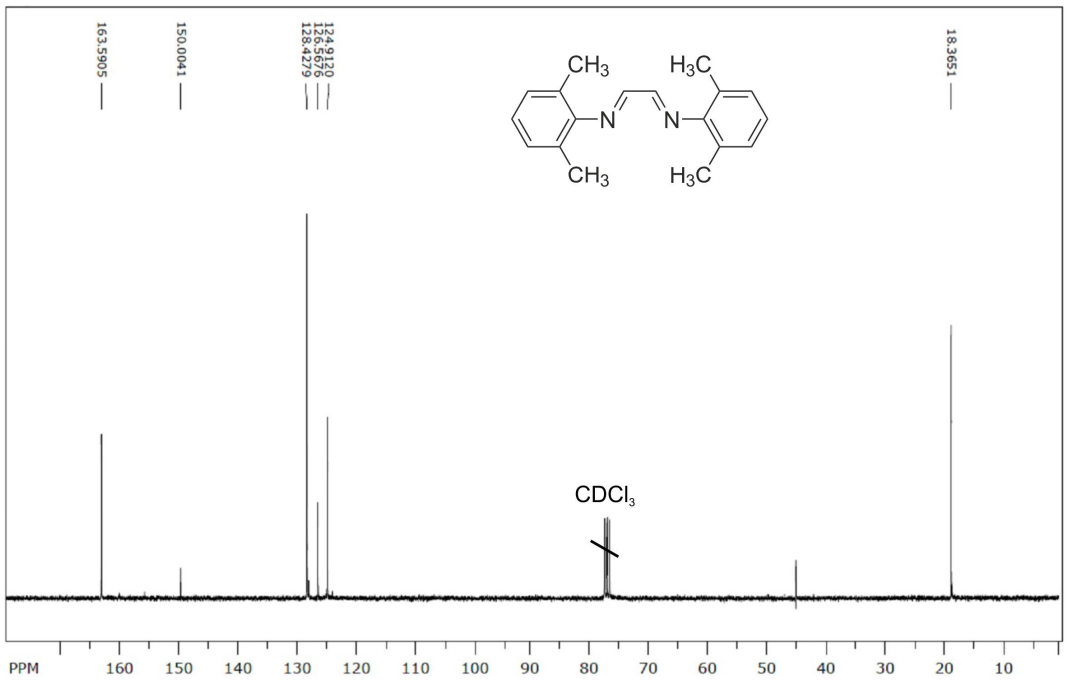

Figure 8-12: *^{13}C NMR spectrum of* N,N-*bis(2,6-dimethylphenyl)-1,2-ethanediimine.*

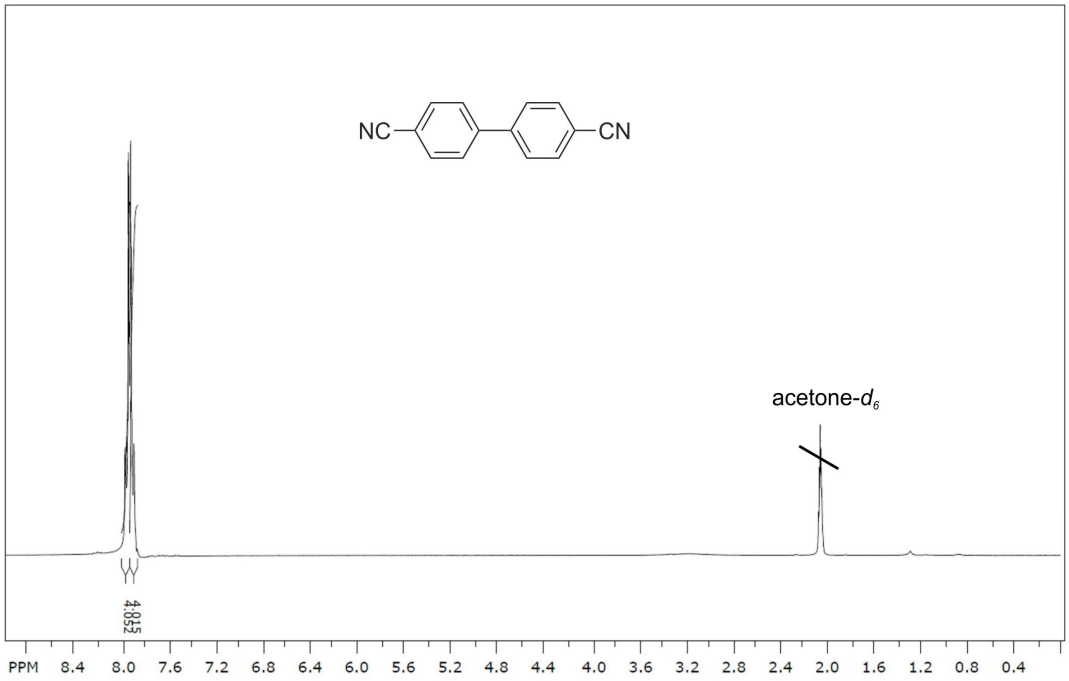

Figure 8-13: *^{1}H NMR spectrum of 4,4'-dicyanobiphenyl.*

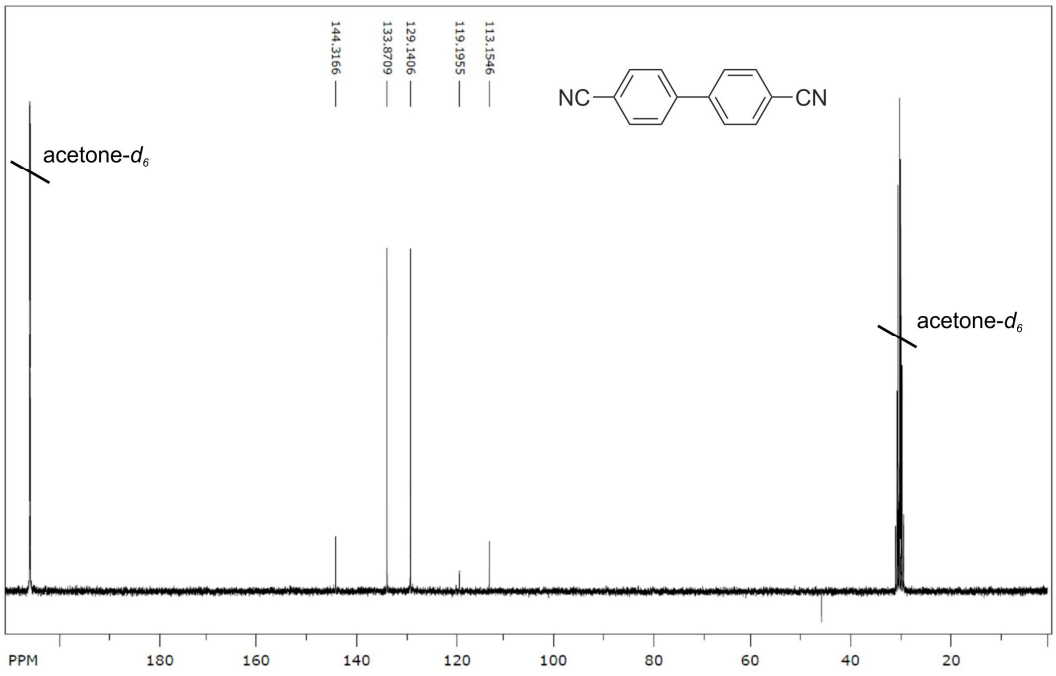

Figure 8-14: *^{13}C NMR spectrum of 4,4'-dicyanobiphenyl.*

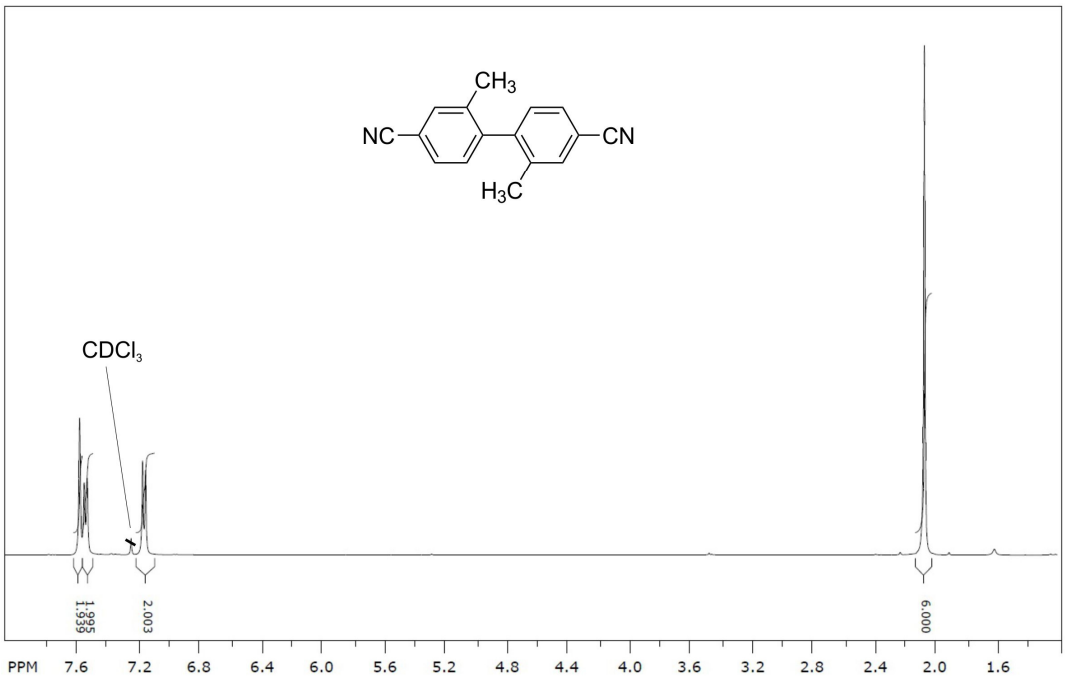

Figure 8-15: *^{1}H NMR spectrum of 4,4'-dicyano-2,2'-dimethylbiphenyl.*

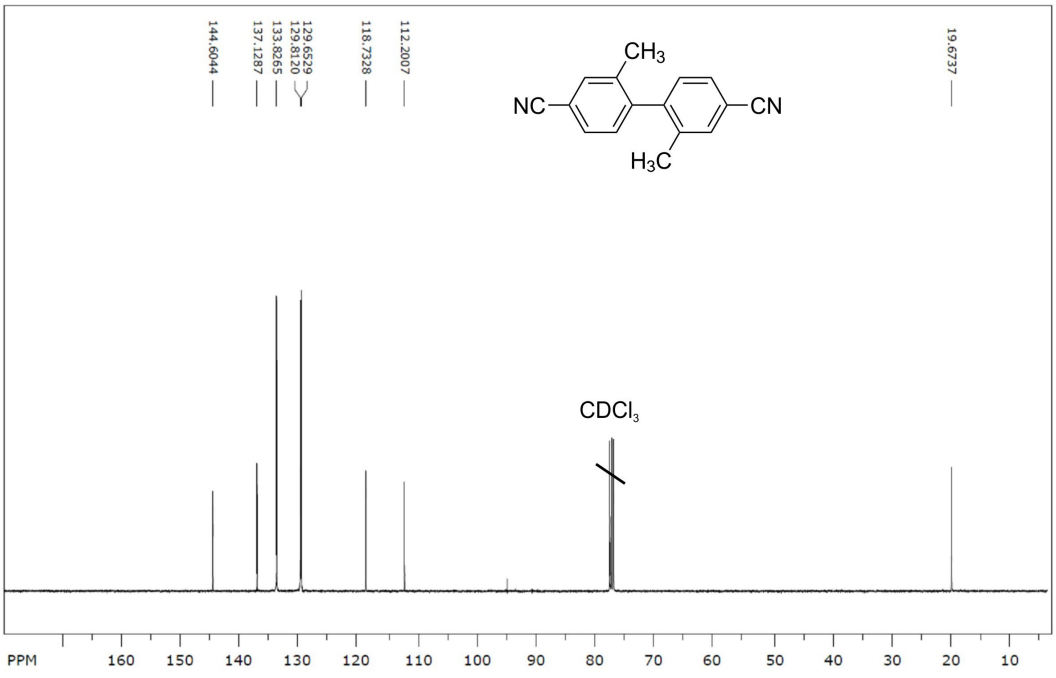

Figure 8-16: *^{13}C NMR spectrum of 4,4'-dicyano-2,2'-dimethylbiphenyl.*

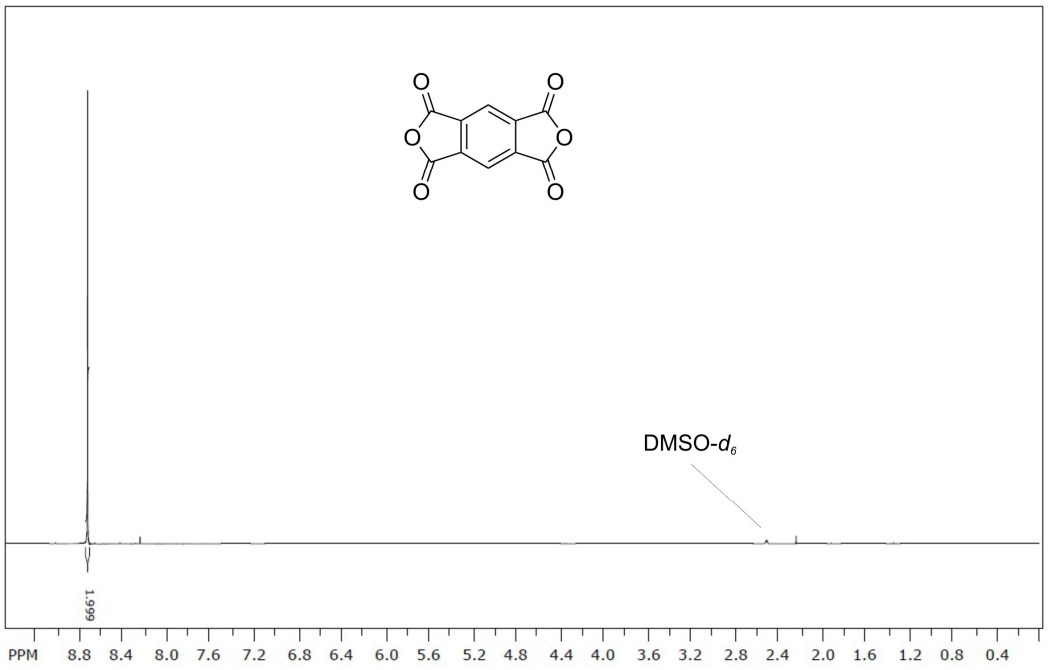

Figure 8-17: *^{1}H NMR spectrum of pyromellitic dianhydride.*

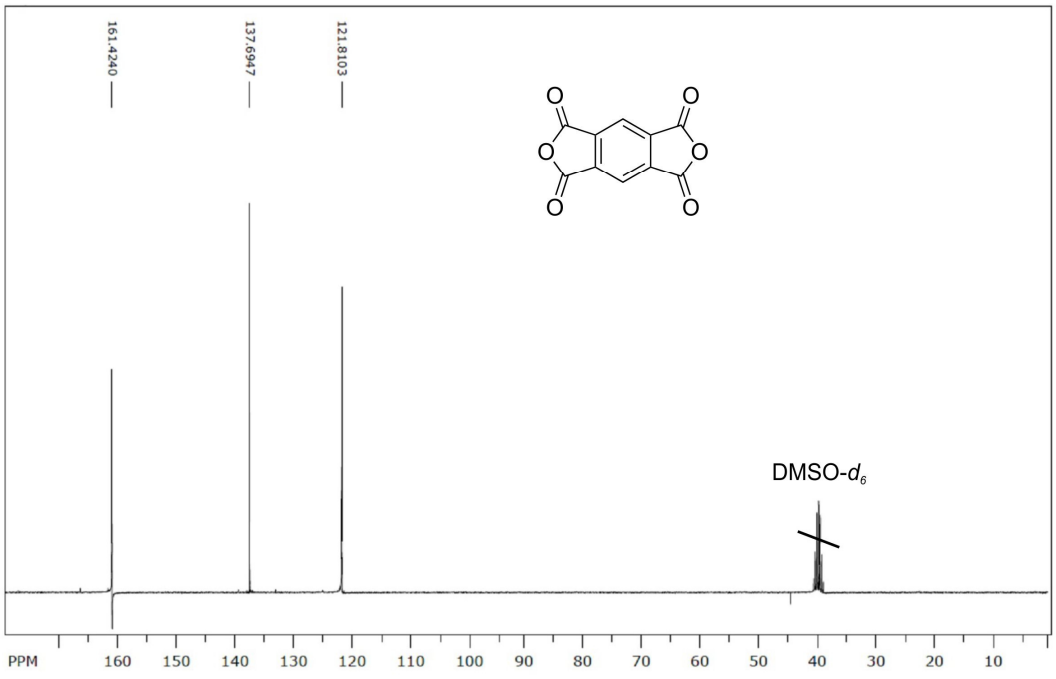

Figure 8-18: *^{13}C NMR spectrum of pyromellitic dianhydride.*

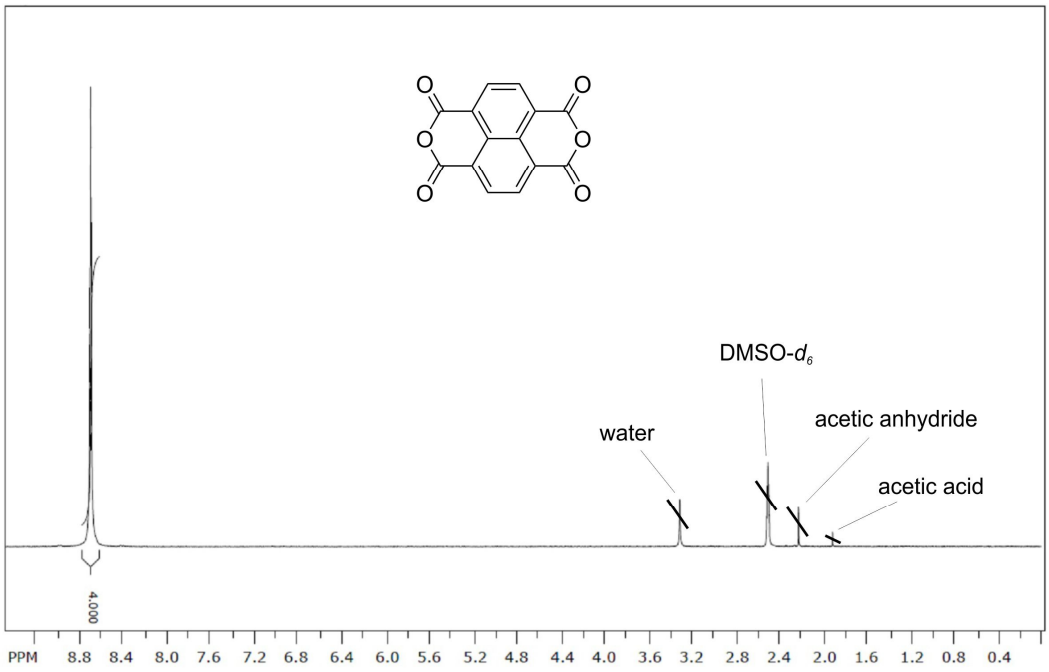

Figure 8-19: *^{1}H NMR spectrum of 1,4,5,8-naphthalenetetracarboxylic acid dianhydride*

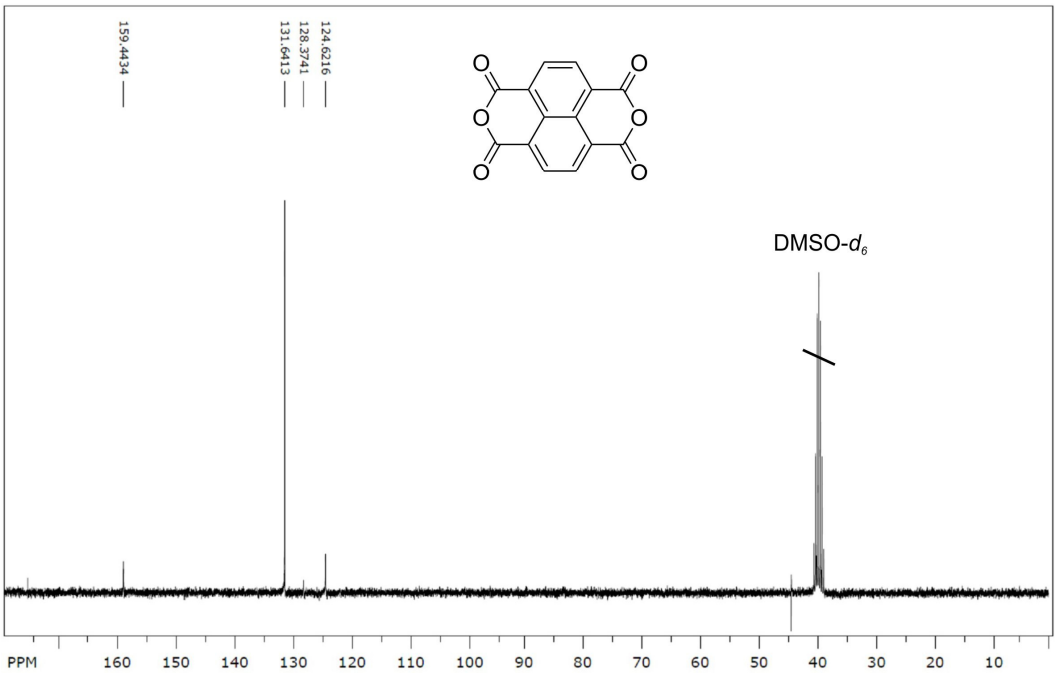

Figure 8-20: *^{13}C NMR spectrum of 1,4,5,8-naphthalenetetracarboxylic acid dianhydride.*

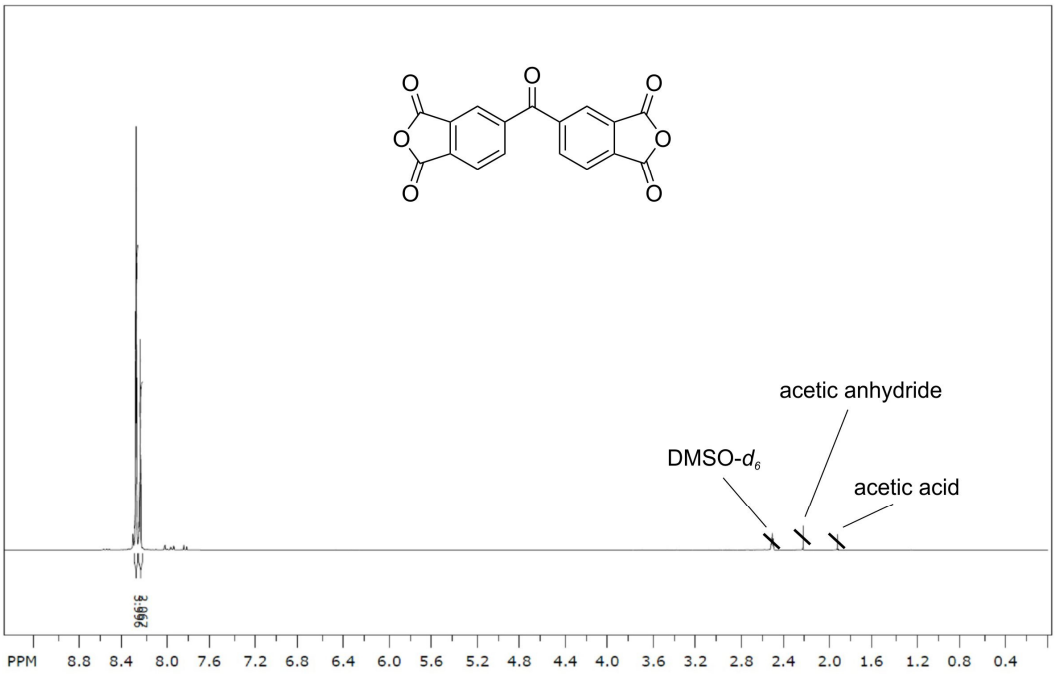

Figure 8-21: *^{1}H NMR spectrum of 3,3',4,4'-benzophenonetetracarboxylic dianhydride.*

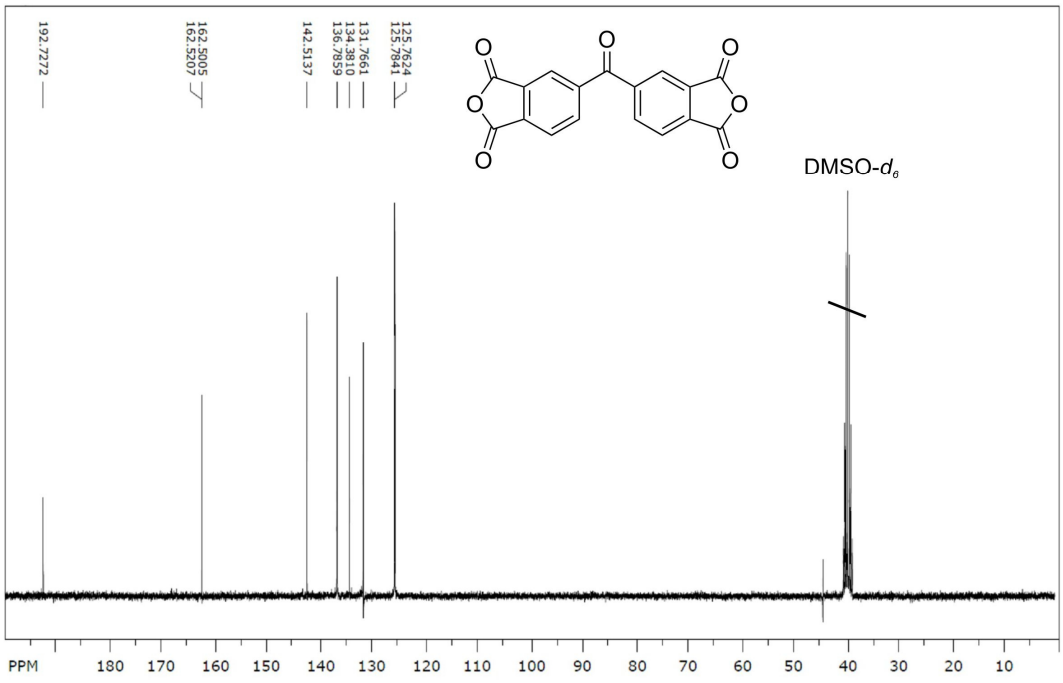

Figure 8-22: *^{13}C NMR spectrum of 3,3',4,4'-benzophenonetetracarboxylic dianhydride.*

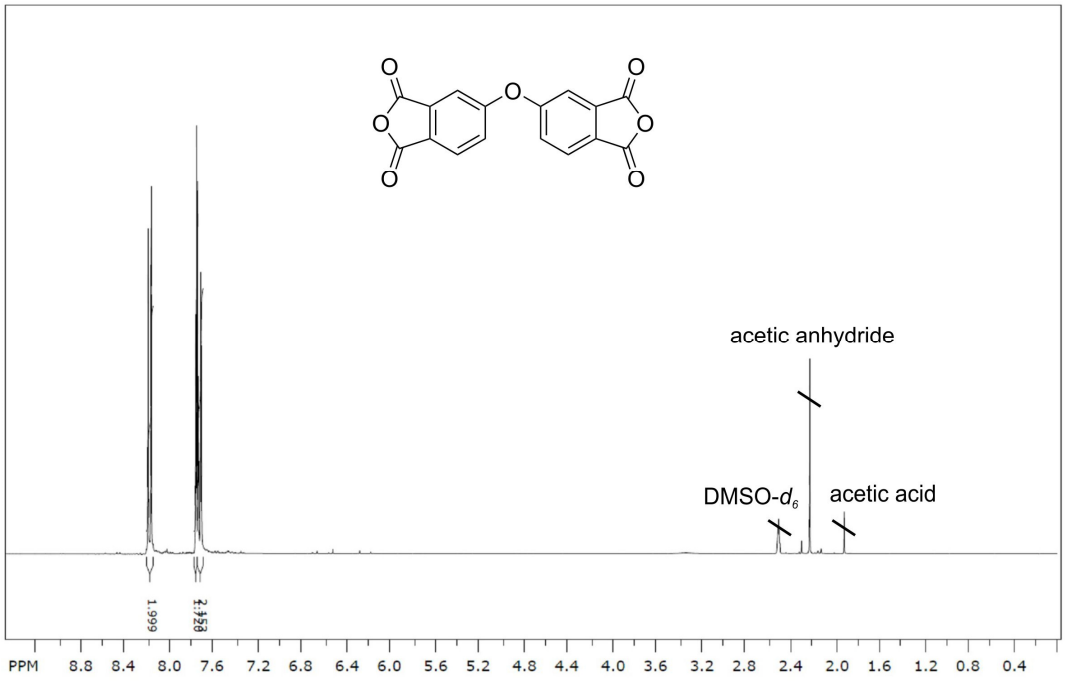

Figure 8-23: *^{1}H NMR spectrum of 3,3',4,4'-diphenyloxytetracarboxylic dianhydride.*

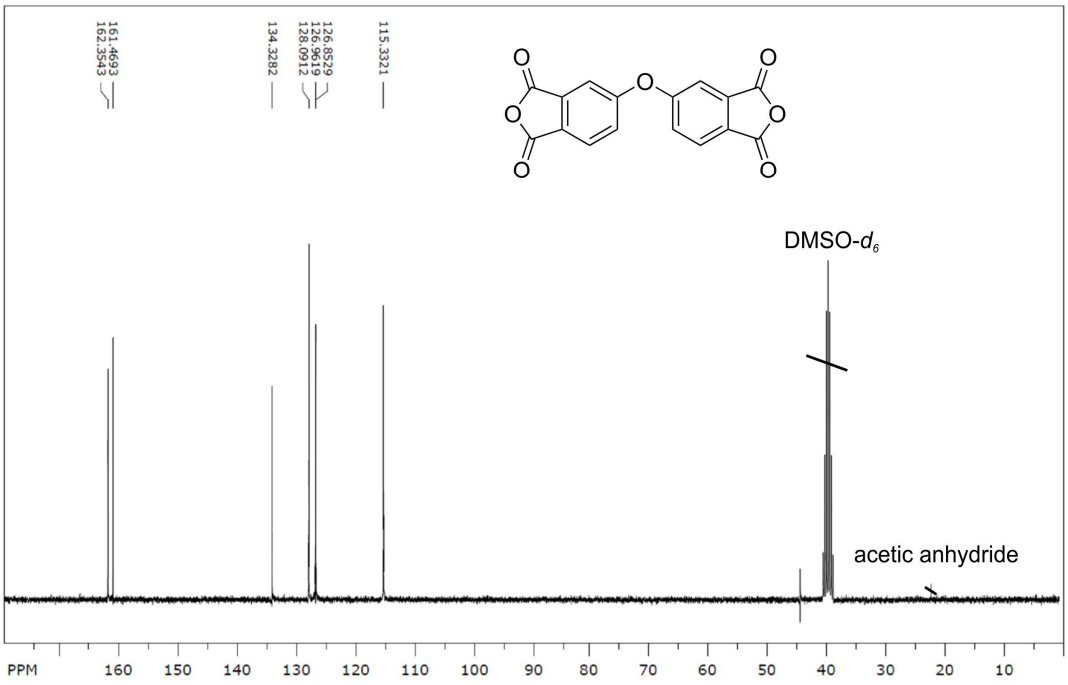

Figure 8-24: *^{13}C NMR spectrum of 3,3',4,4'-diphenyloxytetracarboxylic dianhydride.*

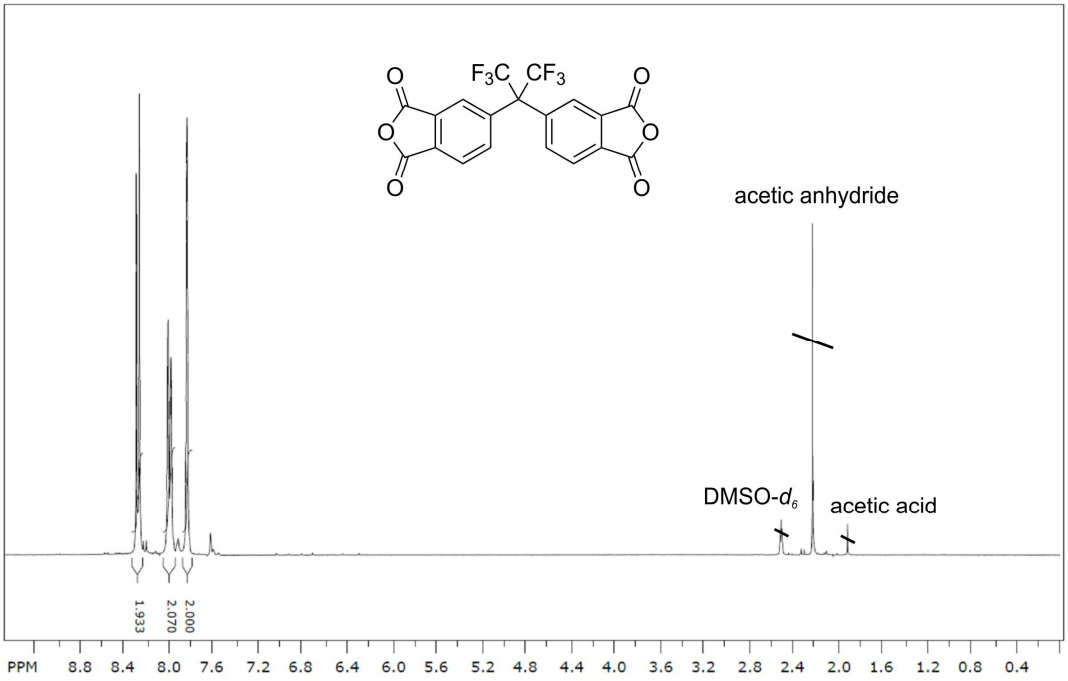

Figure 8-25: *^{1}H NMR spectrum of 4,4'-(hexafluoroisopropylidene)diphthalic anhydride.*

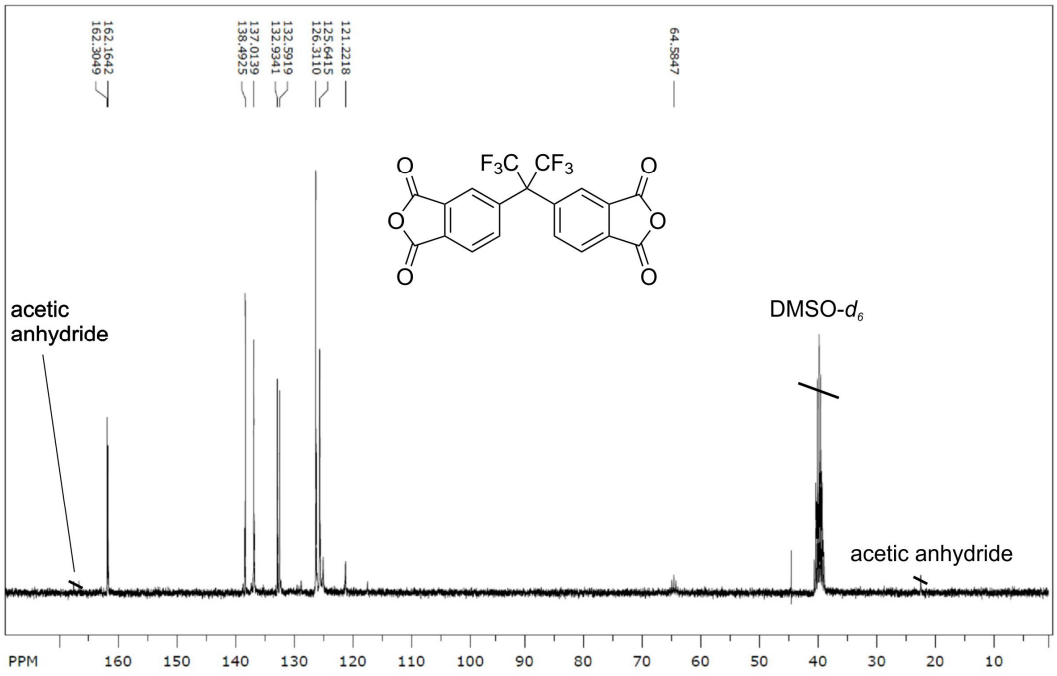

Figure 8-26: *^{13}C NMR spectrum of 4,4'-(hexafluoroisopropylidene)diphthalic anhydride.*

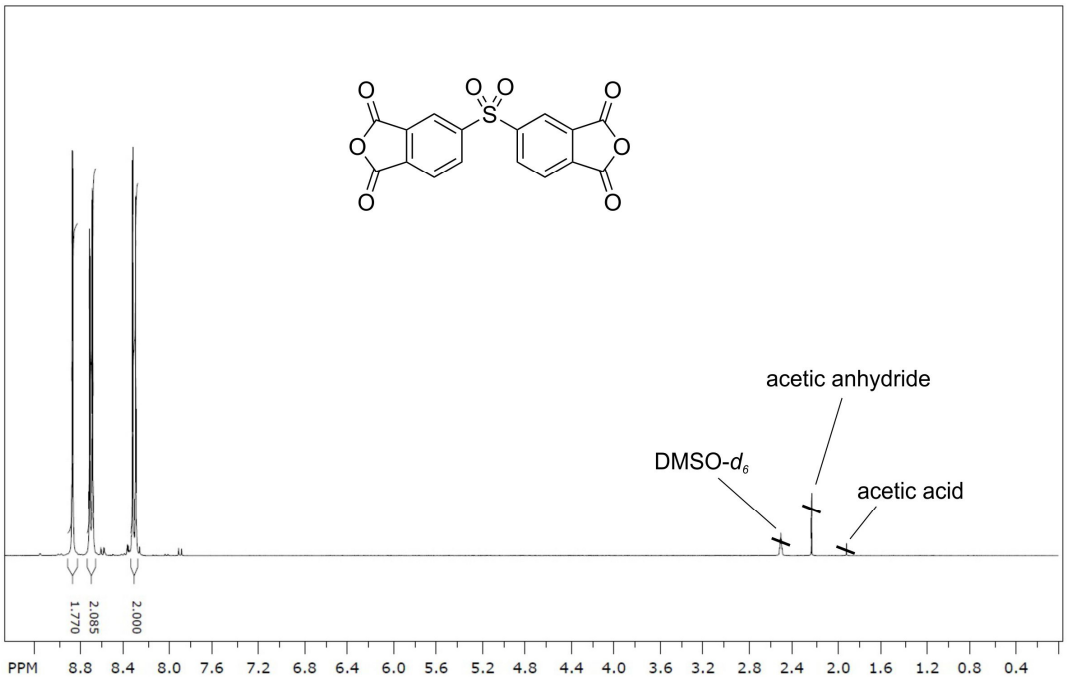

Figure 8-27: *^{1}H NMR spectrum of 4,4'-sulfonyldiphthalic anhydride.*

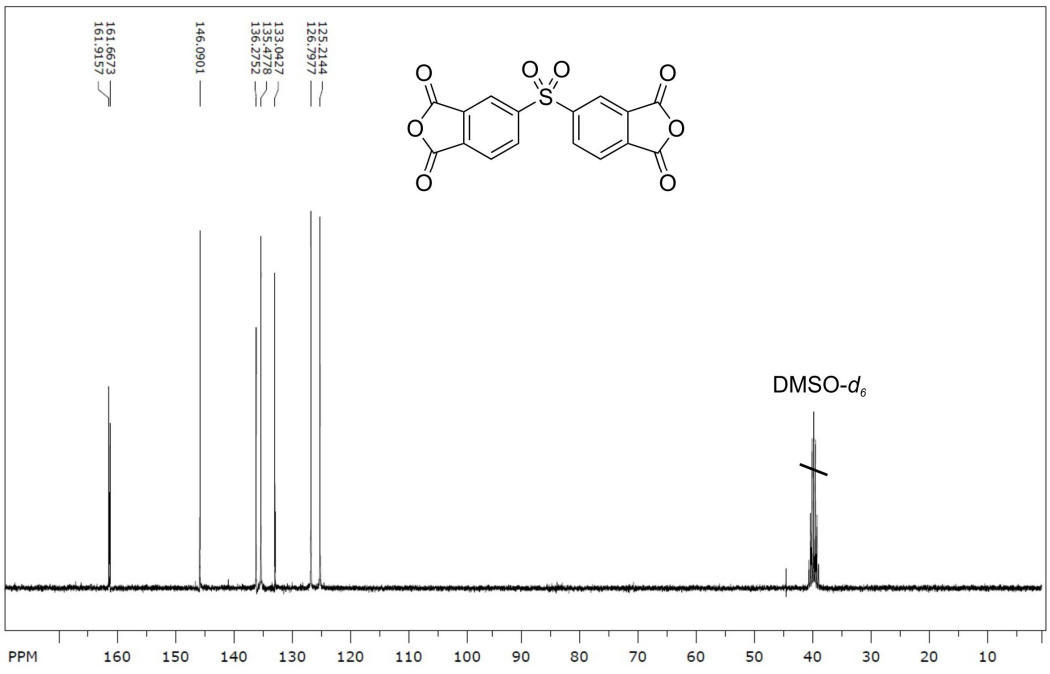

Figure 8-28: *^{13}C NMR spectrum of 4,4'-sulfonyldiphthalic anhydride.*

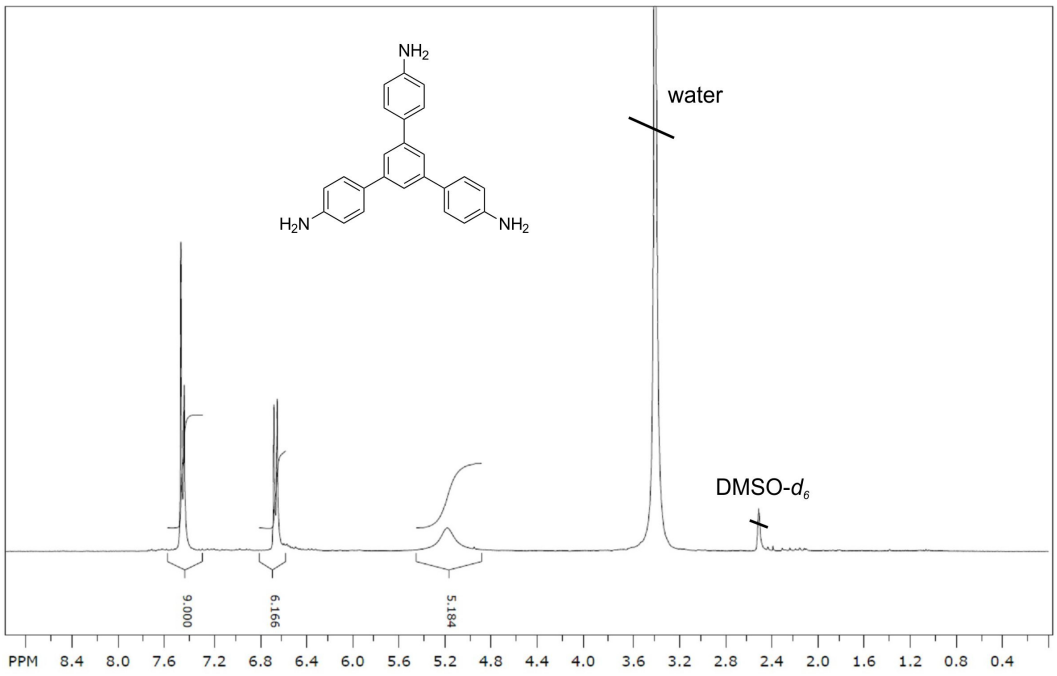

Figure 8-29: *[1]H NMR spectrum of 1,3,5-tris(*p*-aminophenyl)benzene.*

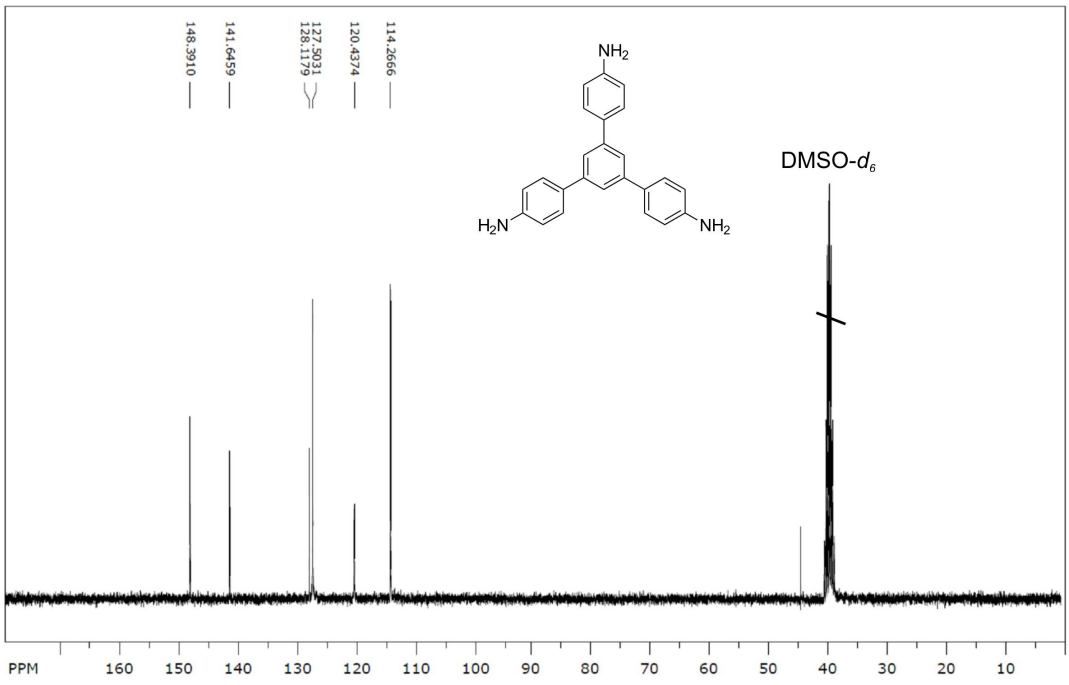

Figure 8-30: *[13]C NMR spectrum of 1,3,5-tris(*p*-aminophenyl)benzene.*

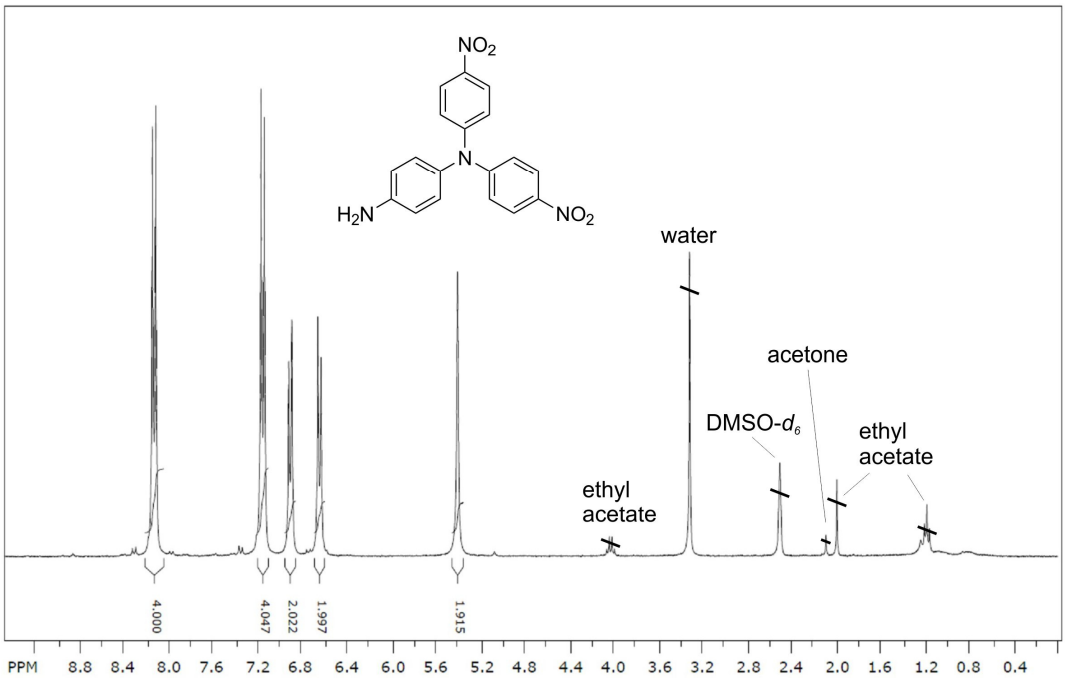

Figure 8-31: *^{1}H NMR spectrum of* N,N-*bis(*p-*nitrophenyl)-1,4-phenylenediamine.*

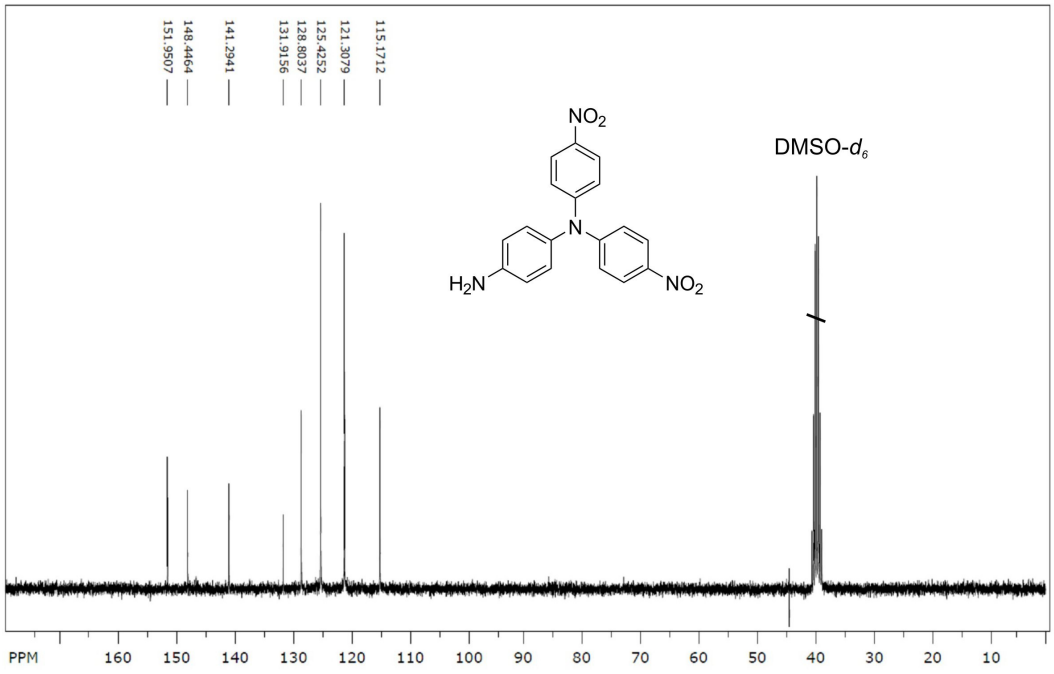

Figure 8-32: *^{13}C NMR spectrum of* N,N-*bis(*p-*nitrophenyl)-1,4-phenylenediamine.*

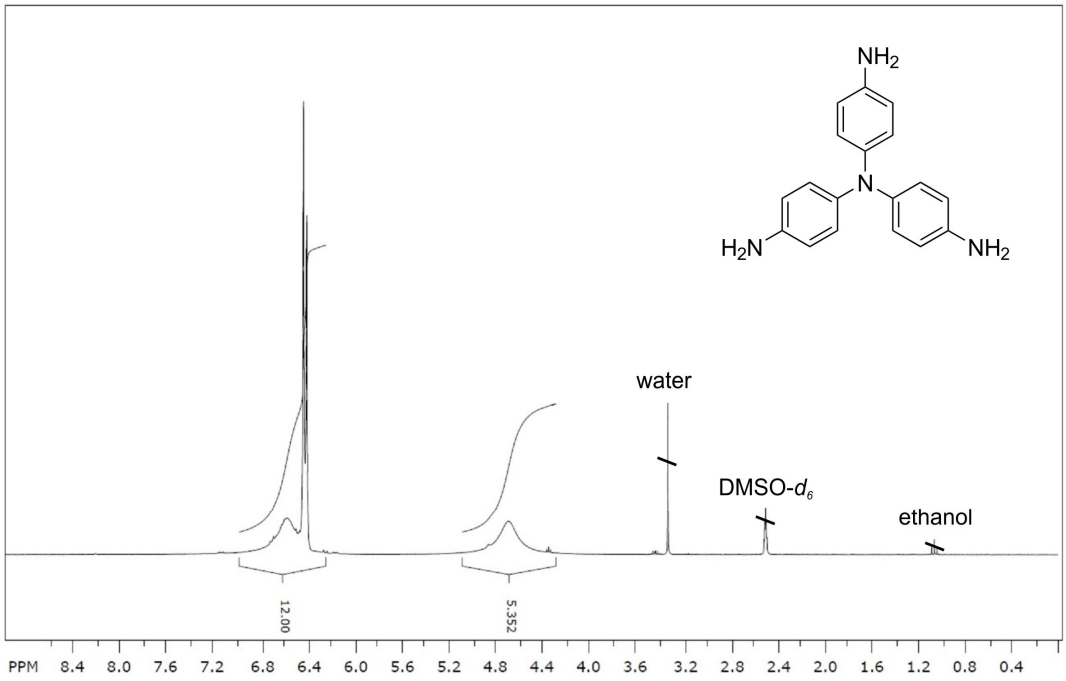

Figure 8-33: *^{1}H NMR spectrum of tris(*p*-aminophenyl)amine.*

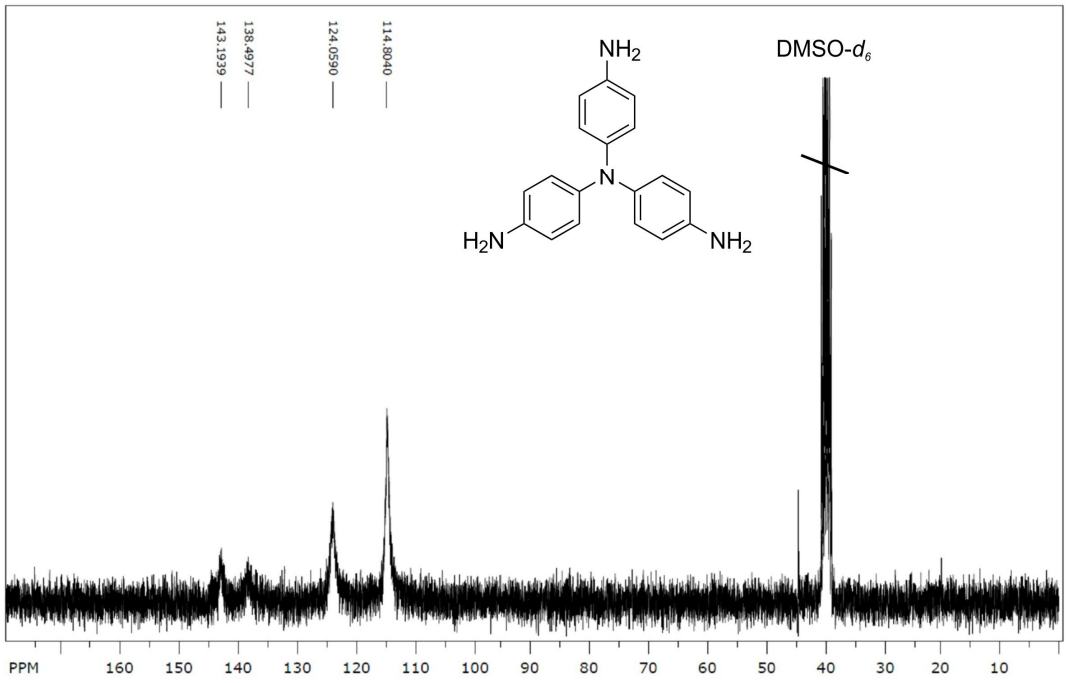

Figure 8-34: *^{13}C NMR spectrum of tris(*p*-aminophenyl)amine.*

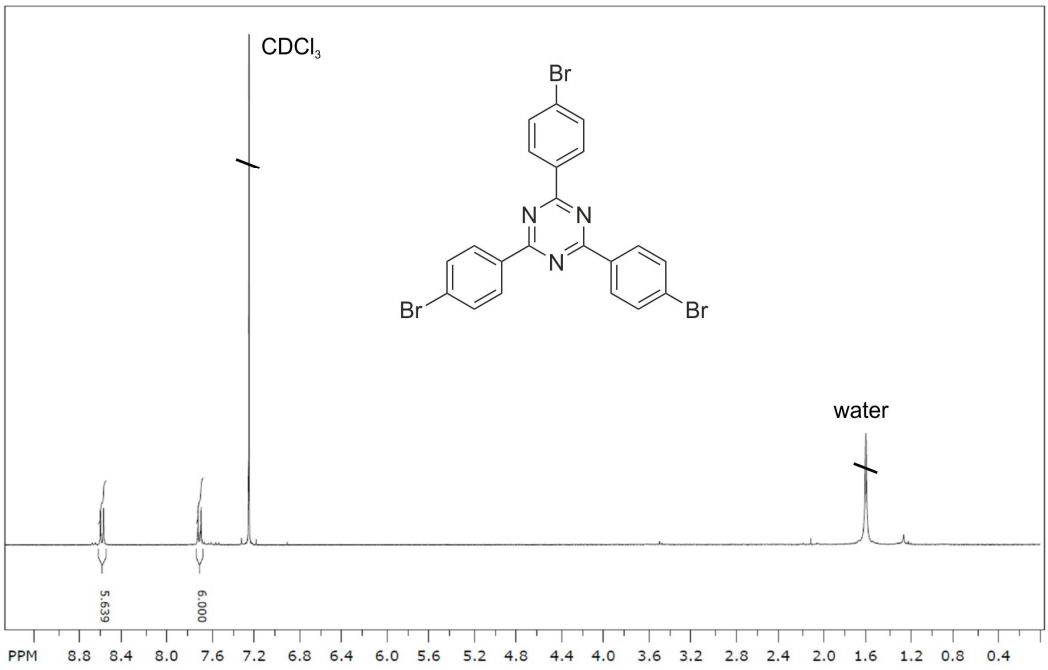

Figure 8-35: *^{1}H NMR spectrum of 2,4,6-tris(*p*-bromophenyl)-1,3,5-triazine.*

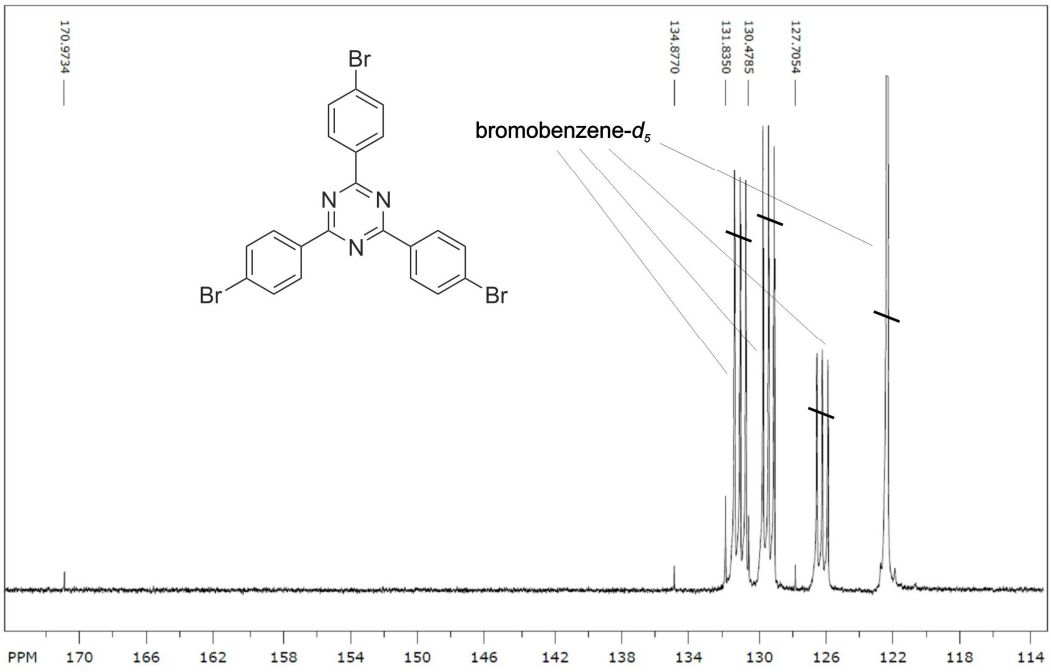

Figure 8-36: *^{13}C NMR spectrum of 2,4,6-tris(*p*-bromophenyl)-1,3,5-triazine.*

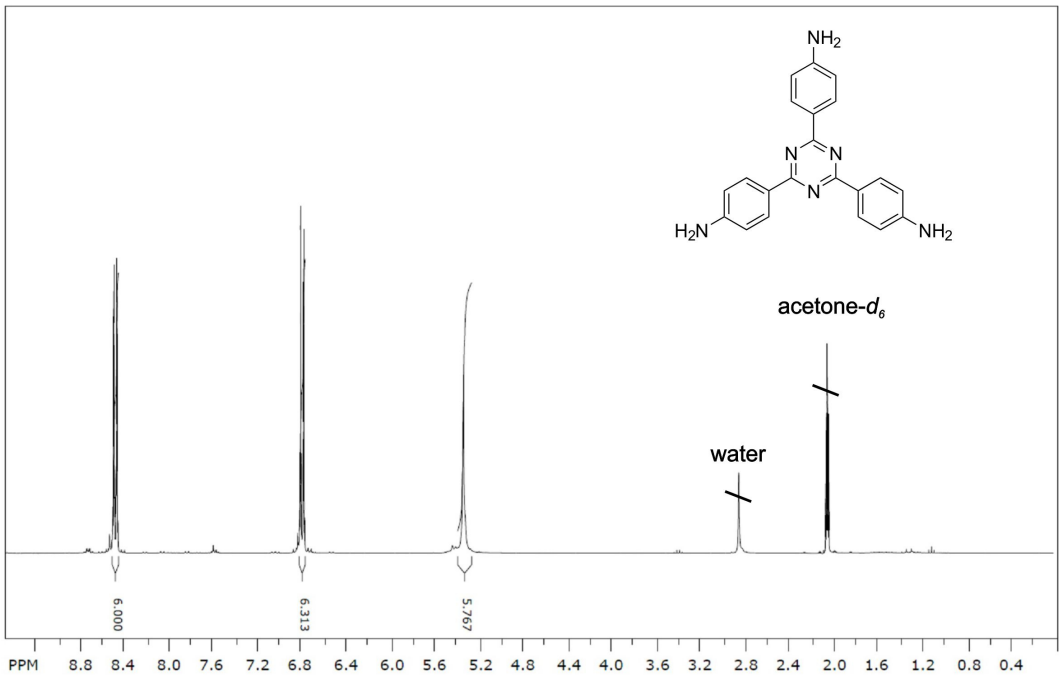

Figure 8-37: *^{1}H NMR spectrum of 2,4,6-tris(*p*-aminophenyl)-1,3,5-triazine.*

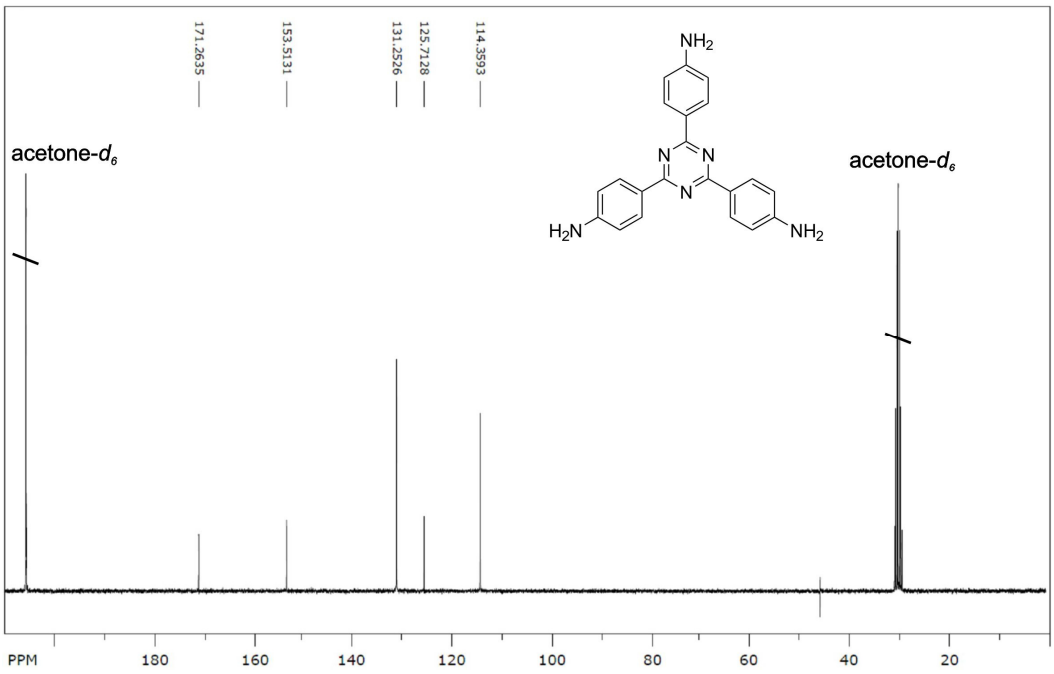

Figure 8-38: *^{13}C NMR spectrum of 2,4,6-tris(*p*-aminophenyl)-1,3,5-triazine.*

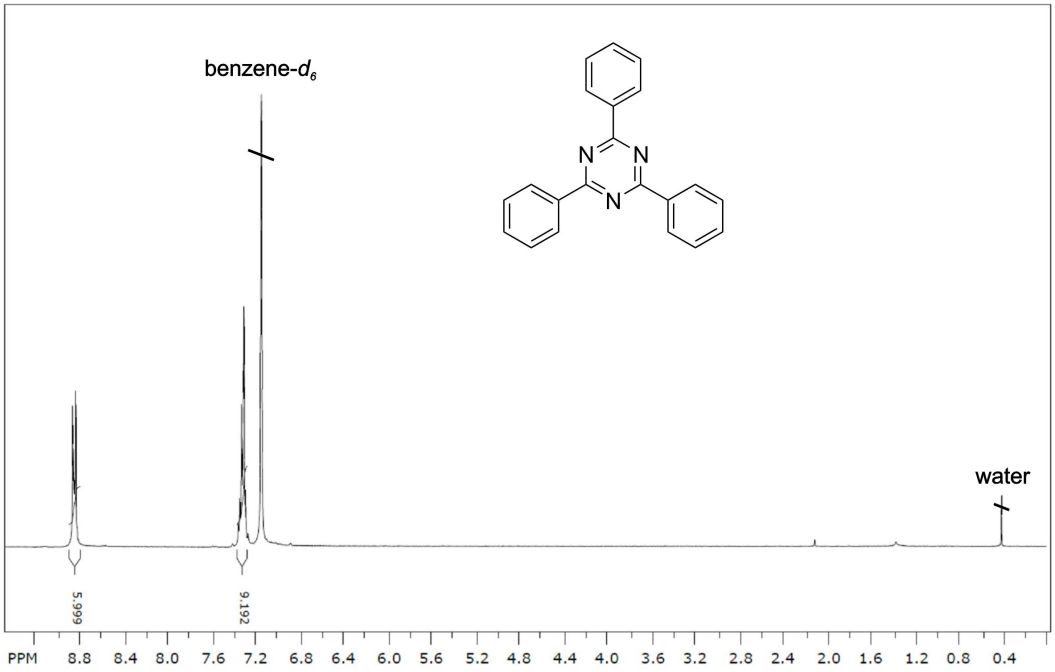

Figure 8-39: *^{1}H NMR spectrum of 2,4,6-triphenyl-1,3,5-triazine.*

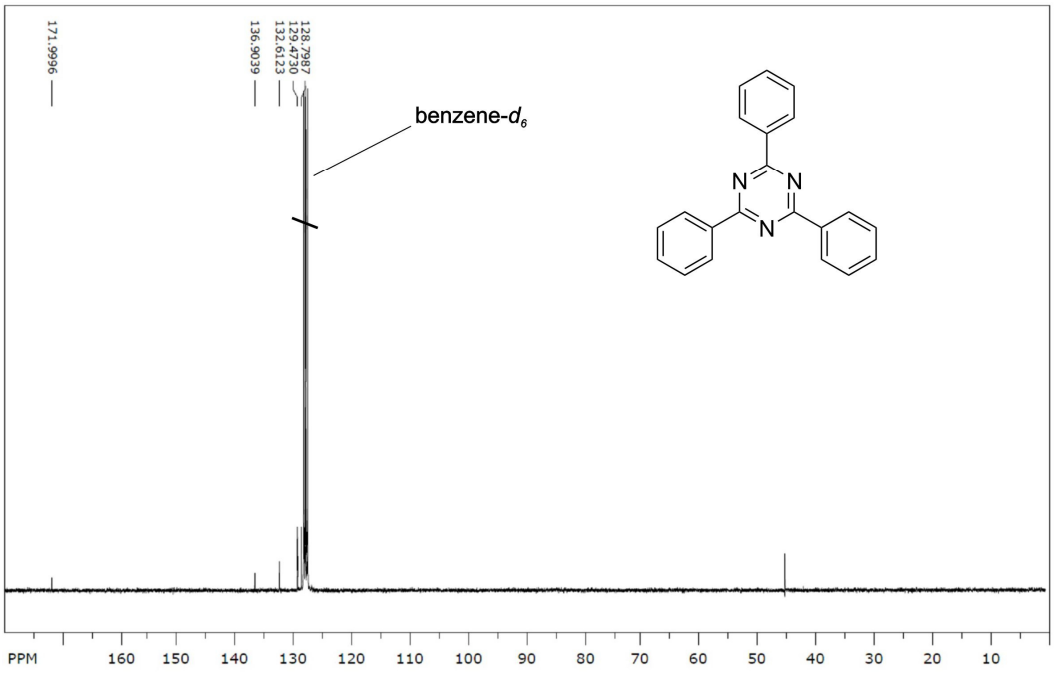

Figure 8-40: *^{13}C NMR spectrum of 2,4,6-triphenyl-1,3,5-triazine.*

9 Literature

[1] J.-R. Li, Y.-G. Ma, M. C. McCarthy, J. Sculley, J.-M. Yu, H.-K. Jeong, P. B. Balbuena, H.-C. Zhou, *Coord. Chem. Rev.* **2011**, *255*, 1791–1823.

[2] S. D. Kenarsari, D. Yang, G. Jiang, S. Zhang, J. Wang, A. G. Russell, Q. Wei, M. Fan, *RSC Adv.* **2013**, *3*, 22739–22773.

[3] *IPCC, 2013: Climate Change 2013: The Physical Science Basis. Contribution of Working Group I to the Fifth Assessment Report of the Intergovernmental Panel on Climate Change*, Cambridge University Press, Cambridge, United Kingdom and New York, NY, USA, **2013**.

[4] B. A. Seibel, P. J. Walsh, *Science* **2001**, *294*, 319–320.

[5] U. Riebesell, I. Zondervan, B. Rost, P. D. Tortell, R. E. Zeebe, F. M. M. Morel, *Nature* **2000**, *407*, 364–367.

[6] J. A. Kleypas, R. W. Buddemeier, D. Archer, J.-P. Gattuso, C. Langdon, B. N. Opdyke, *Science* **1999**, *284*, 118–120.

[7] K. Caldeira, M. E. Wickett, *Nature* **2003**, *425*, 365.

[8] *Submission under the United Nations Framework Convention on Climate Change and the Kyoto Protocol 2013 - National Inventory Report for the German Greenhouse Gas Inventory 1990-2011*, Federal Environment Agency (Umweltbundesamt), Germany, www.umweltbundesamt.de, **2013**.

[9] C. M. White, B. R. Strazisar, E. J. Granite, J. S. Hoffman, H. W. Pennline, *J. Air Waste Manage. Assoc.* **2003**, *53*, 645–715.

[10] N. MacDowell, N. Florin, A. Buchard, J. Hallett, A. Galindo, G. Jackson, C. S. Adjiman, C. K. Williams, N. Shah, P. Fennell, *Energy Environ. Sci.* **2010**, *3*, 1645–1669.

[11] R. S. Haszeldine, *Science* **2009**, *325*, 1647–1652.

[12] N. Hedin, L. J. Chen, A. Laaksonen, *Nanoscale* **2010**, *2*, 1819–1841.

[13] D. M. D'Alessandro, B. Smit, J. R. Long, *Angew. Chem. Int. Ed.* **2010**, *49*, 6058–6082.

[14] Y.-S. Bae, R. Q. Snurr, *Angew. Chem. Int. Ed.* **2011**, *50*, 11586–11596.

[15] W. M. Verdegaal, S. Becker, C. v. Olshausen, *Chem. Ing. Tech.* **2015**, *87*, 340–346.

[16] R. Stanger, T. Wall, R. Spörl, M. Paneru, S. Grathwohl, M. Weidmann, G. Scheffknecht, D. McDonald, K. Myöhänen, J. Ritvanen, S. Rahiala, T. Hyppänen, J. Mletzko, A. Kather, S. Santos, *Int. J. Greenhouse Gas Control* **2015**, *40*, 55 – 125.

[17] G. Scheffknecht, L. Al-Makhadmeh, U. Schnell, J. Maier, *Int. J. Greenhouse Gas Control* **2011**, *5*, S16–S35.

[18] R. Dawson, A. I. Cooper, D. J. Adams, *Polym. Int.* **2013**, *62*, 345–352.

[19] P. Mohanty, L. D. Kull, K. Landskron, *Nat. Commun.* **2011**, *2*, 2:401.

[20] T. C. Drage, C. E. Snape, L. A. Stevens, J. Wood, J. Wang, A. I. Cooper, R. Dawson, X. Guo, C. Satterley, R. Irons, *J. Mater. Chem.* **2012**, *22*, 2815–2823.

[21] N. Du, H. B. Park, M. M. Dal-Cin, M. D. Guiver, *Energy Environ. Sci.* **2012**, *5*, 7306–7322.

[22] A. W. Thornton, D. Dubbeldam, M. S. Liu, B. P. Ladewig, A. J. Hill, M. R. Hill, *Energy Environ. Sci.* **2012**, *5*, 7637–7646.

[23] M. M. Hossain, H. I. de Lasa, *Chem. Eng. Sci.* **2008**, *63*, 4433–4451.

[24] A. Eslamimanesh, A. H. Mohammadi, D. Richon, P. Naidoo, D. Ramjugernath, *J. Chem. Thermodyn.* **2012**, *46*, 62–71.

[25] M. Ramdin, T. W. de Loos, T. J. H. Vlugt, *Ind. Eng. Chem. Res.* **2012**, *51*, 8149–8177.

[26] Q. Wang, J. Bai, Z. Lu, Y. Pan, X. You, *Chem. Commun.* **2016**, *52*, 443–452.

[27] X. Lu, D. Jin, S. Wei, Z. Wang, C. An, W. Guo, *J. Mater. Chem. A* **2015**, *3*, 12118–12132.

[28] Y. Zeng, R. Zou, Y. Zhao, *Adv. Mater.* **2016**, *28*, 2855–2873.

[29] K. Sumida, D. L. Rogow, J. A. Mason, T. M. McDonald, E. D. Bloch, Z. R. Herm, T.-H. Bae, J. R. Long, *Chem. Rev.* **2012**, *112*, 724–781.

[30] A. Samanta, A. Zhao, G. K. H. Shimizu, P. Sarkar, R. Gupta, *Ind. Eng. Chem. Res.* **2012**, *51*, 1438–1463.

[31] B. Unger, K. Schumann, A. Brandt, *Chem. Ing. Tech.* **2010**, *82*, 929–940.

[32] Q. Wang, J. Luo, Z. Zhong, A. Borgna, *Energy Environ. Sci.* **2011**, *4*, 42–55.

[33] J. S. Beck, J. C. Vartuli, W. J. Roth, M. E. Leonowicz, C. T. Kresge, K. D. Schmitt, C. T. W. Chu, D. H. Olson, E. W. Sheppard, et al., *J. Am. Chem. Soc.* **1992**, *114*, 10834–10843.

[34] P. J. E. Harlick, A. Sayari, *Ind. Eng. Chem. Res.* **2007**, *46*, 446–458.

[35] R. Serna-Guerrero, E. Da'na, A. Sayari, *Ind. Eng. Chem. Res.* **2008**, *47*, 9406–9412.

[36] S. Choi, J. H. Drese, C. W. Jones, *ChemSusChem* **2009**, *2*, 796–854.

[37] M. L. Pinto, L. Mafra, J. M. Guil, J. Pires, J. Rocha, *Chem. Mater.* **2011**, *23*, 1387–1395.

[38] R. E. Morris, P. S. Wheatley, *Angew. Chem. Int. Ed.* **2008**, *47*, 4966–4981.

[39] T. A. Makal, J.-R. Li, W. Lu, H.-C. Zhou, *Chem. Soc. Rev.* **2012**, *41*, 7761–7779.

[40] J. Germain, J. M. J. Frechet, F. Svec, *Small* **2009**, *5*, 1098–1111.

[41] Y. Zhang, S. N. Riduan, *Chem. Soc. Rev.* **2012**, *41*, 2083–2094.

[42] P. Kaur, J. T. Hupp, S. T. Nguyen, *ACS Catal.* **2011**, *1*, 819–835.

[43] Z. Xiang, D. Cao, *J. Mater. Chem. A* **2013**, *1*, 2691–2718.

[44] X. Zhu, C. Tian, S. M. Mahurin, S.-H. Chai, C. Wang, S. Brown, G. M. Veith, H. Luo, H. Liu, S. Dai, *J. Am. Chem. Soc.* **2012**, *134*, 10478–10484.

[45] P. Kuhn, M. Antonietti, A. Thomas, *Angew. Chem. Int. Ed.* **2008**, *47*, 3450–3453.

[46] M. R. Liebl, J. Senker, *Chem. Mater.* **2013**, *25*, 970–980.

[47] T. Ben, C. Pei, D. Zhang, J. Xu, F. Deng, X. Jing, S. Qiu, *Energy Environ. Sci.* **2011**, *4*, 3991–3999.

[48] R. W. Tilford, S. J. Mugavero, P. J. Pellechia, J. J. Lavigne, *Adv. Mater.* **2008**, *20*, 2741–2746.

[49] C. Klumpen, M. Breunig, T. Homburg, N. Stock, J. Senker, *Chem. Mater.* **2016**, *28*, 5461–5470.

[50] S. Ren, R. Dawson, A. Laybourn, J.-x. Jiang, Y. Khimyak, D. J. Adams, A. I. Cooper, *Polym. Chem.* **2012**, *3*, 928–934.

[51] E. Robens, *Chem. Ing. Tech.* **2010**, *82*, 763–768.

[52] J. Rouquerol, D. Avnir, C. W. Fairbridge, D. H. Everett, J. H. Haynes, N. Pernicone, J. D. F. Ramsay, K. S. W. Sing, K. K. Unger, *Pure Appl. Chem.* **1994**, *66*, 1739–1758.

[53] M. Thommes, *Chem. Ing. Tech.* **2010**, *82*, 1059–1073.

[54] F. Schueth, *Chem. Ing. Tech.* **2010**, *82*, 769–777.

[55] J. Germain, J. M. J. Frechet, F. Svec, *Chem. Commun.* **2009**, 1526–1528.

[56] L. B. McCusker, F. Liebau, G. Engelhardt, *Pure Appl. Chem.* **2001**, *73*, 381–394.

[57] S. R. Batten, N. R. Champness, X.-M. Chen, J. Garcia-Martinez, S. Kitagawa, L. Ohrstrom, M. O'Keeffe, M. P. Suh, J. Reedijk, *Pure Appl. Chem.* **2013**, *85*, 1715–1724.

[58] L. Ohrstrom, *Crystals* **2015**, *5*, 154–162.

[59] K. S. W. Sing, D. H. Everett, R. A. W. Haul, L. Moscou, R. A. Pierotti, J. Rouquerol, T. Siemieniewska, *Pure Appl. Chem.* **1985**, *57*, 603–619.

[60] M. Thommes, K. Kaneko, A. V. Neimark, J. P. Olivier, F. Rodriguez-Reinoso, J. Rouquerol, K. S. W. Sing, *Pure Appl. Chem.* **2015**, *87*, 1051–1069.

[61] P. Kuhn, A. Forget, D. S. Su, A. Thomas, M. Antonietti, *J. Am. Chem. Soc.* **2008**, *130*, 13333–13337.

[62] D. Wu, F. Xu, B. Sun, R. Fu, H. He, K. Matyjaszewski, *Chem. Rev.* **2012**, *112*, 3959–4015.

[63] S. S.-Y. Chui, S. M.-F. Lo, J. P. H. Charmant, A. G. Orpen, I. D. Williams, *Science* **1999**, *283*, 1148–1150.

[64] M. Kondo, T. Yoshitomi, K. Seki, H. Matsuzaka, S. Kitagawa, *Angew. Chem. Int. Ed.* **1997**, *36*, 1725–1727.

[65] H. Li, M. Eddaoudi, M. O'Keeffe, M. Yaghi, *Nature* **1999**, *402*, 276–279.

[66] S. Kaskel, *Chem. Ing. Tech.* **2010**, *82*, 1019–1023.

[67] O. M. Yaghi, M. O'Keeffe, N. W. Ockwig, H. K. Chae, M. Eddaoudi, J. Kim, *Nature* **2003**, *423*, 705–714.

[68] H. Furukawa, N. Ko, Y. B. Go, N. Aratani, S. B. Choi, E. Choi, A. O. Yazaydin, R. Q. Snurr, M. O'Keeffe, J. Kim, O. M. Yaghi, *Science* **2010**, *329*, 424–428.

[69] O. K. Farha, I. Eryazici, N. C. Jeong, B. G. Hauser, C. E. Wilmer, A. A. Sarjeant, R. Q. Snurr, S. T. Nguyen, A. O. Yazaydin, J. T. Hupp, *J. Am. Chem. Soc.* **2012**, *134*, 15016–15021.

[70] T. C. Wang, W. Bury, D. A. Gomez-Gualdron, N. A. Vermeulen, J. E. Mondloch, P. Deria, K. Zhang, P. Z. Moghadam, A. A. Sarjeant, R. Q. Snurr, J. F. Stoddart, J. T. Hupp, O. K. Farha, *J. Am. Chem. Soc.* **2015**, *137*, 3585–3591.

[71] R. Gruenker, V. Bon, P. Mueller, U. Stoeck, S. Krause, U. Mueller, I. Senkovska, S. Kaskel, *Chem. Commun.* **2014**, *50*, 3450–3452.

[72] I. Senkovska, S. Kaskel, *Chem. Commun.* **2014**, *50*, 7089–7098.

[73] O. K. Farha, A. O. Yazaydin, I. Eryazici, C. D. Malliakas, B. G. Hauser, M. G. Kanatzidis, S. T. Nguyen, R. Q. Snurr, J. T. Hupp, *Nat. Chem.* **2010**, *2*, 944–948.

[74] J. R. Holst, A. I. Cooper, *Adv. Mater.* **2010**, *22*, 5212–5216.

[75] J. L. C. Rowsell, O. M. Yaghi, *J. Am. Chem. Soc.* **2006**, *128*, 1304–1315.

[76] Y.-S. Bae, C. Y. Lee, K. C. Kim, O. K. Farha, P. Nickias, J. T. Hupp, S. T. Nguyen, R. Q. Snurr, *Angew. Chem. Int. Ed.* **2012**, *51*, 1857–1860.

[77] D. Banerjee, A. J. Cairns, J. Liu, R. K. Motkuri, S. K. Nune, C. A. Fernandez, R. Krishna, D. M. Strachan, P. K. Thallapally, *Acc. Chem. Res.* **2015**, *48*, 211–219.

[78] G. F. de Lima, A. Mavrandonakis, H. A. de Abreu, H. A. Duarte, T. Heine, *J. Phys. Chem. C* **2013**, *117*, 4124–4130.

[79] M. Eddaoudi, J. Kim, N. Rosi, D. Vodak, J. Wachter, M. O'Keeffe, O. M. Yaghi, *Science* **2002**, *295*, 469–472.

[80] M. Dinca, J. R. Long, *Angew. Chem. Int. Ed.* **2008**, *47*, 6766–6779.

[81] S. Xiang, W. Zhou, Z. Zhang, M. A. Green, Y. Liu, B. Chen, *Angew. Chem. Int. Ed.* **2010**, *49*, 4615–4618.

[82] L.-C. Lin, J. Kim, X. Kong, E. Scott, T. M. McDonald, J. R. Long, J. A. Reimer, B. Smit, *Angew. Chem. Int. Ed.* **2013**, *52*, 4410–4413.

[83] Y. Peng, V. Krungleviciute, I. Eryazici, J. T. Hupp, O. K. Farha, T. Yildirim, *J. Am. Chem. Soc.* **2013**, *135*, 11887–11894.

[84] Y. He, W. Zhou, G. Qian, B. Chen, *Chem. Soc. Rev.* **2014**, *43*, 5657–5678.

[85] J. Y. Lee, O. K. Farha, J. Roberts, K. A. Scheidt, S. B. T. Nguyen, J. T. Hupp, *Chem. Soc. Rev.* **2009**, *38*, 1450–1459.

[86] D. Feng, Z.-Y. Gu, J.-R. Li, H.-L. Jiang, Z. Wei, H.-C. Zhou, *Angew. Chem. Int. Ed.* **2012**, *51*, 10307–10310.

[87] H. Furukawa, K. E. Cordova, M. O'Keeffe, O. M. Yaghi, *Science* **2013**, *341*, 974.

[88] L. E. Kreno, K. Leong, O. K. Farha, M. Allendorf, R. P. Van Duyne, J. T. Hupp, *Chem. Rev.* **2012**, *112*, 1105–1125.

[89] O. Shekhah, J. Liu, R. A. Fischer, C. Woell, *Chem. Soc. Rev.* **2011**, *40*, 1081–1106.

[90] D. Zacher, O. Shekhah, C. Woell, R. A. Fischer, *Chem. Soc. Rev.* **2009**, *38*, 1418–1429.

[91] P. Horcajada, C. Serre, M. Vallet-Regi, M. Sebban, F. Taulelle, G. Ferey, *Angew. Chem. Int. Ed.* **2006**, *45*, 5974–5978.

[92] P. Horcajada, T. Chalati, C. Serre, B. Gillet, C. Sebrie, T. Baati, J. F. Eubank, D. Heurtaux, P. Clayette, C. Kreuz, J.-S. Chang, Y. K. Hwang, V. Marsaud, P.-N. Bories, L. Cynober, S. Gil, G. Ferey, P. Couvreur, R. Gref, *Nat. Mater.* **2010**, *9*, 172–178.

[93] N. C. Jeong, B. Samanta, C. Y. Lee, O. K. Farha, J. T. Hupp, *J. Am. Chem. Soc.* **2012**, *134*, 51–54.

[94] P. Ramaswamy, N. E. Wong, G. K. H. Shimizu, *Chem. Soc. Rev.* **2014**, *43*, 5913–5932.

[95] M. Eddaoudi, H. Li, O. M. Yaghi, *J. Am. Chem. Soc.* **2000**, *122*, 1391–1397.

[96] A. O. Yazaydin, A. I. Benin, S. A. Faheem, P. Jakubczak, J. J. Low, R. R. Willis, R. Q. Snurr, *Chem. Mater.* **2009**, *21*, 1425–1430.

[97] H. W. Langmi, J. Ren, B. North, M. Mathe, D. Bessarabov, *Electrochim. Acta* **2014**, *128*, 368–392.

[98] Y. W. Li, R. T. Yang, *AIChE J.* **2008**, *54*, 269–279.

[99] M. P. Suh, H. J. Park, T. K. Prasad, D.-W. Lim, *Chem. Rev.* **2012**, *112*, 782–835.

[100] B. Xiao, P. S. Wheatley, X. Zhao, A. J. Fletcher, S. Fox, A. G. Rossi, I. L. Megson, S. Bordiga, L. Regli, K. M. Thomas, R. E. Morris, *J. Am. Chem. Soc.* **2007**, *129*, 1203–1209.

[101] J. Canivet, A. Fateeva, Y. Guo, B. Coasne, D. Farrusseng, *Chem. Soc. Rev.* **2014**, *43*, 5594–5617.

[102] E. Borfecchia, S. Maurelli, D. Gianolio, E. Groppo, M. Chiesa, F. Bonino, C. Lamberti, *J. Phys. Chem. C* **2012**, *116*, 19839–19850.

[103] A. Phan, C. J. Doonan, F. J. Uribe-Romo, C. B. Knobler, M. O'Keeffe, O. M. Yaghi, *Acc. Chem. Res.* **2010**, *43*, 58–67.

[104] Z. Zhang, Y. Zhao, Q. Gong, Z. Li, J. Li, *Chem. Commun.* **2013**, *49*, 653–661.

[105] T. M. McDonald, D. M. D'Alessandro, R. Krishna, J. R. Long, *Chem. Sci.* **2011**, *2*, 2022–2028.

[106] T. M. McDonald, W. R. Lee, J. A. Mason, B. M. Wiers, C. S. Hong, J. R. Long, *J. Am. Chem. Soc.* **2012**, *134*, 7056–7065.

[107] R. Lyndon, K. Konstas, B. P. Ladewig, P. D. Southon, C. J. Kepert, M. R. Hill, *Angew. Chem. Int. Ed.* **2013**, *52*, 3695–3698.

[108] N. C. Burtch, H. Jasuja, K. S. Walton, *Chem. Rev.* **2014**, *114*, 10575–10612.

[109] K. S. Park, Z. Ni, A. P. Cote, J. Y. Choi, R. D. Huang, F. J. Uribe-Romo, H. K. Chae, M. O'Keeffe, O. M. Yaghi, *Proc. Natl. Acad. Sci. U. S. A.* **2006**, *103*, 10186–10191.

[110] R. Banerjee, A. Phan, B. Wang, C. Knobler, H. Furukawa, M. O'Keeffe, O. M. Yaghi, *Science* **2008**, *319*, 939–943.

[111] T. Ahnfeldt, D. Gunzelmann, T. Loiseau, D. Hirsemann, J. Senker, G. Ferey, N. Stock, *Inorg. Chem.* **2009**, *48*, 3057–3064.

[112] T. Loiseau, C. Serre, C. Huguenard, G. Fink, F. Taulelle, M. Henry, T. Bataille, G. Ferey, *Chem. - Eur. J.* **2004**, *10*, 1373–1382.

[113] G. Ferey, C. Mellot-Draznieks, C. Serre, F. Millange, J. Dutour, S. Surble, I. Margiolaki, *Science* **2005**, *309*, 2040–2042.

[114] T. Li, D.-L. Chen, J. E. Sullivan, M. T. Kozlowski, J. K. Johnson, N. L. Rosi, *Chem. Sci.* **2013**, *4*, 1746–1755.

[115] V. Colombo, S. Galli, H. J. Choi, G. D. Han, A. Maspero, G. Palmisano, N. Masciocchi, J. R. Long, *Chem. Sci.* **2011**, *2*, 1311–1319.

[116] X. Feng, X. Ding, D. Jiang, *Chem. Soc. Rev.* **2012**, *41*, 6010–6022.

[117] R. Dawson, A. I. Cooper, D. J. Adams, *Prog. Polym. Sci.* **2012**, *37*, 530–563.

[118] P. J. Waller, F. Gandara, O. M. Yaghi, *Acc. Chem. Res.* **2015**, *48*, 3053–3063.

[119] N. B. McKeown, P. M. Budd, *Chem. Soc. Rev.* **2006**, *35*, 675–683.

[120] P. M. Budd, B. S. Ghanem, S. Makhseed, N. B. McKeown, K. J. Msayib, C. E. Tattershall, *Chem. Commun.* **2004**, 230–231.

[121] N. B. McKeown, P. M. Budd, K. J. Msayib, B. S. Ghanem, H. J. Kingston, C. E. Tattershall, S. Makhseed, K. J. Reynolds, D. Fritsch, *Chem. - Eur. J.* **2005**, *11*, 2610–2620.

[122] N. B. McKeown, S. Hanif, K. Msayib, C. E. Tattershall, P. M. Budd, *Chem. Commun.* **2002**, 2782–2783.

[123] N. B. McKeown, P. M. Budd, *Macromolecules* **2010**, *43*, 5163–5176.

[124] M. Hashem, C. G. Bezzu, B. M. Kariuki, N. B. McKeown, *Polym. Chem.* **2011**, *2*, 2190–2192.

[125] J. Weber, N. Du, M. D. Guiver, *Macromolecules* **2011**, *44*, 1763–1767.

[126] C. G. Bezzu, M. Carta, A. Tonkins, J. C. Jansen, P. Bernardo, F. Bazzarelli, N. B. McKeown, *Adv. Mater.* **2012**, *24*, 5930–5933.

[127] C. R. Mason, L. Maynard-Atem, N. M. Al-Harbi, P. M. Budd, P. Bernardo, F. Bazzarelli, G. Clarizia, J. C. Jansen, *Macromolecules* **2011**, *44*, 6471–6479.

[128] H. A. Patel, C. T. Yavuz, *Chem. Commun.* **2012**, *48*, 9989–9991.

[129] N. Ritter, I. Senkovska, S. Kaskel, J. Weber, *Macromolecules* **2011**, *44*, 2025–2033.

[130] J. Weber, J. Schmidt, A. Thomas, W. Boehlmann, *Langmuir* **2010**, *26*, 15650–15656.

[131] S. Makhseed, F. Ibrahim, J. Samuel, *Polymer* **2012**, *53*, 2964–2972.

[132] J. Vile, M. Carta, C. G. Bezzu, N. B. McKeown, *Polym. Chem.* **2011**, *2*, 2257–2260.

[133] N. A. Rakow, M. S. Wendland, J. E. Trend, R. J. Poirier, D. M. Paolucci, S. P. Maki, C. S. Lyons, M. J. Swierczek, *Langmuir* **2010**, *26*, 3767–3770.

[134] P. M. Budd, A. Butler, J. Selbie, K. Mahmood, N. B. McKeown, B. Ghanem, K. Msayib, D. Book, A. Walton, *Phys. Chem. Chem. Phys.* **2007**, *9*, 1802–1808.

[135] J. Weber, Q. Su, M. Antonietti, A. Thomas, *Macromol. Rapid Commun.* **2007**, *28*, 1871–1876.

[136] N. B. McKeown, P. M. Budd, D. Book, *Macromol. Rapid Commun.* **2007**, *28*, 995–1002.

[137] N. B. McKeown, B. Gahnem, K. J. Msayib, P. M. Budd, C. E. Tattershall, K. Mahmood, S. Tan, D. Book, H. W. Langmi, A. Walton, *Angew. Chem. Int. Ed.* **2006**, *45*, 1804–1807.

[138] A. V. Maffei, P. M. Budd, N. B. McKeown, *Langmuir* **2006**, *22*, 4225–4229.

[139] H. J. Mackintosh, P. M. Budd, N. B. McKeown, *J. Mater. Chem.* **2008**, *18*, 573–578.

[140] F. Y. Li, Y. Xiao, T.-S. Chung, S. Kawi, *Macromolecules* **2012**, *45*, 1427–1437.

[141] N. Du, H. B. Park, G. P. Robertson, M. M. Dal-Cin, T. Visser, L. Scoles, M. D. Guiver, *Nat. Mater.* **2011**, *10*, 372–375.

[142] Y.-C. Zhao, T. Wang, L.-M. Zhang, Y. Cui, B.-H. Han, *ACS Appl. Mater. Interfaces* **2012**, *4*, 6975–6981.

[143] A. P. Katsoulidis, M. G. Kanatzidis, *Chem. Mater.* **2012**, *24*, 471–479.

[144] D.-S. Zhang, Z. Chang, Y.-B. Lv, T.-L. Hu, X.-H. Bu, *RSC Adv.* **2012**, *2*, 408–410.

[145] Y.-C. Zhao, D. Zhou, Q. Chen, X.-J. Zhang, N. Bian, A.-D. Qi, B.-H. Han, *Macromolecules* **2011**, *44*, 6382–6388.

[146] A. P. Katsoulidis, M. G. Kanatzidis, *Chem. Mater.* **2011**, *23*, 1818–1824.

[147] M. Rose, N. Klein, I. Senkovska, C. Schrage, P. Wollmann, W. Bohlmann, B. Bohringer, S. Fichtner, S. Kaskel, *J. Mater. Chem.* **2011**, *21*, 711–716.

[148] R. S. Sprick, A. Thomas, U. Scherf, *Polym. Chem.* **2010**, *1*, 283–285.

[149] Y. G. Zhang, S. N. Riduan, J. Y. Ying, *Chem. - Eur. J.* **2009**, *15*, 1077–1081.

[150] A. Nagai, X. Chen, X. Feng, X. Ding, Z. Guo, D. Jiang, *Angew. Chem. Int. Ed.* **2013**, *52*, 3770–3774.

[151] C. Zhang, Y. Liu, B. Li, B. Tan, C.-F. Chen, H.-B. Xu, X.-L. Yang, *ACS Macro Lett.* **2012**, *1*, 190–193.

[152] S.-Y. Ding, W. Wang, *Chem. Soc. Rev.* **2012**, *42*, 548–568.

[153] F. Vilela, K. Zhang, M. Antonietti, *Energy Environ. Sci.* **2012**, *5*, 7819–7832.

[154] A. Thomas, *Angew. Chem. Int. Ed.* **2010**, *49*, 8328–8344.

[155] A. Thomas, F. Goettmann, M. Antonietti, *Chem. Mater.* **2008**, *20*, 738–755.

[156] A. I. Cooper, *Adv. Mater.* **2009**, *21*, 1291–1295.

[157] A. P. Cote, A. I. Benin, N. W. Ockwig, M. O'Keeffe, A. J. Matzger, O. M. Yaghi, *Science* **2005**, *310*, 1166–1170.

[158] A. P. Cote, H. M. El-Kaderi, H. Furukawa, J. R. Hunt, O. M. Yaghi, *J. Am. Chem. Soc.* **2007**, *129*, 12914–12915.

[159] H. M. El-Kaderi, J. R. Hunt, J. L. Mendoza-Cortes, A. P. Cote, R. E. Taylor, M. O'Keeffe, O. M. Yaghi, *Science* **2007**, *316*, 268–272.

[160] H. Furukawa, O. M. Yaghi, *J. Am. Chem. Soc.* **2009**, *131*, 8875–8883.

[161] S. B. Kalidindi, C. Wiktor, A. Ramakrishnan, J. Wessing, A. Schneemann, G. Van Tendeloo, R. A. Fischer, *Chem. Commun.* **2013**, *49*, 463–465.

[162] N. L. Campbell, R. Clowes, L. K. Ritchie, A. I. Cooper, *Chem. Mater.* **2009**, *21*, 204–206.

[163] J. R. Hunt, C. J. Doonan, J. D. LeVangie, A. P. Cote, O. M. Yaghi, *J. Am. Chem. Soc.* **2008**, *130*, 11872–11873.

[164] E. L. Spitler, B. T. Koo, J. L. Novotney, J. W. Colson, F. J. Uribe-Romo, G. D. Gutierrez, P. Clancy, W. R. Dichtel, *J. Am. Chem. Soc.* **2011**, *133*, 19416–19421.

[165] B. Lukose, A. Kuc, T. Heine, *Chem. - Eur. J.* **2011**, *17*, 2388–2392.

[166] Y. Du, D. Calabro, B. Wooler, Q. Li, S. Cundy, P. Kamakoti, D. Colmyer, K. Mao, P. Ravikovitch, *J. Phys. Chem. C* **2014**, *118*, 399–407.

[167] X. Feng, Y. Dong, D. Jiang, *CrystEngComm* **2013**, *15*, 1508–1511.

[168] S. Jin, K. Furukawa, M. Addicoat, L. Chen, S. Takahashi, S. Irle, T. Nakamura, D. Jiang, *Chem. Sci.* **2013**, *4*, 4505–4511.

[169] D. P. Cao, J. H. Lan, W. C. Wang, B. Smit, *Angew. Chem. Int. Ed.* **2009**, *48*, 4730–4733.

[170] S. S. Han, H. Furukawa, O. M. Yaghi, W. A. Goddard, *J. Am. Chem. Soc.* **2008**, *130*, 11580–11581.

[171] J. Zhao, T. Yan, *RSC Adv.* **2014**, *4*, 15542–15551.

[172] C. J. Doonan, D. J. Tranchemontagne, T. G. Glover, J. R. Hunt, O. M. Yaghi, *Nat. Chem.* **2010**, *2*, 235–238.

[173] L. M. Lanni, R. W. Tilford, M. Bharathy, J. J. Lavigne, *J. Am. Chem. Soc.* **2011**, *133*, 13975–13983.

[174] Z. Kahveci, T. Islamoglu, G. A. Shar, R. Ding, H. M. El-Kaderi, *CrystEngComm* **2013**, *15*, 1524–1527.

[175] T. Faury, F. Dumur, S. Clair, M. Abel, L. Porte, D. Gigmes, *CrystEngComm* **2013**, *15*, 2067–2075.

[176] R. W. Tilford, W. R. Gemmill, H. C. zur Loye, J. J. Lavigne, *Chem. Mater.* **2006**, *18*, 5296–5301.

[177] Y. Du, K. Mao, P. Kamakoti, P. Ravikovitch, C. Paur, S. Cundy, Q. Li, D. Calabro, *Chem. Commun.* **2012**, *48*, 4606–4608.

[178] Y. Du, D. Calabro, B. Wooler, P. Kortunov, Q. Li, S. Cundy, K. Mao, *Chem. Mater.* **2015**, *27*, 1445–1447.

[179] D. N. Bunck, W. R. Dichtel, *Angew. Chem. Int. Ed.* **2012**, *51*, 1885–1889.

[180] D. N. Bunck, W. R. Dichtel, *Chem. Commun.* **2013**, *49*, 2457–2459.

[181] A. Nagai, Z. Guo, X. Feng, S. Jin, X. Chen, X. Ding, D. Jiang, *Nat. Commun.* **2011**, *2*, 2:536.

[182] G. H. V. Bertrand, V. K. Michaelis, T.-C. Ong, R. G. Griffin, D. Mircea, *Proc. Natl. Acad. Sci. U. S. A.* **2013**, *110*, 4923–4928.

[183] S. Wan, J. Guo, J. Kim, H. Ihee, D. L. Jiang, *Angew. Chem. Int. Ed.* **2009**, *48*, 5439–5442.

[184] S. Wan, J. Guo, J. Kim, H. Ihee, D. L. Jiang, *Angew. Chem. Int. Ed.* **2008**, *47*, 8826–8830.

[185] X. Feng, L. Liu, Y. Honsho, A. Saeki, S. Seki, S. Irle, Y. Dong, A. Nagai, D. Jiang, *Angew. Chem. Int. Ed.* **2012**, *51*, 2618–2622.

[186] S. Wan, F. Gandara, A. Asano, H. Furukawa, A. Saeki, S. K. Dey, L. Liao, M. W. Ambrogio, Y. Y. Botros, X.-F. Duan, S. Seki, J. F. Stoddart, O. M. Yaghi, *Chem. Mater.* **2011**, *23*, 4094–4097.

[187] X. Feng, L. Chen, Y. Dong, D. Jiang, *Chem. Commun.* **2011**, *47*, 1979–1981.

[188] V. S. P. K. Neti, X. Wu, M. Hosseini, R. A. Bernal, S. Deng, L. Echegoyen, *CrystEngComm* **2013**, *15*, 7157–7160.

[189] E. L. Spitler, W. R. Dichtel, *Nat. Chem.* **2010**, *2*, 672–677.

[190] X. Ding, X. Feng, A. Saeki, S. Seki, A. Nagai, D. Jiang, *Chem. Commun.* **2012**, *48*, 8952–8954.

[191] X. Ding, L. Chen, Y. Honsho, X. Feng, O. Saengsawang, J. Guo, A. Saeki, S. Seki, S. Irle, S. Nagase, V. Parasuk, D. Jiang, *J. Am. Chem. Soc.* **2011**, *133*, 14510–14513.

[192] X. Ding, J. Guo, X. Feng, Y. Honsho, J. Guo, S. Seki, P. Maitarad, A. Saeki, S. Nagase, D. Jiang, *Angew. Chem. Int. Ed.* **2011**, *50*, 1289–1293.

[193] T. E. Reich, K. T. Jackson, S. Li, P. Jena, H. M. El-Kaderi, *J. Mater. Chem.* **2011**, *21*, 10629–10632.

[194] T. E. Reich, S. Behera, K. T. Jackson, P. Jena, H. M. El-Kaderi, *J. Mater. Chem.* **2012**, *22*, 13524–13528.

[195] K. T. Jackson, M. G. Rabbani, T. E. Reich, H. M. El-Kaderi, *Polym. Chem.* **2011**, *2*, 2775–2777.

[196] K. T. Jackson, T. E. Reich, H. M. El-Kaderi, *Chem. Commun.* **2012**, *48*, 8823–8825.

[197] P. Kuhn, A. Forget, J. Hartmann, A. Thomas, M. Antonietti, *Adv. Mater.* **2009**, *21*, 897–901.

[198] S. Hug, M. E. Tauchert, S. Li, U. E. Pachmayr, B. V. Lotsch, *J. Mater. Chem.* **2012**, *22*, 13956–13964.

[199] P. Katekomol, J. Roeser, M. Bojdys, J. Weber, A. Thomas, *Chem. Mater.* **2013**, *25*, 1542–1548.

[200] P. Kuhn, A. Thomas, M. Antonietti, *Macromolecules* **2009**, *42*, 319–326.

[201] M. J. Bojdys, J. Jeromenok, A. Thomas, M. Antonietti, *Adv. Mater.* **2010**, *22*, 2202–2205.

[202] M. J. Bojdys, S. A. Wohlgemuth, A. Thomas, M. Antonietti, *Macromolecules* **2010**, *43*, 6639–6645.

[203] B. Juergens, E. Irran, J. Senker, P. Kroll, H. Muller, W. Schnick, *J. Am. Chem. Soc.* **2003**, *125*, 10288–10300.

[204] W. Zhang, C. Li, Y. P. Yuan, L. G. Qiu, A. J. Xie, Y. H. Shen, J. F. Zhu, *J. Mater. Chem.* **2010**, *20*, 6413–6415.

[205] S. Ren, M. J. Bojdys, R. Dawson, A. Laybourn, Y. Z. Khimyak, D. J. Adams, A. I. Cooper, *Adv. Mater.* **2012**, *24*, 2357–2361.

[206] A. Bhunia, I. Boldog, A. Moller, C. Janiak, *J. Mater. Chem. A* **2013**, *1*, 14990–14999.

[207] H. A. Patel, F. Karadas, A. Canlier, J. Park, E. Deniz, Y. Jung, M. Atilhan, C. T. Yavuz, *J. Mater. Chem.* **2012**, *22*, 8431–8437.

[208] W. Wang, H. Ren, F. Sun, K. Cai, H. Ma, J. Du, H. Zhao, G. Zhu, *Dalton Trans.* **2012**, *41*, 3933–3936.

[209] C. E. Chan-Thaw, A. Villa, P. Katekomol, D. S. Su, A. Thomas, L. Prati, *Nano Lett.* **2010**, *10*, 537–541.

[210] R. Palkovits, M. Antonietti, P. Kuhn, A. Thomas, F. Schueth, *Angew. Chem. Int. Ed.* **2009**, *48*, 6909–6912.

[211] C. E. Chan-Thaw, A. Villa, L. Prati, A. Thomas, *Chem. - Eur. J.* **2011**, *17*, 1052–1057.

[212] H. Y. Zhao, Z. Jin, H. M. Su, X. F. Jing, F. X. Sun, G. S. Zhu, *Chem. Commun.* **2011**, *47*, 6389–6391.

[213] J. Liu, E. Zong, H. Fu, S. Zheng, Z. Xu, D. Zhu, *J. Colloid Interface Sci.* **2012**, *372*, 99–107.

[214] P. Kuhn, K. Kruger, A. Thomas, M. Antonietti, *Chem. Commun.* **2008**, 5815–5817.

[215] H. Ren, T. Ben, E. Wang, X. Jing, M. Xue, B. Liu, Y. Cui, S. Qiu, G. Zhu, *Chem. Commun.* **2010**, *46*, 291–293.

[216] S. Hug, L. Stegbauer, H. Oh, M. Hirscher, B. V. Lotsch, *Chem. Mater.* **2015**, *27*, 8001–8010.

[217] Y. Zhao, K. X. Yao, B. Teng, T. Zhang, Y. Han, *Energy Environ. Sci.* **2013**, *6*, 3684–3692.

[218] S. Hug, M. B. Mesch, H. Oh, N. Popp, M. Hirscher, J. Senker, B. V. Lotsch, *J. Mater. Chem. A* **2014**, *2*, 5928–5936.

[219] L. Tao, F. Niu, C. Wang, J. Liu, T. Wang, Q. Wang, *J. Mater. Chem. A* **2016**, *4*, 11812–11820.

[220] X. Liu, H. Li, Y. Zhang, B. Xu, S. A, H. Xia, Y. Mu, *Polym. Chem.* **2013**, *4*, 2445–2448.

[221] S. J. Rowan, S. J. Cantrill, G. R. L. Cousins, J. K. M. Sanders, J. F. Stoddart, *Angew. Chem. Int. Ed.* **2002**, *41*, 898–952.

[222] M. E. Belowich, J. F. Stoddart, *Chem. Soc. Rev.* **2012**, *41*, 2003–2024.

[223] Y. Jin, Y. Zhu, W. Zhang, *CrystEngComm* **2013**, *15*, 1484–1499.

[224] H. Schiff, *Justus Liebigs Ann. Chem.* **1864**, *131*, 118–119.

[225] F. J. Uribe-Romo, J. R. Hunt, H. Furukawa, C. Klock, M. O'Keeffe, O. M. Yaghi, *J. Am. Chem. Soc.* **2009**, *131*, 4570–4571.

[226] P. Pandey, A. P. Katsoulidis, I. Eryazici, Y. Y. Wu, M. G. Kanatzidis, S. T. Nguyen, *Chem. Mater.* **2010**, *22*, 4974–4979.

[227] N. C. Duncan, B. P. Hay, E. W. Hagaman, R. Custelcean, *Tetrahedron* **2012**, *68*, 53–64.

[228] M. G. Schwab, B. Fassbender, H. W. Spiess, A. Thomas, X. L. Feng, K. Mullen, *J. Am. Chem. Soc.* **2009**, *131*, 7216–7217.

[229] A. Laybourn, R. Dawson, R. Clowes, J. A. Iggo, A. I. Cooper, Y. Z. Khimyak, D. J. Adams, *Polym. Chem.* **2012**, *3*, 533–537.

[230] Y.-B. Zhang, J. Su, H. Furukawa, Y. Yun, F. Gandara, A. Duong, X. Zou, O. M. Yaghi, *J. Am. Chem. Soc.* **2013**, *135*, 16336–16339.

[231] Q. Fang, S. Gu, J. Zheng, Z. Zhuang, S. Qiu, Y. Yan, *Angew. Chem. Int. Ed.* **2014**, *53*, 2878–2882.

[232] M. G. Schwab, M. Hamburger, X. L. Feng, J. Shu, H. W. Spiess, X. C. Wang, M. Antonietti, K. Mullen, *Chem. Commun.* **2010**, *46*, 8932–8934.

[233] S. Lin, C. S. Diercks, Y.-B. Zhang, N. Kornienko, E. M. Nichols, Y. Zhao, A. R. Paris, D. Kim, P. Yang, O. M. Yaghi, C. J. Chang, *Science* **2015**, *349*, 1208–1213.

[234] E. Verde-Sesto, E. M. Maya, A. E. Lozano, J. G. de la Campa, F. Sanchez, M. Iglesias, *J. Mater. Chem.* **2012**, *22*, 24637–24643.

[235] S.-Y. Ding, J. Gao, Q. Wang, Y. Zhang, W.-G. Song, C.-Y. Su, W. Wang, *J. Am. Chem. Soc.* **2011**, *133*, 19816–19822.

[236] M. K. Bhunia, S. K. Das, P. Pachfule, R. Banerjee, A. Bhaumik, *Dalton Trans.* **2012**, *41*, 1304–1311.

[237] J.-R. Song, J. Sun, J. Liu, Z.-T. Huang, Q.-Y. Zheng, *Chem. Commun.* **2014**, *50*, 788–791.

[238] V. S. P. K. Neti, X. Wu, S. Deng, L. Echegoyen, *Polym. Chem.* **2013**, *4*, 4566–4569.

[239] Y. Zeng, R. Zou, Z. Luo, H. Zhang, X. Yao, X. Ma, R. Zou, Y. Zhao, *J. Am. Chem. Soc.* **2015**, *137*, 1020–1023.

[240] N. Popp, T. Homburg, N. Stock, J. Senker, *J. Mater. Chem. A* **2015**, *3*, 18492–18504.

[241] C. Xu, N. Hedin, *J. Mater. Chem. A* **2013**, *1*, 3406–3414.

[242] S. Kandambeth, V. Venkatesh, D. B. Shinde, S. Kumari, A. Halder, S. Verma, R. Banerjee, *Nat. Commun.* **2015**, *6*, 6:6786.

[243] Y. Zhu, H. Long, W. Zhang, *Chem. Mater.* **2013**, *25*, 1630–1635.

[244] P. A. Kerneghan, S. D. Halperin, D. L. Bryce, K. E. Maly, *Can. J. Chem.* **2011**, *89*, 577–582.

[245] X. Chen, M. Addicoat, S. Irle, A. Nagai, D. Jiang, *J. Am. Chem. Soc.* **2013**, *135*, 546–549.

[246] S. Kandambeth, A. Mallick, B. Lukose, M. V. Mane, T. Heine, R. Banerjee, *J. Am. Chem. Soc.* **2012**, *134*, 19524–19527.

[247] M. G. Rabbani, A. K. Sekizkardes, Z. Kahveci, T. E. Reich, R. Ding, H. M. El-Kaderi, *Chem. - Eur. J.* **2013**, *19*, 3324–3328.

[248] R. Gomes, P. Bhanja, A. Bhaumik, *Chem. Commun.* **2015**, *51*, 10050–10053.

[249] F. J. Uribe-Romo, C. J. Doonan, H. Furukawa, K. Oisaki, O. M. Yaghi, *J. Am. Chem. Soc.* **2011**, *133*, 11478–11481.

[250] L. Stegbauer, K. Schwinghammer, B. V. Lotsch, *Chem. Sci.* **2014**, *5*, 2789–2793.

[251] J. Kalia, R. Raines, *Angew. Chem. Int. Ed.* **2008**, *47*, 7523–7526.

[252] D. N. Bunck, W. R. Dichtel, *J. Am. Chem. Soc.* **2013**, *135*, 14952–14955.

[253] S. Dalapati, S. Jin, J. Gao, Y. Xu, A. Nagai, D. Jiang, *J. Am. Chem. Soc.* **2013**, *135*, 17310–17313.

[254] V. S. Vyas, F. Haase, L. Stegbauer, G. Savasci, F. Podjaski, C. Ochsenfeld, B. V. Lotsch, *Nat. Commun.* **2015**, *6*, 6:8508.

[255] Z. Li, X. Feng, Y. Zou, Y. Zhang, H. Xia, X. Liu, Y. Mu, *Chem. Commun.* **2014**, *50*, 13825–13828.

[256] B. Li, R. Gong, W. Wang, X. Huang, W. Zhang, H. Li, C. Hu, B. Tan, *Macromolecules* **2011**, *44*, 2410–2414.

[257] B. Li, F. Su, H.-K. Luo, L. Liang, B. Tan, *Microporous Mesoporous Mater.* **2010**, *138*, 207–214.

[258] C. D. Wood, B. Tan, A. Trewin, F. Su, M. J. Rosseinsky, D. Bradshaw, Y. Sun, L. Zhou, A. I. Cooper, *Adv. Mater.* **2008**, *20*, 1916–1921.

[259] J.-H. Ahn, J.-E. Jang, C.-G. Oh, S.-K. Ihm, J. Cortez, D. C. Sherrington, *Macromolecules* **2006**, *39*, 627–632.

[260] J. Germain, J. Hradil, J. M. J. Frechet, F. Svec, *Chem. Mater.* **2006**, *18*, 4430–4435.

[261] B. Li, R. Gong, Y. Luo, B. Tan, *Soft Matter* **2011**, *7*, 10910–10916.

[262] M. G. Schwab, I. Senkovska, M. Rose, N. Klein, M. Koch, J. Pahnke, G. Jonschker, B. Schmitz, M. Hirscher, S. Kaskel, *Soft Matter* **2009**, *5*, 1055–1059.

[263] J. Y. Lee, C. D. Wood, D. Bradshaw, M. J. Rosseinsky, A. I. Cooper, *Chem. Commun.* **2006**, 2670–2672.

[264] R. Dawson, L. A. Stevens, T. C. Drage, C. E. Snape, M. W. Smith, D. J. Adams, A. I. Cooper, *J. Am. Chem. Soc.* **2012**, *134*, 10741–10744.

[265] C. F. Martin, E. Stockel, R. Clowes, D. J. Adams, A. I. Cooper, J. J. Pis, F. Rubiera, C. Pevida, *J. Mater. Chem.* **2011**, *21*, 5475–5483.

[266] R. Dawson, T. Ratvijitvech, M. Corker, A. Laybourn, Y. Z. Khimyak, A. I. Cooper, D. J. Adams, *Polym. Chem.* **2012**, *3*, 2034–2038.

[267] J. Germain, F. Svec, J. M. J. Frechet, *Chem. Mater.* **2008**, *20*, 7069–7076.

[268] J. Germain, J. M. J. Frechet, F. Svec, *J. Mater. Chem.* **2007**, *17*, 4989–4997.

[269] Q. Chen, M. Luo, P. Hammershoej, D. Zhou, Y. Han, B. W. Laursen, C.-G. Yan, B.-H. Han, *J. Am. Chem. Soc.* **2012**, *134*, 6084–6087.

[270] Y. Luo, B. Li, W. Wang, K. Wu, B. Tan, *Adv. Mater.* **2012**, *24*, 5703–5707.

[271] M. P. Tsyurupa, V. A. Davankov, *React. Funct. Polym.* **2002**, *53*, 193–203.

[272] M. P. Tsyurupa, V. A. Davankov, *React. Funct. Polym.* **2006**, *66*, 768–779.

[273] R. Dawson, E. Stöckel, J. R. Holst, D. J. Adams, A. I. Cooper, *Energy Environ. Sci.* **2011**, *4*, 4239–4245.

[274] C. D. Wood, B. Tan, A. Trewin, H. J. Niu, D. Bradshaw, M. J. Rosseinsky, Y. Z. Khimyak, N. L. Campbell, R. Kirk, E. Stockel, A. I. Cooper, *Chem. Mater.* **2007**, *19*, 2034–2048.

[275] H. Lim, M. C. Cha, J. Y. Chang, *Polym. Chem.* **2012**, *3*, 868–870.

[276] H. Lim, M. C. Cha, J. Y. Chang, *Macromol. Chem. Phys.* **2012**, *213*, 1385–1390.

[277] M. G. Schwab, A. Lennert, J. Pahnke, G. Jonschker, M. Koch, I. Senkovska, M. Rehahn, S. Kaskel, *J. Mater. Chem.* **2011**, *21*, 2131–2135.

[278] J. Chun, J. H. Park, J. Kim, S. M. Lee, H. J. Kim, S. U. Son, *Chem. Mater.* **2012**, *24*, 3458–3463.

[279] J.-X. Jiang, A. Laybourn, R. Clowes, Y. Z. Khimyak, J. Bacsa, S. J. Higgins, D. J. Adams, A. I. Cooper, *Macromolecules* **2010**, *43*, 7577–7582.

[280] Y. Morisaki, M. Gon, Y. Tsuji, Y. Kajiwara, Y. Chujo, *Macromol. Chem. Phys.* **2012**, *213*, 572–579.

[281] R. Dawson, A. Laybourn, Y. Z. Khimyak, D. J. Adams, A. I. Cooper, *Macromolecules* **2010**, *43*, 8524–8530.

[282] A. Patra, J.-M. Koenen, U. Scherf, *Chem. Commun.* **2011**, *47*, 9612–9614.

[283] J. R. Holst, E. Stockel, D. J. Adams, A. I. Cooper, *Macromolecules* **2010**, *43*, 8531–8538.

[284] R. Dawson, A. Laybourn, R. Clowes, Y. Z. Khimyak, D. J. Adams, A. I. Cooper, *Macromolecules* **2009**, *42*, 8809–8816.

[285] Q. Chen, M. Luo, T. Wang, J.-X. Wang, D. Zhou, Y. Han, C.-S. Zhang, C.-G. Yan, B.-H. Han, *Macromolecules* **2011**, *44*, 5573–5577.

[286] Q. Chen, J.-X. Wang, F. Yang, D. Zhou, N. Bian, X.-J. Zhang, C.-G. Yan, B.-H. Han, *J. Mater. Chem.* **2011**, *21*, 13554–13560.

[287] Q. Chen, Q. Wang, M. Luo, L.-J. Mao, C.-G. Yan, Z.-H. Li, B.-H. Han, *Polymer* **2012**, *53*, 2032–2037.

[288] K. V. Rao, S. Mohapatra, T. K. Maji, S. J. George, *Chem. - Eur. J.* **2012**, *18*, 4505–4509.

[289] K. V. Rao, S. Mohapatra, C. Kulkarni, T. K. Maji, S. J. George, *J. Mater. Chem.* **2011**, *21*, 12958–12963.

[290] L. Chen, Y. Yang, Z.-Q. Guo, D.-L. Jiang, *Adv. Mater.* **2011**, *23*, 3149–3154.

[291] B. G. Hauser, O. K. Farha, J. Exley, J. T. Hupp, *Chem. Mater.* **2013**, *25*, 12–16.

[292] J. Schmidt, M. Werner, A. Thomas, *Macromolecules* **2009**, *42*, 4426–4429.

[293] X. Liu, Y. Xu, D. Jiang, *J. Am. Chem. Soc.* **2012**, *134*, 8738–8741.

[294] Y.-H. Xu, L. Chen, Z.-Q. Guo, A. Nagai, D.-L. Jiang, *J. Am. Chem. Soc.* **2011**, *133*, 17622–17625.

[295] X. Liu, Y. Xu, Z. Guo, A. Nagai, D. Jiang, *Chem. Commun.* **2013**, *49*, 3233–3235.

[296] D. E. Demirocak, M. K. Ram, S. S. Srinivasan, D. Y. Goswami, E. K. Stefanakos, *J. Mater. Chem. A* **2013**, *1*, 13800–13806.

[297] W. G. Lu, D. Q. Yuan, D. Zhao, C. I. Schilling, O. Plietzsch, T. Muller, S. Brase, J. Guenther, J. Blumel, R. Krishna, Z. Li, H. C. Zhou, *Chem. Mater.* **2010**, *22*, 5964–5972.

[298] J. X. Jiang, F. Su, A. Trewin, C. D. Wood, N. L. Campbell, H. Niu, C. Dickinson, A. Y. Ganin, M. J. Rosseinsky, Y. Z. Khimyak, A. I. Cooper, *Angew. Chem. Int. Ed.* **2007**, *46*, 8574–8578.

[299] J. X. Jiang, F. Su, A. Trewin, C. D. Wood, H. Niu, J. T. A. Jones, Y. Z. Khimyak, A. I. Cooper, *J. Am. Chem. Soc.* **2008**, *130*, 7710–7720.

[300] S. Yuan, B. Dorney, D. White, S. Kirklin, P. Zapol, L. Yu, D.-J. Liu, *Chem. Commun.* **2010**, *46*, 4547–4549.

[301] O. Plietzsch, C. I. Schilling, T. Grab, S. L. Grage, A. S. Ulrich, A. Comotti, P. Sozzani, T. Muller, S. Braese, *New J. Chem.* **2011**, *35*, 1577–1581.

[302] P. Pandey, O. K. Farha, A. M. Spokoyny, C. A. Mirkin, M. G. Kanatzidis, J. T. Hupp, S. T. Nguyen, *J. Mater. Chem.* **2011**, *21*, 1700–1703.

[303] L.-H. Xie, M. P. Suh, *Chem. - Eur. J.* **2013**, *19*, 11590–11597.

[304] E. Stöckel, X. Wu, A. Trewin, C. D. Wood, R. Clowes, N. L. Campbell, J. T. A. Jones, Y. Z. Khimyak, A. D. J., A. I. Cooper, *Chem. Commun.* **2009**, 212–214.

[305] D. Tan, W. Fan, W. Xiong, H. Sun, Y. Cheng, X. Liu, C. Meng, A. Li, W.-Q. Deng, *Macromol. Chem. Phys.* **2012**, *213*, 1435–1440.

[306] T. Ben, H. Ren, S. Q. Ma, D. P. Cao, J. H. Lan, X. F. Jing, W. C. Wang, J. Xu, F. Deng, J. M. Simmons, S. L. Qiu, G. S. Zhu, *Angew. Chem. Int. Ed.* **2009**, *48*, 9457–9460.

[307] T. Ben, Y. Li, L. Zhu, D. Zhang, D. Cao, Z. Xiang, X. Yao, S. Qiu, *Energy Environ. Sci.* **2012**, *5*, 8370–8376.

[308] H. Ren, T. Ben, F. Sun, M. Guo, X. Jing, H. Ma, K. Cai, S. Qiu, G. Zhu, *J. Mater. Chem.* **2011**, *21*, 10348–10353.

[309] D. Yuan, W. Lu, D. Zhao, H.-C. Zhou, *Adv. Mater.* **2011**, *23*, 3723–3725.

[310] K. Zhang, D. Kopetzki, P. H. Seeberger, M. Antonietti, F. Vilela, *Angew. Chem. Int. Ed.* **2013**, *52*, 1432–1436.

[311] Y. Zhang, Y. Zhang, Y. L. Sun, X. Du, J. Y. Shi, W. D. Wang, W. Wang, *Chem. - Eur. J.* **2012**, *18*, 6328–6334.

[312] L. Chen, Y. Yang, D. Jiang, *J. Am. Chem. Soc.* **2010**, *132*, 9138–9143.

[313] X. Du, Y. Sun, B. Tan, Q. Teng, X. Yao, C. Su, W. Wang, *Chem. Commun.* **2010**, *46*, 970–972.

[314] J.-X. Jiang, C. Wang, A. Laybourn, T. Hasell, R. Clowes, Y. Z. Khimyak, J. Xiao, S. J. Higgins, D. J. Adams, A. I. Cooper, *Angew. Chem. Int. Ed.* **2011**, *50*, 1072–1075.

[315] Z. Xie, C. Wang, K. E. de Krafft, W. Lin, *J. Am. Chem. Soc.* **2011**, *133*, 2056–2059.

[316] J. P. Paraknowitsch, A. Thomas, J. Schmidt, *Chem. Commun.* **2011**, *47*, 8283–8285.

[317] Z. Xiang, D. Cao, *Macromol. Rapid Commun.* **2012**, *33*, 1184–1190.

[318] B. Kiskan, M. Antonietti, J. Weber, *Macromolecules* **2012**, *45*, 1356–1361.

[319] Y. Xu, A. Nagai, D. Jiang, *Chem. Commun.* **2013**, *49*, 1591–1593.

[320] J. Weber, A. Thomas, *J. Am. Chem. Soc.* **2008**, *130*, 6334–6335.

[321] B. Kiskan, J. Weber, *ACS Macro Lett.* **2012**, *1*, 37–40.

[322] S. Ren, R. Dawson, D. J. Adams, A. I. Cooper, *Polym. Chem.* **2013**, *4*, 5585–5590.

[323] Y. Kou, Y. Xu, Z. Guo, D. Jiang, *Angew. Chem. Int. Ed.* **2011**, *50*, 8753–8757.

[324] R. Dawson, D. J. Adams, A. I. Cooper, *Chem. Sci.* **2011**, *2*, 1173–1177.

[325] A. Modak, M. Nandi, J. Mondal, A. Bhaumik, *Chem. Commun.* **2012**, *48*, 248–250.

[326] M. H. Alkordi, R. R. Haikal, Y. S. Hassan, A.-H. Emwas, Y. Belmabkhout, *J. Mater. Chem. A* **2015**, *3*, 22584–22590.

[327] D. Tan, W. Fan, W. Xiong, H. Sun, A. Li, W. Deng, C. Meng, *Eur. Polym. J.* **2012**, *48*, 705–711.

[328] Z. Xiang, X. Zhou, C. Zhou, S. Zhong, X. He, C. Qin, D. Cao, *J. Mater. Chem.* **2012**, *22*, 22663–22669.

[329] J. H. Choi, K. M. Choi, H. J. Jeon, Y. J. Choi, Y. Lee, J. K. Kang, *Macromolecules* **2010**, *43*, 5508–5511.

[330] H. J. Jeon, J. H. Choi, Y. Lee, K. M. Choi, J. H. Park, J. K. Kang, *Adv. Energy Mater.* **2012**, *2*, 225–228.

[331] Z. Xiang, R. Mercado, J. M. Huck, H. Wang, Z. Guo, W. Wang, D. Cao, M. Haranczyk, B. Smit, *J. Am. Chem. Soc.* **2015**, *137*, 13301–13307.

[332] J.-X. Jiang, A. Trewin, F. Su, C. D. Wood, H. Niu, J. T. A. Jones, Y. Z. Khimyak, A. I. Cooper, *Macromolecules* **2009**, *42*, 2658–2666.

[333] X. Wang, Y. Zhao, L. Wei, C. Zhang, J.-X. Jiang, *J. Mater. Chem. A* **2015**, *3*, 21185–21193.

[334] T. Islamoglu, T. Kim, Z. Kahveci, O. M. El-Kadri, H. M. El-Kaderi, *J. Phys. Chem. C* **2016**, *120*, 2592–2599.

[335] W. Lu, D. Yuan, J. Sculley, D. Zhao, R. Krishna, H.-C. Zhou, *J. Am. Chem. Soc.* **2011**, *133*, 18126–18129.

[336] W. Lu, W. M. Verdegaal, J. Yu, P. B. Balbuena, H.-K. Jeong, H.-C. Zhou, *Energy Environ. Sci.* **2013**, *6*, 3559–3564.

[337] W. Lu, J. P. Sculley, D. Yuan, R. Krishna, Z. Wei, H.-C. Zhou, *Angew. Chem. Int. Ed.* **2012**, *51*, 7480–7484.

[338] J. Weber, K.-D. Kreuer, J. Maier, A. Thomas, *Adv. Mater.* **2008**, *20*, 2595–2598.

[339] D. Mecerreyes, H. Grande, O. M. E. Ochoteco, R. Marcilla, , I. Cantero, *Chem. Mater.* **2004**, *16*, 604–607.

[340] M. G. Rabbani, H. M. El-Kaderi, *Chem. Mater.* **2011**, *23*, 1650–1653.

[341] M. G. Rabbani, A. K. Sekizkardes, O. M. El-Kadri, B. R. Kaafarani, H. M. El-Kaderi, *J. Mater. Chem.* **2012**, *22*, 25409–25417.

[342] M. G. Rabbani, H. M. El-Kaderi, *Chem. Mater.* **2012**, *24*, 1511–1517.

[343] A. K. Sekizkardes, T. Islamoglu, Z. Kahveci, H. M. El-Kaderi, *J. Mater. Chem. A* **2014**, *2*, 12492–12500.

[344] A. K. Sekizkardes, S. Altarawneh, Z. Kahveci, T. Islamoglu, H. M. El-Kaderi, *Macromolecules* **2014**, *47*, 8328–8334.

[345] M. G. Rabbani, T. E. Reich, R. M. Kassab, K. T. Jackson, H. M. El-Kaderi, *Chem. Commun.* **2012**, *48*, 1141–1143.

[346] V. S. P. K. Neti, J. Wang, S. Deng, L. Echegoyen, *RSC Adv.* **2015**, *5*, 10960–10963.

[347] M. Zhang, Z. Perry, J. Park, H.-C. Zhou, *Polymer* **2014**, *55*, 335 – 339.

[348] A. K. Sekizkardes, J. T. Culp, T. Islamoglu, A. Marti, D. Hopkinson, C. Myers, H. M. El-Kaderi, H. B. Nulwala, *Chem. Commun.* **2015**, *51*, 13393–13396.

[349] H. A. Patel, S. Hyun Je, J. Park, D. P. Chen, Y. Jung, C. T. Yavuz, A. Coskun, *Nat. Commun.* **2013**, *4*, 4:1357.

[350] N. Manoranjan, S. I. Woo, *RSC Adv.* **2016**, *6*, 93463–93468.

[351] P. Arab, M. G. Rabbani, A. K. Sekizkardes, T. Islamoglu, H. M. El-Kaderi, *Chem. Mater.* **2014**, *26*, 1385–1392.

[352] P. Arab, E. Parrish, T. Islamoglu, H. M. El-Kaderi, *J. Mater. Chem. A* **2015**, *3*, 20586–20594.

[353] Z. Yang, H. Zhang, B. Yu, Y. Zhao, Z. Ma, G. Ji, B. Han, Z. Liu, *Chem. Commun.* **2015**, *51*, 11576–11579.

[354] J. Lu, J. Zhang, *J. Mater. Chem. A* **2014**, *2*, 13831–13834.

[355] Q.-Q. Dang, X.-M. Wang, Y.-F. Zhan, X.-M. Zhang, *Polym. Chem.* **2016**, *7*, 643–647.

[356] D.-J. Liaw, K.-L. Wang, Y.-C. Huang, K.-R. Lee, J.-Y. Lai, C.-S. Ha, *Prog. Polym. Sci.* **2012**, *37*, 907–974.

[357] W. Chen, W. Yan, S. Wu, Z. Xu, K. W. K. Yeung, C. Yi, *Macromol. Chem. Phys.* **2010**, *211*, 1803–1813.

[358] Z. Song, H. Zhan, Y. Zhou, *Angew. Chem. Int. Ed.* **2010**, *49*, 8444–8448.

[359] J. Fang, H. Kita, K.-i. Okamoto, *Macromolecules* **2000**, *33*, 4639–4646.

[360] H. K. Young, W. W. Owen, *J. Am. Chem. Soc.* **1990**, *112*, 4593–4594.

[361] H. K. Young, *J. Polym. Sci. Part A: Polym. Chem.* **1998**, *36*, 1685–1698.

[362] J. Weber, M. Antonietti, A. Thomas, *Macromolecules* **2008**, *41*, 2880–2885.

[363] Z. G. Wang, B. F. Zhang, H. Yu, L. X. Sun, C. L. Jiao, W. S. Liu, *Chem. Commun.* **2010**, *46*, 7730–7732.

[364] C. Shen, Y. Bao, Z. Wang, *Chem. Commun.* **2013**, *49*, 3321–3323.

[365] Z. Wang, B. Zhang, H. Yu, G. Li, Y. Bao, *Soft Matter* **2011**, *7*, 5723–5730.

[366] O. K. Farha, A. M. Spokoyny, B. G. Hauser, Y. S. Bae, S. E. Brown, R. Q. Snurr, C. A. Mirkin, J. T. Hupp, *Chem. Mater.* **2009**, *21*, 3033–3035.

[367] O. K. Farha, Y.-S. Bae, B. G. Hauser, A. M. Spokoyny, R. Q. Snurr, C. A. Mirkin, J. T. Hupp, *Chem. Commun.* **2010**, *46*, 1056–1058.

[368] K. V. Rao, R. Haldar, C. Kulkarni, T. K. Maji, S. J. George, *Chem. Mater.* **2012**, *24*, 969–971.

[369] K. V. Rao, R. Haldar, T. K. Maji, S. J. George, *Polymer* **2014**, *55*, 1452–1458.

[370] Y.-L. Luo, B.-Y. Li, L.-Y. Liang, B.-E. Tan, *Chem. Commun.* **2011**, *47*, 7704–7706.

[371] Y. Yang, Q. Zhang, Z. Zhang, S. Zhang, *J. Mater. Chem. A* **2013**, *1*, 10368–10374.

[372] G. Li, Z. Wang, *Macromolecules* **2013**, *46*, 3058–3066.

[373] C. Shen, Z. Wang, *J. Phys. Chem. C* **2014**, *118*, 17585–17593.

[374] G. Li, B. Zhang, J. Yan, Z. Wang, *J. Mater. Chem. A* **2016**, *4*, 11453–11461.

[375] S. Lowell, J. E. Shields, M. A. Thomas, M. Thommes, *Characterization of Porous Solids and Powders: Surface Area, Pore Size and Density*, Springer, **2006**.

[376] M. Witanowski, *Pure Appl. Chem.* **1974**, *37*, 225–233.

[377] S. P. Koenig, L. Wang, J. Pellegrino, J. S. Bunch, *Nat. Nanotechnol.* **2012**, *7*, 728–732.

[378] J. Moellmer, E. B. Celer, R. Luebke, A. J. Cairns, R. Staudt, M. Eddaoudi, M. Thommes, *Microporous Mesoporous Mater.* **2009**, *129*, 345–353.

[379] P. I. Ravikovitch, A. Vishnyakov, R. Russo, A. V. Neimark, *Langmuir* **2000**, *16*, 2311–2320.

[380] K. S. W. Sing, R. I. Williams, *Part. Part. Syst. Charact.* **2004**, *21*, 71–79.

[381] J. Jagiello, M. Thommes, *Carbon* **2004**, *42*, 1227–1232.

[382] A. Vishnyakov, P. I. Ravikovitch, A. V. Neimark, *Langmuir* **1999**, *15*, 8736–8742.

[383] T. Morimoto, K. Miura, *Langmuir* **1985**, *1*, 658–662.

[384] A. C. Zettlemoyer, A. Chand, E. Gamble, *J. Am. Chem. Soc.* **1950**, *72*, 2752–2757.

[385] P. D. Sullivan, B. R. Stone, Z. Hashisho, M. J. Rood, *Adsorption* **2007**, *13*, 173–189.

[386] M. H. Polley, W. D. Schaeffer, W. R. Smith, *J. Phys. Chem.* **1953**, *57*, 469–471.

[387] L. Gardner, M. Kruk, M. Jaroniec, *J. Phys. Chem. B* **2001**, *105*, 12516–12523.

[388] E. Greenhalgh, E. Redman, *J. Phys. Chem.* **1967**, *71*, 1151–1152.

[389] C. T. Kresge, M. E. Leonowicz, W. J. Roth, J. C. Vartuli, J. S. Beck, *Nature* **1992**, *359*, 710–712.

[390] N. Ritter, I. Senkovska, S. Kaskel, J. Weber, *Macromol. Rapid Commun.* **2011**, *32*, 438–443.

[391] J. Schmidt, J. Weber, J. D. Epping, M. Antonietti, A. Thomas, *Adv. Mater.* **2009**, *21*, 702–705.

[392] Y. Tsujita, *Prog. Polym. Sci.* **2003**, *28*, 1377–1401.

[393] A. L. McClellan, H. F. Harnsberger, *J. Colloid Interface Sci.* **1967**, *23*, 577–599.

[394] I. Langmuir, *J. Am. Chem. Soc.* **1918**, *40*, 1361–1402.

[395] J. Rouquerol, P. Llewellyn, R. F., *Stud. Surf. Sci. Catal.* **2007**, *160*, 49–56.

[396] S. Brunauer, P. H. Emmett, E. Teller, *J. Am. Chem. Soc.* **1938**, *60*, 309–319.

[397] Y.-S. Bae, A. O. Yazaydin, R. Q. Snurr, *Langmuir* **2010**, *26*, 5475–5483.

[398] K. S. Walton, R. Q. Snurr, *J. Am. Chem. Soc.* **2007**, *129*, 8552–8556.

[399] G. Horvath, K. Kawazoe, *J. Chem. Eng. Jpn.* **1983**, *16*, 470–475.

[400] A. Saito, H. C. Foley, *AIChE J.* **1991**, *37*, 429–436.

[401] M. M. Dubinin, L. V. Radushkevich, *Dokl. Akad. Nauk SSSR* **1947**, *55*, 327–329.

[402] M. M. Dubinin, V. A. Astakhov, *Dokl. Akad. Nauk SSSR* **1971**, 5–11.

[403] E. P. Barrett, L. G. Joyner, P. P. Halenda, *J. Am. Chem. Soc.* **1951**, *73*, 373–380.

[404] M. Thommes, R. Koehn, M. Froeba, *J. Phys. Chem. B* **2000**, *104*, 7932–7943.

[405] M. Thommes, G. H. Findenegg, *Langmuir* **1994**, *10*, 4270–4277.

[406] M. Thommes, R. Koehn, M. Froeba, *Appl. Surf. Sci.* **2002**, *196*, 239–249.

[407] B. C. Lippens, J. H. de Boer, *J. Catal.* **1965**, *4*, 319–323.

[408] P. I. Ravikovitch, S. C. O. Domhnaill, A. V. Neimark, F. Schueth, K. K. Unger, *Langmuir* **1995**, *11*, 4765–4772.

[409] P. I. Ravikovitch, D. Wei, W. T. Chueh, G. L. Haller, A. V. Neimark, *J. Phys. Chem. B* **1997**, *101*, 3671–3679.

[410] P. I. Ravikovitch, A. Vishnyakov, A. V. Neimark, *Phys. Rev. E: Stat. Nonlinear Soft Matter Phys.* **2001**, *64*, 011602/01–011602/20.

[411] A. V. Neimark, P. I. Ravikovitch, M. Grün, F. Schüth, K. K. Unger, *J. Colloid Interface Sci.* **1998**, *207*, 159–169.

[412] P. I. Ravikovitch, A. V. Neimark, *Langmuir* **2006**, *22*, 11171–11179.

[413] H. W. Pennline, J. S. Hoffman, M. L. Gray, R. V. Siriwardane, F. D. J., G. A. Richards, *NETL In-house Postcombustion Sorbent-Based Carbon Dioxide Capture Research*, Annual IEP Contractors Meeting, **2009**.

[414] A. L. Myers, J. M. Prausnitz, *AIChE J.* **1965**, *11*, 121–127.

[415] Z. Xiang, X. Peng, X. Cheng, X. Li, D. Cao, *J. Phys. Chem. C* **2011**, *115*, 19864–19871.

[416] T. Vuong, P. A. Monson, *Langmuir* **1996**, *12*, 5425–5432.

[417] R. Berger, J. Hauser, G. Labat, E. Weber, J. Hulliger, *CrystEngComm* **2012**, *14*, 768–770.

[418] C. Fremerey, *Bachelor Thesis*, **2009**.

[419] A. Moncomble, P. Le Floch, C. Gosmini, *Chem. - Eur. J.* **2009**, *15*, 4770–4774.

[420] H. Turkmen, B. Cetinkaya, *J. Organomet. Chem.* **2006**, *691*, 3749–3759.

[421] D. R. Anderson, J. M. Holovka, *J. Polym. Sci.* **1966**, *4*, 1689–1702.

[422] A. K. Mohamed, N. Auner, M. Bolte, *Acta Crystallogr. Sect. E: Struct. Rep. Online* **2003**, *59*, o476–o477.

[423] J. H. Forsberg, V. T. Spaziano, S. P. Klump, K. M. Sanders, *J. Heterocycl. Chem.* **1988**, *25*, 767–770.

[424] J. H. Forsberg, V. T. Spaziano, T. M. Balasubramanian, G. K. Liu, S. A. Kinsley, C. A. Duckworth, J. J. Poteruca, P. S. Brown, J. L. Miller, *J. Org. Chem.* **1987**, *52*, 1017–1021.

[425] A. Diaz-Ortiz, A. de la Hoz, A. Moreno, A. Sanchez-Migallon, G. Valiente, *Green Chem.* **2002**, *4*, 339–343.

[426] C. Herrmann, *Bachelor Thesis*, **2010**.

[427] F. C. Schaefer, A. P. Krapcho, *J. Org. Chem.* **1962**, *27*, 1255–1258.

[428] L. G. MacDonald, G. S. Perry, J. Smith, S. D. Wilcox, *Thermochim. Acta* **1986**, *97*, 29–35.

[429] S. J. Shaw, G. S. Perry, *Thermochim. Acta* **1989**, *155*, 87–96.

[430] I. N. Nikonova, S. P. Pavlenko, A. G. Bergman, *Bull.Acad. Sci. USSR Classe Sci. Chim.* **1941**, 391–400.

[431] A. A. Coelho, *J. Appl. Crystallogr.* **2003**, *36*, 86–95.

[432] E. Unsal, M. Cakmak, *Macromolecules* **2013**, *46*, 8616–8627.

[433] C. E. Sroog, *J. Polym. Sci. Macromol. Rev.* **1976**, *11*, 161–208.

[434] H.-J. Yen, S.-M. Guo, J.-M. Yeh, G.-S. Liou, *J. Polym. Sci. Part A: Polym. Chem.* **2011**, *49*, 3637–3646.

[435] A. Ghosh, S. K. Sen, S. Banerjee, B. Voit, *RSC Adv.* **2012**, *2*, 5900–5926.

[436] Y. Zheng, Y. Zhai, G. Li, B. Guo, X. Zeng, L. Wang, H. Yu, J. Guo, *J. Appl. Polym. Sci.* **2011**, *121*, 702–706.

[437] C. E. Sroog, A. L. Endrey, S. V. Abramo, C. E. Berr, W. M. Edwards, K. L. Olivier, *J. Polym. Sci.* **1965**, *3*, 1373–1390.

[438] G. M. Bower, L. W. Frost, *J. Polym. Sci.* **1963**, *1*, 3135–3150.

[439] T. Takekoshi, *Polyimides: Fundamentals and Applications*, (Ghosh M. K., Mittal K. L., ed.), Marcel Dekker, New York, Chapter 2, **1996**.

[440] L. W. Frost, I. Kesse, *J. Appl. Polym. Sci.* **1964**, *8*, 1039–1051.

[441] T. Kaneda, T. Katsura, K. Nakagawa, H. Makino, M. Horio, *J. Appl. Polym. Sci.* **1986**, *32*, 3133–3149.

[442] H. Inoue, Y. Sasaki, T. Ogawa, *J. Appl. Polym. Sci.* **1996**, *60*, 123–131.

[443] Z. Y. Wang, Y. Qi, J. P. Gao, G. G. Sacripante, P. R. Sundararajan, J. D. Duff, *Macromolecules* **1998**, *31*, 2075–2079.

[444] D.-J. Liaw, B.-Y. Liaw, L.-J. Li, B. Sillion, R. Mercier, R. Thiria, H. Sekiguchi, *Chem. Mater.* **1998**, *10*, 734–739.

[445] Y. Imai, N. N. Maldar, M. Kakimoto, *J. Polym. Sci. Polym. Chem. Ed.* **1984**, *22*, 2189–2196.

[446] R. Giesa, U. Keller, P. Eiselt, H. W. Schmidt, *J. Polym. Sci. Part A: Polym. Chem.* **1993**, *31*, 141–151.

[447] A. L. Endrey, *US 3179631*, **1965**.

[448] A. L. Endrey, *US 3179630*, **1965**.

[449] Y. Zhao, J. Li, C. Li, K. Yin, D. Ye, X. Jia, *Green Chem.* **2010**, *12*, 1370–1372.

[450] G. Gattuso, G. Grasso, N. Marino, A. Notti, A. Pappalardo, S. Pappalardo, M. F. Parisi, *Eur. J. Org. Chem.* **2011**, *2011*, 5696–5703.

[451] C. Bao, M. Jin, R. Lu, Z. Song, X. Yang, D. Song, T. Xu, G. Liu, Y. Zhao, *Tetrahedron* **2007**, *63*, 7443–7448.

[452] S. Kotha, D. Kashinath, K. Lahiri, R. B. Sunoj, *Eur. J. Org. Chem.* **2004**, 4003–4013.

[453] S. Kotha, K. Chakraborty, E. Brahmachary, *Synlett* **1999**, 1621–1623.

[454] S. S. Elmorsy, A. Pelter, K. Smith, *Tetrahedron Lett.* **1991**, *32*, 4175–4176.

[455] C. Koelmel, C. Ochsenfeld, R. Ahlrichs, *Theor. Chim. Acta* **1992**, *82*, 271–284.

[456] J. H. Gorvin, *J. Chem. Soc. Perkin Trans. 1* **1988**, 1331–1335.

[457] K. R. Idzik, P. Rapta, P. J. Cywinski, R. Beckert, L. Dunsch, *Electrochim. Acta* **2010**, *55*, 4858–4864.

[458] A. Ranganathan, B. C. Heisen, I. Dix, F. Meyer, *Chem. Commun.* **2007**, 3637–3639.

[459] T. Ishi-i, R. Kuwahara, A. Takata, Y. Jeong, K. Sakurai, S. Mataka, *Chem. - Eur. J.* **2006**, *12*, 763–776.

[460] S. Lee, M. Jorgensen, J. F. Hartwig, *Org. Lett.* **2001**, *3*, 2729–2732.

[461] F. Li, L. Huang, Y. Shi, X. Jin, Z. Wu, Z. Shen, K. Chuang, R. E. Lyon, F. W. Harris, S. Z. D. Cheng, *J. Macromol. Sci. Part B: Phys.* **1999**, *B38*, 107–122.

[462] W. Xie, R. Heltsley, X. Cai, F. Deng, J. Liu, C. Lee, W.-P. Pan, *J. Appl. Polym. Sci.* **2002**, *83*, 1219–1227.

[463] H. B. Park, C. H. Jung, Y. M. Lee, A. J. Hill, S. J. Pas, S. T. Mudie, E. Van Wagner, B. D. Freeman, D. J. Cookson, *Science* **2007**, *318*, 254–258.

[464] W.-C. Song, X.-K. Xu, Q. Chen, Z.-Z. Zhuang, X.-H. Bu, *Polym. Chem.* **2013**, *4*, 4690–4696.

[465] E. Neofotistou, C. D. Malliakas, P. N. Trikalitis, *Chem. - Eur. J.* **2009**, *15*, 4523–4527.

[466] H.-S. Lee, A. S. Badami, A. Roy, J. E. McGrath, *J. Polym. Sci. Part A: Polym. Chem.* **2007**, *45*, 4879–4890.

[467] J. Y. Park, K. O. Oh, J. C. Won, H. Han, H. M. Jung, Y. S. Kim, *J. Mater. Chem.* **2012**, *22*, 16005–16010.

[468] A. Damiani, E. Giglio, A. Ripamonti, *Acta Cryst.* **1965**, *19*, 161–168.

[469] J.-S. Huang, M.-K. Li, Y.-Y. Yang, S. W. Ng, E. R. T. Tiekink, *Acta Crystallogr. Sect. E: Struct. Rep. Online* **2012**, *68*, o1463–o1464.

[470] V. R. Thalladi, M. Muthuraman, A. Nangia, G. R. Desiraju, *Acta Crystallogr. Sect. C: Cryst. Struct. Commun.* **1999**, *C55*, 698–700.

[471] D. Belitskus, G. A. Jeffrey, *Spectrochim. Acta* **1965**, *21*, 1563–1567.

[472] J. N. Varghese, A. M. O'Connell, E. N. Maslen, *Acta Cryst.* **1977**, *B33*, 2102–2108.

[473] M. Guin, G. N. Patwari, S. Karthikeyan, K. S. Kim, *Phys. Chem. Chem. Phys.* **2009**, *11*, 11207–11212.

[474] K. Mereiter, *Acta Crystallogr. Sect. E: Struct. Rep. Online* **2011**, *67*, o2321–o2322.

[475] D. Schollmeyer, O. V. Shishkin, T. Ruehl, M. O. Vysotsky, *CrystEngComm* **2008**, *10*, 715–723.

[476] P. Metrangolo, G. Resnati, *Chem. - Eur. J.* **2001**, *7*, 2511–2519.

[477] P. Metrangolo, G. Resnati, T. Pilati, R. Liantonio, F. Meyer, *J. Polym. Sci. Part A: Polym. Chem.* **2006**, *45*, 1–15.

[478] B. M. Fung, A. K. Khitrin, K. Ermolaev, *J. Magn. Reson.* **2000**, *142*, 97–101.

[479] G. R. Fulmer, A. J. M. Miller, N. H. Sherden, H. E. Gottlieb, A. Nudelman, B. M. Stoltz, J. E. Bercaw, K. I. Goldberg, *Organometallics* **2010**, *29*, 2176–2179.

[480] P. E. Werner, L. Eriksson, M. Westdahl, *J. Appl. Crystallogr.* **1985**, *18*, 367–370.

[481] J. W. Visser, *J. Appl. Crystallogr.* **1969**, *2*, 89–95.

[482] A. Boultif, D. Louer, *J. Appl. Crystallogr.* **1991**, *24*, 987–993.

[483] G. S. Pawley, *J. Appl. Crystallogr.* **1981**, *14*, 357–361.

[484] A. A. Coelho, *TOPAS-Academic 5.0, Coelho Software, Brisbane, Australia*, **2012**.

[485] J. P. Perdew, K. Burke, M. Ernzerhof, *Phys. Rev. Lett.* **1996**, *77*, 3865–3868.

[486] S. Wu, Y. Liu, G. Yu, J. Guan, C. Pan, Y. Du, X. Xiong, Z. Wang, *Macromolecules* **2014**, *47*, 2875–2882.

[487] X. Zhu, C.-L. Do-Thanh, C. R. Murdock, K. M. Nelson, C. Tian, S. Brown, S. M. Mahurin, D. M. Jenkins, J. Hu, B. Zhao, H. Liu, S. Dai, *ACS Macro Letters* **2013**, *2*, 660–663.

10 Abbreviations

APTES	(3-aminopropyl)triethoxysilane
BDBA	benzene-1,4-dibronic acid
BET	Brunauer-Emmett-Teller
BILP	benzimidazole-linked polymer
BLP	borazine-linked polymer
BPDA	3,3',4,4'-benzophenonetetracarboxylic dianhydride
CCS	carbon dioxide capture and sequestration
CMP	conjugated microporous polymer
COF	covalent organic framework
CP	cross polarization
CTF	covalent triazine-based organic framework
dba	dibenzylideneacetone
DCB	dicyanobenzene
DCBP	4,4'-dicyanobiphenyl
DCBI	2-(*p*-cyanophenyl)-1*H*-benzo[*d*]imidazole-5-carbonitrile
DCC	dynamic covalent chemistry
DETA	diethylene triamine
DETH	2,5-diethoxyterephthalohydrazide
DFT	density functional theory
DMAC	*N*,*N*-dimethylacetamide
DMF	*N*,*N*-dimethylformamide
DMSO	dimethylsulphoxide
dobdc	2,5-dioxido-1,4-benzenedicarboxylate
dobpdc	4,4'-dioxido-3,3'-biphenyldicarboxylate
DPB	4,4'-diphenylbutadiynebis(boronic acid)
GAI	Generalized Adsorption Isotherm

GCMC	Grand canonical Monte Carlo
GDS	Gibbs dividing surface
GOF	goodness of fit
HATP	2,3,6,7,10,11-hexaaminotriphenylene
HBF	heptazine-based 2D-layered polymer frameworks
HCP	hypercrosslinked polymer
HHTP	2,3,6,7,10,11-hexahydroxytriphenylene
HIDA	4,4'-(hexafluoroisopropylidene)diphthalic anhydride
H_4TTDB	thieno[3,2-*b*]thiophene-2,5-diboronic acid
IAST	ideal adsorbed solution theory
IUPAC	International Union of Pure and Applied Chemistry
LiHMDS	lithium bis(trimethylsilyl)amide
MAS	magic angle spinning
MD	molecular dynamics
Me-CTF	methylated covalent triazine-based framework
Me_2-DCBP	2,2'-dimethyl-4,4'-dicyanobiphenyl
MOF	metal-organic framework
NMP	*N*-methyl-2-pyrrolidone
NMR	nuclear magnetic resonance
NLDFT	non-linear density functional theory
NTDA	naphthalene tetracarboxylic acid dianhydride
ODA	4,4'-oxydiphthalic anhydride
PAE	poly(aryleneethynylene)
PAF	porous aromatic framework
PDBA	2,7-pyrenediyldiboronic acid
PIM	polymer of intrinsic microporosity
PMDA	pyromellitic dianhydride
POP	porous organic polymer

PPN	porous polymer network
PSD	pore size distribution
PTDA	perylenetetracarboxylic acid dianhydride
PTFE	poly(tetraflouroehylene)
QSDFT	quenched solid density functional theory
SDA	4,4'-sulfonyldiphthalic anhydride
SEM	scanning electron microscope
STP	standard temperature and pressure
TABF	2,2',7,7'-tetraaminospirobifluorene
TAPB	1,3,5-tris(*p*-aminophenyl)benzene
TAPM	tetrakis(*p*-aminophenyl)methane
TAPA	tris(*p*-aminophenyl)amine
TAPAD	1,3,5,7-tetrakis(*p*-aminophenyl)adamantane
TAPT	2,4,6-tris(*p*-aminophenyl)-1,3,5-triazine
TAT	2,6,12-triaminotriptycene
TBPT	2,4,6-tris(*p*-bromophenyl)-1,3,5-triazine
TCNQ	tetracyanoquinodimethane
TFMS	trifluoromethanesulfonic acid
TFPM	tetrakis(*p*-formylphenyl)methane
THF	tetrahydrofuran
TLC	thin layer chromatography
TPI	triazine-based polyimide
TPT	2,4,6-triphenyltriazine
TNPM	tetrakis(*p*-nitrophenyl)methane
XRD	X-ray diffraction

11 Danksagung

Mein besonderer Dank gilt meinem Doktorvater Prof. Dr. Jürgen Senker für die Möglichkeit zur Promotion und die Überlassung dieses interessanten und vielseitigen Themas. Ich danke ihm für die investierte Zeit für die vielen produktiven und lehrreichen Diskussionen, für seine Unterstützung während meiner Promotionszeit, für die hervorragenden Arbeitsbedingungen am Lehrstuhl AC III, sowie nicht zuletzt für die große gewährte Freiheit bei meiner wissenschaftlichen Arbeit.

Ich danke dem internationalen Doktorandenkolleg „Struktur, Reaktivität und Eigenschaften Oxidischer Materialien“ im Rahmen des Elitenetzwerks Bayern (ENB) sowie der Deutschen Forschungsgemeinschaft (DFG; SE 1417/5-1 und SFB 840) für die finanzielle Unterstützung dieser Arbeit.

Ich danke meinen Kollegen Dr. Yamini Avadhut, Beate Bojer, Dr. Dunja Hirsemann, Dr. Maria Jordan, Dr. Caroline Keenan, Sonja Lutschinger, Dr. Lena Seyfarth, Dr. Renée Siegel, Dr. Nadine Wedel, Dr. Tim Ahnfeldt, Kilian Bärwinkel, Dominik Greim, Daniel Gunzelmann, Tobias Kemnitzer, Paul Niemietz, Dr. Jan Seyfarth, Dr. Marko Schmidt und Dr. Johannes Wittmann für die schöne Zeit - während und neben dem Laboralltag - am Lehrstuhl AC III.
Mein spezieller Dank geht an dieser Stelle an meine langjährigen Laborkollegen Dr. Nadine Wedel, Paul Niemietz und Dr. Marko Schmidt im „Labor, da ganz hinten im Eck“, für die vielen aufschlussreichen Gespräche über mehr oder auch weniger wissenschaftliche Themen, für die Versorgung mit Schokolade falls es nötig war, für die vorzügliche Musikauswahl (ganz besonders freitags), für lebensbereichernde Weisheiten zitiert aus ausgesuchten Werken internationaler Nischenliteratur und, nicht zuletzt, für ihre Hilfe bei den vielen Herausforderungen im täglichen Laboralltag.

Ich danke Prof. Dr. Bettina Lotsch und Prof. Dr. Wolfgang Schnick sowie Dr. Nicole Braml, Dr. Sophia Makowski, Dr. Katharina Schwinghammer, Dr. Eva Zeuner und Dr. Stephan Hug für die sehr hilfreichen Diskussionen und den produktiven Gedankenaustausch während unserer „CN-Meetings“ an der LMU München und der Universität Bayreuth.

Mein großer Dank gilt Dr. Thomas Martin und Dr. Wolfgang Milius am Lehrstuhl für Anorganische Chemie I für ihre Unterstützung bei diversen Röntgenkristall-strukturanalysen sowie für ihre kompetente Hilfe bei allen meinen Fragen zu diesen.

Ich möchte mich ganz besonders bei Lena Geiling am Lehrstuhl für Anorganische Chemie I für die Durchführung der sehr vielen Gasadsorptionsmessungen sowie für die Aufnahmen am Rasterelektronenmikroskop bedanken.
Ebenfalls danken möchte ich Dieter Will am Lehrstuhl für Anorganische Chemie I für die Durchführung der thermogravimetrischen Analysen.
Ich danke Petra Seider und Iris Raithel für ihre unkomplizierte und freundliche Hilfe bei diversen bürokratischen und verwaltungstechnischen Angelegenheiten.
Ich danke Anna-Maria Dietel am Lehrstuhl für Anorganische Chemie II für die Durchführung der Elementaranalysen.
Ebenfalls möchte ich an dieser Stelle Dr. Ulrike Lacher und Kerstin Hannemann am Lehrstuhl für Organische Chemie I für zahlreiche MS- und NMR-Messungen danken.

Ich bedanke mich bei meinen Praktikantinnen und Praktikanten für ihre Beiträge zu dieser Arbeit. Speziell danken möchte ich an dieser Stelle Christina Herrmann und Christian Fremerey, die im Rahmen ihrer Bachelorarbeiten besonders zum Erfolg dieser Arbeit beigetragen haben.

Ich danke Tamara Ackermann und Dr. Bertram Barnickel für den produktiven Austausch über diverse Synthesen und die praktischen Tipps aus der „Trickkiste“ des organischen Chemikers.

Mein großer Dank geht an dieser Stelle auch an alle Mitglieder des Lehrstuhls Anorganische Chemie I für die gute Zusammenarbeit in angenehmer Arbeitsatmosphäre während meiner Zeit in Bayreuth. Die gefühlt unzähligen „Grillinger“ und die obligatorische Kaffeepause bleiben unvergessen!

Ich möchte mich bei allen Freunden und Kollegen für die vielen wunderbaren Abende - auf der AC-Terrasse, auf diversen Festen und Feiern, im Hofgarten oder wo auch immer sonst - bedanken. Ihr habt mein Leben in dieser Stadt und an dieser Universität bereichert. Ich werde diese schöne Zeit für immer in guter Erinnerung behalten.

Ganz besonders danken möchte ich meinen Eltern für ihre große Unterstützung vor, während und nach meiner Zeit in Bayreuth, ohne die weder mein Studium noch meine Promotion möglich gewesen wären.

In diesen letzten Zeilen möchte ich mich bei meiner Frau Susanne für ihre Unterstützung während meines Studiums und der gesamten Promotion bedanken. Susanne, ich danke dir für dein Verständnis, deine Geduld, dein offenes Ohr an jedem einzelnen Tag und dafür, dass du in all den Jahren immer an mich geglaubt hast. Ich bin glücklich, einen Menschen wie dich an meiner Seite zu haben.

12 (Eidesstattliche) Versicherungen und Erkärungen

(§ 8 Satz 2 Nr. 3 PromO Fakultät)

Hiermit versichere ich eidesstattlich, dass ich die Arbeit selbständig verfasst und keine anderen als die von mir angegebenen Quellen und Hilfsmittel benutzt habe (vgl. Art. 64 Abs. 1 Satz 6 BayHSchG).

(§ 8 Satz 2 Nr. 3 PromO Fakultät)

Hiermit erkläre ich, dass ich die Dissertation nicht bereits zur Erlangung eines akademischen Grades eingereicht habe und dass ich nicht bereits diese oder eine gleichartige Doktorprüfung endgültig nicht bestanden habe.

(§ 8 Satz 2 Nr. 4 PromO Fakultät)

Hiermit erkläre ich, dass ich Hilfe von gewerblichen Promotionsberatern bzw. –vermittlern oder ähnlichen Dienstleistern weder bisher in Anspruch genommen habe noch künftig in Anspruch nehmen werde.

(§ 8 Satz 2 Nr. 7 PromO Fakultät)

Hiermit erkläre ich mein Einverständnis, dass die elektronische Fassung der Dissertation unter Wahrung meiner Urheberrechte und des Datenschutzes einer gesonderten Überprüfung unterzogen werden kann.

(§ 8 Satz 2 Nr. 8 PromO Fakultät)

Hiermit erkläre ich mein Einverständnis, dass bei Verdacht wissenschaftlichen Fehlverhaltens Ermittlungen durch universitätsinterne Organe der wissenschaftlichen Selbstkontrolle stattfinden können.

…….....

Ort, Datum, Unterschrift